THE UNIVERSITY
of ADELAIDE

Faculty of Sciences
School of Physical Sciences
Department of Physics

Strangeness and Charge Symmetry Violation in Nucleon Structure

---

Phiala Elisabeth Shanahan

Supervisors:
Prof. Anthony Thomas
Dr. Ross Young

March 2015

Abstract

The role of strange quarks in generating the structure of the nucleon provides a key testing-ground for our understanding of Quantum Chromodynamics (QCD). Because the nucleon has zero net strangeness, strange observables give tremendous insight into the nature of the vacuum; they can only arise through quantum fluctuations in which strange-antistrange quark pairs are generated. Strange observables are also relevant to searches for physics beyond the Standard Model; the role of the strange quark in generating the nucleon mass—encoded in the strange sigma term—is essential information for the interpretation of dark matter direct-detection experiments. For these reasons, strangeness in the nucleon is currently a particular focus of the nuclear physics community.

We use the numerical lattice gauge theory approach to QCD, and the chiral perturbation theory formalism, to build a clear picture of the role of strange quarks in various nucleon-structure observables. A detailed analysis of the octet baryon masses provides precise new values of the nucleon sigma terms. By combining experimental and lattice input, we deduce the strange electromagnetic form factors of the nucleon over a far larger range of momentum-scales than is accessible experimentally. Our calculation of the strange magnetic moment is an order of magnitude more precise than the closest experimental result.

Until now, the dominant uncertainty in experimental determinations of the strange proton form factors has come from a lack of knowledge about the size of charge symmetry violation (CSV) in these quantities. CSV effects quantify the breaking of the approximate SU(2)-flavour symmetry of the up and down quarks. As well as their relevance to experimental determinations of nucleon strangeness, the precise knowledge of CSV observables has, with increasing experimental precision, become essential to the interpretation of many searches for physics beyond the Standard Model. We develop a formalism for the calculation of CSV observables from isospin-averaged $2 + 1$–flavour lattice QCD simulations.

Applying this formalism to a comprehensive lattice-based study of the electric and magnetic Sachs form factors of the baryon octet reveals that the CSV form factors are an order of magnitude smaller than suggested by previous work. This calculation opens the door for new, precise, experimental measurements of the strange nucleon form factors. We also investigate the proton-neutron mass difference and quantify the long-neglected CSV effects in the low Mellin moments of the spin-dependent and spin-independent parton distribution functions. This analysis improves the interpretation of neutrino-nucleus deep inelastic scattering experiments.

I certify that this work contains no material which has been accepted for the award of any other degree or diploma in any university or other tertiary institution and, to the best of my knowledge and belief, contains no material previously published or written by another person, except where due reference has been made in the text. In addition, I certify that no part of this work will, in the future, be used in a submission for any other degree or diploma in any university or other tertiary institution without the prior approval of the University of Adelaide. I give consent to this copy of my thesis, when deposited in the University Library, being made available for loan and photocopying, subject to the provisions of the Copyright Act 1968. The author acknowledges that copyright of published works contained within this thesis resides with the copyright holder(s) of those works.

Phiala E. Shanahan

Acknowledgements

My journey to a PhD has been remarkably painless and consistently wonderful and exciting. I have had many and varied opportunities and what has felt like limitless support and encouragement on all fronts. I, of course, owe heartfelt thanks to the people who have been responsible for my fairy-tale experience, all of whom I feel truly privileged to be able to call my friends and colleagues.

Firstly, I thank Tony Thomas for accepting me as his student for my first undergraduate research summer more than 5 years ago and for setting me on this path. Tony, you have taught me by example not just a great amount of physics, but how to approach problems and ideas and, perhaps most importantly, how to value people. Your indefatigable work ethic and enthusiasm has inspired and re-invigorated me on the frustrating days when things seemed to have stalled, and has pushed my energy to greater heights on the best. In hindsight, I can see how you have adapted your mentoring style over the years to carefully grow me into a researcher; I will carry your advice and lessons throughout my career and life. Finally, thank you for your friendship, your thoughtfulness, and your endless generosity with your time and attention. You make it your business to care about your colleagues, students, and employees as people with individual lives and hopes and dreams, and that makes all the difference.

I am similarly indebted to Ross Young. Ross, thanks for your limitless patience—for keeping your good humour when I have come bounding into your office with new and exciting results or ideas for the nth time in a day. Your curiosity and enthusiasm is inspiring and humbling, as is your dedication to your students. Thank you for introducing me to a different side of academia, for the hour-long discussions (and explanations) of university politics and of the humours and trials of teaching. Thank you for doing idiot-checks for me, and for coming into my office to ask me to do the same for you. You've not just watched me grow up, as a person and as a physicist, but you've helped and encouraged me grow into someone better (on both fronts). Ross. . . I really don't know what to say or how to thank you for the role model and inspiration you have been over the last 5 years. Of course, thanks as well for going far beyond the call of duty and for (literally) saving my life when everything went wrong at that conference in China.

Although not officially my supervisor, I owe heartfelt thanks to James Zanotti who for the later stages of this work assumed that role in all but name. James, thank you for keeping your door open and for always taking the time to chat about physics and about life. Thanks for never shutting a discussion down, no matter how late it had become. Thanks for your always careful, thoughtful, and honest advice on all manner of things from physics to superannuation, and for your genuine interest in

my progress. You have a real talent for seeing the best in people, and, even more so, for making people see the best in themselves. You have always been the person to voice a compliment when encouragement was most needed, even before we began collaborating; thank you for your support and for your confidence in me. You've unquestioningly encouraged and accepted me as I've taken those steps along the path from student to colleague. Thank you for your friendship.

Several of my fellow PhD students also deserve special thanks. First and foremost, Ben Owen. Thanks for the tea breaks, coffee breaks, hot chocolate breaks, and always-open ear. You have taken the time to support me when I needed it, no matter the reason. Travelling this road—the highs, the lows, and everything in between—with a good friend has made frustrations into hilarious adventures and successes into celebrations. Nathan Hall. Thanks for being patient, always willing to listen, and an entirely motivating rock of discipline as an office-mate. We missed you after you left for Canada. Daniel Trewartha. For your friendship over the last 5 years and your companionship, support, and careful reading of this thesis over the last few months. Your willingness to humour me and debate trivial things like table formatting, hyphen use, and bibtex styles has made the writing process much more entertaining. Elli King and Max Malacari. For putting life into perspective, for having open ears and hearts for hard questions, for believing in me, and for always being up for an adventure. You both have a talent for making me laugh at myself and at life when it is most necessary. I can only hope that I have been able to do the same for you. Adrian Kiratidis, Alex Chambers, and Lewis Tunstall. Thanks for the fun and the good times, both in the office and out.

A number of other people have supported me in less visible ways. For their invaluable and consistent assistance with every administrative hurdle and a huge variety of other things, as well as their interest and moral support, I thank Sharon Johnson, Silvana Santucci, and Bronwyn Gibson. Dave Ottoway, thanks for being both a mentor and a friend and for giving your time so generously. To my collaborators, particularly Gerrit Schierholz who has unquestioningly backed my every endeavour, ambition, and postdoc application, thank you; it has been a privilege and a pleasure. Will Detmold, thanks for your support. I can't wait to join you in Boston.

Finally, I thank my family, particularly my mum and Graham, who have celebrated every success with me and supported me in every way. Without their help I would not have been nearly as happy, productive or successful. To my step-father Graham: for your generosity in treating me in every way as your own daughter, I dedicate this thesis to you.

Contents

Chapter 1

Introduction

Protons and neutrons are the building blocks of atomic nuclei. Collectively called nucleons, they constitute more than 99% of the visible mass in our universe. Quantitatively describing the structure of these particles in terms of the quark and gluon constituents encoded in Quantum Chromodynamics (QCD), our theory of the strong force, remains a defining challenge for hadronic physics research. The ultimate goal is to 'map out' the complete spatial, momentum, spin, flavour, and gluon structure of the nucleon; to understand (and be able to predict) its interactions and resonances precisely. Such a map is not only the key to interpreting our observations of Nature in terms of the currently-accepted fundamental theory, but is essential to inform searches for physics beyond the Standard Model (SM). For example, QCD calculations of the SM background are necessary to constrain direct searches for new physics at the high-energy frontier at the Large Hadron Collider. In the low energy-regime—at the so-called intensity frontier—QCD is typically the limiting factor in indirect searches for non-SM physics, from CP violation in b-quark decays to permanent electric dipole moments in hadrons and nuclei.

Over several decades of experimental investigation and theoretical analysis based on QCD, a complicated picture of the nucleon has emerged. The modern understanding is that its structure is generated not only by three 'valence' quarks—the simplest configuration needed to carry the observed quantum numbers—but additionally any number of 'sea' quark-antiquark pairs and gluons. Deep inelastic scattering of electrons and neutrinos off nuclear targets has demonstrated that, at low values of the probing momentum-scale Q^2, valence-quark effects dominate. For the proton and neutron, with valence-quark content (uud) and (udd) respectively, the u and d quarks are thus of primary importance. However, with larger values of Q^2 the resolving power of scattering probes increases, and the increasingly-significant role of the vacuum-generated $q\overline{q}$ pairs and gluons is exposed. Because the large masses of the heavy quarks ($\mathcal{Q} = c$, b or t) prohibit any significant admixtures of $\mathcal{Q}\overline{\mathcal{Q}}$ pairs in the nucleon wavefunction, strange quarks—the lightest of the sea-only quark flavours—play a unique role. Providing tremendous insight into the nature of the quantum vacuum, strange nucleon observables occupy a position in QCD comparable in significance to that of the Lamb shift in the history of QED. The calculation of these quantities within QCD, and their verification by experiment, is thus of fundamental importance.

As well as providing a key test of our understanding of QCD, strange observables are relevant to searches for physics beyond the SM. The role of the strange quark in generating the nucleon mass—encoded in the strange sigma term—is particularly topical as the uncertainty on this much-debated quantity is the limiting theoretical factor in the interpretation of experimental searches for particle dark matter. The spatial distribution of the nucleon's strange quark content has also received considerable attention in recent decades. Despite significant accelerator facility programs at Jefferson National Laboratory and at Mainz, the best experimental values of the proton's strange electromagnetic form factors are indistinguishable from zero. The limiting uncertainty in future determinations of these quantities is theoretical, arising from the assumption of good charge symmetry.

Charge symmetry violating (CSV) effects quantify the breaking of the approximate SU(2)-flavour symmetry of the u and d quarks. Beyond their relevance to the experimental investigation of strangeness in the nucleon, the precise determination of CSV observables has, with increasing experimental precision, become essential theoretical input for searches for physics beyond the SM. In particular, the long-neglected CSV effects in the low Mellin moments of the spin-independent parton distribution functions are important to the interpretation of neutrino-nucleus deep inelastic scattering experiments. Clearly it has become imperative to determine both strange and CSV observables precisely from QCD.

The only known way to directly probe QCD in the nonperturbative regime is using a numerical technique named lattice QCD. This method involves explicitly calculating observables within a discretised formulation of QCD. First proposed in the mid-1970s, lattice methods, computer infrastructure, and the theoretical techniques used to interpret lattice simulation results, have now reached a level of sophistication that allows truly quantitative predictions to be made from QCD. In this body of work we explore hadron structure from lattice QCD, with a particular focus on both strangeness and CSV in nucleon observables.

After introducing QCD, the lattice approach, and the chiral perturbation theory formalism upon which this work is based, in Chapters 2 and 3, we investigate several nucleon observables in turn. We begin in Chapter 4 by calculating the strong-force contribution to the proton-neutron mass difference. Beyond giving quantitative insight into the breaking of charge symmetry, a precise understanding of this quantity from first principles will inform studies of the evolution of our universe; if there were a stable neutron, and a more massive proton, one would expect a predominance of heavy nuclei, no normal galaxies, stars, or planets would form, and life as we know it would be impossible.

In Chapter 5 we extend this study to investigate sigma terms, which are the matrix elements of the scalar quark currents between baryon states. As many dark matter candidates (e.g., the supersymmetric neutralino) have interactions with hadronic matter which depend quadratically on these terms, the uncertainty of theoretical dark matter scattering cross-sections is largely driven by the poorly-known strange sigma term. Modern revisions of this quantity, including our precise result based on

lattice QCD, have resulted in predicted dark matter cross-sections being reduced by an order of magnitude, with significant increases in precision.

There is an almost-universal assumption of charge symmetry in the literature concerned with parton distributions. In Chapter 6 we quantify the long-neglected CSV effects in the low Mellin moments of the spin-dependent and spin-independent parton distribution functions. Our results confirm that the omission of these effects led to an over-inflated view of the importance of the deviation from SM expectations observed in neutrino-nucleus deep inelastic scattering experiments. By comparing the total spin carried by the quarks in baryons across the octet, we are also able to reveal that the experimentally-measured suppression of the fraction of the proton spin carried by its quarks (relative to quark-model predictions) is not a universal property of baryons, but rather is structure-dependent. This supports the conclusion that the spin-suppression observed in the proton cannot be explained by the axial anomaly.

In Chapter 7 we present a comprehensive lattice-based study of the electric and magnetic Sachs form factors of the baryon octet. This analysis includes the hyperon form factors, which have so far received limited attention in the literature. Notably, we achieve the first accurate determination of the hyperon magnetic radii from lattice QCD. We also investigate strange and CSV effects in the nucleon in this context. By combining experimental and lattice input, we deduce the strange nucleon form factors over a far larger range of momentum-scales than is accessible experimentally. Our calculation of the strange magnetic moment is an order of magnitude more precise than the closest experimental result. Until now, the dominant uncertainty in experimental determinations of the strange proton form factors has come from a lack of knowledge about the size of CSV in these quantities. By revealing that the CSV form factors are an order of magnitude smaller than suggested by previous work, our calculations also open the door for a new generation of experimental tests of QCD through the proton's strange form factors.

Finally, in Chapter 8 we review this body of work to build a coherent picture of the role of both CSV effects and the strange quark in the structure of the nucleon in QCD.

Chapter 2

Quantum Chromodynamics

The Standard Model of Particle Physics (SM) embodies our knowledge of the strong and electroweak interactions. It contains as fundamental degrees of freedom the spin-$\frac{1}{2}$ quarks and leptons, the spin-1 gauge bosons, and the spin-0 Higgs field. Despite the presence of a number of *a-priori* unknown parameters, this model is a mathematical construction of considerable predictive power. Notably, it suggested the existence of the W and Z bosons, the gluon, and the top and charm quarks before these particles were observed. In 2013, the particle content of the SM was made complete by the experimental discovery of the Higgs Boson [1, 2].

Here we focus on the strong-force component of the SM, which specifies how quarks and gluons bind together to form ordinary hadronic matter. This is the theory of Quantum Chromodynamics (QCD), describing all strong-interaction physics at all distance scales, from high energy particle collisions and the decay of heavy nuclei to the properties of matter under extreme conditions such as in the core of a neutron star. This diverse physics is encapsulated in a single formula of alluring simplicity: the Lagrangian of QCD. Despite its apparently simple form, deriving the physical dynamics of a system from this equation poses a tremendous theoretical challenge.

Asymptotic freedom—the property that quarks and gluons interact very weakly in high-energy reactions—ensures that perturbative approaches can be applied to QCD at small distance scales. In this way one can obtain precise theoretical predictions from the SM which may be rigorously tested through high-energy scattering experiments. In the low-energy regime, however, the QCD coupling is large and perturbative techniques cannot be used. The only known first-principles approach to QCD at these scales is numerical: a discretised form of the QCD equations can be solved exactly, using supercomputers, on a finite four-dimensional grid representing space-time. This technique is named lattice QCD.

Of course, although we receive invaluable insight by discretising QCD, we have also lost direct comparison with the physical, continuous, world. To be able to compare the results of lattice QCD simulations with experiment, one must extrapolate to the physical point. Precisely, the continuum limit (as lattice spacing $a \to 0$), the infinite volume limit (as lattice size $L \to \infty$), and, as computation time often limits simulations to larger-than-physical quark masses, the continuation into small quark

masses $\left(\text{as } m_q \to m_q^{(\text{phys.})}\right)$ must be taken. This final limit, the so-called chiral extrapolation, is arguably the most difficult of the three to implement and will be a particular focus of this body of work.

As technological and algorithmic advances now allow lattice simulations to be performed near, or even at, the physical quark masses, it is foreseeable that chiral extrapolation as a means of reaching the physical point will soon become obsolete. With this in mind, we explore this technique not only as an essential link between lattice simulations and Nature, but as an invaluable tool with which to develop a deeper understanding of QCD from unphysical test cases which cannot be explored experimentally. As we will see in later chapters, one can extend chiral extrapolation techniques to isolate vacuum-quark effects, explore the quark-mass dependence of observables and hence extract mass-derivative quantities, and extend SU(2)-flavour–symmetric simulations to the SU(2)-broken world. Combining the insight afforded by unphysical lattice simulations with experimental results allows one to deduce hard-to-calculate quantities to a precision that is yet unreachable by direct computation. In this way, we set the benchmarks for the next generation of experimental tests of the SM.

After outlining the mathematical formulation of QCD in the next section, we briefly discuss the numerical lattice QCD approach. The remainder of this chapter is devoted to the concepts of strangeness and charge symmetry violation in the nucleon, which are the core themes of this body of work.

2.1 Mathematical Formulation

Mathematically, QCD is a gauge field theory describing the interactions of 'colour-charged' particles. It is based on the non-Abelian, compact, and simple Lie group SU(3), commonly represented by the group of 3×3 complex unitary matrices with unit determinant. The gluons A_μ arise as the (spin-1) gauge bosons of this theory. As such, they may be identified with the generators of SU(3) rotations in colour-space[1], $A_\mu = t_a A_\mu^a$, and transform in the adjoint representation of the gauge group. The dimension of the adjoint representation (equal to the number of generators) is $3^2 - 1 = 8$ for SU(3), thus the gluons are colour-octet. The quark fields ψ are spin-$\frac{1}{2}$ fermions in the fundamental representation of the gauge group and carry colour and flavour labels. The dimension of the fundamental representation is the degree of the group, $N = 3$ for SU(3), so the quarks are colour-triplet.

The classical, unrenormalised Lagrangian density of QCD is completely specified by the conditions of renormalisability and invariance under the SU(3) gauge

[1]Here $t_a = \lambda_a/2$, where λ_a, $a = 1, \ldots, 8$ are the Gell-Mann matrices with normalisation $\text{Tr}(\lambda_a \lambda_b) = \delta_{ab}$.

transformations

$$\psi(x) \to \psi'(x) = U(x)\psi(x), \tag{2.1a}$$

$$A_\mu(x) \to A'_\mu(x) = U(x)A_\mu(x)U^{-1}(x) + \frac{i}{g}(\partial_\mu U(x))U^{-1}(x), \tag{2.1b}$$

where $U(x) = \exp(i\phi^a(x)t^a)$ defines an independent SU(3) transformation at every point in space-time. Neglecting a quark-mass mixing phase—the θ parameter associated with the strong CP problem—as it is known to be extremely small [3], one finds[2]

$$\begin{aligned}\mathcal{L}_{\text{QCD}} &= \sum_q \overline{\psi}_q^i \big(i\gamma^\mu D_\mu^{ij} - \delta^{ij} m_q\big)\psi_q^j - \frac{1}{4}F_{\mu\nu}^{(a)}F^{(a)\mu\nu} \\ &= \overline{\psi}\big(i\not{D} - M_q\big)\psi - \frac{1}{4}F_{\mu\nu}F^{\mu\nu}.\end{aligned} \tag{2.2}$$

The second line shows the standard compact notation—fundamental-representation colour indices i, j, adjoint-representation colour indices a, and flavour labels $q = u, d, s, \ldots$ have been suppressed. The Dirac matrix γ^μ, where μ is a Lorentz vector index, expresses the vector nature of the strong force, and the non-zero quark masses are encoded in $M_q = \text{diag}(m_u, m_d, m_s \ldots)$. There is no gauge-invariant way of including a gluon mass. The QCD covariant derivative introduces the coupling g of the quarks to the gluons:

$$D_\mu^{ij} = \delta^{ij}\partial_\mu - igt_a^{ij}A_\mu^a, \tag{2.3}$$

and the non-Abelian gluon field strength tensor is given by

$$F_{\mu\nu}^{(a)} = \partial_\mu A_\nu^a - \partial_\nu A_\mu^a + g f_{abc} A_\mu^b A_\nu^c, \tag{2.4}$$

where f_{abc} are SU(3) Lie group structure constants. This is non-linear in terms of the gauge field and as a result the gluon kinetic energy term of the Lagrangian generates three and four-gluon self-interactions. These interactions are responsible for many of the salient features of QCD.

In particular, because of the gluon self-coupling, the polarisation of virtual gluons in the vacuum antiscreens (i.e., enhances) colour charge. This effect dominates over the screening effect of the quark vacuum-polarisation, which is analogous to that of QED. As a result, the QCD coupling, $\alpha_s = g^2/4\pi$, runs to become small at large scales; at high energy QCD is essentially a theory of free partons—quarks and gluons—which only interact through relatively small quantum corrections that can be systematically, perturbatively, calculated. This is the property of asymptotic freedom, for which Politzer, Gross, and Wilczek were awarded the 2004 Nobel Prize [4, 5].

[2] Counterterms and ghost and gauge-fixing terms are implicit; they are all unnecessary for the lattice QCD approach which we will consider here.

In contrast, at low energies accelerators reveal a particle spectrum which bears no resemblance to the non-interacting theory: free quarks are never observed. Instead, towers of strongly-bound colour-singlet particles named hadrons emerge. This is termed confinement and is understood as a consequence of the property that the force between two colour-charges does not diminish as they are separated. Instead, linear string-like potentials build up between partons. These strings only 'break' when the energy contained is large enough to create an additional quark-antiquark pair out of the vacuum. As a result, one only observes mesons, which have the quantum numbers of a quark-antiquark pair, and baryons, with the quantum numbers of three quarks. The properties of these hadrons are the focus of this body of work.

Analytic derivations of hadron properties have proven to be impossible except in some extreme limiting cases; at the relevant low energy scales the strong coupling becomes large and perturbation theory is no longer valid. While many models and approximations are used to study low-energy processes: the limit of the large number of colours; generalisations of the original Shifman-Vainshtein-Zakharov sum rules; QCD vacuum models and effective string models; the AdS/CFT conjecture; and Schwinger-Dyson equations, the only known way to study QCD in the non-perturbative regime directly is to use numerical methods. As suggested earlier, the most successful of these, and the only one rigorously derived from the fundamental theory, is lattice QCD.

2.2 Lattice Quantum Field Theory

First proposed by Wilson in 1974 [6], lattice QCD is a first-principles method of calculating QCD observables numerically. In short, a discretised version of the full QCD theory is solved explicitly on a four-dimensional lattice of points (3 space, 1 time dimension). Any such lattice is characterised by a finite lattice spacing a which is not physical but acts as a method of regularisation. The limit $a \to 0$ must be taken to connect to the physical theory.

As the only known direct probe of QCD in the nonperturbative regime, the lattice is an important source of information for tests of the SM; it provides results for various low-energy hadronic matrix elements that are complimentary to those obtained using phenomenological approaches. It has also become a viable framework for calculations of nuclear few-body quantities [7,8], and for the exploration of part of the QCD phase diagram [9,10]. As we will see in later chapters, a great advantage of lattice field theory is that the technique allows precise control over the parameters of QCD. By varying these parameters one may probe more than QCD at the physical point—for example, one can 'turn off' vacuum loop contributions or change the quark masses—to develop a deeper understanding of nonperturbative phenomena. In this section we introduce the basic concepts and terminology relevant to lattice QCD. A comprehensive summary of the approach may be found in Refs. [11–13].

2.2.1 The Discretised Action

Lattice gauge theory is based on the Feynman path integral approach to quantum field theory [14]. In this formulation of QCD, observables are given by the expectation values of field operators. These expectation values, known as Green's functions, can be expressed as functional derivatives of the generating functional,

$$\mathcal{Z}_{\mathrm{QCD}} = \int \delta A_\mu \, \delta\overline{\psi} \, \delta\psi \, e^{iS_{\mathrm{QCD}}}, \tag{2.5}$$

with respect to the various sources. If all Green's functions could be calculated, QCD would be solved. In Minkowski space, however, this formulation of QCD does not lend itself to numerical computation because of the complex term $e^{iS_{\mathrm{QCD}}}$ which appears in Eq. (2.5); the oscillatory integrand causes cancellations between different regions of phase space. For this reason lattice QCD is formulated in Euclidean space-time. The partition function

$$\mathcal{Z}^E_{\mathrm{QCD}} = \int \delta A_\mu \, \delta\overline{\psi} \, \delta\psi \, e^{-S_{\mathrm{QCD}}} \tag{2.6}$$

is obtained by a Wick rotation ($t \to -it_E$) of the corresponding expression in Minkowski space (Eq. (2.5)). This form allows a probabilistic interpretation of the functional integral; the exponential factor corresponds exactly to the Boltzmann weighting of a statistical ensemble.

In this section we describe the construction of a discretised lattice action for QCD:

$$S_{\mathrm{QCD}} = S_F[U, \psi, \overline{\psi}] + S_G[U], \tag{2.7}$$

where the subscripts F and G denote the fermion and purely-gauge components, respectively.

Fermions

In Euclidean space-time the Dirac action for a free fermion is written as

$$\int d^4x \, \overline{\psi}(x)\big(\not{D} + m\big)\psi(x). \tag{2.8}$$

In the discretised theory the quark fields $\psi(n)$ reside on the sites n of the lattice, i.e., the fermionic degrees of freedom are

$$\psi(n), \ \overline{\psi}(n), \quad n \in \Lambda. \tag{2.9}$$

We will restrict ourselves to four-dimensional cubic lattices:

$$\Lambda = \big\{ x \in \mathbb{R}^4 \big| x = an, \ n \in \mathbb{Z}^4 \big\}, \tag{2.10}$$

where a is the discrete lattice spacing. While this is the standard topology, others have been explored [15, 16] and there has been a recent resurgence of interest in anisotropic lattices [17, 18]. In practice, of course, the lattices used for numerical simulations have some finite extent. As in the continuum theory, the spinors ψ carry colour, flavour, and Dirac indices (which are suppressed in our notation).

The derivative in Eq. (2.8) may be discretised using a symmetrised finite difference, where appropriate gauge links are included to maintain gauge invariance:

$$\overline{\psi}\not{D}\psi \to \sum_{\mu=1}^{4} \overline{\psi}\gamma_\mu \nabla_\mu \psi = \frac{1}{2a}\overline{\psi}(n) \sum_{\mu=1}^{4} \gamma_\mu \big[U_\mu(n)\,\psi(n+\hat{\mu}) - U_\mu^\dagger(n-\hat{\mu})\,\psi(n-\hat{\mu})\big], \tag{2.11}$$

where the gauge fields $U_\mu(n)$ are elements of the gauge group SU(3). These fields are oriented and attached to the links of the lattice: $U_\mu(n)$ lives on the link connecting the sites (n) and $(n+\hat{\mu})$. Under a gauge transformation $\boldsymbol{\lambda}(n)$,

$$U_\mu(n) \to \boldsymbol{\lambda}(n)\, U_\mu(n)\, \boldsymbol{\lambda}(n+a\hat{\mu})^{-1}. \tag{2.12}$$

Finally, implementing the discretisation of the integral in Eq. (2.8) as a sum over the set of space-time points Λ, we arrive at the 'naive' action for fermions in an external gauge field U:

$$\begin{aligned} S_F^{\mathrm{N}}[U,\psi,\overline{\psi}] &= \sum_{n\in\Lambda} \overline{\psi}(n) \left(\frac{1}{2a} \sum_{\mu=1}^{4} \gamma_\mu \big[U_\mu(n)\,\psi(n+\hat{\mu}) - U_\mu^\dagger(n-\hat{\mu})\,\psi(n-\hat{\mu})\big] + m\psi(n) \right) \\ &= \sum_{n,m\in\Lambda} \overline{\psi}(n)\, M_{nm}^{\mathrm{N}}[U]\, \psi(m), \end{aligned} \tag{2.13}$$

where M^{N} is the naive interaction matrix

$$M_{nm}^{\mathrm{N}}[U] = m\,\delta_{nm} + \frac{1}{2a} \sum_{\mu=1}^{4} \gamma_\mu \Big[U_{n\mu}\,\delta_{n(m-\mu)} - U^\dagger_{(n-\mu)\mu}\,\delta_{n(m+\mu)} \Big]. \tag{2.14}$$

By Taylor-expanding U_μ and ψ in powers of the lattice spacing a, one can see that the naive fermion action has $\mathcal{O}(a^2)$ errors. It is clear, however, that the first-order derivative can only couple lattice sites separated by $2a$. As a result, certain high-momentum modes do not correspond to a large value of the action. This leads to unwanted additional long-range degrees of freedom called doublers; in the continuum limit there are $2^d = 16$ flavours of quark rather than one.

There are two common methods of fixing the doubling problem. The first reduces the number of doublers by 'staggering' the quark degrees of freedom on the lattice. This procedure is described in Ref. [11]. The other technique, which is used in this work, involves adding additional operators to the quark action (which scale with a and so vanish in the continuum limit) to suppress the doublers by driving them to higher energies.

Precisely, the Wilson term—a particular (energy) dimension-five operator—is added to the standard naive lattice fermion action, giving the 'Wilson action':

$$S_F^{\mathrm{W}}[U,\psi,\overline{\psi}] = \sum_{n\in\Lambda}\overline{\psi}(n)\left[\sum_{\mu=1}^{4}\left(\gamma_\mu\nabla_\mu - \frac{1}{2}ra\Delta_\mu\right) + m\right]\psi(n). \tag{2.15}$$

Here ∇ denotes the finite difference defined in Eq. (2.11), and the operator Δ removes the unwanted doublers by coupling adjacent lattice sites:

$$\Delta_\mu\psi(n) = \frac{1}{a^2}\big[U_\mu(n)\,\psi(n+\hat{\mu}) + U_\mu^\dagger(n-\hat{\mu})\,\psi(n-\hat{\mu}) - 2\psi(n)\big]. \tag{2.16}$$

In terms of link variables, the Wilson action is written as

$$S_F^{\mathrm{W}}[U,\psi,\overline{\psi}] = \sum_{n,m\in\Lambda}\overline{\psi}^L(n)\,M_{nm}^{\mathrm{W}}[U]\,\psi^L(m),$$

where

$$aM_{nm}^{\mathrm{W}}[U] = \delta_{nm} - \kappa\sum_{\mu=1}^{4}\Big[(r-\gamma_\mu)\,U_{n\mu}\,\delta_{n(m-\mu)} + (r+\gamma_\mu)\,U_{(n-\mu)\mu}^\dagger\,\delta_{n(m+\mu)}\Big], \tag{2.17}$$

with a field renormalisation

$$\kappa = 1/(2ma+8r), \tag{2.18}$$

$$\psi^L = \psi/\sqrt{2\kappa}. \tag{2.19}$$

It is typical to take $r=1$.

In the continuum limit it is clear that, through the addition of the Wilson term, we have introduced $\mathcal{O}(a)$ discretisation errors into the fermion matrix; the Dirac action of Eq. (2.8) becomes

$$\int d^4x\,\overline{\psi}(x)\left(\not{D} + m - a\frac{r\not{D}^2}{2}\right)\psi(x) + \mathcal{O}\big(a^2\big). \tag{2.20}$$

Numerical simulations using Wilson fermions must thus be performed on very fine lattices, which are computationally expensive, in order for continuum extrapolations to be reliable. It has become standard to improve the uncertainties of the Wilson action through the addition of higher-dimension operators. This procedure is known as the Symanzik improvement program [19].

We discuss here only one choice of improved fermion action, which we use in this work (see Chapter 7). The Sheikholeslami-Wohlert fermion action [20] includes the so-called 'clover' term—a gauge-invariant, local, dimension-five operator—in

addition to the standard terms of the Wilson action:

$$S_F^{\mathrm{SW}}[U,\psi,\overline{\psi}] = S_F^{\mathrm{W}}[U,\psi,\overline{\psi}] - \frac{a\,c_{\mathrm{SW}}\,r}{4}\sum_{n\in\Lambda}\sum_{\mu,\nu=1}^{4}\overline{\psi}(n)\,\sigma_{\mu\nu}\,F_{\mu\nu}(n)\,\psi(n). \tag{2.21}$$

Here c_{SW} is the clover coefficient which can be tuned (typically nonperturbatively using the axial Ward identity [21]) to remove all $\mathcal{O}(a)$ artefacts. Further details may be found in Refs. [11–13].

Gluons

The matrix-valued link variable $U_\mu(x)$ was introduced in Eq. (2.11) to maintain the gauge-invariance of the covariant derivative. Based on its gauge transformation properties (Eq. (2.12)), we interpret $U_\mu(n)$ as a lattice version of the gauge transporter connecting the points (n) and $(n+\hat{\mu})$. Under this identification, we can express the link variable in terms of the algebra-valued continuum gauge field $A_\mu(x)$:

$$U_\mu(n) = \mathcal{P}\exp ig\int_0^a A_\mu(n+\lambda\hat{\mu})d\lambda, \tag{2.22}$$

where the operator $\mathcal{P}$ path-orders the A_μ along the integration path and g is the coupling constant.

From Eq. (2.12) it is clear that the trace over a closed (Wilson) loop of link variables is a gauge-invariant object. Various such loops are used in combination to build the lattice version of the QCD gauge action—the precise construction is arbitrary provided that the usual continuum action is recovered in the $a\to 0$ limit. It is natural to consider the simplest case first; the shortest nontrivial closed loop on the lattice is the so-called plaquette, constructed by the product of four links enclosing an elementary square:

$$P_{\mu\nu}(n) = \mathrm{Re\ Tr}\big[U_\mu(n)\,U_\nu(n+\hat{\mu})\,U_\mu^\dagger(n+\hat{\nu})\,U_\nu^\dagger(n)\big]. \tag{2.23}$$

Using Eq. (2.22), and expanding the integral, we express $P_{\mu\nu}$ in terms of the field A_μ:

$$\begin{aligned} P_{\mu\nu}(n) &= \mathrm{Re\ Tr}\ \mathcal{P}e^{ig\oint_{\square_n}A\cdot dx} \\ &= \mathrm{Tr}\ \mathcal{P}\left[1-\frac{1}{2}\left(g\oint_{\square_n}A\cdot dx\right)^2+\mathcal{O}(A^4)\right]. \end{aligned} \tag{2.24}$$

Stoke's theorem gives an expression for the integral:

$$\oint_{\square_n}A\cdot dx = \int_0^a dx_\mu dx_\nu[\partial_\mu A_\nu(n+x)-\partial_\nu A_\mu(n+x)]$$

$$= \int_0^a dx_\mu dx_\nu F_{\mu\nu}(n+x)$$
$$= a^2 F_{\mu\nu}(n) + \frac{a^4}{24}\big(\partial_\mu^2 + \partial_\nu^2\big) F_{\mu\nu}(n) + \mathcal{O}\big(a^6, A^2\big), \tag{2.25}$$

where the last line follows from a Taylor expansion of $F_{\mu\nu}(n+x)$ about the lattice site (n). Substituting this expression back into Eq. (2.24), the plaquette term becomes

$$P_{\mu\nu}(n) = 1 - \frac{1}{2} g^2 a^4 \operatorname{Tr}\big[F_{\mu\nu}(n)^2\big] + \mathcal{O}\big(g^2 a^6, a^8, g^4 a^6\big). \tag{2.26}$$

This expansion yields the 'Wilson action' for gluons on the lattice:

$$S_G^{\mathrm{W}}[U] = \frac{2}{g^2} \sum_{n\in\Lambda} \sum_{\mu<\nu} [1 - P_{\mu\nu}(n)]$$
$$= \frac{a^4}{2g^2} \sum_{n\in\Lambda} \sum_{\mu<\nu} \operatorname{Tr}\big[F_{\mu\nu}(n)^2\big] + \mathcal{O}\big(a^2, a^2 g^2\big). \tag{2.27}$$

This expression differs from the continuum gluon action by terms which are $\mathcal{O}(a^2)$ and $\mathcal{O}(a^2 g^2)$. These artefacts can be removed, however, by adding other Wilson loops to the action which have different errors at $\mathcal{O}(a^2)$. For example, the Lüscher-Weisz gauge action [22] includes 1×2 rectangular loops and parallelogram-shaped loops as well as the standard plaquette:

$$S_G^{\mathrm{LW}}[U] = \frac{2}{g^2}\left(c_0 \sum_{\text{plaq.}} [1 - P_{\mu\nu}] + c_1 \sum_{\text{rect.}} [1 - R_{\mu\nu}] + c_2 \sum_{\text{par.}} [1 - L_{\mu\nu}] \right), \tag{2.28}$$

where $R_{\mu\nu}$ and $L_{\mu\nu}$ denote products of gauge links, enclosing 1×2 rectangles and parallelograms respectively, defined analogously to $P_{\mu\nu}$ in Eq. (2.23). The relative weighting coefficients c_i (that are generically functions of g^2) are chosen to satisfy $c_0 + 8c_1 + 8c_2 = 1$, which ensures that discretisation errors are cancelled to $\mathcal{O}(a^4)$. Two common choices of the weighting coefficients are the Iwasaki gauge action [23] and the tree-level improved action [24] which we use in Chapter 7. This latter choice sets $c_0 = 20/12$, $c_1 = -1/12$, and $c_2 = 0$.

2.2.2 Lattice Expectation Values

Physical observables are calculated in the lattice approach as expectation values:

$$\langle \mathcal{O} \rangle = \frac{1}{\mathcal{Z}} \int \delta A_\mu \, \delta\overline{\psi} \, \delta\psi \, \mathcal{O} \, e^{-S_{\mathrm{QCD}}}, \tag{2.29}$$

where $\mathcal{O}$ can be any combination of operators expressed in terms of time-ordered products of gauge and quark fields, and $\mathcal{Z}$ is the Euclidean–space-time partition function (Eq. (2.6)). One can remove any dependence of $\mathcal{O}$ on the quark fields as dynamical variables by performing Wick contractions to re-express them in terms

of propagators. The propagators, for a given background field U, are determined by inverting the Dirac operator. In terms of an interaction matrix M (e.g., Eq. (2.14) or (2.17)),

$$S_f(m,n,U) = (M[U]^{-1})_{nm} \tag{2.30}$$

gives the amplitude for the propagation of a quark from site (n) to site (m) (where the spin-colour indices are suppressed). Now, integrating over the fermion field (recalling that the fermion action is given by $S_F = \overline{\psi} M \psi$, Eq. (2.13)),

$$\langle \mathcal{O} \rangle = \frac{\int \delta A_\mu \det[M]\, \mathcal{O}\, e^{-S_G}}{\int \delta A_\mu \det[M]\, e^{-S_G}}. \tag{2.31}$$

As the gauge group SU(3) is continuous, there are infinitely many gauge configurations that contribute to this expression. For this reason the integral over the gauge fields is approximated statistically:

$$\langle \mathcal{O} \rangle \approx \frac{1}{N} \sum_{i=1}^{N} \mathcal{O}\big(U^{[i]}\big). \tag{2.32}$$

Here $\mathcal{O}(U^{[i]})$ is the operator $\mathcal{O}$ evaluated for the i^{th} field configuration $U^{[i]}$ of an ensemble of N such configurations which have been randomly generated based on the acceptance probability of the weight function $\det[M[U]]e^{-S_{G[U]}}$. This generation is performed iteratively using a Markov process; beginning from an initial configuration $U^{[0]}$, a chain of configurations $\{U^{[1]}, U^{[2]}, \ldots\}$ is generated using a Monte-Carlo–style algorithm satisfying

$$P\big(U^{[i-1]} \to U^{[i]}\big) P\big[U^{[i-1]}\big] = P\big(U^{[i]} \to U^{[i-1]}\big) P\big[U^{[i]}\big], \tag{2.33}$$

where $P(U \to U')$ is the transition probability between configurations U and U'. General criteria exist that guarantee that the configurations visited are indeed distributed according to the desired probability distribution after a sufficient number of iterations.

The generation of gauge configurations is computationally expensive. The cost of calculating the fermion determinant $\det[M[U]]$ depends not only on the number of configurations generated, but on the number of lattice sites, the lattice volume, and the quark masses. Because of the sheer size of the fermion matrix M, its determinant is approximated numerically. This is done using iterative algorithms which involve inverting matrices that become progressively more singular as the quark masses become lighter. Similarly, the quark propagators, which must be calculated explicitly for each gauge configuration, become more expensive to calculate at light masses. Moreover, the lattice volume required becomes increasingly large. For this reason calculations at or near the physical masses are only now becoming tractable [25].

A further cost-saving approximation is that quark propagators are typically calculated from a fixed source point to every other point on the lattice; 'all-to-all' propagators from every lattice site to every other site are simply too expensive. As

a result, contributions to observables from quark-line–disconnected loops—which could appear at any point on the lattice—are neglected in most simulations (see Section 2.3.1). The effects of this omission in the case of baryon electromagnetic form factors will be discussed in detail in Chapter 7.

2.2.3 Scale Setting

A characteristic of lattice simulations is that all quantities are calculated in units of the unknown lattice spacing a, which must be determined by matching an observable to its physical value[3]. This can be done in a variety of ways. Two common methods, often referred to as the 'mass-independent' and 'mass-dependent' scale-setting schemes, are of particular interest to us here:

1. **Mass-independent.** The inverse bare coupling β determines the lattice spacing a. That is, simulations at some fixed value of β are extrapolated to the physical point (usually linearly in the bare quark mass $am_{q_{\text{sea}}}$), and the value of some observable at that point is used to set the common scale a for *all* lattice ensembles at that common β.

2. **Mass-dependent.** The lattice spacing varies with bare quark mass. That is, a is determined separately for each set of bare parameters $(\beta, am_{q_{\text{sea}}})$ by using a physical observable that is assumed to be independent of the quark masses. A typical choice of observable is the Sommer scale, r_0, which is related to the force between static quarks at relatively short distance, or any of a range of similar quantities.

We could think of these two choices of scale-setting prescription as different ways of absorbing the observed quark-mass dependence of the ratio r_0/a at fixed β. Method 1 essentially assumes that this dependence may be attributed to the variation of r_0 with quark mass, while method 2 instead assumes that a is changing. What is not often considered is that both r_0 and a may have some dependence on the sea-quark mass, which would lead to an intermediate scale in some sense. Such a 'mixed' scale-setting procedure would be nontrivial to implement.

Of course, in the continuum limit, and after the chiral extrapolation to physical quark masses has been performed, the results of each method of scale setting must agree for physical observables. When considering quantities which are expressed as derivatives with respect to quark mass, however, the choice of scale-setting method becomes far more significant; these quantities, by the very definition of the derivative, depend on the scale away from the physical point and hence on the scale-setting scheme chosen. This distinction will be particularly relevant to the discussion of Chapter 5, where we calculate the octet baryon sigma terms as derivatives via the Feynman-Hellmann theorem.

[3]The lattice spacing is not physical, but acts as a method of regularisation. The only physical quantities are mass-ratios.

2.3 Strangeness and Charge Symmetry Violation in the Nucleon

We finish this chapter with an introduction to the concepts of strangeness and charge symmetry violation (CSV) in nucleon structure; these topics are the unifying themes of this body of work. Both strange and CSV observables are associated with deviations from approximate features of the nucleon in QCD. They are hence benchmark quantities for modern precision tests of the theory.

In particular, strange nucleon observables occupy a position of comparable importance in QCD to that of the Lamb shift in the history of QED. While lattice QCD and models have described a number of valence-quark–dominated hadronic properties extremely accurately [26], strange observables can only arise through quantum fluctuations of the vacuum in which a strange-antistrange quark pair briefly bubble into and out of existence. The calculation of such quantities directly within QCD, and their verification by experiment, is thus the ideal test of our understanding of virtual sea quarks in the nucleon.

Charge symmetry, defined formally in Section 2.3.2, is related in QCD to the near mass-degeneracy of the u and d quarks. At the quark level this symmetry is, of course, very badly broken, but this is hidden by dynamical chiral symmetry breaking; in nuclear reactions charge symmetry holds to better than about 1% [27]. Precise calculations of CSV observables therefore also provide SM benchmarks for tests of QCD. In our discussion, the themes of strangeness and CSV are connected through the electromagnetic form factors (Chapter 7); the strange quark and CSV contributions to these quantities cannot be distinguished experimentally.

2.3.1 Nucleon Strangeness

The net strangeness of the nucleon is, of course, zero; its quantum numbers correspond to those of two u quarks and a single d. In QCD, however, these light valence quarks are accompanied by a fluctuating sea of all flavours of $q\overline{q}$ pairs. The magnitude of the vacuum contributions to observables from different flavours scales with quark mass. Clearly, the lightest non-valence quark flavour—the s for the nucleon—will provide the dominant vacuum contribution, and hence be the most interesting phenomenologically.

Other than the valuable information about the quantum vacuum which strange observables provide in their own right, these quantities are also relevant in other arenas. Most importantly, the strange nucleon sigma terms (Chapter 5) are essential input for the interpretation of dark matter direct-detection experiments. In general, however, the uncertainties in both experimental and theoretical determinations of the strangeness matrix elements, including the strange sigma terms, are large. Clearly lattice QCD promises significant improvement by facilitating the calculation of definitive quantitative results for these observables.

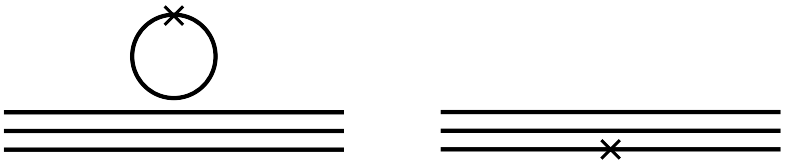

(a) Disconnected insertion. (b) Connected insertion.

Figure 2.1: Quark-line 'skeleton' diagrams showing connected and disconnected insertions of some operator (represented by the crossed vertex). All gluons and additional (spectator) quark-antiquark pairs are omitted for clarity.

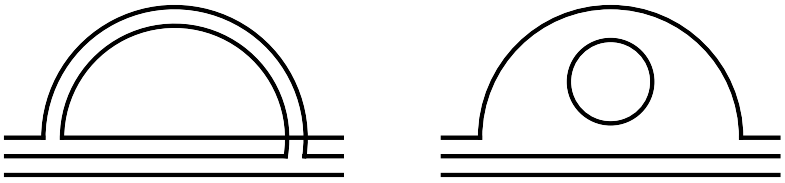

(a) Quark-line–connected meson loop. (b) Quark-line–disconnected meson loop.

Figure 2.2: Quark-line 'skeleton' diagrams showing the meson cloud contributions to hadronic observables. All gluons and additional quark-antiquark pairs are omitted for clarity. Any operator insertion into a connected quark line (i.e., any line other than the vacuum bubble in Fig. 2.2(b)) is included in a connected-only calculation.

The challenge in determining strange nucleon observables in lattice QCD lies in the evaluation of the so-called disconnected insertions, illustrated in Fig. 2.1(a). Determining these terms explicitly requires the calculation of all-to-all propagators—from every point on the lattice to every other point—which is prohibitively expensive compared to the evaluation of the connected insertions. Consequently, there are very few lattice calculations of disconnected observables [28, 29]. In these studies the all-to-all propagators are stochastically estimated. For these reasons, the lattice QCD simulations which we use and develop in this body of work will include only connected insertions. We emphasise here that this does *not* omit the entire meson cloud of QCD. This distinction is illustrated explicitly in Fig. 2.2.

We investigate the role of strange quarks in generating different nucleon observables by combining connected-only lattice QCD simulations, chiral effective field theory, and experimental input; the aim is to build a cohesive picture of the contribution not only from the strange quark, but from the dynamical vacuum more generally, in QCD. In particular, we investigate the strange nucleon sigma terms (Chapter 5) and the strange contribution to the electromagnetic form factors of the nucleon (Chapter 7).

2.3.2 Charge Symmetry Violation

Charge symmetry is formally defined as the invariance of the strong interaction under an isospin rotation exchanging u and d quarks; it corresponds precisely to a

rotation by π about the '2' axis in isospin space (compared to isospin symmetry, which is invariance under an arbitrary rotation in this space). The violation of this symmetry is arguably small: the proton-neutron mass difference is one part in a thousand [30] and many nuclear reactions proceed identically if protons and neutrons are interchanged. The effects of this small CSV, however, may be hugely significant. For example, if the proton-neutron mass difference were reversed, protons could undergo beta decay, atoms such as carbon, the building block of all organic matter, could not form, and life as we know it would be impossible. CSV also explains the discrepancy between the calculated and measured binding energy differences of mirror nuclei (Okamoto-Nolen-Schiffer anomaly [31]) and may play a role in precision tests of the SM [32], including those at the LHC [33].

In lattice QCD studies, however, the small effects of CSV are in general ignored; it is standard to perform '2+1-flavour' simulations where the light quarks are mass-degenerate. A full '1+1+1-flavour'—isospin-broken—study would involve a significantly more complicated tuning procedure in order to find the lattice parameters corresponding to the close-to-physical space of interest. With the majority of lattice simulations not yet at the physical average light-quark mass, the effect of CSV has thus long been a secondary concern; only very recently have lattice studies been performed that partially (for the valence quarks only) [34] or fully [35] include strong CSV contributions.

CSV effects have also, until very recently [36–38], been neglected in many standard analyses of experimental results. For example, the assumption of good charge symmetry at the parton level has been applied to global fits of parton distribution functions to experimental data [33, 39] in order to reduce the number of independent functions by a factor of two. Experimental tests of the SM are now, however, reaching a level of precision where CSV effects may be important. For example, it has been suggested [40] that CSV artefacts could significantly reduce the 3-sigma discrepancy with the SM value for the weak mixing angle found by the NuTeV collaboration [41] in neutrino-nucleus deep inelastic scattering. For this reason, we devote considerable attention to the role of CSV in the nucleon (returning to a discussion of the NuTeV anomaly in Chapter 6).

In future chapters we combine 2+1-flavour lattice QCD simulations with input from chiral effective field theory to determine CSV effects in a number of nucleon observables. In particular, we separate the strong and electromagnetic contributions to the proton-neutron mass difference (Chapter 4), as well as determining the level of CSV in the baryon sigma terms (Chapter 5), and in moments of parton distribution functions (Chapter 6). In Chapter 7 we describe the first lattice-QCD–based calculation of the CSV electromagnetic form factors and, importantly, present the remarkable result that these quantities are constrained to be an order of magnitude smaller than previous best estimates. This revelation paves the way for a new generation of experimental determinations of the strange nucleon form factors to constrain these quantities to an unprecedented level of precision. Moreover, because

of the extremely small SM background, measurements of CSV in the electromagnetic form factors may in the future provide some insight in searches for new physics.

Chapter 3

Chiral Perturbation Theory

One of the prime motivators for lattice QCD is its potential to confront experiment in the nonperturbative regime. Its success on this front has historically been tied to chiral effective theory, whose essential role was to bridge the gap between the physical region of light quark masses and simulations with computationally less demanding, heavier, masses. Even in the current era of high-precision lattice studies approaching the physical point, chiral extrapolation techniques are not obsolete. As will be described in the coming chapters, the formalism has become a refined tool with which one can correct a variety of lattice artefacts in near-physical simulations or glean understanding from unphysical test cases which are not accessible experimentally.

In this chapter we provide an introduction to chiral perturbation theory with a focus on understanding properties of the low-lying baryon octet. After discussing effective field theories, of which the chiral theory is arguably the canonical example, we consider the symmetry-breaking pattern of QCD and describe the emergent Nambu-Goldstone bosons, exposing their universal low-energy dynamics through an effective chiral Lagrangian. Through the example of the chiral extrapolation of the mass of the nucleon we introduce the finite-range regularisation scheme which is applied throughout this body of work. The final section describes the use of chiral perturbation theory to correct artefacts resulting from a finite lattice volume.

In later chapters we develop and use more complex chiral extrapolations for particular observables of interest. Throughout that discussion we maintain a focus on applications tailored to lattice QCD in the high-precision era; beyond quark-mass extrapolation formulae, we address extensions needed to account for the quark-line–connected approximation to QCD (Chapter 7), and the breaking of the commonly-employed light quark mass degeneracy $m_u = m_d$ (Chapter 4).

3.1 Effective Field Theory

Effective field theories (EFTs) provide a standard way to analyse physical systems with widely-separated energy scales. Such systems are common in arenas ranging from the high-energy domain of particle physics beyond the SM to the low-energy domain of nuclear physics which is of interest to us here. In essence, EFTs encode the expectation that the details of high-energy interactions will have little influence

on the low-energy dynamics of a system; parameters encoding physics at energy scales that are very large or small with respect to the scale of interest are taken to infinity or zero, respectively. This provides a simpler, approximate, description of the system, which can be improved to arbitrary order by treating corrections induced by higher and lower energy scales—i.e., by the finite physical values of the parameters which have been removed—as perturbations.

This process is very familiar and intuitive; it is the basis of the multi-pole expansion in electrodynamics, the use of Newtonian rather than relativistic mechanics for systems with scales $v \ll c$, and the replacement of a physical dielectric with a uniform one. In a relativistic, quantum mechanical theory where particles may be created and destroyed, however, it is complicated considerably by the necessity of ultraviolet regularisation; the limit in which small distance scales are taken to zero must be handled carefully. Furthermore, the renormalisation-group running of coupling constants is modified in an effective theory—the usual logarithmic dependence on heavy particle masses is traded for scale-dependence.

The machinery of EFTs in the modern sense grew out of the chiral Lagrangian techniques developed by Weinberg, Dashen and others in the late 1960s as a shortcut to current-algebra derivations [42–48]. On the grounds of perturbative unitarity and analyticity, Weinberg argued that the correct effective Lagrangian consists of all operators with the desired fields and symmetries. Thus, to construct an EFT describing physics below some energy scale Λ_χ, only relevant degrees of freedom—states with $m \ll \Lambda_\chi$—are considered explicitly, while heavier excitations with $M \geq \Lambda_\chi$ are 'integrated out' of the action, generating non-local terms. One then writes an expansion of interactions among the light states in powers of (energy/Λ_χ), replacing the non-local interactions from virtual heavy particle exchange with a set of local interactions which are constructed to give the same physics at low energies. The leading terms in the expansion will dominate in the low-energy region of interest.

While the EFT has the same infrared behaviour as the underlying fundamental theory, it has different ultraviolet behaviour; the only remnants of high-energy dynamics are contained in the symmetries of the EFT and in the (*a-priori* unknown) couplings of the resulting low-energy Lagrangian. In our applications of chiral effective field theory to lattice QCD studies in future chapters, these couplings will be determined by fits to lattice simulation results. In the next section we describe the construction of the chiral Lagrangian which was established by Gasser and Leutwyler [49] as the canonical example of the use of effective field theory.

3.2 Chiral Symmetry

The possibility of building a phenomenological effective theory of low-energy QCD exists because there is a mass gap between the pseudoscalar mesons $(\vec{\pi}, \vec{K}, \eta)$, which are the lightest hadrons, and all other states and resonances. This is elegantly explained by the Nambu-Goldstone mechanism: in the limit of vanishing quark mass the mesons are massless bosons arising from the spontaneous breaking of the chiral

symmetry. The construction of an effective Lagrangian describing only the low-energy Goldstone-boson modes, but incorporating the full chiral symmetry of QCD, allows a systematic analysis of the implications of the symmetries and symmetry-breaking pattern, with higher-order corrections treatable in the sense of perturbative field theory.

The QCD Lagrangian was introduced in Chapter 2:

$$\mathcal{L}_{\rm QCD} = \overline{\psi}\big(i\not{D} - M_q\big)\psi - \frac{1}{4}F^{\mu\nu}F_{\mu\nu}. \tag{3.1}$$

Two approximate symmetries of $\mathcal{L}_{\rm QCD}$ concern us here. If all quark masses are equal, the Lagrangian is invariant under global unitary-vector transformations:

$$\psi(x) \to \psi'(x) = e^{iw^a t_a}\psi(x), \tag{3.2}$$

where, as in previous sections, $t_a = \lambda_a/2$ are the generators of flavour-SU(N_f) (and N_f is the number of quark flavours in the theory). These transformations form the group SU$(N_f)_V$, a generalisation of the familiar isospin symmetry SU$(2)_V$. If all quark masses vanish, then $\mathcal{L}_{\rm QCD}$ is also invariant under global axial-vector transformations which form the group SU$(N_f)_A$:

$$\psi(x) \to \psi'(x) = e^{iw^a t_a\gamma_5}\psi(x). \tag{3.3}$$

The combined symmetry group SU$(N_f)_V \otimes$SU$(N_f)_A$ is termed chiral symmetry; the limit $M_q \to 0$ is named the chiral limit. Noether's theorem gives the corresponding classically-conserved vector and axial-vector currents:

$$\mathbf{V}^\mu = \overline{\psi}\gamma^\mu \boldsymbol{t}\psi, \qquad \mathbf{A}^\mu = \overline{\psi}\gamma^\mu\gamma_5\boldsymbol{t}\psi, \tag{3.4}$$

with associated classically-conserved charges

$$\mathbf{Q}_V = \int d^3x \mathbf{V}^0 \quad \text{and} \quad \mathbf{Q}_A = \int d^3x \mathbf{A}^0, \tag{3.5}$$

respectively.

It is useful for future sections to re-write the chiral symmetry group using the notion of chirality, defined by the operators

$$\Gamma_{L,R} = \frac{1}{2}(1 \pm \gamma_5), \tag{3.6}$$

which project left and right-handed[1] components of the Dirac wavefunction:

$$\psi_L = \Gamma_L\psi, \quad \psi_R = \Gamma_R\psi, \quad \text{with} \quad \psi = \psi_L + \psi_R. \tag{3.7}$$

[1]The terms left and right-handed come from the high-energy (or massless) limit in which chirality becomes identical to helicity.

In terms of these chirality states, the QCD Lagrangian (Eq. (3.1)) may be re-expressed as

$$\mathcal{L}_{\rm QCD} = \overline{\psi}_L i \not{D} \psi_L + \overline{\psi}_R i \not{D} \psi_R - \overline{\psi}_L M_q \psi_R - \overline{\psi}_R M_q \psi_L - \frac{1}{4} F^{\mu\nu} F_{\mu\nu}. \tag{3.8}$$

In the chiral limit ($M_q \to 0$), the left and right-handed quark fields decouple and $\mathcal{L}_{\rm QCD}$ becomes invariant under global $\mathrm{SU}(N_f)_L \otimes \mathrm{SU}(N_f)_R$ symmetry transformations.

Chiral symmetry is spontaneously broken in nature by the vacuum state. If it were unbroken, the axial current would be exactly conserved and the axial charge operators, $\hat{Q}^a_A$, would commute with the Hamiltonian: $\left[\hat{Q}^a_A, \hat{H}\right] = 0$. Then, given an eigenstate of the Hamiltonian, $|N^+\rangle$ (e.g., the nucleon, with positive parity and mass $M = 0.940\,\mathrm{GeV}$), such that

$$\hat{H}|N^+\rangle = M|N^+\rangle, \tag{3.9}$$

another state, of opposite parity because of the γ_5 structure of the axial current, must be defined by $|N^-\rangle = \hat{Q}^a_A|N^+\rangle$. By the commutation relation, this state is degenerate with $|N^+\rangle$ in mass. Such pairs of mass-degenerate states of opposite parity are not observed in the low-energy hadron spectrum (the lowest excitations of the nucleon, $N(1535)$ and $\Delta(1620)$, have masses more than 500 MeV greater than that of the N). Clearly, $\hat{Q}^a_A|0\rangle \neq 0$.

The Goldstone theorem [50] states that, in a physical system in which a continuous symmetry is broken by the vacuum state, there exists a massless, spinless boson carrying the quantum numbers of the symmetry transformation; a 'Goldstone boson'. For QCD with $N_f = 3$, there are $2(N_f^2 - 1) = 16$ generators of the chiral symmetry, 8 of which are broken spontaneously by the vacuum state (as $\mathrm{SU}(3)_L \otimes \mathrm{SU}(3)_R \overset{\text{vac.}}{\Longrightarrow} \mathrm{SU}(3)_V$). The 8 associated Goldstone bosons are identified with the pseudoscalar meson octet.

The physical octet mesons are only approximately Goldstone because of the *explicit* chiral symmetry breaking by the finite quark masses; the quark-mass term in the Lagrangian, $-M_q\overline{\psi}\psi$, is not invariant under axial-vector transformations. Nevertheless, as the physical QCD vacuum lies very close to a spontaneously broken phase of an exact chiral symmetry, we can treat the explicit breaking as a perturbation about the chiral limit, giving rise to the small masses of the physical octet mesons.

Ever since the phenomenological importance of chiral symmetry was realised [51], there has been great interest in quantifying its breaking in nature (comprehensive early reviews are given in Refs. [52, 53]). This is complicated by confinement; one cannot simply measure the mass of a free quark. Instead, matrix elements of the scalar quark currents, called sigma commutators, can be determined (to first order) from on-shell scattering amplitudes. The sigma terms vanish identically in the chiral limit and hence their non-zero values in Nature provide some information on the

form and size of explicit chiral symmetry breaking. These quantities are the focus of Chapter 5.

3.3 The Chiral Effective Lagrangian

By the formalism outlined in Section 3.1, the chiral Lagrangian is given by the most general expression of the form

$$\mathcal{L}_{\text{eff.}} = \mathcal{L}_0 + \mathcal{L}_{\text{SB}}, \tag{3.10}$$

which satisfies the following conditions:

- $\mathcal{L}_0$ possesses the same symmetries as the chirally-symmetric part of the QCD Lagrangian. That is, it is invariant under the chiral flavour group $\text{SU}(3)_L \otimes \text{SU}(3)_R$.
- The symmetry group is spontaneously broken to $\text{SU}(3)_V$ by the ground state of the theory.
- The Goldstone modes resulting from the broken symmetry are the only massless, strongly-interacting particles.
- The explicit symmetry-breaking part, $\mathcal{L}_{\text{SB}}$, is small, can be treated perturbatively, and generates small masses for the pseudo-Goldstone mesons.

By construction this Lagrangian will produce the same low-energy expansion as QCD itself. The systematic framework underpinning that expansion—an ordering in powers of energies and momenta (generically denoted by p) of the interacting particles such that any matrix element or scattering amplitude is organised as a Taylor series in p—is called chiral perturbation theory.

The following subsections outline the construction of the various (meson, baryon) components of $\mathcal{L}_{\text{eff.}}$. More detail may be found in Refs. [54, 55], with the 'heavy-baryon' formalism used here presented in Ref. [56].

3.3.1 Pseudo-Goldstone Bosons

In order to construct $\mathcal{L}_{\text{eff.}}$ in the meson sector with $N_f = 3$, it is convenient to represent the pseudoscalar pseudo-Goldstone bosons by a 3×3 matrix field $\Sigma(x) = \xi^2(x) \in \text{SU}(3)$. This matrix transforms linearly under chiral rotations of left and right-handed quarks: under $\text{SU}(3)_L \otimes \text{SU}(3)_R$,

$$\Sigma \to L\Sigma R^\dagger, \tag{3.11a}$$

$$\xi \to L\xi U^\dagger = U\xi R^\dagger, \tag{3.11b}$$

where U is defined implicitly as a function of L, R and ξ by Eq. (3.11b). Explicitly,

$$\Sigma = \xi^2 = \exp\left(\frac{2i\Phi}{f_\pi}\right), \tag{3.12}$$

$$\Phi = \frac{1}{\sqrt{2}} \begin{pmatrix} \frac{1}{\sqrt{2}}\pi_0 + \frac{1}{\sqrt{6}}\eta & \pi^+ & K^+ \\ \pi^- & -\frac{1}{\sqrt{2}}\pi_0 + \frac{1}{\sqrt{6}}\eta & K^0 \\ K^- & \overline{K}^0 & -\frac{2}{\sqrt{6}}\eta \end{pmatrix}, \tag{3.13}$$

where f_π is a low-energy constant which describes the normalisation of the field Σ. From its relation to the axial current this constant is identified, as the notation suggests, with the pion decay constant in the SU(3) chiral limit. A chiral perturbation theory estimate is $f_\pi = 87\,\mathrm{MeV}$, with this normalisation[2] [57]. We note that the symbol 'η' in Eq. (3.13) denotes the octet component of the η field, rather than a representation of the observed η meson.

The meson part of $\mathcal{L}_{\text{eff.}}$ may now be written in terms of the field $\Sigma(x)$ and its derivatives. At low energy, an expansion in powers of the meson momenta is equivalent to an expansion in powers of $\partial^\mu\Sigma$. By Lorentz invariance, only terms with even numbers of derivatives will appear. At leading order in chiral perturbation theory, which corresponds to $\mathcal{O}(p^2)$ in the energy/momentum expansion, the effective Lagrangian is thus [54]

$$\mathcal{L}^{\Phi}_{\text{eff.}} = \frac{f_\pi^2}{4}\,\mathrm{Tr}\big(\partial^\mu\Sigma^\dagger\partial_\mu\Sigma\big) + \lambda\,\mathrm{Tr}\,M_q\big(\Sigma^\dagger + \Sigma\big). \tag{3.14}$$

All two-derivative terms can be incorporated into this form. The low-energy constant λ, which relates the quark-mass matrix to the meson masses, could in principle be calculated explicitly in terms of fundamental QCD parameters. Without exact solutions to QCD Green's functions, however, this constant is determined phenomenologically.

Taylor-expanding the symmetry-breaking part of $\mathcal{L}^{\phi}_{\text{eff.}}$ in powers of the meson field, one finds

$$\begin{aligned} \mathcal{L}^{\Phi}_{\text{SB}} &= \lambda\,\mathrm{Tr}\,M_q\big(\Sigma^\dagger + \Sigma\big) \\ &= 2\lambda\,\mathrm{Tr}(M_q) - \frac{4\lambda}{f_\pi^2}\,\mathrm{Tr}\big(M_q\Phi^2\big) + \mathcal{O}\big(\Phi^4\big) \\ &= 2\lambda(m_s + 2\overline{m}) - \frac{4\lambda}{f_\pi^2}\left(\vec{\pi}\cdot\vec{\pi}\,\overline{m} + \frac{1}{2}\vec{K}\cdot\vec{K}(\overline{m} + m_s) + \frac{1}{3}\eta^2(\overline{m} + 2m_s)\right) + \mathcal{O}\big(\Phi^4\big), \end{aligned} \tag{3.15}$$

where the first term is a vacuum energy contribution, higher-order interaction terms have been neglected, and we have taken the isospin-symmetric limit by approximating $m_u = m_d = \overline{m}$ (i.e., $M_q = \mathrm{diag}(\overline{m}, \overline{m}, m_s)$). The meson masses to leading order

[2] The two most common conventions for the normalisation of f_π differ by a factor of $\sqrt{2}$.

can be simply read from this equation:

$$m_\pi^2 = \frac{8\lambda}{f_\pi^2}\overline{m}, \quad m_K^2 = \frac{4\lambda}{f_\pi^2}(\overline{m} + m_s), \quad m_\eta^2 = \frac{8\lambda}{3f_\pi^2}(\overline{m} + 2m_s). \tag{3.16}$$

We have clearly recovered the Gell-Mann–Oakes–Renner relation [58] $m_\pi^2 \propto \overline{m}$ and the Gell-Mann–Okubo mass relation [59, 60]

$$3m_\eta^2 + m_\pi^2 - 4m_K^2 = 0. \tag{3.17}$$

By taking both the pion and the vacuum matrix-elements of the symmetry-breaking Lagrangian, the low-energy constant λ, and hence the meson masses (from Eq. (3.16)), can also be related directly to the quark condensate:

$$-2\lambda = \langle \overline{u}u \rangle_{\text{vac.}} = \langle \overline{d}d \rangle_{\text{vac.}} = \langle \overline{s}s \rangle_{\text{vac.}}, \tag{3.18}$$

$$f_\pi^2 m_\pi^2 = -\overline{m}\langle \overline{u}u + \overline{d}d \rangle_{\text{vac.}}. \tag{3.19}$$

Other tree-level results can be derived just as simply; expanding $\mathcal{L}^{\Phi}_{\text{eff.}}$ to $\mathcal{O}(\Phi^4)$ yields an interaction term between four mesons:

$$\frac{1}{24f_\pi^2}\big(\text{Tr}([\Phi, \partial_\mu\Phi]\Phi\,\partial^\mu\Phi) + 2\lambda f_\pi^2\,\text{Tr}\big(\Phi^4 M_q\big)\big). \tag{3.20}$$

This expression leads trivially to the celebrated $\pi\pi$ scattering lengths obtained by Weinberg in the 1960s [61] using current algebra techniques (as well as to predictions for the scattering amplitudes for any other four pseudoscalar mesons).

Contributions at next-to-leading order are systematically included by incorporating terms involving higher derivatives and increased powers of the quark masses into the chiral Lagrangian. In addition to the resulting tree-level contributions at $\mathcal{O}(p^4)$, loops with interaction vertices taken from the leading-order Lagrangian must be considered, i.e., chiral perturbation theory corresponds to an expansion in both quark-mass and momentum-dependent interactions and increasing loop complexity. The ordering of this expansion is termed chiral power counting and is the focus of Section 3.4. While formally possible, calculations at arbitrarily high order in the chiral expansion are not practical; at each order there is a significant increase in the number of undetermined coefficients (12 at $\mathcal{O}(p^4)$ and 90 at $\mathcal{O}(p^6)$) which must be input from phenomenology, experiment, or lattice QCD, limiting the predictive power of the theory [62].

3.3.2 Octet Baryons

In the meson sector, chiral perturbation theory gives rise to a power-series expansion of the effective Lagrangian in terms of derivatives and the quark-mass matrix M_q. Progressively higher-dimension operators are suppressed by higher inverse powers of the chiral symmetry breaking scale Λ_χ. Physically, this scale corresponds to the range of validity of the effective theory. As the first non-Goldstone mode is

the ρ meson, perturbation theory with only the pseudo-Goldstone octet mesons is sensible at scales up to $\Lambda_\chi \approx m_\rho \approx 770\,\mathrm{MeV}$. An alternate argument, based on loop geometry, suggests $\Lambda_\chi = 4\pi f_\pi \approx 1\,\mathrm{GeV}$—the same order of magnitude. For baryons, if M_B denotes the baryon-mass matrix, $M_B/\Lambda_\chi \sim \mathcal{O}(1)$. This indicates that higher-derivative operators involving baryon fields are not suppressed in the same way as those involving the meson fields.

To see this explicitly, consider a Lagrangian consisting of the baryon kinetic energy term plus a higher-dimension term with two additional derivatives: for a baryon field B,

$$\mathcal{L} = \overline{B}\big(i\partial\!\!\!/ - M_B\big)B + \overline{B}\big(i\partial\!\!\!/ - M_B\big)\frac{\partial^2}{\Lambda_\chi^2}B. \tag{3.21}$$

As the time derivatives in $\partial^2/\Lambda_\chi^2$ produce a factor of M_B^2/Λ_χ^2, which is not small, this term is important even for processes involving small momenta. A similar problem occurs in the loop expansion; higher-order loop graphs may produce terms which scale as $M_B/\Lambda_\chi \sim \mathcal{O}(1)$ relative to the leading-order contributions and hence cannot be neglected. This complicates the low-energy structure of the meson-baryon system considerably; there is no longer a one-to-one mapping between the loop and small-momentum expansions. To overcome this difficulty and include the octet baryons into the chiral Lagrangian, we use a formalism, pioneered by Jenkins and Manohar (based on earlier work by Georgi for the study of heavy quarks [63]), in which baryons are treated as heavy static fermions [56].

In the chiral limit, the momentum that is transferred between baryons by pion exchange is small with respect to the baryon mass. Thus, baryon velocity is effectively conserved. This suggests a parameterisation of the momentum of a close-to-on-shell baryon as

$$p_\mu = M_B v_\mu + k_\mu, \tag{3.22}$$

where $v^2 = 1$ and $v \cdot k \ll \Lambda_\chi$ is proportional to the amount by which the baryon is off-shell. The effective theory can now be reformulated in terms of new baryon fields B_v, with definite four-velocity v^μ, which are related to the original baryon fields B by

$$B_v(x) = \frac{1 + v\!\!\!/}{2}\exp(iM_B v \cdot x)B(x). \tag{3.23}$$

As $[v^\mu, x^\nu] = i\hbar g^{\mu\nu}/M_B \to 0$ in the heavy fermion limit, this field with definite position and velocity is allowed. The factor $\frac{1}{2}(1 + v\!\!\!/)$ projects out the particle components of the Dirac spinors. The antiparticle fields are integrated out of the theory (generating $\mathcal{O}(1/M_B)$ corrections—this is detailed in Appendix A) and the effects of virtual baryon loops are absorbed into higher-order terms in the chiral expansion. The new baryon fields obey a modified Dirac equation, $v\!\!\!/ B_v = 0$, which no longer has a baryon mass term:

$$\overline{B}\big(i\partial\!\!\!/ - M_B\big)B = \overline{B}_v i\partial\!\!\!/ B_v + \mathcal{O}\left(\frac{1}{M_B}\right). \tag{3.24}$$

It is clear from Eq. (3.23) that derivatives acting on B_v produce powers of k rather than p, so higher-derivative terms in the reformulated effective field theory are suppressed by powers of the small quantity k/Λ_χ. The heavy-baryon formalism thus allows a systematic and consistent expansion in powers of derivatives.

As in the meson case, it is convenient to represent the octet baryons by a 3×3 matrix field[3]

$$\mathbf{B} = B_v = \begin{pmatrix} \frac{1}{\sqrt{2}}\Sigma_0 + \frac{1}{\sqrt{6}}\Lambda & \Sigma^+ & p \\ \Sigma^- & -\frac{1}{\sqrt{2}}\Sigma_0 + \frac{1}{\sqrt{6}}\Lambda & n \\ \Xi^- & \Xi^0 & -\frac{2}{\sqrt{6}}\Lambda \end{pmatrix}. \tag{3.25}$$

Under $\mathrm{SU}(3)_L \otimes \mathrm{SU}(3)_R$, this field transforms as

$$\mathbf{B} \to U\mathbf{B}U^\dagger, \tag{3.26}$$

where U is defined by Eq. (3.11b). Velocity-dependent Pauli-Lubanski spin operators $\mathbf{S}^\mu = S_v^\mu = \frac{i}{2}\gamma_5\sigma^{\mu\nu}v_\nu$ act on the baryon fields. These satisfy[4]

$$v \cdot \mathbf{S} = 0, \quad \mathbf{S}^2\mathbf{B} = -\frac{3}{4}\mathbf{B}, \tag{3.27a}$$

$$\{\mathbf{S}^\lambda, \mathbf{S}^\sigma\} = \frac{1}{2}\big(v^\lambda v^\sigma - g^{\lambda\sigma}\big), \quad \big[\mathbf{S}^\lambda, \mathbf{S}^\sigma\big] = i\epsilon^{\lambda\sigma\alpha\beta}v_\alpha\mathbf{S}_\beta. \tag{3.27b}$$

For a non-relativistic spin-$\frac{1}{2}$ particle in its rest frame the spin operators reduce to the usual expression, $\vec{\sigma}/2$.

The effective Lagrangian in the baryon sector is the most general expression that can be written using the baryon field $\mathbf{B}$, the meson field Σ, the spin operator $\mathbf{S}_\mu$, and derivatives. At lowest order [56],

$$L = \int \frac{d^3v}{2v^0}\mathcal{L}^B_{\text{eff.}}, \tag{3.28}$$

with

$$\begin{aligned} \mathcal{L}^B_{\text{eff.}} \;=\; & i\,\mathrm{Tr}\,\overline{\mathbf{B}}(v\cdot\mathcal{D})\mathbf{B} + 2D\,\mathrm{Tr}\,\overline{\mathbf{B}}\mathbf{S}^\mu\{A_\mu, \mathbf{B}\} + 2F\,\mathrm{Tr}\,\overline{\mathbf{B}}\mathbf{S}^\mu[A_\mu, \mathbf{B}] \\ & + b_D\,\mathrm{Tr}\,\overline{\mathbf{B}}\{\xi^\dagger M_q\xi^\dagger + \xi M_q\xi, \mathbf{B}\} + b_F\,\mathrm{Tr}\,\overline{\mathbf{B}}\big[\xi^\dagger M_q\xi^\dagger + \xi M_q\xi, \mathbf{B}\big] \\ & + \sigma_0\,\mathrm{Tr}\,M_q\big(\Sigma + \Sigma^\dagger\big)\,\mathrm{Tr}\,\overline{\mathbf{B}}\mathbf{B}, \end{aligned} \tag{3.29}$$

where

$$\mathcal{D}^\mu\mathbf{B} = \partial^\mu\mathbf{B} + [V^\mu, \mathbf{B}], \tag{3.30}$$

$$V^\mu = \frac{1}{2}\big(\xi\partial^\mu\xi^\dagger + \xi^\dagger\partial^\mu\xi\big), \quad A^\mu = \frac{i}{2}\big(\xi\partial^\mu\xi^\dagger - \xi^\dagger\partial^\mu\xi\big). \tag{3.31}$$

[3]Subscripts v are implicit on the velocity-dependent heavy baryon fields.
[4]We use the convention $\epsilon_{0123} = +1$.

Here the spin operators and a host of associated identities, which can be found in Appendix B, have been used to eliminate γ-matrix structure; all tensors made from spinors can be written in terms of v^μ and $\mathbf{S}^\mu$. The integral over v in Eq. (3.28), which we suppress for clarity in future expressions, ensures that the theory is Lorentz-invariant. The mass term $M_B\overline{\mathbf{B}}\mathbf{B}$ which appears in the usual chiral Lagrangian was removed by the redefinition of baryon fields in Eq. (3.23).

One could at this point use the Lagrangian given above to develop Feynman rules and form a perturbative expansion of observables such as the octet baryon masses. However, as outlined in the following section, it is important to first consider and include contributions arising from the decuplet baryons.

3.3.3 Decuplet Baryons and Resonances

The lowest-lying decuplet of spin-$\frac{3}{2}$ baryon resonances plays a particularly important role in low-energy baryon phenomenology because of the closeness of the average decuplet mass M_T to the average octet baryon mass M_B; the physical N-Δ mass splitting is $\delta \approx 300\,\text{MeV}$. In our application of chiral perturbation theory to lattice simulation results, this scale is comparable to relevant values of the pseudo-Goldstone boson mass m. As we cannot claim that $m \ll \delta$, it is in general prudent to retain explicit decuplet fields, rather than integrate them out. Integrating the decuplet out would generate higher-order contributions suppressed by powers of $\mathcal{C}^2/\delta$ (where $\mathcal{C}$ is the $TB\phi$ coupling)[5]. Given that the coupling $\mathcal{C}$ is approximately 1.5 (calculated using SU(6) symmetry), and higher-dimension operators from typical short-distance QCD effects are suppressed by $1/\Lambda_\chi$, decuplet contributions are thus significantly more important than other higher-dimension operators in the chiral theory.

Higher baryon resonances are, in general, sufficiently heavy to be consistently integrated out of the low-energy effective theory. Even allowing for unphysically-large meson masses $m \approx 500\,\text{MeV}$—of a comparable scale to the mass gap between the nucleon and higher N^* resonances—these fields do not necessarily need to be included explicitly but can be mimicked by higher-dimension operators whose effects are of a similar size. For example, the $N(1440)$ lies only 500 MeV above the $N(939)$, but it is estimated that the contribution to typical octet baryon amplitudes from this state is no more than 10% that of the $\Delta(1232)$ [56]. This can be understood physically using an intuitive argument provided by the quark model: the wavefunctions of the octet and decuplet baryons differ only in the arrangement of spin, while higher resonances have different spatial wavefunctions. As the hyperfine spin-spin interaction is relatively weak, it is energetically easier for an octet baryon to be converted into a decuplet baryon than for it to transition to other excited states.

For these reasons we include the spin-$\frac{3}{2}$ decuplet, but no higher baryon resonances, into the effective chiral theory. The decuplet is represented by a Rarita-Schwinger field $(T^\mu)_{abc}$, which is totally symmetric under the exchange of flavour

[5]Here T represents decuplet baryons, B represents octet baryons, and ϕ stands for the octet mesons.

indices and contains both spin-$\frac{1}{2}$ and spin-$\frac{3}{2}$ components. The constraint $\gamma^\mu T_\mu = 0$ projects out the spin-$\frac{1}{2}$ pieces. Explicitly,

$$T = \left\{ \begin{pmatrix} \Delta^{++} & \frac{\Delta^+}{\sqrt{3}} & \frac{\Sigma^{*+}}{\sqrt{3}} \\ \frac{\Delta^+}{\sqrt{3}} & \frac{\Delta^0}{\sqrt{3}} & \frac{\Sigma^{*0}}{\sqrt{6}} \\ \frac{\Sigma^{*+}}{\sqrt{3}} & \frac{\Sigma^{*0}}{\sqrt{6}} & \frac{\Xi^{*0}}{\sqrt{3}} \end{pmatrix}, \begin{pmatrix} \frac{\Delta^+}{\sqrt{3}} & \frac{\Delta^0}{\sqrt{3}} & \frac{\Sigma^{*0}}{\sqrt{6}} \\ \frac{\Delta^0}{\sqrt{3}} & \Delta^- & \frac{\Sigma^{*-}}{\sqrt{3}} \\ \frac{\Sigma^{*0}}{\sqrt{6}} & \frac{\Sigma^{*-}}{\sqrt{3}} & \frac{\Xi^{*-}}{\sqrt{3}} \end{pmatrix}, \begin{pmatrix} \frac{\Sigma^{*+}}{\sqrt{3}} & \frac{\Sigma^{*0}}{\sqrt{6}} & \frac{\Xi^{*0}}{\sqrt{3}} \\ \frac{\Sigma^{*0}}{\sqrt{6}} & \frac{\Sigma^{*-}}{\sqrt{3}} & \frac{\Xi^{*-}}{\sqrt{3}} \\ \frac{\Xi^{*0}}{\sqrt{3}} & \frac{\Xi^{*-}}{\sqrt{3}} & \Omega^- \end{pmatrix} \right\}. \quad (3.32)$$

Under $\mathrm{SU}(3)_L \otimes \mathrm{SU}(3)_R$, T^μ transforms as

$$T^\mu_{abc} \to U^d_a U^e_b U^f_c T^\mu_{def}, \quad (3.33)$$

where U is defined in Eq. (3.11b). Just as was done for the octet baryons (Eq. (3.23)), it is convenient to define the velocity-dependent field

$$T^\mu_v(x) = \frac{1+\not{v}}{2} \exp(iM_T v \cdot x) T^\mu(x). \quad (3.34)$$

To avoid the introduction of factors of $\exp(i(M_T - M_B)v \cdot x)$ into the Lagrangian, which would otherwise appear in terms that involve both B and T, one can define

$$\mathbf{T}^\mu = \exp(iM_B v \cdot x) T^\mu_v(x). \quad (3.35)$$

The modified Dirac equation for the re-defined decuplet fields is $\big(i\not{\partial} - \delta\big)\mathbf{T}_\mu = 0$; the decuplet mass term has been replaced by the octet-decuplet mass splitting δ. Spin operators $\mathbf{S}^\mu$, which satisfy the same spin algebra as the octet baryon spin operators, act on the spinor indices[6] of $\mathbf{T}^\mu$. It is again useful to note identities which can be used to eliminate Dirac structures from the theory, in particular,

$$v^\mu \mathbf{T}_\mu = 0, \quad \mathbf{S}^\mu \mathbf{T}_\mu = 0. \quad (3.36)$$

A more complete collection of such identities is given in Appendix B.

To lowest order, the decuplet baryon contribution to the effective Lagrangian may be written as

$$\begin{aligned} \mathcal{L}^T_{\text{eff.}} &= -i\overline{T}^\mu (v \cdot \mathcal{D}) T_\mu + \delta \overline{T}^\mu T_\mu + \mathcal{C}\big(\overline{T}^\mu A_\mu B + \overline{B} A_\mu T^\mu\big) + 2\mathcal{H}\overline{T}^\mu \mathbf{S}_\nu A^\nu T_\mu \\ &\quad + c\overline{T}^\mu \big(\xi^\dagger M_q \xi^\dagger + \xi M_q \xi\big) T_\mu - \tilde{\sigma}\,\mathrm{Tr}\, M\big(\Sigma + \Sigma^\dagger\big)\overline{T}^\mu T_\mu, \end{aligned} \quad (3.37)$$

where we have suppressed the SU(3) tensor indices and the bold typeface on T^μ. Flavour-space contractions denoted by brackets $(\ldots)$ are given by

$$(\overline{B}AB) = \overline{B}^{kji} A^l_i B_{ljk}, \quad (3.38a)$$

$$(\overline{B}BA) = \overline{B}^{kji} A^l_k B_{ijl}, \quad (3.38b)$$

[6] It is important to note that $\mathbf{S}^\mu$ is now *not* the total spin operator. Instead, $\mathbf{S}^\alpha \mathbf{T}^\mu = \frac{1}{2}(\sigma^\alpha - (\sigma \cdot v)v^\alpha)\mathbf{T}^\mu$, i.e., $\mathbf{S}^\mu$ acts only on the spinor portion of the Rarita-Schwinger field.

where B represents either the decuplet baryon tensor T^μ or

$$B_{abc} = \frac{1}{\sqrt{6}}(\epsilon_{abd}\mathbf{B}_{dc} + \epsilon_{acd}\mathbf{B}_{db}). \tag{3.39}$$

The Lagrangian in Eq. (3.37) contains an explicit mass term proportional to the octet-decuplet mass splitting δ because the transformation to velocity-dependent fields has the effect of removing only part of the decuplet baryon mass. The complete first-order Lagrangian for the effective field theory is given by the sum of the meson, octet and decuplet Lagrangians which appear in Eqs. (3.14), (3.29) and (3.37). From this one can derive Feynman rules for meson-baryon interactions (summarised in Section 3.3.4) and use diagrammatic perturbation theory to calculate expansions for hadronic properties, including the octet baryon masses. This is the topic of Section 3.6.

Of course, to obtain meaningful expansions of physical observables in this way, one must include all diagrams to a given order in perturbation theory. The process of assigning a rigorous order to each type of Feynman diagram is the subject of chiral power counting, which is outlined in Section 3.4.

3.3.4 Feynman Rules

Using the complete first-order Lagrangian which was developed in the previous sections (Eqs. (3.14), (3.29) and (3.37)), one can derive Feynman rules within the heavy-baryon formalism. The octet and decuplet baryon propagators, meson propagator, and baryon-meson vertices are summarised in standard notation below.

$$\text{Octet Baryon Propagator:} \qquad \frac{i}{k\cdot v + i\epsilon}, \tag{3.40a}$$

$$\text{Decuplet Baryon Propagator:} \qquad \frac{iP^{\mu\nu}}{k\cdot v - \delta + i\epsilon}, \tag{3.40b}$$

$$\text{Meson Propagator:} \qquad \frac{i}{k^2 - m_\phi^2 + i\epsilon}, \tag{3.40c}$$

$$BB'\phi \text{ Vertex (Fig. 3.1(a)):} \qquad \frac{k\cdot \mathbf{S}}{f_\pi} C_{BB'\phi}, \tag{3.40d}$$

$$BT\phi \text{ Vertex (Fig. 3.1(b)):} \qquad \frac{k_\mu}{f_\pi} C_{BT\phi}. \tag{3.40e}$$

Here v^μ denotes the four-velocity of the heavy baryon B or T, k^μ in a propagator refers to the momentum of the relevant baryon or meson and in a vertex to the (outgoing) momentum of the meson, $P^{\mu\nu} = v^\mu v^\nu - g^{\mu\nu} - (4/3)\mathbf{S}^\mu\mathbf{S}^\nu$ is a spin-polarisation projector that projects onto the spin-$\frac{3}{2}$ solutions to the equation of motion, and δ denotes the average octet-baryon–decuplet-baryon mass splitting. The flavour algebra is encompassed in the definitions of the (Clebsch-Gordan) coefficients C which are given explicitly in Appendix F. Subscripts B, T, and ϕ on these coefficients label the octet baryon, decuplet baryon, and meson which appear in the corresponding

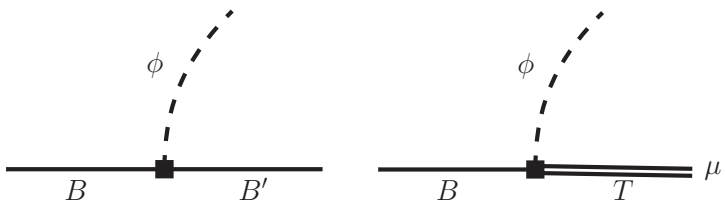

(a) $BB'\phi$ vertex. (b) $BT\phi$ vertex.

Figure 3.1: Diagrammatic representation of the leading-order strong interaction vertices (solid squares). The single, double, and dashed lines denote octet baryons, decuplet baryons, and mesons, respectively.

vertex (illustrated in Fig. 3.1). This list of Feynman rules will be extended in future chapters, where we generalise the Lagrangian to include external sources as needed for the calculation of various current matrix elements.

3.4 Chiral Power Counting

Chiral power counting is a systematic method for assigning a chiral dimension to each Feynman diagram. This dimension plays a role analogous to that of the fine-structure constant α in QED expansions; naive dimensional analysis shows that contributions to physical observables from diagrams with chiral dimension D are suppressed by p^D (where p is the momentum-scale of the chiral expansion—see Section 3.3).

The chiral dimension of a particular Feynman diagram is given by a combination of the dimensions of its propagator and vertex components; each component contributes as specified by the powers of external momenta and meson masses which appear. Using the Feynman rules summarised in the previous section, one finds that [64]:

- **Meson propagators** are given by $\frac{i}{k^2-m_\phi^2+i\epsilon}$, where k is the four-momentum of the meson field and m_ϕ is its mass. They hence have chiral dimension $D=-2$. The total dimension associated with all meson propagators in a given diagram is written as I_M.

- **Octet baryon propagators** and **decuplet baryon propagators** may be expressed as $\frac{i}{v\cdot k+i\epsilon}$ and $\frac{iP^{\mu\nu}}{v\cdot k-\delta+i\epsilon}$ respectively, where k^μ is the four-momentum of the baryon field and v^μ is its four-velocity. The chiral dimension of a baryon propagator is thus[7] $D=-1$. The symbol I_B denotes the total chiral dimension of the baryon propagators in a diagram.

- The chiral dimension $D=d_M$ of a particular **mesonic vertex** is given by the dimension of the term of the chiral Lagrangian from which it originates. Recall

[7]Subtleties regarding transitions between octet and decuplet baryon multiplets will be discussed later in this section.

that by Lorentz covariance only even dimensions contribute: $d_M = 2, 4, 6, \ldots$. The number of mesonic vertices of dimension d_M in a given diagram is denoted by $N^M_{d_M}$.

- Similarly, the dimensions $D = d_B$ of **meson-baryon vertices** are obtained from the dimensions of the terms of the chiral Lagrangian from which they originate. The number of meson-baryon vertices of dimension $d_B = 1, 2, 3, \ldots$ is denoted by $N^{MB}_{d_B}$.

These components combine to give the chiral dimension D of a complete diagram:

$$D = 4L - 2I_M - I_B + \sum_{d_M} d_M N^M_{d_M} + \sum_{d_B} d_B N^{MB}_{d_B}, \tag{3.41}$$

where L is the total number of loops. In the case of fully-connected diagrams, one can eliminate I_M by substituting the general topological identity

$$L = I_M + I_B - \sum_{d_M} N^M_{d_M} - \sum_{d_B} N^{MB}_{d_B} + 1 \tag{3.42}$$

to obtain the relation

$$D = 2L + 2 + I_B + \sum_{d_M} (d_M - 2) N^M_{d_M} + \sum_{d_B} (d_B - 2) N^{MB}_{d_B}. \tag{3.43}$$

The diagrams which are relevant to this body of work have a single baryon line running through the diagram. In this case $\sum_{d_B} N^{MB}_{d_B} = I_B + 1$. Substituting this into Eq. (3.43), we find

$$D = 2L + 1 + \sum_{d_M} (d_M - 2) N^M_{d_M} + \sum_{d_B} (d_B - 1) N^{MB}_{d_B} \geq 2L + 1. \tag{3.44}$$

This shows that tree diagrams contribute at order p, and that one-loop graphs begin to contribute at order p^3.

There is some ambiguity in this power counting scheme for diagrams which include transitions between baryon multiplets, for example *octet* $\rightarrow$ *decuplet* $\rightarrow$ *octet*. In general (for example in their application to lattice QCD simulation results), one wishes chiral extrapolations to be valid for a reasonably large range of values of m_ϕ. Thus one can claim neither $\delta \ll m_\phi$ nor $\delta \gg m_\phi$, and, as a result, the appropriate chiral dimension of loops involving transitions is debatable. Because of the particular significance of decuplet effects, as outlined in Section 3.3.3, we choose to consider self-energy loops involving transitions between octet and decuplet baryons at the same order as the analogous loops without transitions. This will be our choice of convention throughout this body of work. In our scheme, terms which enter a chiral expansion of octet baryon self-energy with chiral dimension $D = 3$ thus arise from the one-loop diagrams shown in Fig. 3.2.

Figure 3.2: One-loop graphs which contribute to an expansion of octet baryon self-energy at order p^3. Single, dashed, and double lines represent octet baryons, mesons, and decuplet baryons, respectively. The solid squares denote leading-order strong-interaction vertices.

When these loops are regularised using the finite-range regularisation scheme (FRR) (introduced in Section 3.5), the simple power counting described in this section is modified; FRR introduces an additional mass parameter Λ with the result that loop processes renormalise chiral parameters at different orders in the energy expansion. In the small meson mass limit, however, FRR gives the same result as other regularisation schemes and the standard power counting is restored. From this one can conclude that the *order* in which loops contribute in FRR is still dictated by the standard formalism [65]. When the meson masses are set to their physical values, FRR expressions include a partial resummation of higher-order effects which combine to cancel unphysical small-distance behaviour. This resummation will be shown explicitly for an example given in Section 3.6.

3.5 Finite-Range Regularisation

As for any physical description in quantum field theory, one must regularise and renormalise infinities arising from self-interactions in chiral perturbation theory. Developed in [66–70], finite-range regularisation (FRR) is a regularisation prescription which takes into account the extended nature of fields of finite structure; the scheme is characterised by the suppression of the ultraviolet behaviour of loop integrals.

FRR was motivated in part by the poor convergence of the traditional approach of dimensional regularisation (DR). DR is a regularisation scheme based on the fact that logarithmically divergent integrals in a four-dimensional theory become convergent in $d = (4 - 2\epsilon)$ dimensions, where $\epsilon > 0$. An analytic continuation to d dimensions is performed, rendering the integral finite, and a finite four-dimensional result is recovered by taking $\epsilon \to 0$ and subtracting terms which diverge in this limit. This process involves integrals over all possible loop (i.e., meson) momenta. This allows meson propagation over distances smaller than typical hadronic size. That is, DR introduces model-dependent effects; it treats meson-baryon couplings as point-like and does not take into account the finite size of the baryon, instead integrating over loop momenta far beyond the scale where the particular EFT has any significance [71, 72].

It is clear that physical results should be independent of regularisation and renormalisation schemes. It is the physical insight recognised above which informs the

development of FRR. In QCD, Goldstone bosons are emitted and absorbed by composite objects made of quarks and gluons. Because these objects have some finite size R, the emission and absorption of probes with momenta greater than $\Lambda \approx R^{-1}$ is suppressed. So, for $m_\phi > \Lambda$, we expect pseudo-Goldstone boson loops to be suppressed by powers of Λ/m_ϕ, not enhanced by powers of m_ϕ/Λ_χ. If $\Lambda > \Lambda_\chi$, this physics would be included in the standard formulation of the effective theory. Evidence suggests, however, that $\Lambda \leq \Lambda_\chi$ [66–70]. FRR thus introduces a finite ultraviolet cutoff (i.e., a mass parameter Λ), which physically corresponds to the fact that the source of the meson cloud is an extended structure [65, 73–75]. The form of the regulator used, which could for example be chosen to be a sharp cutoff or dipole, does not affect the leading-order non-analytic structure of the expansion [70]. Furthermore, the renormalisation constants may be fixed by matching to lattice simulation results, eliminating dependence on the regulator.

FRR also offers improved convergence over dimensionally-regulated SU(3) chiral expansions. This stems from the fact that the parameter Λ remains finite; FRR effectively resums the chiral expansion, leaving only the long-distance model-independent physics at the lower orders. In the limit $m_\phi/\Lambda \to 0$, however, FRR becomes equivalent to DR.

It is worth commenting here on a subtlety which arises when using FRR rather than DR in chiral perturbation theory. As with any theory involving derivative couplings, there is an occasional change of the Feynman rules for the FRR-regularised theory from their prescribed form. The canonical momentum conjugate to a field variable is given by

$$\pi(x) = \frac{\delta \mathcal{L}}{\delta \partial_0 \phi(x)}. \tag{3.45}$$

Time-derivatives in the interaction Lagrangian then lead to canonical momenta which carry portions of the interaction; the interaction Hamiltonian is no longer simply the negative of the interaction Lagrangian. Since the Feynman rules for a theory are derived from the interaction Hamiltonian, it is clear that they are modified, potentially in a nontrivial way [76].

Dimensionally-regularised chiral perturbation theory has the fortunate peculiarity that these changes, which can be accounted for by adding a specific contact interaction proportional to $\delta^4(0)$ to the mesonic part of the theory, vanish. In this case the naive Feynman rules may be used without modification. While this is not the case for the theory with FRR, it has been verified that, to the order of our calculations, the extrapolation of observables such as baryon mass are not affected [65]. We will use the FRR regularisation scheme throughout this work.

3.6 The Nucleon Mass

We illustrate the FRR technique using the chiral extrapolation of the nucleon mass M_N as a test case. Here we account for pion loops only (and neglect η, $\vec{K}$)—a full

SU(3) perturbation theory study of the octet baryon masses will be presented in the next chapter.

The physical nucleon mass M_N is defined as the pole position of the full propagator:

$$S_0(p) = \frac{1}{\not{p} - M_0 - \Sigma(\not{p})}, \tag{3.46}$$

where M_0 denotes the nucleon mass in the chiral limit and $\Sigma(\not{p})$ refers to the (one-particle irreducible) self-energy. Determining the mass M_N thus reduces to a calculation of the self-energy: one must solve

$$M_N - M_0 - \Sigma(M_N) = 0 \tag{3.47}$$

for M_N.

From the discussion of baryon self-energy in Section 3.4, the chiral expansion of M_N may be formulated in terms of $m_\pi^2 \sim m_q$ as

$$M_N = \{a_0 + a_2 m_\pi^2 + a_4 m_\pi^4 + \ldots\} + \{\chi_\pi I_\pi(m_\pi) + \chi_{\pi\Delta} I_{\pi\Delta}(m_\pi) + \ldots\}, \tag{3.48}$$

where the second term corresponds, at leading order, to contributions from the loops displayed in Fig. 3.2. That is, the expansion takes the form

$$M_N = \{\text{terms analytic in } m_q\} + \{\text{chiral loop corrections}\}, \tag{3.49}$$

where the coefficients of the analytic terms are not constrained by chiral symmetry (and will be determined from lattice QCD calculations in future chapters), and the chiral loops account for non-analytic behaviour in the quark masses. The coefficients of the loop terms are model-independent and can be derived using the effective field theory Lagrangian of Section 3.3.

For example, the nucleon self-energy, i.e., the first of the diagrams shown in Fig. 3.2, gives an additive correction $\chi_\pi I_\pi$ to the mass of the nucleon, where

$$-i\delta_{ij}\frac{I_\pi}{24\pi} := \int \frac{d^4k}{(2\pi)^4}\frac{k_i k_j}{(k_0 - i\epsilon)(k^2 - m_\pi^2 + i\epsilon)}. \tag{3.50}$$

Using the results of Appendix C.1 to simplify the integral, and writing χ_π explicitly, this can be expressed as

$$\chi_\pi I_\pi(m_\pi) = -\frac{3g_A^2}{32\pi f_\pi^2}\frac{2}{\pi}\int_0^\infty dk \frac{k^4}{k^2 + m_\pi^2}, \tag{3.51}$$

where $g_A = (D+F)$ in the notation of Eq. (3.29). Both DR and FRR were outlined in Section 3.5. Choosing DR with $\epsilon \to 0$, the nucleon expansion of Eq. (3.48) becomes

$$M_N = c_0 + c_2 m_\pi^2 + \chi_\pi m_\pi^3 + c_4 m_\pi^4 + \ldots, \tag{3.52}$$

where the coefficients c_i denote the a_i of Eq. (3.48) after they have undergone an infinite renormalisation. As previously discussed, DR allows a large contribution from the $k \to \infty$ portion of the integral, and short distance physics is highly overestimated. Numerical estimates of the terms in Eq. (3.52) give [77]

$$M_N = \left(1 + 1.1\left(\frac{m_\pi}{m_R}\right)^2 - 1.0\left(\frac{m_\pi}{m_R}\right)^3 + \ldots\right)[0.89\ \text{GeV}], \tag{3.53}$$

where $m_R = 0.54\,\text{GeV}$. This resembles a geometric series with no sign of convergence for pion masses $m_\pi \gtrsim 0.5\,\text{GeV}$. Pion masses of this magnitude are still typical of many lattice simulations.

If one instead uses FRR, introducing a dipole regulator (the form suggested by a comparison of the nucleon's axial and induced pseudoscalar form factors [78])

$$u(k) = \left(\frac{\Lambda^2}{\Lambda^2 + k^2}\right)^2 \tag{3.54}$$

at each pion-nucleon vertex, the integral becomes

$$I_\pi^{\text{FRR}} = \frac{2}{\pi}\int_0^\infty dk \frac{k^4}{k^2 + m_\pi^2} u^2(k), \tag{3.55}$$

which is convergent for $k \to \infty$ and can be evaluated explicitly:

$$I_\pi^{\text{FRR}} = \frac{1}{16}\frac{\Lambda^5(m_\pi^2 + 4m_\pi\Lambda + \Lambda^2)}{(m_\pi + \Lambda)^4}. \tag{3.56}$$

Taylor-expanding about $m_\pi = 0$, the difference between the two regularisation schemes becomes apparent:

$$I_\pi^{\text{FRR}} \to \frac{\Lambda^3}{16} - \frac{5\Lambda}{16}m_\pi^2 + m_\pi^3 - \frac{35}{16\Lambda}m_\pi^4 + \frac{4}{\Lambda^2}m_\pi^5 + \ldots\,. \tag{3.57}$$

Higher-order DR terms are resummed in the FRR scheme with the result that loop contributions $I_\pi \to 0$ as m_π becomes large. Writing out the FRR expansion of M_N to leading non-analytic order, one recovers the renormalised expansion coefficients c_i obtained using DR:

$$\begin{aligned} M_N &= \left(a_0 + \chi_\pi\frac{\Lambda^3}{16}\right) + \left(a_2 - \chi_\pi\frac{5\Lambda}{16}\right)m_\pi^2 + \chi_\pi m_\pi^3 + \left(a_4 - \chi_\pi\frac{35}{16\Lambda}\right)m_\pi^4 + \ldots \\ &= c_0 + c_2 m_\pi^2 + \chi_\pi m_\pi^3 + c_4 m_\pi^4 + \ldots, \end{aligned} \tag{3.58}$$

just as was claimed in Section 3.4.

3.7 Finite-Volume Corrections

The discussion of chiral perturbation theory in this chapter has, to a large extent, been motivated by our intent to apply this formalism to extrapolate lattice QCD simulation results from unphysically-large pseudoscalar meson masses to the physical masses. As was described in Section 2.2.2, however, there are other systematic effects which must be considered before lattice studies can confront experiment. In particular, simulations are necessarily performed on lattices with some finite spatial extent. In this section we describe an application of effective field theory to the modelling and correction of finite-volume artefacts.

Lattice QCD simulations must satisfy several conditions if the low-energy chiral EFT is to provide an appropriate framework for the estimation of finite-volume effects. Of course, the EFT can only be applied where the standard hierarchy of mass scales is maintained:

$$|\vec{p}\,|, m_\pi \ll \Lambda_\chi \ll a^{-1}. \tag{3.59}$$

Here p is a typical momentum in the system of interest, m_π is the pion mass, Λ_χ is the scale of chiral symmetry breaking which separates soft from hard momenta, and a is the lattice spacing. In a box of finite spatial extent L, momenta are quantised such that $\vec{p} = 2\pi\vec{n}/L$ (with $\vec{n} \in \mathbb{Z}^3$). Equation (3.59) then places a condition on L:

$$\frac{2\pi}{L} \ll \Lambda_\chi \Rightarrow L \gg \frac{2\pi}{\Lambda_\chi} \approx \frac{1}{2\pi f_\pi} \approx 1\,\text{fm}. \tag{3.60}$$

The constraint $L \gg 2R$, where R corresponds approximately to the size of the system of interest, must also be satisfied for (non-pionic) hadronic physics to be completely contained inside the lattice. In this body of work we consider single baryon systems, i.e., $R \approx 1\,\text{fm} \Rightarrow L \gg 2\,\text{fm}$. This is a more stringent requirement than that given in Eq. (3.60).

In addition, to ensure that the box size has no effect on spontaneous chiral symmetry breaking, the lattice must be sufficiently large that $m_\pi L \gg 1$ for simulation values of the pion mass. If this is not maintained, there will be a deformation of the vacuum state and the momentum-zero modes of the pseudo-Goldstone bosons must be treated nonperturbatively [79,80]. Physically, if $m_\pi L \lesssim 1$—that is, the Compton wavelength $1/m_\pi$ (approximately 1.4 fm for the physical pion mass) is of a similar size to L—the pion does not have enough space to propagate before interacting with the boundaries of the finite lattice. If $m_\pi L \gg 1$ and the pion fits comfortably inside the box, however, the explicit symmetry breaking of the low-energy behaviour of the system is more important than that resulting from the finite volume. Like in the infinite volume, contributions from zero modes can be neglected in this case.

In the regime where all conditions are satisfied, quantities calculated on a finite lattice are expected to display behaviour which is qualitatively similar to that on the infinite volume. Furthermore, one can model finite-volume artefacts using the chiral perturbation theory formalism. This approach is based on the understanding that the dominant finite-volume effects come from the exchange of mesons ‘around

the world' of the lattice as a result of the periodic boundary conditions. As a consequence, the mass of a hadron, for example, receives corrections of order $e^{-m_\pi L}$ to its asymptotic value. For typical numerical simulations, such as those performed in Chapter 7, $m_\pi L \geq 3$ and the finite-volume corrections are small compared to the statistical uncertainties.

Formalising this approach, explicit expressions for finite-volume artefacts can be written in terms of the loop integrals which represent the meson cloud in the chiral perturbation theory formalism. The finite-volume shift to the value of some observable is modelled as

$$\delta_L^{\text{tot.}} = \sum_{\mathcal{I}} \chi_{\mathcal{I}}\, \delta_L(\mathcal{I}), \tag{3.61}$$

where the sum runs over all loops $\mathcal{I}$ contributing to the chiral expansion of the observable of interest, and $\chi_{\mathcal{I}}$ is the appropriate chiral coefficient that scales the contribution of loop $\mathcal{I}$ to that observable. The volume-dependence of $\mathcal{I}$ is given by

$$\delta_L(\mathcal{I}) \equiv \mathcal{I}_L - \mathcal{I}_\infty. \tag{3.62}$$

Here $\mathcal{I}_L$ and $\mathcal{I}_\infty$ denote the loop expression evaluated on a lattice of length L and on the infinite volume, respectively:

$$\delta_L(\mathcal{I}) \equiv \left(\frac{1}{L_x L_y L_z} \sum_{n_x n_y n_z} \mathcal{I} - \int \frac{d^3k}{(2\pi)^3}\, \mathcal{I} \right), \tag{3.63}$$

where the n_i are integers. Throughout this body of work we consider symmetric lattices, for which $L_x = L_y = L_z = L$.

While Eq. (3.63) can be evaluated by explicitly performing the finite-volume sum and the integral, this procedure is computationally intensive. It is more efficient to use the well-known decomposition of δ_L in terms of Bessel functions [81, 82]. For a typical integrand

$$\begin{aligned} \delta_L\left(\frac{1}{[\vec{l}^{\,2} + \mathcal{M}^2]^m} \right) &\equiv \frac{1}{L^3} \sum_{\vec{n}} \frac{1}{(\vec{n}^{\,2} + \mathcal{M}^2)^m} - \int \frac{d^3l}{(2\pi)^3} \frac{1}{(\vec{l}^{\,2} + \mathcal{M}^2)^m} \\ &= \frac{2^{-\frac{1}{2}-m} \mathcal{M}^{3-2m}}{\pi^{\frac{3}{2}} \Gamma(m)} \sum_{\vec{n}\neq 0} (L\mathcal{M}|\vec{n}|)^{-\frac{3}{2}+m} K_{\frac{3}{2}-m}(L\mathcal{M}|\vec{n}|), \end{aligned} \tag{3.64}$$

where $\vec{n} \in \mathbb{Z}^3$ and $K_m(z)$ is a modified Bessel function of the second kind. In general, it is necessary to use Feynman parameters to express integrands in the standard form used above. In Appendix C.2 we do this explicitly for an integral discussed in the previous section in the context of a chiral expansion of the nucleon mass. The example we use is

$$I_\pi^{\text{dip.}} = \frac{2}{\pi} \int dk \frac{k^4}{k^2 + m^2} \left(\frac{\Lambda^2}{\Lambda^2 + k^2} \right), \tag{3.65}$$

where a dipole regulator has been chosen within the FRR scheme. Making the identification $\delta_L(\mathcal{M}, m) \equiv \delta_L\Big(\frac{1}{[\vec{l}^{\,2}+\mathcal{M}^2]^m}\Big)$, we find

$$\delta_L\big(I_\pi^{\text{dip.}}\big) = 4\pi\Lambda^8\delta_L(\Lambda, 4) - 16\pi m^2\Lambda^8 \int_0^1 dx(1-x)^3\delta_L\Big(\sqrt{xm^2+(1-x)\Lambda^2}, 5\Big). \tag{3.66}$$

The accuracy of this model has been confirmed, for the case of the octet baryon masses, by a detailed numerical study using multiple lattice volumes [83].

We will use this model in future chapters to correct lattice simulation results for finite-volume artefacts before performing chiral extrapolations. Since finite-size effects should be insensitive to short-distance physics, varying the FRR regulator form and mass within the integrands can also provide an estimate of the model-dependence associated with the ultraviolet part of the loop integrals.

Chapter 4

Octet Baryon Mass Splittings

Charge symmetry violation in the nucleon mass is arguably small—the neutron-proton mass difference is one part in a thousand. The effects of this small CSV, however, are of tremendous significance; it is precisely this which ensures that the hydrogen atom is stable against weak decay and that neutrons can decay into protons (plus electrons and antineutrinos) in radioactive beta decay. Moreover, the elemental abundances established during the first few minutes after the big bang depended on the neutron-proton mass difference and neutron lifetime. If there were a stable neutron, and a more massive proton, our universe would be radically different; one would expect a predominance of heavy nuclei, no normal galaxies, stars, or planets would form, and life as we know it would be impossible [84]. Beyond giving quantitative insight into the breaking of charge symmetry, a precise understanding of the neutron-proton mass difference from first principles will inform studies of the evolution of our universe.

In the framework of the Standard Model, the neutron-proton mass difference is generated by the electroweak interactions. It may be expressed (to leading order) as the sum of two terms:

$$M_n - M_p = \Delta_{\mathrm{EM}} + \Delta_{m_d - m_u}. \tag{4.1}$$

The electromagnetic contribution, Δ_{EM}, arises because of the different electromagnetic charges of the proton and neutron. This contribution is negative and is compensated by the strong isospin breaking contribution $\Delta_{m_d-m_u}$. In a quark picture this second term results from the difference in the masses of the up and down quarks; this is ultimately determined by the values of the Yukawa couplings and by the vacuum expectation value of the Higgs field. The total mass difference $M_n - M_p$, and the analogous physical mass splittings between members of the other baryonic isospin multiplets, have been measured extremely precisely experimentally [30, 85]:

$$M_n - M_p = 1.2933322(4)\,\mathrm{MeV}, \tag{4.2a}$$
$$M_{\Sigma^-} - M_{\Sigma^+} = 8.079(76)\,\mathrm{MeV}, \tag{4.2b}$$
$$M_{\Xi^-} - M_{\Xi^0} = 6.85(21)\,\mathrm{MeV}. \tag{4.2c}$$

The decomposition of each into its electromagnetic and strong components, however, is far less well known.

In recent years there has been considerable effort invested in lattice-based determinations of both the QCD contribution to the baryon mass splittings [86–90] and the electromagnetic contribution [91–94]. However, $1+1+1$–flavour simulations—at this stage the only way to directly probe the full flavour-dependence of QCD observables—are not yet widely available (the first set of $1+1+1+1$–flavour ensembles has recently appeared [35]).

In this chapter we describe the use of SU(3) chiral perturbation theory to determine the strong contribution to the mass splittings among members of octet baryon isospin multiplets using *isospin-averaged* $(2+1$–flavour) lattice calculations [95, 96]. This procedure takes advantage of the high-precision simulations which are currently available for the octet baryon masses using mass-degenerate light quarks. The symmetries of low-energy QCD are used to break this mass-degeneracy—the unknown low-energy constants in the chiral expansion are the same whether or not the SU(2) symmetry is broken—while describing the meson mass dependence of the masses of the entire baryon octet simultaneously.

This study is of particular interest in the light of recent results which suggest that the accepted value for the electromagnetic contribution to the neutron-proton mass difference calculated using the Cottingham formula, $\Delta_{\rm EM} = -0.76 \pm 0.30\,\text{MeV}$ [97], may be too small. Walker-Loud *et al.* (WLCM) claim to find an omission in the traditional analysis[1] and present a larger value of $-1.30 \pm 0.03 \pm 0.47$ MeV [98]. From these estimates, one infers strong isospin breaking contributions of $\Delta_{m_d - m_u} = 2.05 \pm 0.30\,\text{MeV}$ (traditional) and $2.60 \pm 0.47\,\text{MeV}$ (WLCM), respectively. Clearly, independent theoretical estimates of the size of the strong contribution to $M_n - M_p$, such as that reported here, are of considerable value.

4.1 SU(3) Chiral Extrapolation

In this section we develop an SU(3) chiral perturbation theory expansion for the octet baryon masses. This is an extension of the formalism presented in Section 3.6 for the mass of the nucleon to the entire baryon octet, now including not only pion, but also eta and kaon loops. We also revisit the discussion of the meson fields in Section 3.3.1 to allow for a non-zero light quark mass splitting, i.e., $m_u \neq m_d$.

[1] WLCM found that the application of the Cottingham formula with two different Lorentz decompositions of the Compton scattering tensor yields incompatible results. The ambiguity can be removed using a subtracted dispersive analysis, which leads to the updated results.

For $m_u \neq m_d$, mixing occurs between the π^0 and η: expanding the mass term of the meson Lagrangian, Eq. (3.14), in powers of the meson field,

$$\begin{aligned}\mathcal{L}^{\Phi}_{\text{kin}} =& \mathcal{B}\,\text{Tr}\big(M_q\Phi^2\big) && \text{(4.3a)}\\ =& \mathcal{B}(m_u+m_d)\pi^+\pi^- + \mathcal{B}(m_s+m_d)K^0\overline{K}^0 \\ &+ \mathcal{B}(m_s+m_u)K^+K^- + \frac{\mathcal{B}}{2}(m_u+m_u)(\pi^0)^2 \\ &+ \frac{\mathcal{B}}{6}(m_d+m_u+4m_s)\eta^2 + \frac{\mathcal{B}}{\sqrt{3}}(m_u-m_d)\eta\pi^0, && \text{(4.3b)}\end{aligned}$$

where $\mathcal{B} = 4\lambda/f_\pi^2$. This may be diagonalised into the mass basis via a field rotation:

$$\pi^0 \to \pi^0\cos\epsilon - \eta\sin\epsilon, \tag{4.4a}$$

$$\eta \to \pi^0\sin\epsilon + \eta\cos\epsilon, \tag{4.4b}$$

where the mixing angle ϵ is defined[2] by

$$\tan 2\epsilon = \frac{\sqrt{3}\ (m_d - m_u)}{2m_s - (m_d+m_u)}. \tag{4.5}$$

The meson masses may be expressed as

$$m^2_{\pi^\pm} = \mathcal{B}(m_u+m_d), \tag{4.6a}$$

$$m^2_{\pi^0} = \mathcal{B}(m_u+m_d) - \frac{2\mathcal{B}}{3}(2m_s-(m_u+m_d))\frac{\sin^2\epsilon}{\cos 2\epsilon}, \tag{4.6b}$$

$$m^2_{K^\pm} = \mathcal{B}(m_s+m_u), \tag{4.6c}$$

$$m^2_{K^0} = \mathcal{B}(m_s+m_d), \tag{4.6d}$$

$$m^2_{\eta} = \frac{\mathcal{B}}{3}(4m_s+m_u+m_d) + \frac{2\mathcal{B}}{3}(2m_s-(m_u+m_d))\frac{\sin^2\epsilon}{\cos 2\epsilon}, \tag{4.6e}$$

where m_{π^0} and m_η now contain some dependence on the mixing angle ϵ. In the limit $\epsilon \to 0$ these expressions clearly reduce to the isospin-averaged results of Eq. (3.16).

Using the formalism of Chapter 3, the mass of an octet baryon B can now be expressed as a series

$$M_B = M^{(0)} + \delta M_B^{(1)} + \delta M_B^{(3/2)} + \ldots, \tag{4.7}$$

where the superscript indicates the order of the expansion in powers of the quark mass—the explicit chiral symmetry breaking parameter of QCD. The leading term, $M^{(0)}$, denotes the degenerate mass of the octet baryons in the SU(3) chiral limit, and the leading dependence on M_q, which is encoded in $\delta M_B^{(1)}$, arises from terms in the octet Lagrangian (Eq. (3.29)) with coefficients b_D, b_F, and σ_0. In anticipation of the

[2]This notion of a π^0-η mixing angle is well-defined only at leading order in the quark mass expansion.

	C_{Bu}	C_{Bd}	C_{Bs}
p	$\frac{5}{3}\alpha + \frac{2}{3}\beta + 2\sigma$	$\frac{1}{3}\alpha + \frac{4}{3}\beta + 2\sigma$	2σ
n	$\frac{1}{3}\alpha + \frac{4}{3}\beta + 2\sigma$	$\frac{5}{3}\alpha + \frac{2}{3}\beta + 2\sigma$	2σ
Λ	$\frac{1}{2}\alpha + \beta + 2\sigma$	$\frac{1}{2}\alpha + \beta + 2\sigma$	$\alpha + 2\sigma$
Σ^+	$\frac{5}{3}\alpha + \frac{2}{3}\beta + 2\sigma$	2σ	$\frac{1}{3}\alpha + \frac{4}{3}\beta + 2\sigma$
Σ^-	2σ	$\frac{5}{3}\alpha + \frac{2}{3}\beta + 2\sigma$	$\frac{1}{3}\alpha + \frac{4}{3}\beta + 2\sigma$
Ξ^0	$\frac{1}{3}\alpha + \frac{4}{3}\beta + 2\sigma$	2σ	$\frac{5}{3}\alpha + \frac{2}{3}\beta + 2\sigma$
Ξ^-	2σ	$\frac{1}{3}\alpha + \frac{4}{3}\beta + 2\sigma$	$\frac{5}{3}\alpha + \frac{2}{3}\beta + 2\sigma$

Table 4.1: Coefficients of the terms in Eq. (4.7) which are linear in the up, down, and strange quark masses, expressed in terms of the SU(3)-breaking parameters α, β, and σ.

extension to the partially-quenched formalism which we will consider in later chapters, where it becomes notationally convenient to use a different parameterisation of the Lagriangian, we define parameters α, β, and σ:

$$\alpha = \frac{2}{3}b_D + 2b_F, \quad \beta = -\frac{5}{3}b_D + b_F, \quad \sigma = b_D - b_F + \sigma_0. \tag{4.8}$$

In terms of these parameters,

$$\delta M_B^{(1)} = -C_{Bu}\,\mathcal{B}m_u - C_{Bd}\,\mathcal{B}m_d - C_{Bs}\,\mathcal{B}m_s, \tag{4.9}$$

where the coefficients C_{Bq} are given explicitly in Table 4.1.

The first non-analytic term, $\delta M_B^{(3/2)}$, encodes the leading loop corrections to the baryon masses; as discussed in Section 3.4, these correspond to the diagrams shown in Fig. 3.2 and include both octet and decuplet baryon intermediate states. The relevant coefficients and integrals may be derived from the appropriate terms of the chiral Lagrangian, just as was shown for the nucleon mass in Section 3.6. Explicitly,

$$\delta M_B^{(3/2)} = -\frac{1}{16\pi f_\pi^2}\sum_\phi [\chi_{B\phi}\, I_R(m_\phi, 0, \Lambda) + \chi_{T\phi}\, I_R(m_\phi, \delta, \Lambda)], \tag{4.10}$$

where the meson loops involve the integrals

$$I_R(m_\phi, \delta, \Lambda) = \frac{2}{\pi}\int dk \frac{k^4}{\sqrt{k^2 + m_\phi^2}\Big(\delta + \sqrt{k^2 + m_\phi^2}\Big)} u^2(k) - b_0 - b_2 m_\phi^2. \tag{4.11}$$

The subtraction constants, $b_{0,2}$, are defined so that the parameters $M^{(0)}$ and C_{Bq} are renormalised. Explicit expressions for these terms can be readily evaluated by Taylor-expanding the integrand in m_ϕ^2, as was done for the nucleon expressions in Eqs. (3.57) and (3.58). This is done in Ref. [70]. The mass scale Λ is introduced through the finite range regulator $u(k)$ (for details see Section 3.5), and the chiral

	$\chi_{B\phi}$
	π^0
p	$\frac{1}{6}(2(D^2+3F^2)+(D^2+6DF-3F^2)\cos(2\epsilon)-\sqrt{3}(D-3F)(D+F)\sin(2\epsilon))$
n	$\frac{1}{6}(2(D^2+3F^2)+(D^2+6DF-3F^2)\cos(2\epsilon)+\sqrt{3}(D-3F)(D+F)\sin(2\epsilon))$
Λ	$\frac{2}{3}D^2$
$\Sigma^\pm$	$F^2+F^2\cos(2\epsilon)+\frac{2}{3}D\sin\epsilon(\pm 2\sqrt{3}F\cos\epsilon+D\sin\epsilon)$
$\Xi^{0/-}$	$\frac{1}{6}(2(D^2+3F^2)+(D^2-6DF-3F^2)\cos(2\epsilon)\pm\sqrt{3}(D+3F)(D-F)\sin(2\epsilon))$
	η
p	$\frac{1}{6}(2(D^2+3F^2)-(D^2+6DF-3F^2)\cos(2\epsilon)+\sqrt{3}(D-3F)(D+F)\sin(2\epsilon))$
n	$\frac{1}{6}(2(D^2+3F^2)-(D^2+6DF-3F^2)\cos(2\epsilon)-\sqrt{3}(D-3F)(D+F)\sin(2\epsilon))$
Λ	$\frac{2}{3}D^2$
$\Sigma^\pm$	$\frac{2}{3}(D^2\cos^2\epsilon\mp 2\sqrt{3}DF\cos\epsilon\sin\epsilon+3F^2\sin^2\epsilon)$
$\Xi^{0/-}$	$\frac{1}{6}(2(D^2+3F^2)-(D^2-6DF-3F^2)\cos(2\epsilon)\mp\sqrt{3}(D+3F)(D-F)\sin(2\epsilon))$

	$\pi^\pm$	K^0	$K^\pm$
p	$(D+F)^2$	$(D-F)^2$	$\frac{2}{3}(D^2+3F^2)$
n	$(D+F)^2$	$\frac{2}{3}(D^2+3F^2)$	$(D-F)^2$
Λ	$\frac{4}{3}D^2$	$\frac{1}{3}(D^2+9F^2)$	$\frac{1}{3}(D^2+9F^2)$
$\Sigma^\pm$	$\frac{2}{3}(D^2+3F^2)$	$(D\mp F)^2$	$(D\pm F)^2$
Ξ^0	$(D-F)^2$	$\frac{2}{3}(D^2+3F^2)$	$(D+F)^2$
Ξ^-	$(D-F)^2$	$(D+F)^2$	$\frac{2}{3}(D^2+3F^2)$

Table 4.2: Chiral SU(3) coefficients for the coupling of an octet baryon to other octet baryons through the pseudoscalar octet meson ϕ.

coefficients $\chi_{B\phi}$ and $\chi_{T\phi}$ relevant to this particular calculation are given in Tables 4.2 and 4.3.

In the most general case, each octet baryon receives distinct loop contributions from each of the mesons $\pi^\pm, \pi^0, K^\pm, K^0, \eta$, where the $\pi^\pm$ and $K^\pm$ remain pairwise mass-degenerate. In the isospin-averaged scenario ($\epsilon \to 0$), to which we turn in the next section, the sum in Eq. (4.10) runs only over π, K, and η: $\chi_{B\pi} = \chi_{B\pi^\pm} + \chi_{B\pi^0}$, with the contributions from the charged and neutral kaons combined in an analogous way. Clearly, the coefficients of terms linear in the light quark masses may also be combined: $C_{Bl} = C_{Bu} + C_{Bd}$. Our calculation of the octet baryon mass splittings in Section 4.3 will be based on the observation that the *a-priori* unknown low-energy constants which appear in these coefficients, namely α, β, and σ, remain linearly independent in this limit (when considering the entire baryon octet) and hence can be determined using isospin-symmetric $2+1$–flavour lattice QCD simulations.

	$\chi_{T\phi}\mathcal{C}^{-2}$				
	π^0	$\pi^\pm$	K^0	$K^\pm$	η
p	$\frac{4}{9}\cos^2\epsilon$	$\frac{8}{9}$	$\frac{2}{9}$	$\frac{1}{9}$	$\frac{4}{9}\sin^2\epsilon$
n	$\frac{4}{9}\cos^2\epsilon$	$\frac{8}{9}$	$\frac{1}{9}$	$\frac{2}{9}$	$\frac{4}{9}\sin^2\epsilon$
Λ	$\frac{1}{3}\cos^2\epsilon$	$\frac{2}{3}$	$\frac{1}{3}$	$\frac{1}{3}$	$\frac{1}{3}\sin^2\epsilon$
Σ^+	$\frac{1}{9}(\cos\epsilon+\sqrt{3}\sin\epsilon)^2$	$\frac{1}{9}$	$\frac{2}{9}$	$\frac{8}{9}$	$\frac{1}{9}(-\sqrt{3}\cos\epsilon+\sin\epsilon)^2$
Σ^-	$\frac{1}{9}(-\cos\epsilon+\sqrt{3}\sin\epsilon)^2$	$\frac{1}{9}$	$\frac{8}{9}$	$\frac{2}{9}$	$\frac{1}{9}(\sqrt{3}\cos\epsilon+\sin\epsilon)^2$
Ξ^0	$\frac{1}{9}(\cos\epsilon+\sqrt{3}\sin\epsilon)^2$	$\frac{2}{9}$	$\frac{1}{9}$	$\frac{8}{9}$	$\frac{1}{9}(-\sqrt{3}\cos\epsilon+\sin\epsilon)^2$
Ξ^-	$\frac{1}{9}(-\cos\epsilon+\sqrt{3}\sin\epsilon)^2$	$\frac{2}{9}$	$\frac{8}{9}$	$\frac{1}{9}$	$\frac{1}{9}(\sqrt{3}\cos\epsilon+\sin\epsilon)^2$

Table 4.3: Chiral SU(3) coefficients for the coupling of an octet baryon to the decuplet baryons through the pseudoscalar octet meson ϕ.

4.2 Fits to Isospin-Averaged Lattice QCD Simulation Results

Here we describe the application of the octet-baryon–mass chiral extrapolation formalism developed in the previous section to recent $2+1$–flavour (i.e., isospin-averaged, with $m_u = m_d$) lattice QCD simulation results. The fits described will form the basis for the extraction of the strong contribution to the octet baryon mass splittings in Section 4.3.

We consider two distinct sets of simulations, generated by the PACS-CS [95] and QCDSF-UKQCD [96] collaborations. There are significant systematic differences between the two sets of ensembles, including the lattice volumes, lattice spacings, and methods of determining these spacings. Furthermore, they follow quite different trajectories in the light-strange quark mass plane, as shown in Fig. 4.1. While the PACS-CS collaboration results are generated at what is essentially a fixed strange quark mass, the QCDSF-UKQCD collaboration simulations follow paths of constant singlet quark mass ($m_K^2 + m_\pi^2/2$), beginning at several SU(3)-symmetric points. We perform independent analyses on these two lattice data sets.

Before fitting the chiral perturbation theory expressions of the previous section to the lattice simulation results, we correct for finite-volume effects using the formalism outlined in Section 3.7. The corrections are small; for the PACS-CS collaboration results ($L^3 \times T = 32^3 \times 64$, $L \approx 2.9\,\text{fm}$) they are less than 1% at all masses. The corrections to the QCDSF-UKQCD simulation results range between approximately 5% on the smallest volume ($L^3 \times T = 24^3 \times 48$, $L \approx 1.8\,\text{fm}$) to less than 0.5% on the largest ($L^3 \times T = 48^3 \times 96$, $L \approx 3.6\,\text{fm}$). We also allow for an uncertainty on these corrections, determined by allowing the dipole mass of the FRR regulator used in the finite-volume estimation to range between 0.8 GeV and 4 GeV; while 0.8 GeV is a typical value (e.g., based on a comparison of the nucleon's axial and induced

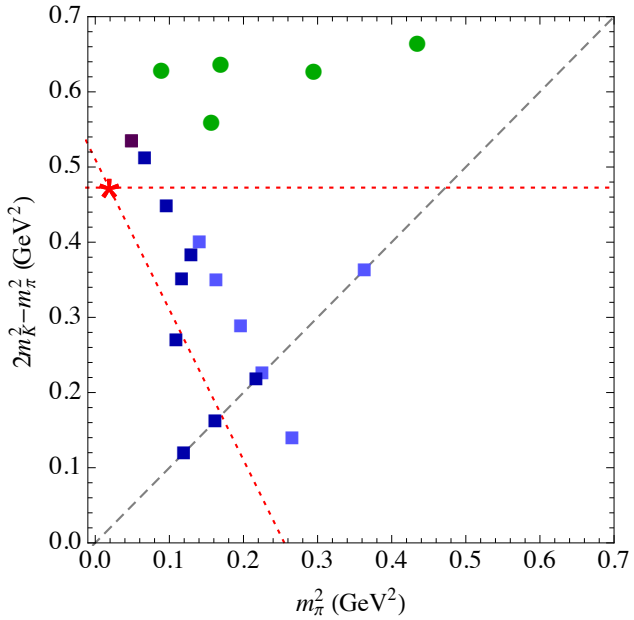

Figure 4.1: Locations of the lattice simulations in the m_l–m_s plane. The green circles show the PACS-CS [95] data set, while the squares denote QCDSF-UKQCD collaboration results [96] where the light blue, dark blue, and purple colours indicate lattice volumes of dimension $L^3 \times T = 24^3 \times 48$, $32^3 \times 64$, and $48^3 \times 96$, respectively. The red star represents the physical point and the dashed line indicates the SU(3)-symmetric trajectory. The dotted red lines show the trajectories plotted in Figs. 4.2 and 4.3: constant strange quark mass and constant singlet quark mass ($m_K^2 + m_\pi^2/2 = \text{fixed}$), passing through the physical point.

pseudoscalar form factors [78]), the limit of large regulator mass corresponds to the regulator-independent formalism.

After correcting to infinite volume, we fit to the simulation results for the entire baryon octet simultaneously. Of course, separate fits are performed to the results of the two collaborations, which have different sources of systematic uncertainty because of the different lattice configurations and simulation parameters. While our formal chiral power counting scheme treats the octet and decuplet baryons as degenerate (as outlined in Section 3.4), we retain the octet-decuplet mass splitting, δ, in numerical evaluations, setting this to the physical N-Δ splitting: $\delta = 0.292\,\text{GeV}$. The baryon-baryon-meson coupling constants are taken from phenomenology; $D + F = g_A = 1.27$, $F = \frac{2}{3}D$ and $\mathcal{C} = -2D$, and f_π is set to 87 MeV, a chiral perturbation theory estimate for the pion decay constant in the SU(3) chiral limit [57]. The fit parameters are the octet baryon mass in the chiral limit $M^{(0)}$, the SU(3) chiral symmetry breaking parameters α, β, σ, and the finite-range regulator mass Λ. Of course, ϵ, which parameterises the light-quark mass splitting, is zero for this fit to $2+1$–flavour lattice simulations.

The fit to the PACS-CS baryon octet data is shown in Fig. 4.2, while that to the QCDSF-UKQCD set is shown in Fig. 4.3 (and also in Fig. D.2 in Appendix D).

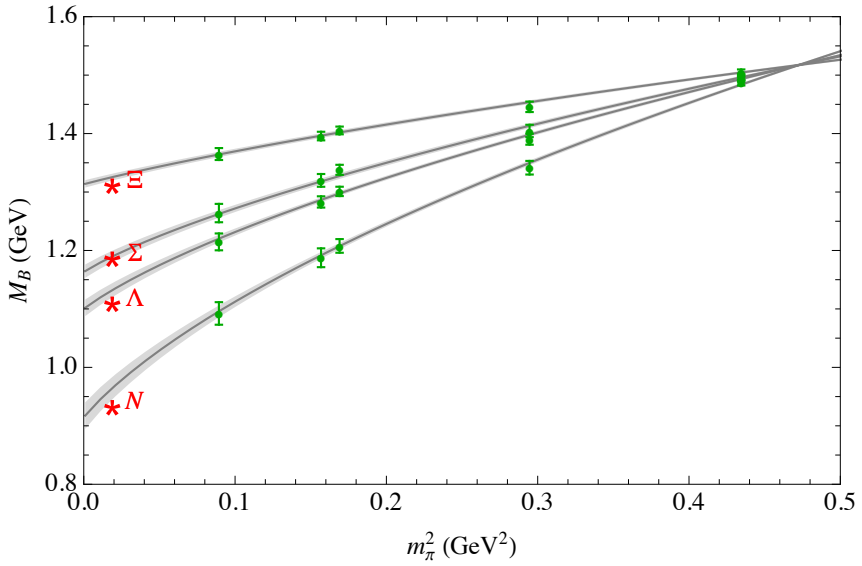

Figure 4.2: Fit to the PACS-CS lattice simulation results. The error bands shown are purely statistical and incorporate correlated uncertainties between all fit parameters. The lattice data was corrected for the effects of the finite lattice volume before fitting. For display the data has been shifted (based on the fit—see Eq. (4.12)) from the simulation strange quark mass, which was somewhat larger than the physical value, to the physical value. The red stars show the experimentally-determined baryon masses [30].

For illustration, the lattice simulation results ($M_B^{\text{latt.}}$) have been shifted onto the trajectories shown in Fig. 4.1 using the chiral fit:

$$M_B^{\text{latt.}} \to M_B^{\text{latt.}} - \left[M_B^{\text{fit}}\left(m_\pi^{(\text{sim.})}, m_K^{(\text{sim.})}\right) - M_B^{\text{fit}}\left(m_\pi^{(\text{traj.})}, m_K^{(\text{traj.})}\right)\right]. \tag{4.12}$$

Here $m_\phi^{(\text{sim.})}$ denotes the simulation value of the meson mass, while $m_\phi^{(\text{traj.})}$ denotes the closest point on the desired trajectory (relative to the axes of Fig. 4.1). The shifts are illustrated explicitly in Appendix D. This process allows us to show both the comparison of our extrapolated results with the experimental values of the baryon masses, and the quality of fit to the lattice data, on a single figure.

The quality of fit is clearly excellent in each case; the χ^2/d.o.f. are 0.5 and 0.6 for the PACS-CS and QCDSF-UKQCD results, respectively. The dipole regulator masses, $\Lambda = 1.0(1)$ GeV and 0.8(2) GeV, are in close agreement with the value deduced from an analysis of nucleon magnetic moment data [99] and, from the phenomenological point of view, remarkably close to the value suggested by a comparison of the nucleon's axial and induced pseudoscalar form factors [78]. While we use the dipole regulator to calculate the central values, we allow the form of the UV regulator to vary between monopole, dipole, Gaussian, and sharp cutoff forms as an estimate of the model-dependence. This is the smallest systematic uncertainty.

A comparison of the octet baryon masses extrapolated to the physical point with the experimental values is given in Table 4.4. The results are largely consistent; we

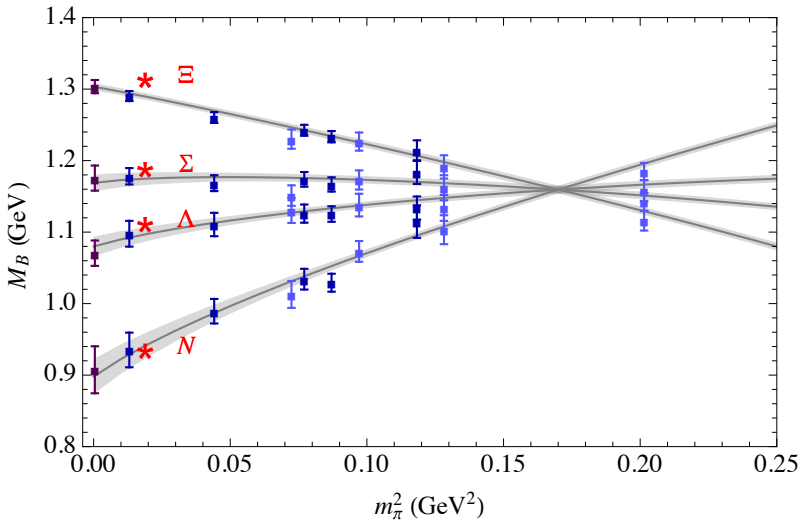

(a) Physical singlet-mass trajectory.

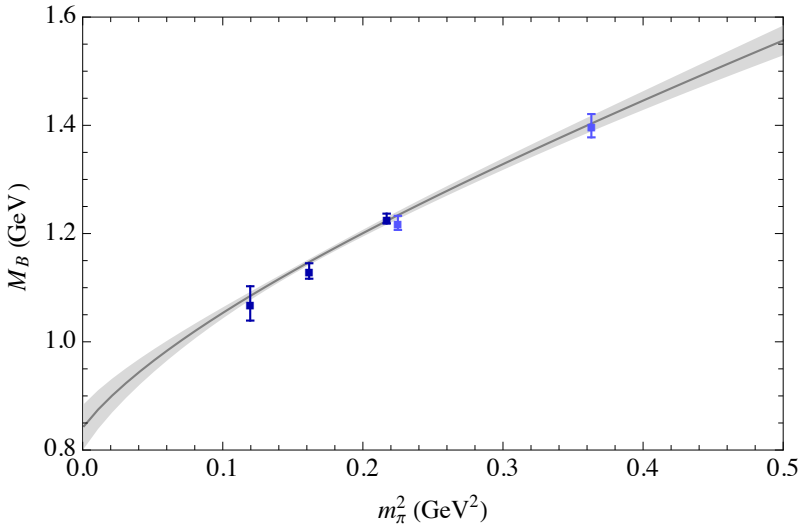

(b) SU(3)-symmetric line: $m_K = m_\pi$.

Figure 4.3: Fit to the QCDSF-UKQCD baryon octet data, plotted along the physical singlet-mass trajectory ($m_K^2 + m_\pi^2/2 =$ constant) and SU(3)-symmetric line. The error bands shown are purely statistical, with a dipole regulator chosen in the FRR formalism, and incorporate correlated uncertainties between all fit parameters. The lattice data was corrected for finite-volume effects before fitting. For display the lattice points in (a) have been shifted (based on the fit—see Eq. (4.12)) from the simulation values of the pion and kaon masses to the physical singlet trajectory. These shifts are shown in Fig. D.1. Lattice data points on the SU(3)-symmetric line are only shown on figure (b). Colour-coding is as in Fig. 4.1. The red stars show the experimental values of the baryon masses [30].

B	Mass (GeV) PACS-CS	QCDSF-UKQCD	Experimental
N	0.964(19)(23)	0.940(18)(9)	0.939
Λ	1.132(12)(15)	1.110(10)(5)	1.116
Σ	1.190(10)(10)	1.174(9)(4)	1.193
Ξ	1.325(6)(3)	1.289(5)(1)	1.318

Table 4.4: Octet baryon masses in the infinite-volume after chiral extrapolation to the physical point. The first uncertainty quoted is statistical, while the second allows for variation of the form of the FRR UV regulator and for a 10% deviation of f_π, F, $\mathcal{C}$, and δ from their central values. The experimental baryon masses are taken from Ref. [30].

thus expect these fits to provide a good basis for the extraction of the mass splittings among members of the baryon isospin multiplets as described in the next section.

4.3 Mass Splittings

Using the chiral extrapolation formulae developed in Section 4.1 (summarised in Eqs. (4.7), (4.9) and (4.10)) it is straightforward to write expressions for the strong mass splittings between members of the baryon isospin multiplets: $(M_n - M_p)$, $(M_{\Sigma^-} - M_{\Sigma^+})$, and $(M_{\Xi^-} - M_{\Xi^0})$. The isospin-averaged fits described in Section 4.2 can then be used to reduce these expressions to functions of quark mass only; all other free parameters, namely the SU(3)-breaking parameters α, β, and σ, as well as the regulator mass Λ, are specified by the fits.

We choose to express our results in terms of the light-quark mass ratio $R = m_u/m_d$. The Gell-Mann–Oakes–Renner relation suggests the definition

$$\omega = \frac{\mathcal{B}(m_d - m_u)}{2} = \frac{1}{2}\frac{(1-R)}{(1+R)} m^2_{\pi_{(\text{phys.})}}, \tag{4.13}$$

which leads to the identifications of the quark mass terms in Eq. (4.9) as

$$\mathcal{B}m_u = \frac{1}{2}m^2_{\pi_{(\text{phys.})}} - \omega, \tag{4.14a}$$

$$\mathcal{B}m_d = \frac{1}{2}m^2_{\pi_{(\text{phys.})}} + \omega, \tag{4.14b}$$

$$\mathcal{B}m_s = m^2_{K_{(\text{phys.})}} - \frac{1}{2}m^2_{\pi_{(\text{phys.})}}. \tag{4.14c}$$

Here we take $m_{\pi_{(\text{phys.})}} = 137.3\,\text{MeV}$ and $m_{K_{(\text{phys.})}} = 497.5\,\text{MeV}$ to be the physical isospin-averaged meson masses [30]. The loop meson masses are calculated using Eq. (4.6).

The resulting octet baryon mass splittings are summarised, as a function of ω, in Table 4.5, and the strong neutron-proton mass difference is shown graphically

	$\Delta_{m_d-m_u} \times \left[m^2_{\pi_{(\text{phys.})}}/\omega\right]$(MeV)	
	PACS-CS	QCDSF-UKQCD
$M_n - M_p$	20.1(13)	17.5(10)
$M_{\Sigma^-} - M_{\Sigma^+}$	52.2(24)	52.6(13)
$M_{\Xi^-} - M_{\Xi^0}$	32.0(18)	35.2(14)

Table 4.5: Strong mass splittings between members of the baryon isospin multiplets, based on a chiral extrapolation of lattice QCD simulation results. The quoted uncertainties contain all statistical and systematic errors (discussed in the text) combined in quadrature. The constant ω, defined in Eq. (4.13), encodes the mass difference between the light quarks.

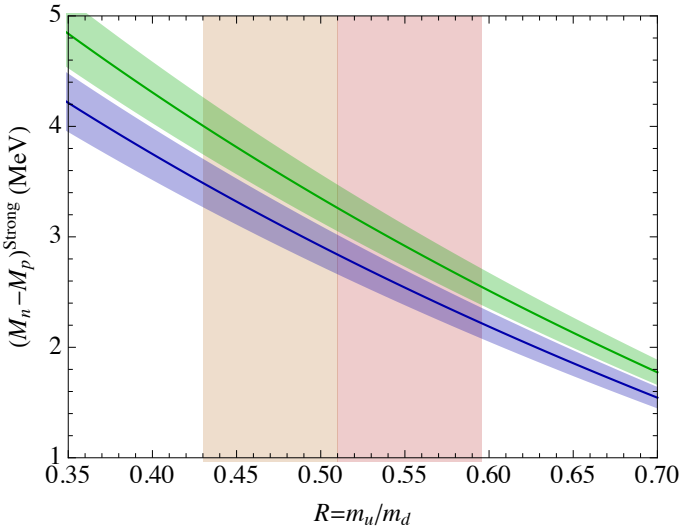

Figure 4.4: Strong contribution to the neutron-proton mass difference as a function of the light-quark mass ratio R. The green (upper) and blue (lower) bands show the result of fits to the PACS-CS and QCDSF-UKQCD collaboration simulations, respectively. The vertical pink (right) and orange (left) shaded bands correspond to two recent estimates of the physical up-down quark mass ratio [100, 101] as described in the text (see Eq. (4.15)).

as a function of R in Fig. 4.4. The results using the fits based on the PACS-CS and QCDSF-UKQCD collaboration simulations are largely consistent; the mass splittings between the members of the sigma and cascade baryon isospin multiplets agree at the 1-sigma level, while the two results for the strong neutron-proton mass difference differ by just over one sigma.

To determine these quantities in physical units we take two recent estimates for the up-down quark mass ratio [100, 101],

$$R = \frac{m_u}{m_d} = 0.553 \pm 0.043, \quad \text{and} \quad 0.47 \pm 0.04. \tag{4.15}$$

The first of these is determined by a fit to meson decay rates. This value is compatible with more recent estimates of the ratio from $2+1$ and 3-flavour QCD and QED [87, 102]. The second is the result from the FLAG[3] [101].

Numerical results in physical units are summarised in Table 4.6. The error bands quoted are the result of a complete analysis taking into account the correlated uncertainties arising from all of the fit parameters, as well as the quoted uncertainty on R. Monopole, dipole, Gaussian, and sharp cutoff regulators $u(k)$ are considered within the FRR scheme; the variation of the final results as $u(k)$ is changed is of order 1% of the total mass differences. The deviation as the parameters f_π, F, $\mathcal{C}$, and δ are perturbed by $\pm 10\%$ from their central values is similarly small, and the statistical uncertainty arising from the fit to lattice data is smaller still. In fact, the dominant uncertainty is that arising from the quoted error band on the light-quark mass ratio R. It is clear that better estimates of this quantity will allow our results to be greatly improved in precision, without the need for further lattice data. Conversely, a precise determination of the electromagnetic contribution to the neutron-proton mass difference could possibly facilitate an improved estimate of R by this method. This is shown clearly in Fig. 4.5, which illustrates that our results are more consistent with both the traditional and WLCM calculations of the electromagnetic neutron-proton mass difference, and with direct lattice QCD calculations of the strong contribution, when taken with the larger estimate of R (Leutwyler [100]) than with the smaller value (FLAG [101]).

It is interesting to compare our results with those from a different analysis of the same QCDSF-UKQCD collaboration simulation set. Horsley and collaborators [90] have recently calculated the strong contribution to the baryon mass splittings from this lattice data using a linear and quadratic SU(3)-flavour-symmetry–breaking expansion in the quark masses. As the expansion coefficients depend only on the average quark mass, provided this is kept constant at its physical value (as it is along the primary QCDSF-UKQCD simulation trajectory), a fit of these coefficients to the isospin-averaged lattice results allows an estimation of the baryon mass splittings at the physical point. The results using this method are [90]:

$$M_n - M_p\big|_{\text{strong}} = 3.13(15)(53)\,\text{MeV}, \tag{4.16a}$$

$$M_{\Sigma^-} - M_{\Sigma^+}\big|_{\text{strong}} = 8.10(14)(135)\,\text{MeV}, \tag{4.16b}$$

$$M_{\Xi^-} - M_{\Xi^0}\big|_{\text{strong}} = 4.98(10)(84)\,\text{MeV}. \tag{4.16c}$$

The first uncertainty quoted in Eq. (4.16) is statistical, while the second allows for violations of Dashen's theorem[4]. While in this approach one can only make use of lattice data calculated along a trajectory which holds the average quark mass fixed,

[3] FLAG stands for the FLAVIAnet Lattice Averaging Group which provides world-averages of lattice simulation results for a number of observables.

[4] This is the statement that the squares of the electromagnetic contributions to the mass differences between the charged and neutral pseudoscalar mesons are equal in the chiral SU(3) limit, i.e., $\left(m^2_{\pi^\pm} - m^2_{\pi^0}\right)_{\text{EM}} = \left(m^2_{K^\pm} - m^2_{K^0}\right)_{\text{EM}}$.

	$\Delta_{m_d - m_u}$(MeV)			
	PACS-CS		QCDSF-UKQCD	
R	0.553(43)	0.47(4)	0.553(43)	0.47(4)
$M_n - M_p$	2.90(18)(36)	3.63(23)(37)	2.51(15)(31)	3.15(19)(32)
$M_{\Sigma^-} - M_{\Sigma^+}$	7.51(35)(93)	9.40(44)(97)	7.57(19)(94)	9.49(24)(98)
$M_{\Xi^-} - M_{\Xi^0}$	4.60(26)(57)	5.77(33)(59)	5.06(20)(63)	6.34(25)(65)

Table 4.6: Strong mass splittings between members of the baryon isospin multiplets, based on a chiral extrapolation of lattice QCD simulation results. For the fits to each data set we display the results using two different estimates of the up-down quark mass ratio R [100, 101]. The second uncertainty—by far the dominant contribution in all cases—results from propagating the uncertainty on R, while the first includes all other statistical and systematic uncertainties combined in quadrature.

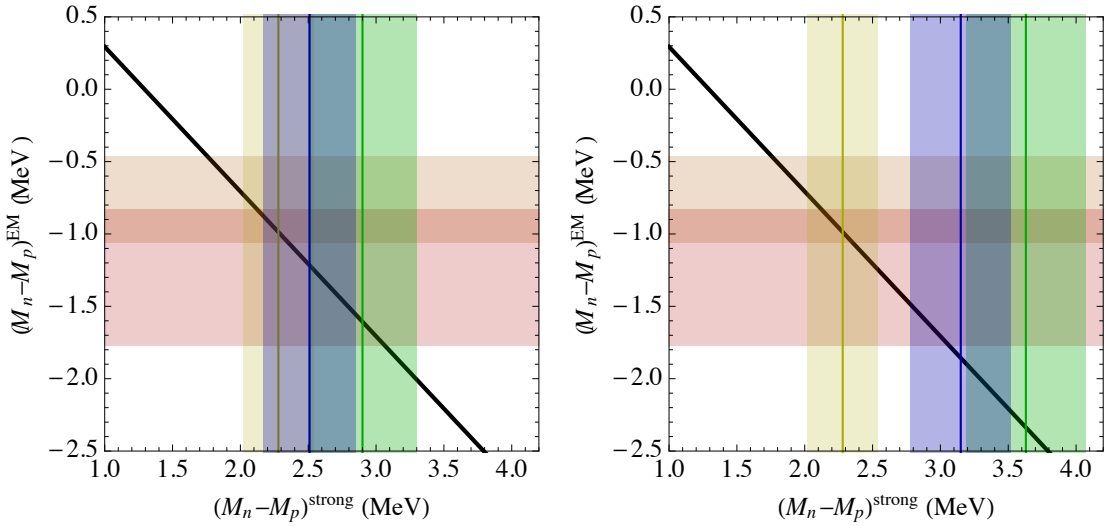

(a) Leutwyler: $R = 0.553(43)$ [100].

(b) FLAG: $R = 0.47(4)$ [101].

Figure 4.5: Strong and electromagnetic contributions to the neutron-proton mass difference. The black line indicates the experimental constraint on the total [30]. The green and blue shaded bands show the result of fits to the PACS-CS and QCDSF-UKQCD collaboration simulations, respectively, with the given values of the light-quark mass ratio R. The yellow vertical band indicates a recent direct lattice calculation of the strong mass splitting by the BMW collaboration [34]. The horizontal bands show the traditional (orange) and WLCM (pink) estimates for the EM contribution.

	$\Delta_{m_d-m_u}$ (MeV)	$M_n - M_p$	$M_{\Sigma^-} - M_{\Sigma^+}$	$M_{\Xi^-} - M_{\Xi^0}$
1	Chiral (PACS-CS)	2.9(4)	7.5(10)	4.6(6)
2	Chiral (QCDSF-UKQCD)	2.5(3)	7.6(9)	5.0(6)
3	QCDSF-UKQCD	3.1(6)	8.1(14)	5.0(9)
4	Exp. & EM (traditional)	2.0(3)	7.9(3)	6.0(3)
5	Exp. & EM (WLCM)	2.6(5)		
6	Exp. & EM [103]	2.3(4)	8.1(11)	6.5(11)

Table 4.7: Strong contribution to the octet baryon mass splittings. Lines 1 and 2 show the results of our chiral extrapolations of PACS-CS and QCDSF-UKQCD lattice data, respectively, with the up-down quark mass ratio set to $R = 0.553(43)$. Line 3 shows the QCDSF-UKQCD collaboration analysis of their data as described in the text, while lines 4 and 5 give estimates deduced from the total mass splittings and electromagnetic contributions, as determined by Gasser and Leutwyler (traditional) or Walker-Loud *et al.* (WLCM). An update and extension of the WLCM dispersion analysis is shown in line 6 [103].

our chiral fit (results presented in Table 4.6) also includes simulations which lie away from this line. This is the primary reason for our smaller uncertainties. We also point out that both methods require some theoretical input: we input the up-down quark mass ratio R, while the Horsley *et al.* calculation uses Dashen's theorem (with some uncertainty) to estimate 'pure QCD' meson masses at the physical point. The clear consistency between the two calculations is encouraging.

4.4 Summary and Discussion

We have calculated the strong contribution to the mass splittings between members of the octet baryon isospin multiplets using a formal chiral expansion based on broken SU(3)-flavour symmetry, fit to lattice QCD simulation results. Our results, based on independent analyses of PACS-CS and QCDSF-UKQCD lattice data sets, are summarised in Table 4.7. Both calculations yield compatible values, despite significant differences between the two lattice studies, including in particular different lattice volumes, lattice spacings, and different methods of determining these spacings. Of course, as emphasised previously, the two sets of lattice ensembles also follow quite different trajectories in m_π–m_K space. Furthermore, the results of a flavour-symmetry–breaking expansion in the quark masses [90], fit to a subset of the QCDSF-UKQCD collaboration lattice data set, are entirely consistent with our values despite the different phenomenological input used (that calculation used Dashen's theorem, with some uncertainty, while we input $R = m_u/m_d$).

While more lattice data for the isospin-averaged octet baryon masses, on larger lattice volumes and at lighter meson masses, would allow the precision of our calculation to be somewhat improved, we emphasise that the dominant contribution

to the uncertainty of our result arises not from the lattice simulations but from the up-down quark mass ratio R. A more precise value of $R = m_u/m_d$ could reduce the uncertainty of our determination of the strong baryon mass splittings considerably, without the need for further simulations. Conversely, direct lattice (or phenomenological) determinations of the electromagnetic contributions to the mass splittings, with the analysis presented here, may allow a significantly improved determination of R. At the current level of precision it is already clear from Fig. 4.5 that, for consistency with direct lattice calculations [34] and experiment, this analysis favours the larger value $R = 0.553(43)$ over the smaller $R = 0.47(4)$.

Our results using the larger value of R are consistent with both the traditional and Walker-Loud *et al.* (WLCM) determinations of the strong contribution to the proton-neutron mass difference from the electromagnetic component, as shown in Table 4.7. The WLCM subtracted dispersion approach was adapted to the hyperons in Ref. [103] (and some minor updates were implemented for the proton-neutron system[5]). For the hyperons, the dispersive estimates have significantly larger uncertainties than for the nucleon; these are dominated by the lack of knowledge of the hyperon isovector polarisabilities. Certainly further theoretical (or experimental) work on this aspect of hyperon structure would be of interest, particularly as the present uncertainties are too large to provide a meaningful counterpoint to our current work.

In the next chapter, we use the chiral extrapolation for the octet baryon masses presented here to investigate the size and nature of chiral symmetry breaking in the context of the octet baryon sigma commutators. Our focus is, in particular, on the strange nucleon sigma term, which can be interpreted as a direct measure of strangeness in the nucleon.

[5]The minor differences in the nucleon analysis arise from two sources: significant spurious CSV effects in the Delta region realised by the Bosted-Christy structure functions have been suppressed in the new analysis, generating a rather small increase in the self-energy, and an inelastic subtraction is suppressed more rapidly in order to appropriately match onto the ultraviolet behaviour dictated by the operator product expansion. This acts to reduce the size of that term, and consequently lessen the sensitivity to the poorly-known isovector polarisability. Details are given in Ref. [103].

Chapter 5

Sigma Commutators

Approximate chiral symmetry forms the backbone of the phenomenological low-energy effective theory of QCD—chiral perturbation theory—which we use in this work (c.f., Section 3.2). The central importance of this symmetry to our understanding of the strong interaction, however, predates the explicit formulation of QCD, having been established by the successes of the current algebra and partially conserved axial-vector current techniques of the 1960s [51–53]. Since then, there have been significant efforts to calculate and measure quantities named sigma terms, which provide crucial information about the size and mechanism of chiral symmetry breaking in nature.

Sigma terms are defined as the matrix elements of the scalar quark currents between baryon states[1], and as such quantify the contribution of explicit chiral symmetry breaking to the baryon masses [104]. Most commonly, one considers the 'pion-nucleon' and 'strange nucleon' sigma terms:

$$\sigma_{\pi N} = m_l \langle N | \overline{u}u + \overline{d}d | N \rangle, \tag{5.1a}$$

$$\sigma_{Ns} = m_s \langle N | \overline{s}s | N \rangle, \tag{5.1b}$$

where $m_l = (m_u + m_d)/2$. These fundamental parameters of low-energy hadron physics are closely related to hadronic physics topics as diverse as the mass spectrum, meson-nucleon scattering amplitudes (through Ward identities), quark mass ratios, properties of hadronic atoms, and nuclear matter at finite temperature and density. In the context of this body of work, our focus is on σ_{Ns}, which provides a direct measure of strangeness in the nucleon.

[1] Historically, a sigma term (or sigma commutator) is in fact defined as any matrix element of an even number of charge commutators of the Hamiltonian [53]. The modern definition corresponds to the double commutator: for a baryon B,

$$\sigma_B^{ab} = \left\langle B \middle| \left[\hat{Q}_A^a, \left[\hat{Q}_A^b, H \right] \right] \middle| B \right\rangle,$$

where $\hat{Q}_A^a$ denote the axial-vector charge operators (defined in Section 3.2) with SU(3)-octet label a, and the commutator explicitly picks out the symmetry-breaking part of H (for QCD, $\overline{q}Mq = \sum_q m_q \overline{q}q$). In this notation the usual meson-nucleon sigma terms are $\sigma_{\pi N} = \sigma_N^{11}$ and $\sigma_{KN}^{u/d} = \sigma_N^{44/66}$.

The strange nucleon sigma term has historically been poorly known. It is traditionally calculated from the small difference between $\sigma_{\pi N}$, deduced from pion-nucleon scattering data using a dispersion relation analysis [105, 106], and the non-singlet quantity $\sigma_0 = m_l\langle N|\overline{u}u + \overline{d}d - 2\overline{s}s|N\rangle$ which is determined based on observations of the baryon mass spectrum. An EFT-improved estimate is $\sigma_0 = 36 \pm 7\,\text{MeV}$ [107]. Given this value, even a perfect determination of $\sigma_{\pi N}$ would result in σ_{Ns} having an uncertainty of order 100% [108]. Far from perfect, the benchmark value $\sigma_{\pi N} = 45 \pm 5\,\text{MeV}$ remains that of Gasser, Leutwyler and Sainio [109] from the early 1990s; the experimental status of pion-nucleon scattering data has not improved substantially in the last two decades. The long-standing conclusion from these numbers was that σ_{Ns} is of the order of 300 MeV. Such a large value would imply that as much as one third of the nucleon mass can be attributed to non-valence quarks, a conclusion apparently incompatible with the success of constituent quark models. This puzzle has generated much theoretical interest over the last decades.

In recent years, the best value for σ_{Ns} has seen an enormous revision. Advances in lattice QCD have revealed a strange sigma term of 20–50 MeV [90, 110–118], an order of magnitude smaller than previous determinations and significantly more precise. This revelation has far-reaching consequences, in particular for the interpretation of experimental searches for particle candidates of dark matter [119–124]. As many such candidates (e.g., the favoured neutralino) have interactions with hadronic matter which are determined by couplings to the squares of the sigma terms, the uncertainty of their theoretical cross-sections is largely driven by the poorly-known σ_{Ns}. The lattice QCD revision of this quantity has resulted in predicted dark matter cross-sections being reduced by an order of magnitude, with significant increases in precision. Clearly, ever-better determinations of the sigma terms, in particular the strange nucleon term, using lattice methods, are essential for the progress of dark matter research.

In this chapter we describe a calculation of the sigma terms of the octet baryons, based on the chiral extrapolation of lattice results for the baryon masses which was presented in Chapter 4. While we deduce both light and strange quark sigma terms for the entire baryon octet, we focus in particular on the strange nucleon sigma term σ_{Ns}. The small statistical uncertainty, and considerably smaller model-dependence, in our analysis allows a significantly more precise determination of this quantity than hitherto possible, subject to an unresolved issue concerning the lattice scale setting which is discussed in detail in Section 5.1. Our technique allows comparison with recent direct lattice QCD calculations of the flavour-singlet matrix elements at unphysical meson masses [111–113, 125, 126].

5.1 The Feynman-Hellmann Theorem

The Feynman-Hellmann theorem relates the derivative of the energy of a system, with respect to some parameter, to the expectation value of the derivative of the Hamiltonian with respect to the same parameter. This relation may be used to ex-

press the sigma terms as derivatives of baryon mass with respect to quark mass [127]. Using generic notation for the sigma term of any octet baryon B with quark flavour q,

$$\sigma_{Bq} \equiv m_q \langle B|\bar{q}q|B\rangle \tag{5.2}$$

$$= m_q \frac{\partial M_B}{\partial m_q}, \tag{5.3}$$

where the second line is the statement of the Feynman-Hellmann relation in this context. To the order of the chiral expansion described in Section 4.1, one can replace the quark masses m_q with meson masses squared: $\mathcal{B}m_l \to m_\pi^2/2$ and $\mathcal{B}m_s \to (m_K^2 - m_\pi^2/2)$ (where $\mathcal{B}$ is related to the parameter λ of Eq. (3.14) by $\mathcal{B} = 4\lambda/f_\pi^2$). Clearly, given closed-form expressions for baryon mass M_B as a function of the meson masses, which were developed in Chapter 4, the scalar form factors can be evaluated by simple differentiation.

This method has a considerable advantage over the direct calculation of the sigma terms in lattice QCD; it does not require the evaluation (or estimation) of contributions from quark-line–disconnected diagrams which are represented by noisy and expensive 'all-to-all' propagators on the lattice. However, it also has a disadvantage; the application of the Feynman-Hellmann relation requires taking a partial derivative with respect to quark mass. That is, all other parameters must be held fixed, including the strong coupling α (or, equivalently, Λ_{QCD}). In lattice QCD, there is an apparent ambiguity as to how to define a fixed renormalised coupling α [128, 129]. This is precisely the issue of lattice scale setting, which was discussed in Section 2.2.3—while lattice simulation results extrapolated to the physical point must be independent of scale-setting scheme, derivative quantities, by definition, make reference to the scale away from the physical point and hence their values may depend on the scheme chosen.

We consider here two independent scale-setting schemes which are described in detail in Section 2.2.3. The mass-dependent approach is based on the assumption that the dimensionful Sommer scale, r_0, which is related to the force between static quarks at relatively short distance, is essentially disconnected from chiral physics and should therefore vary slowly with changes in quark mass. Using this scheme, the Feynman-Hellmann relation applied to lattice simulation results involves the derivative

$$\frac{\partial\left(\frac{r_0}{a} a M_B\right)}{\partial m_q}\,. \tag{5.4a}$$

If this expression is to generate the physical sigma terms, one requires $\partial r_0/\partial m_q = 0$. Applying the theorem within the mass-independent scheme instead, where the lattice scale at constant bare coupling (e.g., β) is taken to be independent of the bare quark mass, amounts to calculating

$$\frac{\partial\left(\frac{r_0^*}{a^*} a M_B\right)}{\partial m_q}\,, \tag{5.4b}$$

where the asterisk denotes a value extrapolated to the physical point. This, in contrast to the first approach, will give physical results if $a/a^* = 1$ (or equivalently, $\partial a/\partial m_q = 0$).

One might expect the difference between the nucleon sigma terms evaluated in each scheme to be particularly significant for the strange quark. One reason is the shift in the ratio r_0/a which is observed when unquenching lattice simulations [130]. This effect can be interpreted as a sea-quark dependence of either r_0 or the lattice spacing a. As this shift can be significant, the choice of scale setting absorbs a possibly large effect, and hence will lead to non-negligible differences in the results of derivatives with respect to sea-quark mass calculated with each of the two choices. Additionally, the strange quark is considerably heavier than the light quarks, which serves to amplify the effect of any scale-setting prescription dependence on the strange sigma term.

For the chiral extrapolation of octet baryon masses in Chapter 4, the scale for the PACS-CS lattice data was set using the mass-dependent approach, while the mass-independent scheme was used for the QCDSF-UKQCD simulation results. In the coming sections we give results based on these extrapolations and on an otherwise identical analysis of the PACS-CS collaboration simulation results where the scale was set using the mass-independent scheme, allowing us to investigate the scale-dependence of our extraction of the sigma terms. We do not have access to the lattice values of r_0 necessary to apply the mass-dependent scheme to an analysis of the QCDSF-UKQCD lattice data.

5.2 Light and Strange Sigma Terms

Light and strange quark sigma terms, calculated using Eq. (5.3) applied to the chiral extrapolations of octet baryon masses described in Chapter 4, are presented in Table 5.1. The fit to the QCDSF-UKQCD lattice simulation results yields a value for σ_{Ns} with a much larger uncertainty than the analyses of the PACS-CS collaboration data set. This is as expected; the leading-order term in a chiral expansion for the strangeness nucleon sigma commutator is determined by the parameter σ, as made explicit in Table 4.1. This parameter is common to all baryons in the octet, and is sensitive only to the singlet combination of the quark masses (see Eqs. (3.29) and (4.8)). Figure 4.1 shows that the variation of the singlet quark mass across the PACS-CS ensemble is quite large relative to the extrapolation necessary to reach the physical point. In contrast, the QCDSF-UKQCD data set covers a much smaller range of singlet quark masses; by design, most simulation ensembles lie on one close-to-physical singlet quark mass line.

It is also clear that there is a significant dependence on the scale-setting scheme, despite the otherwise small uncertainties of the calculation. While the chiral extrapolations of the PACS-CS collaboration octet baryon masses using the mass-dependent and independent schemes agree at the physical point, as expected, and the qualities of the two fits are similar (χ^2/d.o.f. 0.43 and 0.78, respectively), the value of the

B	PACS-CS (MD)	PACS-CS (MI)	QCDSF-UKQCD (MI)
		σ_{Bl} (MeV)	
N	43.8(69)	45.7(73)	39.6(72)
Λ	28.6(43)	30.7(47)	27.0(43)
Σ	23.5(33)	25.7(36)	21.9(34)
Ξ	11.5(14)	13.8(16)	12.3(14)
		σ_{Bs} (MeV)	
N	20(6)	52(8)	26(15)
Λ	158(8)	185(12)	163(14)
Σ	202(9)	227(14)	234(14)
Ξ	315(10)	337(16)	334(14)

Table 5.1: Light and strange quark sigma terms for the octet baryons based on chiral extrapolations of PACS-CS and QCDSF-UKQCD collaboration lattice simulation results for the baryon masses. The labels (MD) and (MI) denote results where the lattice scale has been set using mass-dependent and mass-independent schemes respectively. The uncertainty quoted includes the statistical uncertainty and allows for the variation of various chiral parameters and the form of the UV regulator as described in Chapter 4.

strangeness sigma term in the nucleon changes from 20 ± 6 MeV to 52 ± 8 MeV. This is by far the most significant shift; the light-quark sigma terms are entirely consistent within uncertainties, while the other strange sigma terms are consistent within 2-sigma.

Given the large systematic scale-setting effect, we consider it prudent to check that the order of the chiral expansion used in the analysis is sufficient; as the PACS-CS collaboration data set includes pseudoscalar masses significantly larger than the physical values, it is possible (although unexpected, based on previous studies of the FRR formalism [69]) that higher-order terms become significant, distorting the results. By performing the fit to progressively fewer data points, that is, by dropping the heaviest mass points, we confirm that the results are independent of the truncation of the data. This can be seen clearly in Fig. 5.1. Although we have displayed results with the mass-dependent scale-setting scheme, this conclusion holds equally for the results with the mass-independent prescription.

Alternatively, we can check the possible contribution from higher-order terms by explicitly including them in the fit. Adding all analytic terms at order m_ϕ^4 to the baryon mass expansion, and re-fitting to the PACS-CS lattice results with the coefficients of the new terms generously constrained to twice the dimensional estimate $\left(M^{(0)}/(4\pi f_\pi)^4\right)$ at 1-sigma, yields new values for the baryon sigma terms. Although the uncertainties are large, as one would expect given the excellent fit quality at lower order, the fact that the central values for all sigma terms shift very little—e.g., $\sigma_{Ns} = 22 \pm 46$ MeV and $\sigma_{Nl} = 43 \pm 3$ MeV for the PACS-CS collaboration results with the mass-dependent scale-setting scheme (where only the

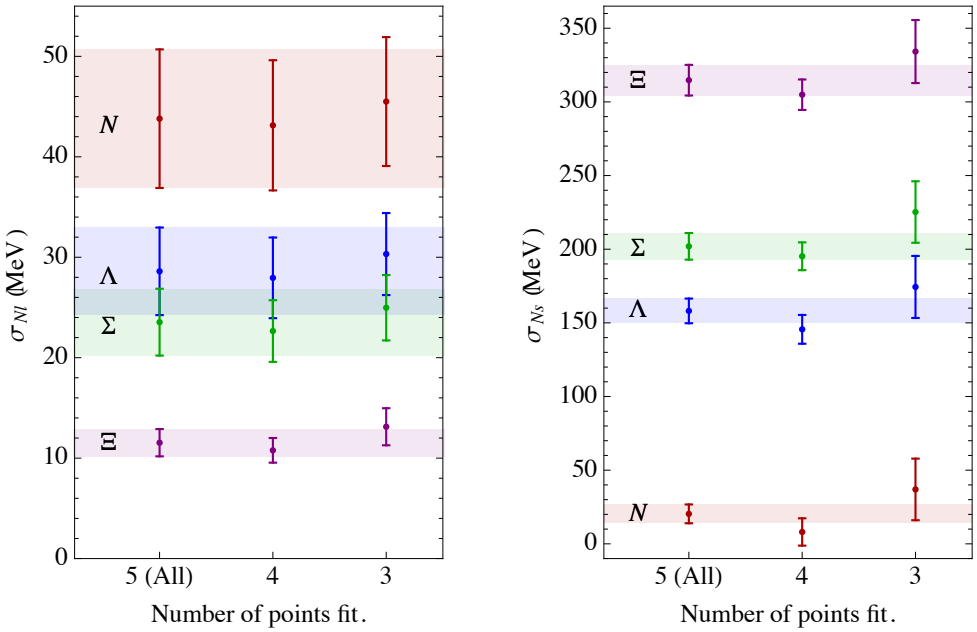

Figure 5.1: Baryon sigma terms, evaluated using the Feynman-Hellmann theorem following a fit to PACS-CS collaboration lattice simulation results for the octet baryon masses. The horizontal scale shows the number of pseudoscalar meson masses included in the fit. The lattice scale was set using the mass-dependent scheme.

statistical uncertainties of the new fit are quoted)—does indicate that our fit is robust. Including in quadrature the shift in central values from the higher-order fit as an estimate of the systematic uncertainty resulting from our choice of resummation (i.e., through the FRR prescription) does not increase the uncertainties quoted in Table 5.1.

With a view to finding a physically significant result for σ_{Ns}, we point out that *direct* lattice calculations of this quantity should not have a large dependence on the scale-setting scheme. As we can easily evaluate sigma terms from our fit at any pion or kaon mass, we may compare our results explicitly with such calculations, including preliminary calculations performed at only one set of pseudoscalar masses. Such a comparison is given in Table 5.2. The available direct calculations include 2 and $2+1+1$–flavour simulations [112, 113] at a single set of pion and kaon masses, and $2+1$–flavour calculations which have been chirally extrapolated to the physical point [125, 126]. The MILC collaboration calculation is not a direct three-point calculation, but rather uses a 'hybrid' method to find the sigma term [111]. The collaboration indicates that this method corresponds most closely to the mass-independent scale-setting scheme [131]. The results of our analysis using the mass-dependent scale-setting approach for the PACS-CS simulations agree extremely well with the direct QCDSF and ETM calculations at the simulation values of m_π and m_K. We regard this comparison as particularly significant as those calculations involved no chiral extrapolation. A similar level of agreement is found with the (chirally-extrapolated) JLQCD result. Finally, the Engelhardt result sits

		σ_{Ns} (MeV)			
	(m_π, m_K) MeV	direct	MD (P)	MI (P)	MI (Q)
QCDSF [113]	(281,547)	12^{+23}_{-16}	16(6)	50(7)	24(16)
ETM [112]	(390,580)	13(5)(1)	12(5)	46(6)	22(16)
Engelhardt [125]	physical	43(10)	20(6)	52(8)	26(14)
JLQCD [126]	physical	8(14)(15)	20(6)	52(8)	26(14)
MILC [111]	physical	59(6)(8)	20(6)	52(8)	26(14)

Table 5.2: Recent direct lattice calculations of σ_{Ns} compared with the results of our analysis. Columns labelled MD and MI correspond to our analysis of the PACS-CS collaboration (P) or QCDSF-UKQCD collaboration (Q) lattice results, evaluated at the indicated (m_π, m_K) values, with the scale set using the mass-dependent or independent scale-setting prescriptions, respectively. Those simulations listed at the physical point denote values after chiral extrapolation (by the relevant lattice groups).

between the values of σ_{Ns} given by the two scale-setting schemes, while the MILC result favours the mass-independent scheme. The extrapolated QCDSF-UKQCD collaboration simualtion results, analysed using only the mass-independent scheme, have somewhat larger uncertainties and are compatible with all direct simulations at the 1-sigma level.

There is no consensus in the literature as to the most appropriate way to set the scale for a spectral determination of the sigma terms; both Refs. [129] and [132] argue for the mass-independent scheme, in the former case based on observations of scaling violation, while others (e.g., Refs. [133,134]) favour the mass-dependent scheme. We choose the mass-dependent prescription to calculate our preferred central values because, for the PACS-CS simulation results where we can compare scale-setting schemes, it yields values for σ_{Ns} which are more consistent with direct calculations. Of course, we cannot rule out the possibility of 'mixed scale setting', as discussed in Section 2.2.3. Nevertheless, we emphasise that our results are more significant than the general statement that σ_{Ns} lies in the 45 MeV range spanned by all determinations would indicate; within each scale-setting prescription we find results which are very precise, with small statistical and systematic uncertainties. More lattice data for the octet baryon masses will not improve the results significantly compared to the scale-setting problem. Future direct lattice calculations for the strange nucleon sigma commutator, however, will not only more precisely constrain this term as needed for dark matter calculations, but will provide significant insight into the problem of scale setting on the lattice and indeed into QCD itself.

Finally, we note again that our results for the light quark sigma terms using each scale-setting method—and both the PACS-CS and QCDSF-UKQCD collaboration simulation sets—are precise and compatible within uncertainties, and that we are for this reason extremely confident in our determination $\sigma_{Nl} = 44 \pm 7\,\text{MeV}$.

	σ_{Bq} (MeV)		
B	u	d	s
p	19(3)	23(4)	22(7)
n	12(2)	34(5)	19(6)
Λ	10(2)	18(3)	158(8)
Σ^0	8(1)	15(2)	201(9)
Σ^+	16(2)	2(1)	205(10)
Σ^-	1(1)	29(4)	199(8)
Ξ^0	8(1)	−0.46(42)	317(11)
Ξ^-	−0.11(23)	15(2)	313(10)

Table 5.3: Individual quark sigma terms for the octet baryons based on a chiral extrapolation of PACS-CS collaboration lattice simulations of the baryon masses. The lattice scale was set using the mass-dependent prescription.

5.3 Charge Symmetry Violation

Individual up, down, and strange quark sigma terms are relevant to searches for supersymmetric dark matter candidates [119, 135, 136]. These terms may be calculated in precisely the same way as the isospin-averaged sigma commutators were obtained via the Feynman-Hellmann theorem applied to a chiral extrapolation of lattice QCD simulation results for the octet baryon masses in the last section. As described in Chapter 4, the only additional input needed to break the light-quark mass degeneracy in the baryon mass extrapolations is a value for $R = m_u/m_d$. Based on the discussion of Section 4.4, we use the Leutwyler [100] value, $R = 0.553(43)$, determined by a fit to meson decay rates.

Our results, calculated using the PACS-CS collaboration lattice simulation results with the mass-dependent scale-setting scheme, are shown in Table 5.3. For the reasons given in Section 5.2 this is our preferred scale-setting scheme. Results calculated using the mass-independent scheme applied to both this data set and to the QCDSF-UKQCD lattice results are given in Appendix E. Re-scaling the sigma terms by the relevant quark masses to make dimensionless quantities and match the notation of Ellis *et al.* [119, 135, 136], we define

$$B_q^{(B)} \equiv \sigma_{Bq}/m_q. \tag{5.5}$$

These terms for the proton (p) and neutron (n) are related to the usual σ_{Ns} and $\sigma_{\pi N}$ by

$$\sigma_{\pi N} = \frac{1}{4}(m_u + m_d)\Big(B_u^{(p)} + B_d^{(p)} + B_u^{(n)} + B_d^{(n)}\Big), \tag{5.6a}$$

$$\sigma_{Ns} = \frac{1}{2}m_s\big(B_s^{(p)} + B_s^{(n)}\big). \tag{5.6b}$$

Our calculation yields

$$\frac{B_u^{(p)} - B_s^{(p)}}{B_d^{(p)} - B_s^{(p)}} = 1.5(4), \qquad \frac{B_d^{(p)}}{B_u^{(p)}} = 0.7(2), \qquad \frac{m_l}{M_N}\langle p|\overline{u}u - \overline{d}d|p\rangle = 0.009(5). \tag{5.7}$$

The quoted errors include correlated uncertainties between all fit parameters and also allow for some variation of phenomenologically-set quantities including the up-down quark mass ratio R, as described in Chapter 4. These results, and our values for the nucleon light quark sigma terms (see Table 5.3), are consistent with those obtained by Ellis *et al.* in Ref. [136] based on SU(6) symmetry and the same R-value used here. The strange sigma terms $\sigma_{p/n,s}$ resulting from our work, however, are significantly smaller; the Ellis values are $\sigma_{ns} = \sigma_{ps} = 110(60)\,\text{MeV}$ (and no results are presented for the hyperons). Of course, the discussion of the previous section regarding the effect of lattice scale setting on σ_{Ns} applies equally here: choosing the mass-independent scale-setting scheme yields larger values for the strange nucleon sigma terms, namely $\sigma_{ps} = 53(8)$ MeV and $\sigma_{ns} = 50(8)$ MeV, but values of the light quark sigma terms and $\left(B_u^{(p)} - B_s^{(p)}\right)\Big/\left(B_d^{(p)} - B_s^{(p)}\right)$ and $B_d^{(p)}/B_u^{(p)}$ which are identical with those given above, to the quoted precision.

5.4 Summary and Discussion

Using the isospin-broken chiral extrapolations of lattice QCD simulation results for the octet baryon masses which were presented in Chapter 4, we determine precise values for the baryon sigma terms by simple differentiation. This indirect approach allows us to achieve small statistical uncertainties while minimising any model-dependence, most importantly for the strange nucleon sigma terms which are extremely expensive to calculate directly. These quantities provide a measure of vacuum quark components in the nucleon, and are a key theoretical ingredient for the interpretation of dark matter direct-detection experiments. With a given choice of lattice-scale–setting prescription, our results for the strange nucleon sigma terms are the most precise to date. The choice of scale-setting method, however, constitutes a significant systematic uncertainty.

A comparison of our results for σ_{Ns} with those of recent direct lattice calculations of this quantity—which should not suffer from the scale-setting ambiguity—informs our choice of the mass-dependent prescription as our preferred method. Setting the lattice scale for the PACS-CS collaboration simulation results using this scheme, we find $\sigma_{Ns} = 20 \pm 6\,\text{MeV}$ at the physical point. The pion-nucleon sigma term is $\sigma_{\pi N} = 44 \pm 7\,\text{MeV}$. This value is consistent with the results $\sigma_{\pi N} = 46 \pm 7\,\text{MeV}$ and 40 ± 7 MeV found within the mass-independent scheme from the same PACS-CS collaboration results and from an entirely independent analysis of QCDSF-UKQCD collaboration simulation results, respectively. A comparison of these values with those from other lattice QCD studies and analyses is displayed in Fig. 5.2. Our results are comparatively precise (up to the scale-setting ambiguity which was not considered in previous work), and broadly consistent with the latest numbers from other collaborations. We emphasise that future direct lattice calculations for the

strange nucleon sigma commutator will provide significant insight into the problem of scale setting on the lattice and, through this, into QCD itself.

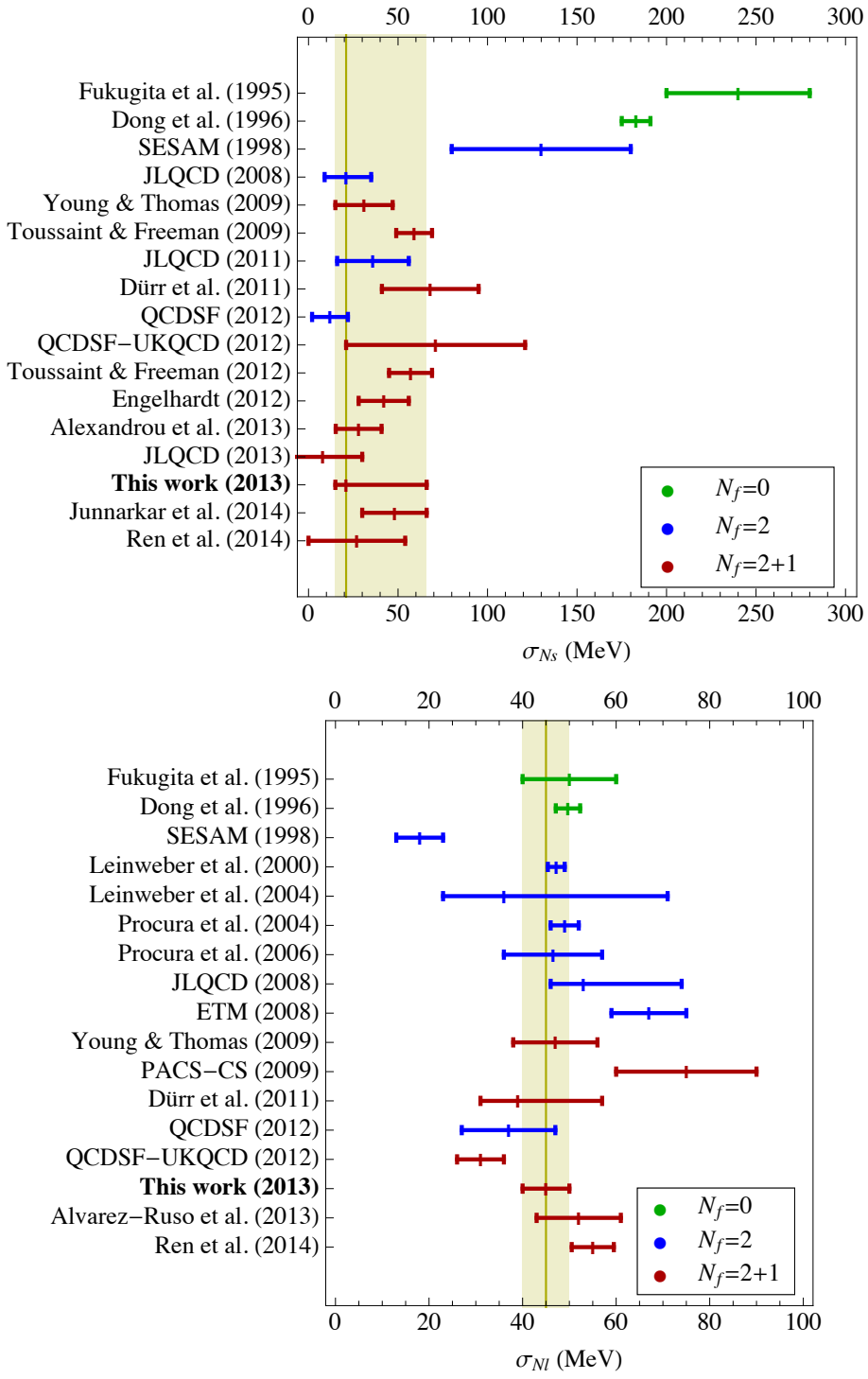

Figure 5.2: Summary of values for σ_{Ns} and σ_{Nl} from lattice QCD with N_f quark flavours [70, 90, 110, 111, 115, 117, 118, 125, 126, 131, 137–150]. The yellow vertical bands indicate the results of this work. The central values are taken at our preferred results (using the mass-dependent scale-setting scheme), while the error bands encompass the full 1-sigma range of both this result and those generated using the mass-independent prescription.

Chapter 6

Parton Distribution Moments

The revelation of the late 1960s that the proton has distinct substructure[1] raised a pivotal question: how are hadron observables generated from more fundamental degrees of freedom? Answering this question—where the generic point-like 'parton' constituents originally introduced by Feynman [154] are now identified with the asymptotically-free quarks and gluons of QCD—remains one of the most basic challenges of particle and nuclear physics. Perhaps most notably, the decomposition of the proton's spin into quark and gluon spin and orbital angular momentum contributions has been much-debated since the quark-spin component was measured to be only a small percentage of the total [155]. The current value is approximately 33% [156]. We return to the discussion of this 'proton spin puzzle' in Section 6.4.

In the modern language, hadron structure as probed in high-energy scattering is parameterised through structure functions which encode both short and long-distance effects. It follows from asymptotic freedom that contributions from the two scales can be systematically separated. This is known as factorisation; structure functions may be written as the convolution of a perturbatively-calculable hard scattering cross-section—a process-dependent factor—and a nonperturbative function encoding the hadron structure. These functions are named parton distribution functions (PDFs) for inclusive processes (or parton distribution amplitudes for exclusive processes). In the infinite-momentum frame, PDFs represent the number density of partons of each type carrying the Bjorken momentum fraction[2] x at a renormalisation scale μ^2.

The utility and importance of PDFs comes from their universality; they encode the process-independent partonic structure of hadrons. Once determined (e.g., experimentally, from some limited set of reactions), the PDFs can thus be used for the analysis of other processes, ranging from deep inelastic scattering to Drell-Yan or

[1] This hinged in particular on a series of deep inelastic scattering (DIS) experiments at MIT and SLAC in late 1967 [151,152]. Two unexpected features emerged. The first was that the probability of DIS decreased much more slowly with Q^2, the momentum transfer to the proton, than that of elastic scattering, suggesting the existence of some 'hard core' within the target protons. The second was scaling [153], i.e., that in the DIS regime the proton structure functions depend only on the ratio $\omega = \nu/Q^2$ (ν being the energy lost by the electron), not ν and Q^2 independently—an indication that proton structure always appears the same to an electromagnetic probe, regardless of how hard the proton is struck.

[2] The Bjorken variable is $x = Q^2/2M_B\nu \propto 1/\omega$, where M_B is the mass of the relevant baryon.

$W^{\pm}$ production. They are also essential to experimental physics programs searching for physics beyond the SM, for example through the scattering of ultra-high-energy cosmic ray particles or fixed target and colliding beam experiments.

PDFs have been well determined experimentally [157–160] and widely studied within models [161–167]. The majority of these investigations, however, have relied on the assumption of good charge symmetry [33, 39] to reduce the number of independent quark distribution functions by a factor of two. Recently, CSV effects have been included in phenomenological PDFs for the first time [36–38]. Experimental upper limits on partonic CSV are in the range 5–10% [33, 39, 168]; effects of this magnitude would significantly affect a number of tests of the SM, such as those based on neutrino deep inelastic scattering experiments [40, 169].

Ultimately, one wishes to determine PDFs, and in particular the size of CSV effects in these quantities, directly from QCD itself. Lattice field theory is currently the only quantitative tool available with this facility. Until very recently it was not known how one might calculate PDFs directly on the lattice [170]; deep inelastic scattering and related processes are dominated by distances that are light-like, and as such are inaccessible in Euclidean-space calculations. Use of the operator product expansion, however, allows Mellin moments of PDFs, which represent averages over the momentum fraction x carried by the parton, to be evaluated using standard lattice calculations of hadronic matrix elements of local operators [32, 171–173]. Details of the operator product expansion, as well as an overview of the connection between deep inelastic scattering, hadron structure functions, and PDFs, are given in Appendix G.

In this chapter we develop a formalism for the chiral extrapolation of the spin-dependent and spin-independent Mellin moments of the quark distributions of the octet baryons. The analysis allows for isospin-breaking and may thus be used to calculate CSV effects from isospin-averaged lattice QCD simulation results, just as was outlined for the octet baryon masses and sigma terms in the previous chapters.

6.1 Moments of Quark Distribution Functions

The spin-independent ($q^B(x)$) and spin-dependent ($\Delta q^B(x)$) quark distribution functions are defined as

$$q^B(x) = q^B_\uparrow(x) + q^B_\downarrow(x), \tag{6.1a}$$
$$\Delta q^B(x) = q^B_\uparrow(x) - q^B_\downarrow(x), \tag{6.1b}$$

where $q^B_{\uparrow(\downarrow)}$ represents the number density of quarks whose spin is parallel (antiparallel) to the longitudinal spin direction of a baryon B. For clarity of notation, we suppress the dependence of these distributions on a renormalisation scale μ^2 throughout this discussion. We define the $(n-1)$th spin-independent (SI) and mth

spin-dependent (SD) Mellin moments of the parton distributions, respectively, as

$$\langle x^{n-1}\rangle_q^B = \int_0^1 dx\, x^{n-1}\big(q^B(x) + (-1)^n \overline{q}^B(x)\big), \tag{6.2a}$$

$$\langle x^m\rangle_{\Delta q}^B = \int_0^1 dx\, x^m\big(\Delta q^B(x) + (-1)^m \Delta\overline{q}^B(x)\big), \tag{6.2b}$$

i.e., our definitions alternate between C-even (+) and odd (−) distributions,

$$q^{\pm}(x) = q(x) \pm \overline{q}(x), \tag{6.3}$$

with increasing n and m. These alternating towers of moments can be related to the matrix elements of local twist-two operators

$$\mathcal{O}_q^{\mu_1\cdots\mu_n} = i^{n-1}\overline{q}\gamma^{\mu_1}\overleftrightarrow{D}^{\mu_2}\cdots\overleftrightarrow{D}^{\mu_n}q, \tag{6.4a}$$

$$\mathcal{O}_{\Delta q}^{\mu_0\cdots\mu_m} = i^{m}\overline{q}\gamma_5\gamma^{\mu_0}\overleftrightarrow{D}^{\mu_1}\cdots\overleftrightarrow{D}^{\mu_m}q, \tag{6.4b}$$

where $\overleftrightarrow{D} = \frac{1}{2}\Big(\overrightarrow{D} - \overleftarrow{D}\Big)$, through the operator product expansion described in Appendix G. One finds:

$$\big\langle B(\vec{p})\big|\big[\mathcal{O}_q^{\{\mu_1\cdots\mu_n\}} - \mathrm{Tr}\big]\big|B(\vec{p})\big\rangle = 2\langle x^{n-1}\rangle_q^B\big[p^{\{\mu_1}\cdots p^{\mu_n\}} - \mathrm{Tr}\big], \tag{6.5a}$$

$$\big\langle B(\vec{p})\big|\big[\mathcal{O}_{\Delta q}^{\{\mu_0\cdots\mu_m\}} - \mathrm{Tr}\big]\big|B(\vec{p})\big\rangle = 2\langle x^{m}\rangle_{\Delta q}^B M_B\big[S^{\{\mu_0}p^{\mu_1}\cdots p^{\mu_m\}} - \mathrm{Tr}\big]. \tag{6.5b}$$

The braces, $\{\ldots\}$, indicate total symmetrisation of the enclosed indices, and trace terms involving $g^{\mu_i\mu_j}$ have been subtracted to ensure that the operators transform irreducibly under the Lorentz group. The spin operator, S^μ, is as in Eq. (3.27); we have suppressed the bold typeface here.

In recent years, several collaborations have presented lattice QCD studies of the matrix elements of twist-two operators relevant to both the spin-independent and spin-dependent parton distributions [32, 173]. Because of the reduced symmetry of a cubic lattice compared with continuous space (the symmetry group O(4) → H(4)), these simulations have been restricted to the lowest few Mellin moments by power-divergent operator mixing—one can choose irreducible representations of H(4) which are safe from such mixings only for $\{n, m\} \leq 4$. Furthermore, renormalisation becomes extremely complex for larger moments.

Although the lowest several moments of the quark distribution functions do not provide enough information for a reconstruction of the PDFs, they are interesting in their own right. For example, the zeroth spin-dependent moment, $\langle 1\rangle_{\Delta q}^B$, corresponds to the spin of baryon B carried by quark flavour q. Lattice results for this quantity can thus give insight into the proton spin puzzle (see Section 6.4). Moreover, determinations of CSV effects in the Mellin moments are relevant to experimental tests of the SM. Perhaps most notably, CSV effects in the lowest spin-independent PDF moments could act to significantly reduce the 3-sigma discrepancy with the SM found by the NuTeV collaboration [41] in neutrino-nucleus DIS experiments.

6.2 Chiral Perturbation Theory

Here we outline the derivation of chiral extrapolation formulae for the spin-independent and spin-dependent quark distribution moments, to leading non-analytic order. The analysis allows for (strong) isospin-breaking, that is, for $m_u \neq m_d$. We begin by writing down effective Lagrange densities which represent the twist-two operators $\mathcal{O}$ (Eqs.(6.4a) and (6.4b)) within the framework of chiral effective field theory. The appropriate flavour structure for each operator will be isolated by insertions of the matrices

$$\lambda_q = \frac{1}{2}\big(\xi\overline{\lambda}_q\xi^\dagger + \xi^\dagger\overline{\lambda}_q\xi\big), \tag{6.6}$$

where for each quark flavour q, $\overline{\lambda}_q$ is given by

$$\overline{\lambda}_u = \begin{pmatrix} 1 & & \\ & & \\ & & \end{pmatrix}, \quad \overline{\lambda}_d = \begin{pmatrix} & & \\ & 1 & \\ & & \end{pmatrix}, \quad \overline{\lambda}_s = \begin{pmatrix} & & \\ & & \\ & & 1 \end{pmatrix}. \tag{6.7}$$

Effective operators relevant to the isovector quark distributions, for example, will be expressed in terms of the matrix $\lambda = \lambda_u - \lambda_d$.

The interactions of the octet baryons, decuplet baryons, and mesons, with no operator insertions, are encoded in the usual effective Lagrangian which was presented in Chapter 3. We refer to that chapter, in particular Section 3.3, for a summary of the notation and conventions used here (note that we now suppress the bold typeface on matrices of heavy-baryon fields). The only new notation needed is the generalisation of the quark-mass matrix M_q to include higher powers of the meson field Φ:

$$M = \frac{1}{2}\big(\xi M_q\xi + \xi^\dagger M_q\xi^\dagger\big). \tag{6.8}$$

We note from the outset that the expressions given in the following sections differ from those of related works [174–176] by factors of the baryon mass M_B. We have chosen our convention to make the *a-priori* unknown low-energy coefficients which appear in the effective matrix elements dimensionless.

Spin-Independent

Here we list effective matrix elements of the trace-subtracted spin-independent twist-two operators $\Big(\mathcal{O}_q^{\{\mu_1\ldots\mu_n\}} - \mathrm{Tr}\Big)$. All terms involving zero or one mass-insertion (M) are included. The total symmetrisation of all Lorentz indices, which is usually denoted by braces, $\{\ldots\}$, may also be written as '+ permutations' where this is notationally more convenient. This always indicates the symmetric sum with no normalisation factor, i.e., $\{\mu\nu\} = \mu\nu + \nu\mu = (\mu\nu + \text{permutations})$. Superscripts (n) on the undetermined low-energy coefficients indicate that these constants are distinct for each operator, that is, $\alpha^{(0)} \neq \alpha^{(1)}$ etc.

At leading order, the relevant effective Lagrange density is

$$\big[\alpha^{(n)}\big(\overline{B}B\lambda_q\big) + \beta^{(n)}\big(\overline{B}\lambda_q B\big) + \sigma^{(n)}\big(\overline{B}B\big)\,\mathrm{Tr}(\lambda_q)\big]p^{\{\mu_1}\ldots p^{\mu_n\}} - \mathrm{Tr}. \tag{6.9}$$

The $\mathcal{O}(m_q)$ counterterms are given by

$$\begin{aligned}\Big(&b_1^{(n)}\,\mathrm{Tr}\big[\overline{B}[[\lambda_q,B],M]\big] + b_2^{(n)}\,\mathrm{Tr}\big[\overline{B}\{[\lambda_q,B],M\}\big] + b_3^{(n)}\,\mathrm{Tr}\big[\overline{B}[\{\lambda_q,B\},M]\big]\\ &+ b_4^{(n)}\,\mathrm{Tr}\big[\overline{B}\{\{\lambda_q,B\},M\}\big] + b_5^{(n)}\,\mathrm{Tr}\big[\overline{B}B\big]\,\mathrm{Tr}[\lambda_q M] + b_6^{(n)}\,\mathrm{Tr}\big[\overline{B}B\lambda_q\big]\,\mathrm{Tr}[M]\\ &+ b_7^{(n)}\,\mathrm{Tr}\big[\overline{B}\lambda_q B\big]\,\mathrm{Tr}[M] + b_8^{(n)}\,\mathrm{Tr}\big[\overline{B}MB\big]\,\mathrm{Tr}[\lambda_q] + b_9^{(n)}\,\mathrm{Tr}\big[\overline{B}BM\big]\,\mathrm{Tr}[\lambda_q]\\ &+ b_{10}^{(n)}\,\mathrm{Tr}\big[\overline{B}\lambda_q\big]\,\mathrm{Tr}[MB]\Big)p^{\{\mu_1}\ldots p^{\mu_n\}} - \mathrm{Tr},\end{aligned} \tag{6.10}$$

and the decuplet insertions may be represented by

$$\gamma^{(n)}\big(\overline{T}^{\nu}\lambda_q T_{\nu}\big)p^{\{\mu_1}\ldots p^{\mu_n\}} + \gamma'^{(n)}M_B^2\Big(\overline{T}^{\{\mu_1}\lambda_q T^{\mu_2}\Big)p^{\mu_3}\ldots p^{\mu_n\}} - \mathrm{Tr}. \tag{6.11}$$

The contractions between field tensors are defined in Eq. (3.38).

Spin-Dependent

The spin-dependent operators have effective matrix elements very similar in structure to those given in the previous section for the spin-independent case. The term analogous to Eq. (6.9) has the form

$$\begin{aligned}&\big[\Delta\alpha^{(m)}\big(\overline{B}S^{\mu_0}B\lambda_q\big) + \Delta\beta^{(m)}\big(\overline{B}S^{\mu_0}\lambda_q B\big) + \;\Delta\sigma^{(m)}\big(\overline{B}S^{\mu_0}B\big)\,\mathrm{Tr}(\lambda_q)\big]p^{\mu_1}\ldots p^{\mu_m}\\ &+ \text{permutations} - \mathrm{Tr}.\end{aligned} \tag{6.12}$$

For $m = 0$, the Goldberger-Treiman relation provides the identification of the low-energy constants with the meson-baryon coupling constants:

$$\Delta\alpha^{(0)} = 2\bigg(\frac{2}{3}D + 2F\bigg), \qquad \Delta\beta^{(0)} = 2\bigg(-\frac{5}{3}D + F\bigg), \tag{6.13}$$

where F and D are defined by Eq. (3.29). The effective Lagrange density with insertions of the quark-mass matrix M is entirely analogous to Eq. (6.10):

$$\begin{aligned}\Big(&\Delta b_1^{(m)}\,\mathrm{Tr}\big[\overline{B}S^{\mu_0}[[\lambda_q,B],M]\big] + \Delta b_2^{(m)}\,\mathrm{Tr}\big[\overline{B}S^{\mu_0}\{[\lambda_q,B],M\}\big]\\ &+ \Delta b_3^{(m)}\,\mathrm{Tr}\big[\overline{B}S^{\mu_0}[\{\lambda_q,B\},M]\big] + \Delta b_4^{(m)}\,\mathrm{Tr}\big[\overline{B}S^{\mu_0}\{\{\lambda_q,B\},M\}\big]\\ &+ \Delta b_5^{(m)}\,\mathrm{Tr}\big[\overline{B}S^{\mu_0}B\big]\,\mathrm{Tr}[\lambda_q M] + \Delta b_6^{(m)}\,\mathrm{Tr}\big[\overline{B}S^{\mu_0}B\lambda_q\big]\,\mathrm{Tr}[M]\\ &+ \Delta b_7^{(m)}\,\mathrm{Tr}\big[\overline{B}S^{\mu_0}\lambda_q B\big]\,\mathrm{Tr}[M] + \Delta b_8^{(m)}\,\mathrm{Tr}\big[\overline{B}S^{\mu_0}MB\big]\,\mathrm{Tr}[\lambda_q]\\ &+ \Delta b_9^{(m)}\,\mathrm{Tr}\big[\overline{B}S^{\mu_0}BM\big]\,\mathrm{Tr}[\lambda_q] + \Delta\, b_{10}^{(m)}\,\mathrm{Tr}\big[\overline{B}S^{\mu_0}\lambda_q\big]\,\mathrm{Tr}[MB]\Big)p^{\mu_1}\ldots p^{\mu_m}\\ &+ \text{permutations} - \mathrm{Tr}\,.\end{aligned} \tag{6.14}$$

Decuplet contributions may be represented by

$$\Delta\gamma^{(m)}\big(\overline{T}^{\nu}S^{\{\mu_0}\lambda_q T_{\nu}\big)p^{\mu_1}\ldots p^{\mu_m\}} + \Delta\gamma'^{(m)}M_B^2\Big(\overline{T}^{\{\mu_1}S^{\mu_0}\lambda_q T^{\mu_2}\Big)p^{\mu_3}\ldots p^{\mu_m\}} - \text{Tr.} \tag{6.15}$$

Clearly, because of the number of available indices, $\Delta\gamma'^{(0,1)} = 0$. Other approximate relations between the unknown coefficients may be derived using SU(6) symmetry. In our numerical calculations, for example, we set $\Delta\gamma^{(0)} = 2\mathcal{H} = -6D$. The analogous relation for the first moment is $\Delta\gamma^{(1)} = -\frac{3}{2}\big(\Delta\alpha^{(1)} - 2\Delta\beta^{(1)}\big)$.

Transitions between octet and decuplet baryons via an operator insertion are also allowed in the spin-dependent case. These are represented by the effective matrix element

$$\sqrt{\frac{3}{2}}\,\omega^{(m)}\big[\big(\overline{T}^{\mu_0}\lambda_q B\big) + \big(\overline{B}\lambda_q T^{\mu_0}\big)\big]p^{\mu_1}\ldots p^{\mu_m} + \text{permutations} - \text{Tr.} \tag{6.16}$$

Here, by the nucleon-delta Goldberger-Treiman relation, we make the identification $\omega^{(0)} = \mathcal{C}$. This parameter appears in Eq. (3.37) and encodes the octet-decuplet baryon transition via meson emission or absorption. To reduce the number of free low-energy constants, we use the SU(6) approximation to set $\omega^{(1)} = -\frac{1}{2}\big(\Delta\alpha^{(1)} - 2\Delta\beta^{(1)}\big)$ for our numerical study of the first spin-independent moment (see Section 6.3).

6.2.1 Feynman Rules

Feynman rules corresponding to the twist-two operator insertion vertices may be read directly from the effective Lagrangian terms given in the previous section. Following the notation introduced in Section 3.3.4, the octet baryon, decuplet baryon, and meson which appear in a particular vertex are indicated by subscripts B, T, and ϕ on the (Clebsch-Gordan) coefficients C which encompass the flavour algebra. The subscript O_q indicates that the couplings listed here correspond to operator insertion vertices. All coefficients C are given explicitly in Appendix F.

For the spin-independent operators,

BB'_{SI} Operator Insertion 6.1(a): $$\frac{1}{M_B}C^{(n)}_{BB'O_q}p^{\{\mu_1}\ldots p^{\mu_n\}}, \tag{6.17a}$$

TT'_{SI} Operator Insertion 6.1(b) #1: $$\frac{1}{M_B}C^{(n)}_{TT'O_q}g_{\nu\beta}p^{\{\mu_1}\ldots p^{\mu_n\}}, \tag{6.17b}$$

TT'_{SI} Operator Insertion 6.1(b) #2: $$\frac{1}{M_B}C^{(n)}_{TT'O_q}g_{\nu}^{\{\mu_1}g_{\beta}^{\mu_2}p^{\mu_3}\ldots p^{\mu_n\}}, \tag{6.17c}$$

$BB'\phi\phi'_{\text{SI}}$ Vertex Insertion 6.1(d): $$\frac{1}{M_B f_\pi^2}C^{(n)}_{BB'\phi\phi'O_q}p^{\{\mu_1}\ldots p^{\mu_n\}}. \tag{6.17d}$$

The labels indicate the panel of Fig. 6.1 in which each vertex is depicted, and the TT' operator insertions labelled #1 and #2 correspond to the first and second

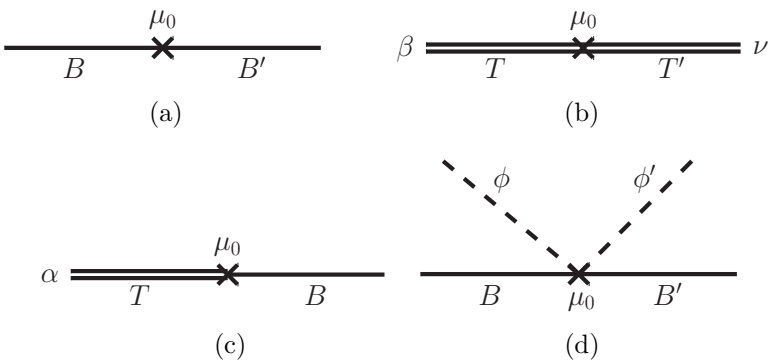

Figure 6.1: Feynman diagrams illustrating the vertices which appear in the leading non-analytic contributions to moments of quark distribution functions. The twist-two operator insertion (denoted by a cross) carries a Lorentz index μ_0 in the spin-dependent case only. Single, double and dashed lines denote octet baryons, decuplet baryons and mesons, respectively.

terms of the decuplet effective operator contributions respectively (see Eqs. (6.11) and (6.15)). Similarly, for the spin-dependent operators,

$$BB'_{\rm SD}\text{ Operator Insertion 6.1(a):} \qquad C^{(m)}_{BB'O_{\Delta q}} S^{\{\mu_0} p^{\mu_1} \dots p^{\mu_m\}}, \tag{6.18a}$$

$$TT'_{\rm SD}\text{ Operator Insertion 6.1(b) \#1:} \qquad C^{(m)}_{TT'O_{\Delta q}} g_{\nu\beta} S^{\{\mu_0} p^{\mu_1} \dots p^{\mu_m\}}, \tag{6.18b}$$

$$TT'_{\rm SD}\text{ Operator Insertion 6.1(b) \#2:} \qquad C^{(m)}_{TT'O_{\Delta q}} g_\nu{}^{\{\mu_1} g_\beta{}^{\mu_2} S^{\mu_0} p^{\mu_3} \dots p^{\mu_m\}}, \tag{6.18c}$$

$$TB_{\rm SD}\text{ Operator Insertion 6.1(c):} \qquad C^{(m)}_{TBO_{\Delta q}} g_\alpha{}^{\{\mu_0} p^{\mu_1} \dots p^{\mu_m\}}, \tag{6.18d}$$

$$BB'\phi\phi'_{\rm SD}\text{ Vertex Insertion 6.1(d):} \qquad \frac{1}{f_\pi^2} C^{(m)}_{BB'\phi\phi'O_{\Delta q}} S^{\{\mu_0} p^{\mu_1} \dots p^{\mu_m\}}. \tag{6.18e}$$

By symmetry, the $BT_{\rm SD}$ vertex (i.e., the reflection of Fig. 6.1(c) in a vertical plane) is identical to the $TB_{\rm SD}$ vertex given here.

6.2.2 Feynman Diagrams

This section gives details of the Feynman diagrams which contribute to the Mellin moments of the PDFs to leading non-analytic order. These are shown in Fig. 6.2 and include loops with both octet and decuplet baryon intermediate states, tadpole loops, and wavefunction renormalisation terms. Diagrams 6.2(h)–6.2(j) contribute only to the odd-n spin-independent moments at order $m_\pi^{n+1}\log(m_\pi)$ and are thus included for the $n = 1$ spin-independent moment only. For this moment they serve to cancel the contributions of diagrams 6.2(a)–6.2(e) to give the usual quark flavour sum rule; for this reason we do not write out their contribution explicitly.

Figure 6.3 shows the loop diagrams which include Weinberg-Tomozawa contact terms. These contribute only to the spin-dependent matrix elements at higher order than we consider here (they have non-analytic behaviour of order $m_\pi^3\log(m_\pi)$ or

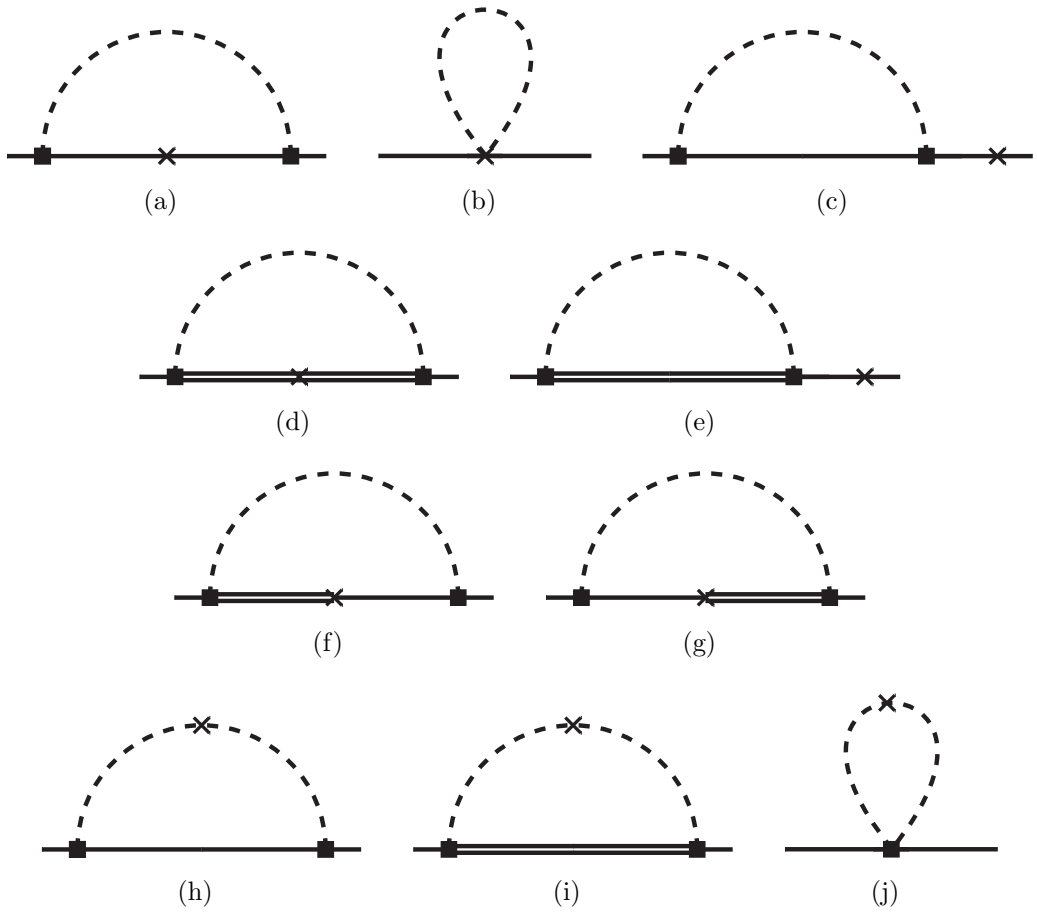

Figure 6.2: Chiral loops included in the present calculation. Single, double, and dashed lines denote octet baryons, decuplet baryons, and mesons, respectively. Crosses (squares) denote twist-two operator (leading-order strong interaction) insertions. Diagram 6.2(a) is hereafter referred to as the 'octet loop' diagram, Fig. 6.2(d) is the 'decuplet loop', and diagram 6.2(b) is referred to as the 'tadpole' diagram. Diagrams 6.2(c) and 6.2(e) represent wavefunction renormalisation. The transition diagrams, shown in Figs. 6.2(f) and 6.2(g), contribute only in the spin-dependent case. Diagrams 6.2(h)–6.2(j) are included for the $n = 1$ spin-independent moment only, as explained in the text.

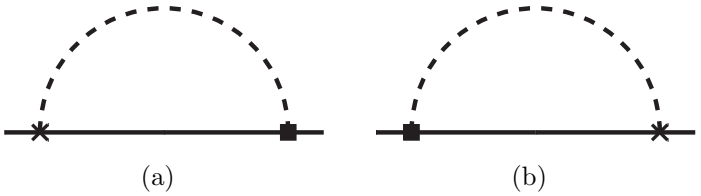

Figure 6.3: Loop diagrams which include Weinberg-Tomozawa contact terms. These contribute only to the spin-dependent matrix elements at higher order (they have non-analytic behaviour of order $m_\pi^3 \log(m_\pi)$ or higher), and are thus excluded from our calculation.

higher), and are thus excluded from our analysis, although it has been argued that these terms may indeed be significant [171].

6.2.3 Loop Integrals

Here we summarise the integral expressions needed for the evaluation of the Feynman diagrams depicted in the previous section. We use the finite-range regularisation scheme which was introduced in Section 3.5, but also make explicit the simple substitutions which relate our expressions to those generated in the DR formalism [177].

Loops with octet baryon intermediate states (e.g., Fig. 6.2(a)) involve the term

$$\int \frac{d^4k}{(2\pi)^4} \frac{k^i k^j}{(k_0 - i\epsilon)^2 (k^2 - m_\phi^2 + i\epsilon)} \underset{\text{FRR}}{=} -i\delta^{ij} \frac{J(m^2)}{16\pi^2}, \tag{6.19}$$

where

$$J(m^2) = \frac{4}{3} \int_0^\infty dk \frac{k^4 u^2(k)}{(\sqrt{k^2 + m^2})^3}, \tag{6.20}$$

with the finite-range regulator $u(k)$ inserted into the integrand. The normalisation of $J(m^2)$ has been defined so that the non-analytic part is simply related to the common form of dimensionally regularised results: $J(m^2) \underset{\text{DR}}{\to} m^2 \ln(m^2/\mu^2)$.

Entirely analogous expressions can be written for integrals with decuplet propagators replacing one or more of the octet propagators in the above loop integral expression. We define

$$\int \frac{d^4k}{(2\pi)^4} \frac{k^i k^j}{(k_0 + \delta - i\epsilon)(k_0 - i\epsilon)(k^2 - m_\phi^2 + i\epsilon)} \underset{\text{FRR}}{=} -i\delta^{ij} \frac{J_1(m^2, \delta)}{16\pi^2}, \tag{6.21}$$

$$\int \frac{d^4k}{(2\pi)^4} \frac{k^i k^j}{(k_0 + \delta - i\epsilon)^2 (k^2 - m_\phi^2 + i\epsilon)} \underset{\text{FRR}}{=} -i\delta^{ij} \frac{J_2(m^2, \delta)}{16\pi^2}, \tag{6.22}$$

where

$$J_1(m^2, \delta) = \frac{4}{3} \int_0^\infty dk \frac{k^4 u^2(k)}{(\sqrt{k^2 + m^2})^2 (\sqrt{k^2 + m^2} + \delta)}, \tag{6.23}$$

$$J_2(m^2, \delta) = \frac{4}{3} \int_0^\infty dk \frac{k^4 u^2(k)}{(\sqrt{k^2 + m^2})(\sqrt{k^2 + m^2} + \delta)^2}, \tag{6.24}$$

with one and two decuplet propagators, respectively. The non-analytic parts of these integrals give the corresponding DR expressions:

$$J_1(m^2, \delta) \underset{\text{DR}}{\to} \left(m^2 - \frac{2}{3}\right) \ln\left(\frac{m^2}{\mu^2}\right) + \frac{2}{3\delta}\left(\delta^2 - m^2\right)^{\frac{3}{2}} \ln\left(\frac{\delta - \sqrt{\delta^2 - m^2}}{\delta + \sqrt{\delta^2 - m^2}}\right) + \frac{2\pi}{3\delta} m^3 - \frac{4}{3} m^2, \tag{6.25}$$

$$J_2(m^2,\delta) \underset{\text{DR}}{\to} \left(m^2-2\delta^2\right)\ln\left(\frac{m^2}{\mu^2}\right)+2\delta\sqrt{\delta^2-m^2}\ln\left(\frac{\delta-\sqrt{\delta^2-m^2}}{\delta+\sqrt{\delta^2-m^2}}\right). \tag{6.26}$$

We also define

$$J_T(m^2) = 4\int_0^\infty dk \frac{k^2u^2(k)}{\sqrt{k^2+m^2}}, \tag{6.27}$$

which has the same non-analytic structure as J, i.e., $J_T(m^2) \underset{\text{DR}}{\to} m^2\ln(m^2/\mu^2)$. This integral will appear in the evaluation of tadpole loops in Section 6.2.4.

To make a comparison with DR expressions clear, and to avoid absorbing loop terms into known parameters such as F and D, constant terms are subtracted by the integral replacement

$$\mathcal{I}(m) \to \widetilde{\mathcal{I}}(m) = [\mathcal{I}(m) - \mathcal{I}(m=0)], \tag{6.28}$$

where $\mathcal{I}$ stands for any of the integrals defined earlier. Terms analytic in m^2 are absorbed by redefinition of the unknown low-energy coefficients $(\Delta)b_i$. With this convention, DR expressions can be recovered by simply replacing each loop integral expression by its non-analytic DR form given above.

6.2.4 Loop Contributions

This section gives explicit expressions for the contribution from each loop diagram shown in Section 6.2.2 to the chiral extrapolation of the Mellin moments of the PDFs. Each term may be derived using the Feynman rules of Section 6.2.1 and is written in terms of the subtracted integrals defined in Section 6.2.3. In each case, the subscripts P and U indicate the polarised (spin-dependent) and unpolarised cases, while the superscripts 8 and 10 indicate diagrams with octet and decuplet baryon intermediate states. All Clebsch-Gordon coefficients C, the momenta $p^{\mu_1}\ldots p^{\mu_{n,m}}$, and the associated symmetrisation of Lorentz indices are suppressed for clarity of notation.

Wavefunction Renormalisation

The contributions from wavefunction renormalisation correspond to Figs. 6.2(c) and 6.2(e) and reduce to

$$Z^8_{2,\{P,U\}} = \frac{1}{16\pi^2 f_\pi^2}\left(\frac{3}{8}\right)\widetilde{J}(m^2), \tag{6.29}$$

$$Z^{10}_{2,\{P,U\}} = \frac{1}{16\pi^2 f_\pi^2}\widetilde{J}_2(m^2,\delta). \tag{6.30}$$

Tadpole Loops

The tadpole loop contributions correspond to Fig. 6.2(b).

$$Z^{\text{tad}}_{1,\{P,U\}} = \frac{1}{16\pi^2 f_\pi^2}\left(\frac{1}{2}\right)\widetilde{J}_T(m^2). \tag{6.31}$$

Octet Intermediate-State Loops

The contribution from Fig. 6.2(a), with an operator insertion into an octet baryon intermediate state, differs from the octet loop wavefunction renormalisation term only in the spinor algebra.

$$Z^{(8,8)}_{1,P} = \frac{1}{16\pi^2 f_\pi^2}\left(-\frac{1}{8}\right)\widetilde{J}(m^2), \tag{6.32}$$

$$Z^{(8,8)}_{1,U} = \frac{1}{16\pi^2 f_\pi^2}\left(\frac{3}{8}\right)\widetilde{J}(m^2). \tag{6.33}$$

Decuplet Intermediate-State Loops

The contribution from decuplet loops with one operator insertion (i.e., Fig. 6.2(d)) mimics that of the decuplet loop wavefunction renormalisation term. While there is an extra $P^{\mu\nu}$ polarisation projector in the spin algebra, as there are two decuplet propagators, the wavefunction renormalisation term (with one propagator) has the identical integral form, J_2, because of the derivative with respect to external momentum.

There are two separate terms which contribute to the decuplet loop (Fig. 6.2(d)), arising from the two terms in each of Eqs. (6.11) and (6.15). We label these contributions as '1' and '2', matching the notation used when defining the relevant Feynman rules in Eqs. (6.17) and (6.18).

$$Z^{(10,10)}_{1,P1} = \frac{1}{16\pi^2 f_\pi^2}\left(-\frac{5}{9}\right)\widetilde{J}_2(m^2,\delta), \tag{6.34}$$

$$Z^{(10,10)}_{1,P2} = \frac{1}{16\pi^2 f_\pi^2}\left(\frac{1}{9}\right)\widetilde{J}_2(m^2,\delta), \tag{6.35}$$

$$Z^{(10,10)}_{1,U1} = \frac{1}{16\pi^2 f_\pi^2}(-1)\widetilde{J}_2(m^2,\delta), \tag{6.36}$$

$$Z^{(10,10)}_{1,U2} = \frac{1}{16\pi^2 f_\pi^2}\left(\frac{1}{3}\right)\widetilde{J}_2(m^2,\delta). \tag{6.37}$$

Octet-Decuplet Transition Loops

By symmetry, the contributions from diagrams 6.2(f) and 6.2(g) are the same. These diagrams do not contribute in the spin-independent case.

$$Z_{1,P}^{(10,8)} = Z_{1,P}^{(8,10)} = \frac{1}{16\pi^2 f_\pi^2}\left(\frac{2}{3}\right)\widetilde{J}_1(m^2,\delta).$$

6.2.5 Fit Functions

Here we finally present complete expressions for the chiral extrapolation of quark distribution moments. The Clebsch-Gordon coefficients C are those given in the Feynman rules in Eqs. (3.40), (6.17) and (6.18). We emphasise that these coefficients, while labelled identically, have distinct numerical values for each moment. Expressions for each C in terms of the low-energy constants introduced in the effective Lagrange densities are given in Appendix F. In the expressions below, summation over repeated indices, e.g., B', T, ϕ (but not B) is implied. The overall factor of 2 arises from the corresponding factor in Eqs. (6.5a) and (6.5b). We remind the reader that the terms $p^{\{\mu_1}\ldots p^{\mu_n\}}$ and $S^{\{\mu_0}p^{\mu_1}\ldots p^{\mu_m\}}$, arising from the Feynman rules and spinor algebra for the chiral extrapolation of the matrix elements, factor out when writing out the quark moment chiral extrapolation (again see Eqs. (6.5a) and (6.5b)).

The master expression for the spin-independent Mellin moments with $n \geq 2$ is

$$\begin{aligned}
2\langle x^{n-1}\rangle_q^B =& \left(C_{BBO_q}^{(n)} + C_{BBO_qM}^{(n)}\right) + C_{BB'\phi}^{(n)} C_{B'B''O_q}^{(n)} C_{B''B\phi}^{(n)} Z_{1,U}^{(8,8)}\left(m_\phi^2\right) \\
&+ C_{BB\phi\phi O_q}^{(n)} Z_{1,U}^{\text{tad}}\left(m_\phi^2\right) + C_{BT\phi}^{(n)} C_{TT'O_q}^{(n)} C_{T'B\phi}^{(n)}\left[Z_{1,U1}^{(10,10)}\left(m_\phi^2\right) + Z_{1,U2}^{(10,10)}\left(m_\phi^2\right)\right] \\
&- \left(C_{BB'\phi}^{(n)}\right)^2 C_{BBO_q} Z_{2,U}^{8}\left(m_\phi^2\right) - \left(C_{BT\phi}^{(n)}\right)^2 C_{BBO_q}^{(n)} Z_{2,U}^{10}\left(m_\phi^2\right),
\end{aligned} \tag{6.38}$$

while the $n = 1$ case is simply the quark flavour sum rule. The spin-dependent moments are given, for $m \geq 1$, by

$$\begin{aligned}
2\langle x^{m}\rangle_{\Delta q}^B =& \left(C_{BBO_q}^{(m)} + C_{BBO_{\Delta q}M}^{(m)}\right) + C_{BB'\phi}^{(m)} C_{B'B''O_{\Delta q}}^{(m)} C_{B''B\phi}^{(m)} Z_{1,P}^{(8,8)}\left(m_\phi^2\right) \\
&+ C_{BB\phi\phi O_{\Delta q}}^{(m)} Z_{1,P}^{\text{tad}}\left(m_\phi^2\right) + C_{BT\phi}^{(m)} C_{TT'O_{\Delta q}}^{(m)} C_{T'B\phi}^{(m)} Z_{1,P1}^{(10,10)}\left(m_\phi^2\right) \\
&+ C_{BT\phi}^{(m)} C_{TB'O_{\Delta q}}^{(m)} C_{B'B\phi}^{(m)}\left[Z_{1,P}^{(8,10)}\left(m_\phi^2\right) + Z_{1,P}^{(10,8)}\left(m_\phi^2\right)\right] \\
&- \left(C_{BB'\phi}^{(m)}\right)^2 C_{BBO_{\Delta q}}^{(m)} Z_{2,P}^{8}\left(m_\phi^2\right) - \left(C_{BT\phi}^{(m)}\right)^2 C_{BBO_{\Delta q}} Z_{2,P}^{10}\left(m_\phi^2\right).
\end{aligned} \tag{6.39}$$

These expressions match those of previous studies [174–176, 178–182] in the limit where $m_u = m_d$, i.e., $\epsilon \to 0$ in the expressions for the couplings C and the meson masses m_ϕ (see Eq. (4.6)).

To facilitate direct comparison with, and use of, these expressions, the chiral expansions for some of the commonly-investigated combinations of moments, namely $\langle 1 \rangle^p_{\Delta u - \Delta d} = g_A$ and $\langle x \rangle^p_{u-d}$, are given explicitly in Appendix H.

6.3 Fits to Lattice QCD Simulation Results

In this section we describe the application of the theory developed here to the chiral extrapolation of lattice results provided by the CSSM and QCDSF-UKQCD collaborations for the first few Mellin moments of the quark distributions [24,32,173]. In particular, we consider the first spin-independent moment and the zeroth and first spin-dependent moments.

The simulations [24,32,173] were performed on a lattice volume $L^3 \times T = 24^3 \times 48$ (with $a = 0.083\,\text{fm}$), and include results for the doubly and singly-represented quark[3] contributions to the Mellin moments of all outer-ring octet baryons (i.e., no Λ or Σ^0 baryons) at five different sets of pseudoscalar masses (m_π, m_K). The locations of the simulations in the light-strange quark mass plane are indicated by the light blue squares along the single constant singlet-mass line in Fig. 4.1. All numbers are expressed as ratios of the moments for different octet baryons (as in Fig. 6.4); overall normalisations are not given.

For our analysis we use a dipole regulator, $u(k) = \left(\frac{\Lambda^2}{\Lambda^2 + k^2}\right)^2$, and a regulator mass $\Lambda = 1\,\text{GeV}$, within the FRR scheme. All results are insensitive to this choice; selecting, for example, monopole, Gaussian, or sharp cutoff forms for the regulator does not change the results of the analysis within the quoted uncertainties. We explicitly allow Λ to vary by $\pm 20\%$ for our final results.

The fit to the simulation results is performed by minimising the sum of χ^2 for each set of moments independently. As lattice data is available only for the doubly and singly-represented quark moments, not all of the parameters which appear in the equations in the previous sections are linearly independent in the relevant fit functions. Replacements are made:

$$\begin{aligned} n_1 &= b_1 + b_3, & n_2 &= b_2 + b_4, & n_3 &= b_5, \\ n_4 &= b_7, & n_5 &= b_8, & n_6 &= b_9, \end{aligned} \tag{6.40}$$

with entirely analogous relations defining Δn_i in the spin-dependent cases.

There are 24 lattice data points available for each of the three moments considered. The fit parameters are different (and the fits independent), for each moment. As indicated earlier, we use SU(6) relations between unknown quantities to reduce the number of free parameters to eight or nine:

- For the **zeroth spin-dependent** moment, $\Delta n_i^{(0)}$, $\Delta\sigma^{(0)}$, and D are fit; the low-energy constants $\Delta\alpha^{(0)}$ and $\Delta\beta^{(0)}$ have been related to D by Eq. (6.13). We

[3] For a baryon with valence quark content xxy, the doubly-represented contribution is the total from quarks of flavour x, while the singly-represented contribution is the total from y-flavoured quarks. For example, in the proton the u and d quarks are doubly and singly-represented, respectively.

	First SI ($i=2$)	Zeroth SD ($i=0$)	First SD ($i=1$)
$(\Delta)n_1^{(i)}$	1.1(25)(0)	4.9(84)(9)	−1.5(13)(15)
$(\Delta)n_2^{(i)}$	−7.0(28)(27)	0.5(98)(12)	6.3(29)(26)
$(\Delta)n_3^{(i)}$	8.3(26)(31)	−2.2(58)(9)	−3.9(16)(23)
$(\Delta)n_4^{(i)}$	0.5(27)(1)	−15(17)(0)	−7.0(46)(11)
$(\Delta)n_5^{(i)}$	11(4)(4)	0.2(50)(9)	−1.0(11)(8)
$(\Delta)n_6^{(i)}$	6.2(24)(23)	−1.1(88)(7)	−6.0(28)(34)
$(\Delta)\alpha^{(i)}$	−4.1(17)(12)		0.41(50)(29)
$(\Delta)\beta^{(i)}$	−8.6(31)(21)		−1.5(10)(3)
$(\Delta)\sigma^{(i)}$	7.5(26)(23)	−0.22(26)(0)	−0.93(61)(14)
D		0.74(24)(6)	

Table 6.1: Values of the fit parameters corresponding to the fits shown in Fig. 6.4. All $(\Delta)n_i^{(j)}$ have dimensions (GeV^{-2}), other parameters are dimensionless. The first error range given is statistical, while the second indicates the uncertainty resulting from a ±20% variation in the FRR cutoff Λ.

use SU(6) symmetry to set $F = \frac{2}{3}D$ and $\Delta\gamma^{(0)} = -6D$. $\mathcal{C} \to \mathcal{C}_{\text{phys.}} = -\frac{6}{5}g_{A_{\text{phys.}}}$ is also fixed. This gives a total of eight free parameters.

- The nine fit parameters for the **first spin-dependent** moment are $\Delta n_i^{(1)}$, $\Delta\alpha^{(1)}$, $\Delta\beta^{(1)}$, and $\Delta\sigma^{(1)}$. Fixed parameters are $D \to D_{\text{phys.}} = \frac{3}{5}g_{A_{\text{phys.}}}$, $F \to F_{\text{phys.}} = \frac{2}{3}D_{\text{phys.}}$, $\mathcal{C} \to \mathcal{C}_{\text{phys.}}$, and, using SU(6) symmetry, $\Delta\gamma^{(1)} = -\frac{3}{2}\big(\Delta\alpha^{(1)} - 2\Delta\,\beta^{(1)}\big)$, as outlined in the text (see Eq. (6.15)).

- For the **first spin-independent** moment, nine parameters, $n_i^{(2)}$, $\alpha^{(2)}$, $\beta^{(2)}$, and $\sigma^{(2)}$, are fit, with D, F, and $\mathcal{C}$ again fixed to their physical values. As no phenomenological estimate of the combination $\left(\gamma^{(2)} - \frac{\gamma'^{(2)}}{3}\right)$ is available, this quantity is fixed to a 'physical' value through its relationship to the tree-level delta insertion, SU(6) symmetry, and the best experimental value of the isovector proton moment (at a scale of $4\,\mathrm{GeV}^2$) [183]:

$$\left(\gamma^{(2)} - \frac{\gamma'^{(2)}}{3}\right) = 6\langle x\rangle_{u-d}^{\Delta^+} \qquad \text{at tree level,} \tag{6.41a}$$

$$= 6\langle x\rangle_{u-d}^{p} \qquad \text{using SU(6) symmetry,} \tag{6.41b}$$

$$\underset{\text{exp.}}{=} 6(0.157) = 0.942. \tag{6.41c}$$

The fits to the available lattice simulation results (expressed as ratios of Mellin moments) are shown in Fig. 6.4. The horizontal axes are normalised with respect to the simulation centre-of-mass of the pseudoscalar meson octet, $X_\pi = \sqrt{(2m_K^2 + m_\pi^2)/3} = 411\,\mathrm{MeV}$, so that the figures may be easily compared against

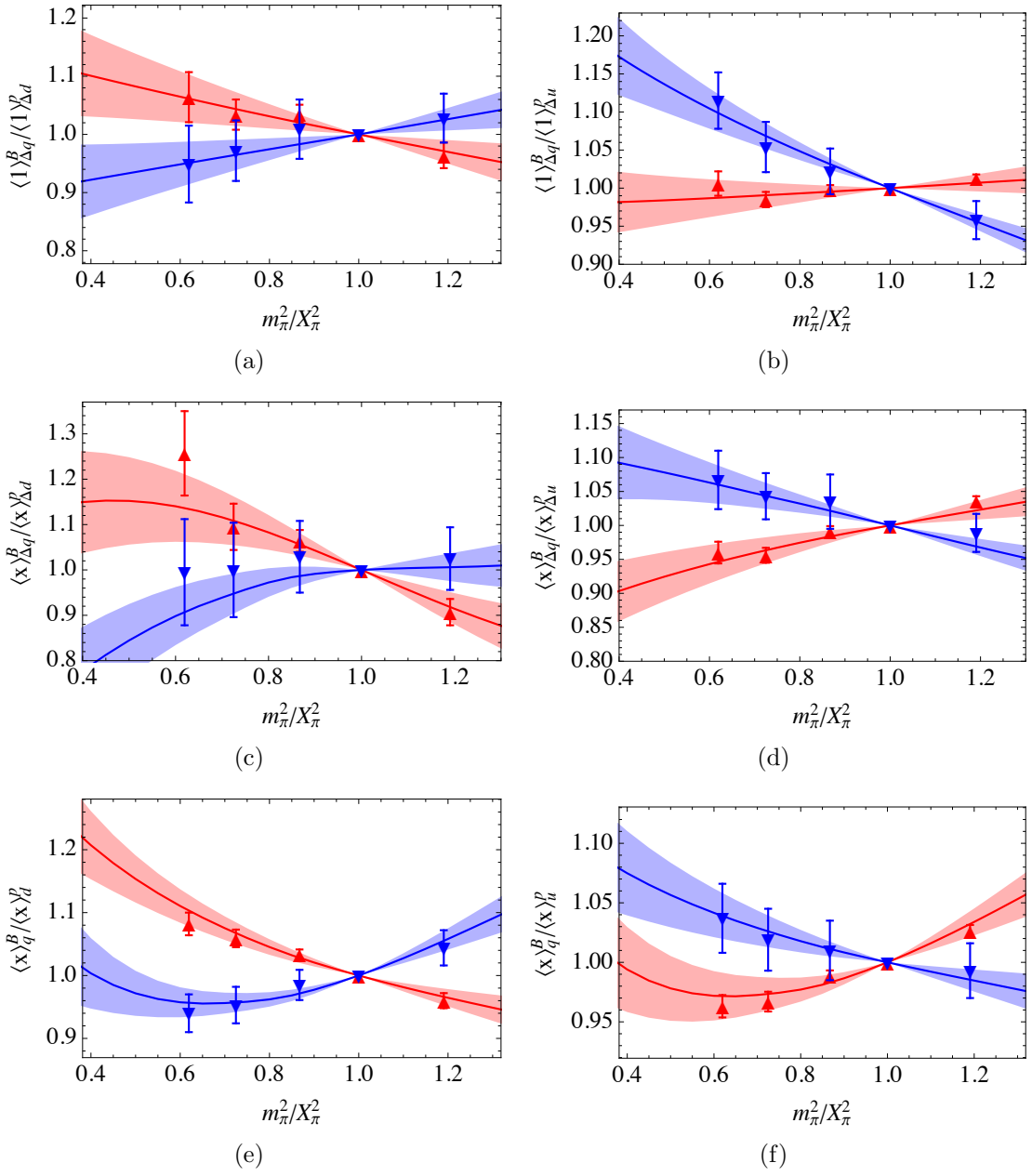

Figure 6.4: Illustration of the fits to the zeroth spin-dependent moment (Figs. 6.4(a) and 6.4(b)), the first spin-dependent moment (Figs. 6.4(c) and 6.4(d)), and the first spin-independent moment (Figs. 6.4(e) and 6.4(f)). Figures in left (right) hand panels correspond to the ratios of singly (doubly) represented quark distribution moments for the Σ (red upward triangles) and Ξ (blue downward triangles) baryons to those of the nucleon. Lattice data is taken from Refs. [32, 173].

previously published analyses which used linear fits to the lattice results [32, 173]. The quality of fit is clearly acceptable in each case, with the χ^2/d.o.f. between 0.6 and 0.9 for each moment. All χ^2 values are less than one as we were not able to take into account the effect of correlations between the original lattice data points. Best-fit parameters for each fit are given in Table 6.1.

In Section 6.5 we describe the use of these fits to determine the magnitude of CSV effects in each of the Mellin moments. This analysis is based on the same principles introduced in Chapter 4 to determine the mass splittings among members of baryon isospin multiplets from 2+1–flavour lattice simulation results. First, however, we use the chiral extrapolation for the zeroth spin-dependent moment, which directly probes the distribution of the spin of a baryon among its quarks, to gain some insight into the proton spin puzzle.

6.4 Hyperon Spin Fractions and the Proton Spin Puzzle

Since the discovery by the European Muon collaboration [155, 184–186] that quarks carry a relatively small fraction of the spin of the proton—the proton spin puzzle—there have been decades of careful experimental investigation of that claim. The puzzle, however, has persisted; the quark contribution to the proton spin currently stands at [156] $33 \pm 3 \pm 5\%$ if one relies on SU(3) symmetry for the octet axial charge, g_A^8 . This is a dramatic suppression with respect to the value of 100% expected in a naive quark model, or even the 65% expected in a relativistic quark model. The value deduced from experiment increases only marginally, to $36 \pm 3 \pm 5\%$, if g_A^8 is reduced by 20%, as suggested by model calculations [187] and a recent lattice simulation [188].

A number of possible theoretical explanations for the spin puzzle have been offered, ranging from a key role for the axial anomaly [189–195] to the effect of gluon exchange currents [196–198], the effects of chiral symmetry [199, 200], and, in the light of insights gained from lattice QCD studies, a combination of both of these effects[4] [203]. It is clearly of great interest to find new ways to shed light on the origin of this phenomenon.

The analysis of lattice QCD simulation results described in previous sections can give some insight into the spin puzzle. In particular, the zeroth spin-dependent Mellin moment of the quark distribution function for quark flavour q in baryon B corresponds identically to the spin carried by that quark flavour:

$$\Delta q_B \equiv \langle 1 \rangle_{\Delta q}^B = \int_0^1 dx \left(\Delta q^B(x) + \Delta \overline{q}^B(x) \right). \tag{6.42}$$

[4]The relatively small values of the gluon spin in the proton, found in both fixed target and collider experiments [201, 202], have eliminated the possibility that the axial anomaly alone might explain the observed suppression, although its effect may still be quantitatively significant.

B	Model	Lattice
N	1.0	1.0
Λ	1.35(2)	
Σ	0.97(1)	0.92(13)
Ξ	1.49(5)	1.61(33)

Table 6.2: Ratio of the spin fraction for each hyperon to that of the nucleon. For the model calculation, the uncertainties quoted result from choosing a bag radius $R = 0.8\,\text{fm}$ rather than the default 1 fm. The lattice uncertainties include all statistical and systematic effects described in previous sections combined in quadrature.

As the lattice QCD simulation results used here were presented in ratio form by the lattice groups (because the analysis of the renormalisation of the lattice operators had not been completed), the absolute values of the spin fractions cannot be extracted from our analysis. We can, however, use our results—which extend to the entire outer-ring baryon octet—to determine whether the suppression observed for the proton is a general property or varies across the baryon octet. Despite early proposals [204] to measure the quark contribution to the Δ baryon spin, there is at this stage no experimental indication as to whether spin-suppression is a universal feature of baryons or not.

Unfortunately, as the lattice data set does not include any calculations for the Λ hyperon[5], we are unable to present results in that case. However, for the other members of the octet one can simply sum Δu, Δd, and Δs to obtain the (connected quark-line contribution to the) spin fractions carried by the quarks in each baryon. These values, determined from the fit functions of Section 6.3 evaluated at the physical meson masses, are shown in the final column of Table 6.2. Although the uncertainties are substantial, there is a remarkable degree of variation with the structure of the baryon, with the ratio of spin fractions equal to 0.92(13) for $\Sigma : N$ while it is 1.61(33) for $\Xi : N$. This variation is not merely an artefact of the (significant) chiral extrapolation in pion mass which is necessary to reach the physical point; it is in fact distinct in the lattice results themselves. This is illustrated in Fig. 6.5.

These results clearly do not support the hypothesis that the spin suppression observed for the proton might be a universal property. In order to understand this effect qualitatively it is of considerable interest to investigate the predictions of models in which the suppression of the spin carried by quarks is dependent on baryon structure. In Ref. [206], the cloudy bag model (CBM), developed in Refs. [196,197,199,201], was applied to this problem. The model includes relativity [207–210], gluon exchange currents [196, 211, 212], and the meson cloud required by chiral symmetry [199]. As

[5]Since the completion of this work, calculations of the quark spin fractions in the Λ baryon have been performed for a subset of the simulation ensembles used here [205]. At this stage, however, the results do not span a sufficient range of meson masses to constrain an extrapolation of the Λ spin fraction to the physical point (when included in our analysis).

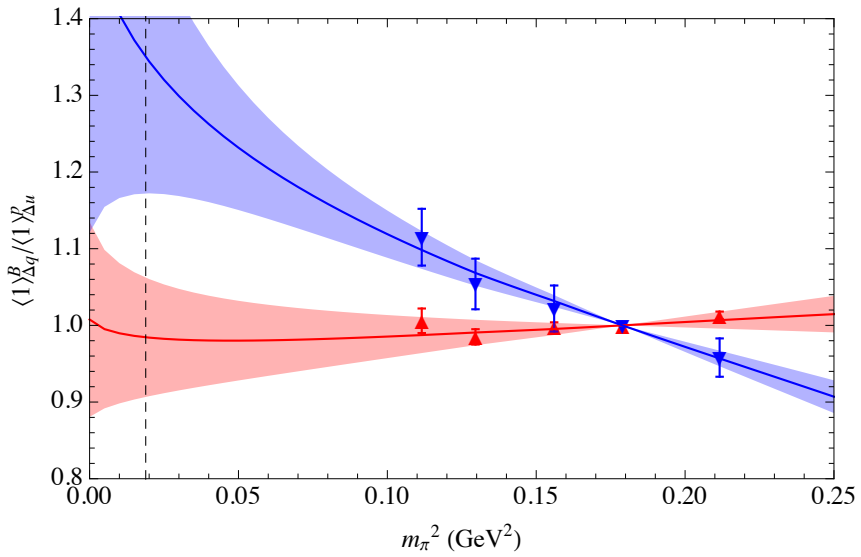

Figure 6.5: As in Fig. 6.4(b), with dimensionful units on the horizontal axis. Red upward (blue downward) triangles show the ratio of the lattice moments of the u in the Σ^+ (s in the Ξ) to the u in the proton. The vertical dashed line indicates the physical pion mass.

can be seen from Table 6.2, the predicted variation of the fraction of the spin carried by quarks across the octet is striking, and is in excellent agreement with the results of our lattice study. Within the quark model, this variation in spin-suppression can be easily interpreted; the meson cloud correction is considerably smaller in the Ξ than in the nucleon. That, combined with the less relativistic motion of the heavier strange quark, results in the quark spin fraction in the Ξ being substantially larger than that in the nucleon.

6.5 Charge Symmetry Violation

As discussed in the introduction to this chapter, the assumption of good charge symmetry has been widely applied in parton phenomenology [33, 39] despite experimental upper limits on partonic CSV falling in the range 5–10%. CSV of that magnitude would produce important effects in tests of physics beyond the SM, for example in neutrino-nucleus deep inelastic scattering experiments [40]. We use the analysis of lattice simulation results presented in Section 6.3 to more precisely constrain the size of CSV effects in the lowest several lattice-accessible Mellin moments of the PDFs.

In terms of quark distributions, charge symmetry implies

$$u^p\big(x,Q^2\big) = d^n\big(x,Q^2\big), \qquad d^p\big(x,Q^2\big) = u^n\big(x,Q^2\big), \tag{6.43}$$

with analogous relations for the antiquark distributions. A measure of the size of the violation of charge symmetry is given by the 'CSV parton distributions', defined

in terms of the Mellin moments as

$$\delta u^{m\pm} = \int_0^1 dx\, x^m \big(u^{p\pm}(x) - d^{n\pm}(x)\big) = \langle x^m \rangle_u^{p\pm} - \langle x^m \rangle_d^{n\pm} \tag{6.44a}$$

and

$$\delta d^{m\pm} = \int_0^1 dx\, x^m \big(d^{p\pm}(x) - u^{n\pm}(x)\big) = \langle x^m \rangle_d^{p\pm} - \langle x^m \rangle_u^{n\pm} \tag{6.44b}$$

for the spin-independent distributions, with analogous expressions for the spin-dependent case. Here, the plus (minus) superscripts indicate C-even (C-odd) distributions:

$$q^{\pm}(x) = q(x) \pm \overline{q}(x). \tag{6.45}$$

As the CSSM and QCDSF-UKQCD collaboration lattice simulation results [32, 173] analysed in Section 6.3 use mass-degenerate light quarks, the CSV terms cannot be directly evaluated using Eqs. (6.44a) and (6.44b) (as this would give zero in each case). The problem can, however, be approached indirectly; because the simulations lie along a line of constant singlet quark mass (light blue squares in Fig. 4.1), an approximation to the CSV moments may be found using a linear flavour expansion about the SU(3)-symmetric point. This approach is described in Section 6.5.1.

The results may be improved using the chiral fits which were presented in Section 6.3. Just as was described in detail in the context of determining the mass splittings among members of baryon isospin multiplets from $N_f = 2 + 1$ lattice simulation results (Section 4.3), the only additional input needed to determine the CSV moments from the previously-described isospin-averaged fits is a value for the light-quark mass ratio $R = m_u/m_d$. The chirally-improved extraction of the CSV terms is described in Section 6.5.2.

6.5.1 Linear Flavour Expansion

If one takes the light-quark mass difference $m_\delta = (m_d - m_u)$ to be small, the CSV Mellin moments may be expanded as

$$\delta u = m_\delta \left(-\frac{\partial \langle x \rangle_u^p}{\partial m_u} + \frac{\partial \langle x \rangle_u^p}{\partial m_d} \right) + \mathcal{O}\big(m_\delta^2\big), \tag{6.46}$$

with a similar expression for δd. The equivalence of the u and d quarks in the lattice simulations to which we will apply this expansion, i.e., that $\partial \langle x \rangle_d^n / \partial m_d = \partial \langle x \rangle_u^p / \partial m_u$ and $\partial \langle x \rangle_d^n / \partial m_u = \partial \langle x \rangle_u^p / \partial m_d$, has been used to simplify the expression. Near the SU(3)-symmetric point, the strange quark can be considered as a heavy light-quark; the lattice results for the hyperon Mellin moments can thus be substituted for information about the light-quark derivatives:

$$\frac{\partial \langle x \rangle_u^p}{\partial m_u} \approx \frac{\langle x \rangle_s^{\Xi^0} - \langle x \rangle_u^p}{m_s - m_l}, \qquad \frac{\partial \langle x \rangle_u^p}{\partial m_d} \approx \frac{\langle x \rangle_u^{\Sigma^+} - \langle x \rangle_u^p}{m_s - m_l}, \tag{6.47a}$$

$$\frac{\partial\langle x\rangle_d^p}{\partial m_u} \approx \frac{\langle x\rangle_u^{\Xi^0} - \langle x\rangle_d^p}{m_s - m_l}, \qquad \frac{\partial\langle x\rangle_d^p}{\partial m_d} \approx \frac{\langle x\rangle_s^{\Sigma^+} - \langle x\rangle_d^p}{m_s - m_l}. \tag{6.47b}$$

Rearranging these expressions, and invoking the Gell-Mann–Oakes–Renner relation, the CSV momentum fractions can be written as[6]

$$\frac{\delta u}{\langle x\rangle_{u-d}^p} = \frac{1}{2}\frac{m_\delta}{\overline{m}_q}\frac{\left(\langle x\rangle_u^{\Sigma^+} - \langle x\rangle_s^{\Xi^0}\right)/\langle x\rangle_{u-d}^p}{(m_K^2 - m_\pi^2)/X_\pi^2}, \tag{6.48a}$$

$$\frac{\delta d}{\langle x\rangle_{u-d}^p} = \frac{1}{2}\frac{m_\delta}{\overline{m}_q}\frac{\left(\langle x\rangle_s^{\Sigma^+} - \langle x\rangle_u^{\Xi^0}\right)/\langle x\rangle_{u-d}^p}{(m_K^2 - m_\pi^2)/X_\pi^2}, \tag{6.48b}$$

where $\overline{m}_q = (2m_l + m_s)/3$ and $X_\pi^2 = (2m_K^2 + m_\pi^2)/3$. Similar expressions hold for the spin-dependent CSV moments. Written in this way, the fractional CSV terms are simply the slopes of straight lines drawn through the data displayed in Fig. 6.6 (evaluated at the SU(3)-symmetric point), multiplied by the ratio $m_\delta/\overline{m}_q$. Taking the Leutwyler value, $R = m_u/m_d = 0.553(43)$, based on the discussion of Section 4.4, we find $m_\delta/\overline{m}_q = 0.066(7)$ for the lattice simulations considered here. The normalisations of each moment are set using the best experimental values at the physical point at a scale of 4 GeV^2 [30, 183, 213]:

$$g_A = \langle 1\rangle_{\Delta u-\Delta d}^p \underset{\text{exp.}}{=} 1.2695(29), \tag{6.49a}$$

$$\langle x\rangle_{\Delta u-\Delta d}^p \underset{\text{exp.}}{=} 0.190(8), \tag{6.49b}$$

$$\langle x\rangle_{u-d}^p \underset{\text{exp.}}{=} 0.157(9). \tag{6.49c}$$

Results for all six CSV moments are given in the first column of Table 6.3. Because this method gives estimates of the magnitude of CSV at the simulation SU(3)-symmetric point, the results may have chiral corrections which are more significant than the $\mathcal{O}(m_\delta^2)$ counting suggested by the Taylor expansion in Eq. (6.46). Using the chiral extrapolations detailed in Section 6.3 we can improve on this linear expansion and explicitly calculate the corrections involved in moving away from the simulation SU(3) value to the physical (SU(3)-broken) point.

6.5.2 Chiral Expansion

To evaluate the CSV terms at the physical (rather than the simulation SU(3)-symmetric) point, we use the chiral extrapolations detailed in Section 6.3. As the isospin-averaged and broken expressions for the Mellin moments as functions of pseudoscalar mass have the same unknown parameters, the CSV terms given in Eq. (6.44) may be evaluated by simply substituting the best-fit parameters of the previously-described fits into the full isospin-broken expressions. These expressions

[6] In Refs. [32, 173] the factor of $\frac{1}{2}$ appearing at the beginning of the following equations was erroneously omitted. As a result, the values quoted for the CSV terms were too large by a factor of two.

Moment	Linear: SU(3)-sym.	Chiral: SU(3)-sym.	Chiral: physical
$\delta\Delta u^{0+}$	−0.0057(14)	−0.0063(13)	−0.0061(13)
$\delta\Delta d^{0+}$	−0.0018(6)	−0.0019(6)	−0.0018(6)
$\delta\Delta u^{1-}$	−0.0010(3)	−0.0007(2)	−0.0007(2)
$\delta\Delta d^{1-}$	−0.0004(1)	−0.0003(1)	−0.0002(1)
δu^{1+}	−0.0012(3)	−0.0013(3)	−0.0023(7)
δd^{1+}	0.0010(2)	0.0012(2)	0.0017(4)

Table 6.3: Comparison of CSV PDF moment results. The column labelled 'Linear' gives the results which were published with the lattice simulations [32, 173], calculated using a linear flavour expansion about the SU(3)-symmetric point. These have been corrected from the values quoted in Refs. [32,173], as explained in the footnote preceding Eq. (6.48a). 'Chiral' gives the results of this work, i.e., including chiral physics, both at the comparable 'SU(3)-symmetric' point (with $(m_d + m_u) = 2m_s$ but the physical $(m_d - m_u)$), labelled 'SU(3)-sym.', and at the physical pseudoscalar masses.

can then be evaluated at any pseudoscalar masses, in particular at the physical point. As described in Chapter 4, the only additional input needed is a value for the light-quark mass ratio which we set to the Leutwyler value, $R = m_u/m_d = 0.553(43)$, based on the discussion of Section 4.4.

For example, $\delta\Delta u^m$ may be expressed as a function of meson mass in the form:

$$\delta\Delta u^m = \langle x^m\rangle^p_{\Delta u} - \langle x^m\rangle^n_{\Delta d} = a^{(m)}_\Delta + \frac{1}{16\pi^2 f_\pi^2}\Big(b^{(m)}_\Delta + d^{(m)}_\Delta + g^{(m)}_\Delta\Big), \tag{6.50}$$

where

$$a^{(m)}_\Delta = \frac{1}{2}\Big(-\Delta n^{(m)}_1 + \Delta n^{(m)}_2 + \Delta n^{(m)}_3 + \Delta n^{(m)}_6\Big) B(m_u - m_d), \tag{6.51a}$$

$$\begin{aligned} b^{(m)}_\Delta =& \frac{1}{6\sqrt{3}}\big(D^2 - 2DF - 3F^2\big)\sin(2\epsilon)\big(5\Delta\alpha^{(m)} + 2\Delta\beta^{(m)} + 6\Delta\sigma^{(m)}\big) \\ &\times\Big[\widetilde{J}\big(m^2_{\pi_0}\big) - \widetilde{J}\big(m^2_\eta\big)\Big] \\ &+ \frac{1}{24}\big[-D^2\big(9\Delta\alpha^{(m)} + 2\Delta\beta^{(m)} + 8\Delta\sigma^{(m)}\big) \\ &\qquad +2DF\big(19\Delta\alpha^{(m)} + 10\Delta\beta^{(m)} + 24\Delta\sigma^{(m)}\big) \\ &\qquad +3F^2\big(5\Delta\alpha^{(m)} + 2\Delta\beta^{(m)} + 8\Delta\sigma^{(m)}\big)\big]\Big[\widetilde{J}\big(m^2_{K^0}\big) - \widetilde{J}\big(m^2_{K^\pm}\big)\Big] \\ &+ \frac{1}{24}\big(5\Delta\alpha^{(m)} + 2\Delta\beta^{(m)}\big)\Big[\widetilde{J}_T\big(m^2_{K^0}\big) - \widetilde{J}_T\big(m^2_{K^\pm}\big)\Big], \end{aligned} \tag{6.51b}$$

$$\begin{aligned} d^{(m)}_\Delta =& -\frac{1}{72}\big(5\Delta\alpha^{(m)} + 2\Delta\beta^{(m)} + 6\Delta\sigma^{(m)}\big)\mathcal{C}^2\Big[\widetilde{J}_2\big(m^2_{K^0},\delta\big) - \widetilde{J}_2\big(m^2_{K^\pm},\delta\big)\Big] \\ &- \frac{1}{108}\big(5\Delta\gamma^{(m)} - \Delta\gamma'^{(m)}\big)\mathcal{C}^2\Big[\widetilde{J}_2\big(m^2_{K^0},\delta\big) - \widetilde{J}_2\big(m^2_{K^\pm},\delta\big)\Big], \end{aligned} \tag{6.51c}$$

$$g_\Delta^{(m)} = -\frac{4}{9\sqrt{3}}(D-3F)\sin(2\epsilon)\Delta\omega^{(m)}\Big[\widetilde{J}_1\big(m_{\pi^0}^2,\delta\big)+\widetilde{J}_1\big(m_\eta^2,\delta\big)\Big] + \frac{2}{9}(D-3F)\Delta\omega^{(m)}\Big[\widetilde{J}_1\big(m_{K^0}^2,\delta\big)-\widetilde{J}_1\big(m_{K^\pm}^2,\delta\big)\Big], \quad (6.51d)$$

where expressions for the (subtracted) integrals $\widetilde{J}$ are given in Section 6.2.3. Clearly, entirely analogous expressions may be written for $\delta\Delta d^m$ and the spin-independent CSV terms. These are given in Appendix H.2. To the same order in the broken SU(3) symmetry, analogous expressions for each quark flavour combination in each octet baryon are expressed in terms of different linear combinations of the same coefficients; the general chiral expansion is given in Section 6.2.5.

Figure 6.6 shows the fits to the isospin-averaged lattice data in a form which emphasises the SU(3)-symmetry–breaking in the simulation results. It is clear from these plots that, before extrapolation to the physical masses, there are only small chiral corrections to the CSV moments; the slopes of the fit functions at the SU(3)-symmetric point are comparable to those of the straight-line fits described in the previous section.

As the available QCDSF-UKQCD collaboration lattice results are presented only in terms of ratios of moments, there is an unknown constant scaling factor, Z, associated with all data points. The Zs are distinct for each moment (zeroth and first spin-dependent and first spin-independent) under consideration and are fixed by matching the extrapolations for the isovector moments to experimental values at a scale of 4 GeV^2 [30,183,213], just as was done for the linear flavour expansion analysis (see Eq. (6.49)). The uncertainty of the experimental numbers is propagated into the final results. The full error analysis also takes account of correlated uncertainties between all of the fit parameters in the original fits, as well as allowing for the stated variation of R. The regulator mass, $\Lambda = 1\,\text{GeV}$, is allowed to vary by $\pm 20\%$, which is again propagated into the final uncertainty. Changing the functional form of the regulator $u(k)$ within the FRR scheme leads to small variations of order 1%.

An advantage of the chiral method is that the CSV moments may be evaluated at any pseudoscalar masses. In particular, evaluating the chiral perturbation theory expressions at the point where $(m_d+m_u) = 2m_s$ and both (m_d-m_u) and $(m_u+m_d+m_s)$ take their physical values, labelled 'SU(3)-sym.' in Table 6.3, gives results which may be directly compared with the linear flavour expansion calculation. As might be anticipated from an inspection of Figs. 6.6(a)–6.6(c) which show fits qualitatively consistent with straight lines, chiral loop corrections to the CSV terms at this point are small and do not change the results within the quoted uncertainties, even given the small shift from the simulation SU(3) value to the physical symmetric point.

Moreover, comparison of these results with the CSV moments evaluated at the physical pseudoscalar masses gives an indication of the size of any chiral corrections which appear in moving away from the SU(3) point. Again, these corrections are small in the spin-dependent case, while being more significant in the spin-independent case. In contrast to the results of the linear flavour expansion, the chiral perturbation theory results are based on fits to all lattice data simultane-

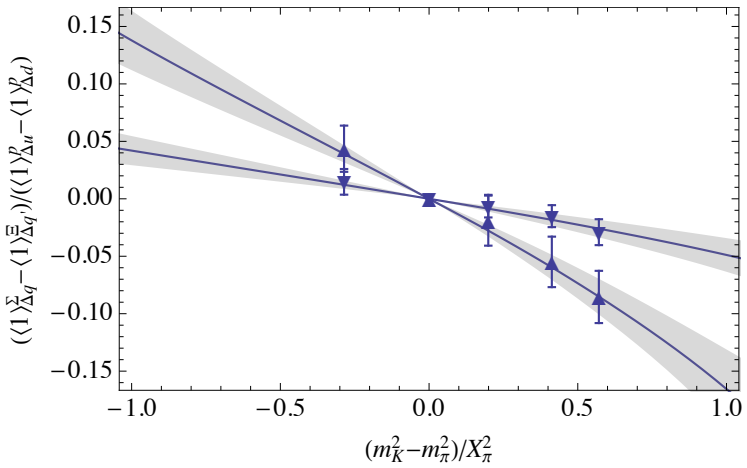

(a) Zeroth spin-dependent Mellin moments.

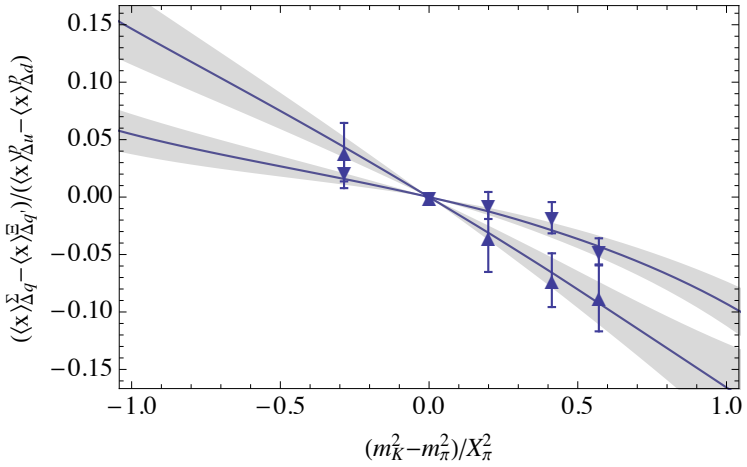

(b) First spin-dependent Mellin moments.

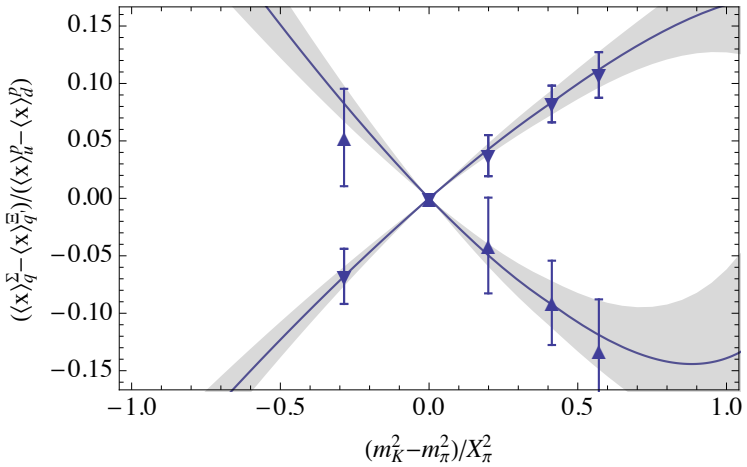

(c) First spin-independent Mellin moments.

Figure 6.6: Illustration of the fits to the lattice data from Refs. [32, 173] for the lowest several Mellin moments of the PDFs. Upward and downward triangles indicate the ratios of doubly and singly-represented quark moments, respectively.

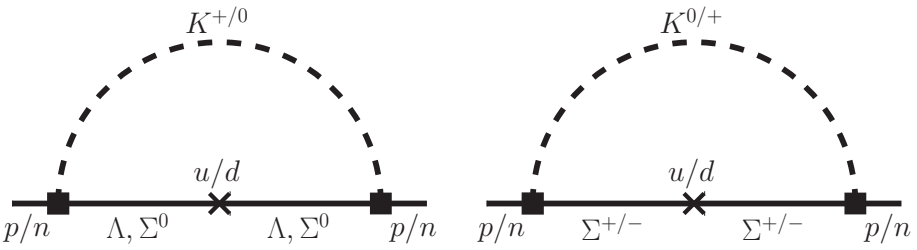

Figure 6.7: Illustration of some of the octet loop terms contributing to $\delta\Delta u^m = \langle x^m \rangle^p_{\Delta u} - \langle x^m \rangle^n_{\Delta d}$ or $\delta u^m = \langle x^m \rangle^p_u - \langle x^m \rangle^n_d$. These contributions are non-vanishing when the loop pseudoscalar masses are different, i.e., when $m^2_{K^0} \neq m^2_{K^\pm}$.

ously (for each moment), and thus include the proper correlations between quark moments in each of the baryons. As a consequence, even with more fit parameters, the uncertainties are comparable to the simple linear fits.

The origin of the chiral loop contributions to the CSV terms can be seen clearly from the form of Eq. (6.50) (and the analogous Eqs. (H.5), (H.7a) and (H.7b) in Appendix H.2). One contribution to the $\delta(\Delta)u$ moments is illustrated diagrammatically in Fig. 6.7. The kaon loop diagrams shown, and the analogous diagrams for the $\delta(\Delta)d$ moments, give contributions to the CSV terms proportional to $\left[\widetilde{J}\left(m^2_{K^0}\right) - \widetilde{J}\left(m^2_{K^\pm}\right)\right]$, which is non-vanishing when $m^2_{K^0} \neq m^2_{K^\pm}$. The corresponding wavefunction renormalisation terms, as well as tadpole and decuplet kaon-loop diagrams, also contribute to the CSV terms proportional to $\left[\widetilde{J}\left(m^2_{K^0}\right) - \widetilde{J}\left(m^2_{K^\pm}\right)\right]$. In the spin-independent case, this kaon mass difference effect yields the only chiral loop corrections to the CSV terms. For the spin-dependent moments, however, additional terms proportional to $\left[\widetilde{J}\left(m^2_{\pi_0}\right) - \widetilde{J}\left(m^2_{\eta}\right)\right]$ also contribute. Cancellation between the octet loop terms and wavefunction renormalisation contributions ensures that these terms vanish in the spin-independent case.

The chiral loops also account for the corrections in moving from the 'SU(3) point' to the physical point. For example, as one moves along the line of constant singlet quark mass ($(m_u + m_d + m_s) =$ constant) from the SU(3)-symmetric point to the physical point, the difference $\left[\widetilde{J}\left(m^2_{K^0}\right) - \widetilde{J}\left(m^2_{K^\pm}\right)\right]$ decreases in magnitude by approximately 30%.

6.6 Summary and Discussion

We have used the chiral perturbation theory formalism to extrapolate QCDSF-UKQCD collaboration lattice data for the first several Mellin moments of quark distribution functions to the physical pseudoscalar meson masses. By performing a consistent analysis including the entire outer-ring baryon octet, we have clearly shown that the experimentally-measured suppression of the fraction of the proton spin carried by its quarks (relative to the predictions from a naive or relativistic

quark model) is not a universal property across the baryon octet, but rather is structure-dependent. This conclusion is supported by a calculation within a relativistic quark model which includes gluon exchange currents and the meson cloud required by chiral symmetry.

Furthermore, our study allows the CSV parton distribution moments to be evaluated at the physical pseudoscalar masses. Comparing our results with those of a previous analysis based on a linear flavour expansion about the SU(3)-symmetric point [32,173], we find that both the chiral corrections at the SU(3) point, as well as the shifts resulting from the extrapolation to the physical pseudoscalar masses, are small. The latter corrections, however, are more significant for the spin-independent than spin-dependent moments.

At the physical point, our analysis gives the spin-dependent CSV terms to be

$$\delta\Delta u^{0+} = -0.0061(13), \qquad \delta\Delta d^{0+} = -0.0018(6), \tag{6.52a}$$

$$\delta\Delta u^{1-} = -0.0007(2), \qquad \delta\Delta d^{1-} = -0.0002(1). \tag{6.52b}$$

As a result, one would expect CSV corrections to the Bjorken sum rule [214, 215] to appear at the half-percent level. Measuring these corrections would require significant improvement over the current best determination of the sum rule to 8% precision at $Q^2 = 3$ GeV^2 from a recent COMPASS collaboration experiment [216]. For the spin-independent moments, this analysis gives

$$\delta u^{1+} = -0.0023(7), \qquad \delta d^{1+} = 0.0017(4), \tag{6.53}$$

in good agreement with previous phenomenological estimates of CSV both within the MIT bag model [37,40] and using the MRST analysis [36]. These results support the conclusion [33,40,217] that partonic CSV effects may reduce the 3-sigma discrepancy with the Standard Model reported by the NuTeV collaboration [41] by up to 30%.

Chapter 7

Electromagnetic Form Factors

More than a decade before the partonic substructure of the proton was revealed through DIS (see Chapter 6), elastic electron-proton scattering experiments at Stanford University High Energy Physics Laboratory [218] were used to probe the spatial distribution of the charge and magnetisation density in the nucleon. These properties were encoded in so-called electromagnetic form factors [219], expressed as functions of the probing momentum scale, Q^2. The first measurements of proton form factors were reported in 1955 [220], followed by the first measurement of the neutron magnetic form factor in 1958 [221]. Half a century later, the precise determination of these quantities, and their interpretation within the framework of QCD, remains a defining challenge for hadronic physics research [222].

In particular, with ever-improving experimental measurements of the nucleon form factors revealing slight deviations from the phenomenological dipole form [223–226], it is of renewed importance to calculate precise QCD benchmarks for these functions. As the only first-principles approach which can quantitatively probe the nonperturbative domain of QCD, lattice simulation [227–241] can not only set these benchmarks, but it can give theoretical predictions of the hyperon form factors [235, 238–242] which are extremely challenging to measure and as a result are poorly determined, if at all.

Importantly, lattice studies also provide an *interpretation* of the experimental results for the baryon electromagnetic form factors in the context of QCD. For example, the simulations give general insight into the environmental sensitivity of the distribution of quarks inside a hadron [235, 242] by discriminating between different quark-flavour contributions to the form factors. The lattice method can also reveal the dependence of these quantities on quark mass [118, 243, 244] and allows a separation of quark-line–connected and disconnected terms, providing both a great deal of physical insight and valuable information for model-building [245].

In this chapter we present two sets of new dynamical $2+1$–flavour lattice QCD simulation results for the electric and magnetic form factors of the outer-ring octet baryons, at a range of discrete Q^2-values up to $1.3\,\mathrm{GeV}^2$. To interpret these simulations we develop a novel chiral extrapolation formalism—applied at each fixed value of Q^2—which is based on the principles of effective field theory. For the hyperons in particular, which have so far received limited attention in the literature [235, 238–242], our results represent the state-of-the-art in such simulations.

The hyperon form factors are of significant interest both in their own right and because they provide valuable insight into the environmental sensitivity of the distribution of quarks inside a hadron. For example, one may learn how the distribution of u quarks in the proton differs from that in the Σ^+, an effect caused by the mass difference of the spectator d and s quarks.

The last sections of this chapter are devoted to an exploration of our core themes, strangeness and CSV in the nucleon, in the context of the electromagnetic form factors. By combining our lattice simulation results with experimental input, we deduce values for the strange electromagnetic form factors of the proton which are consistent with available direct measurements of these quantities but span a far larger range of values of Q^2 [28, 246–248]. Our calculation of the strange magnetic moment, in particular, is an order of magnitude more precise than the closest experimental result. The dominant uncertainty in the experimental numbers for the strange proton form factors arises from the assumption of good charge symmetry which informs their extraction. By applying the methods for calculating CSV quantities which were developed in previous chapters, we present the first determination of CSV in the electromagnetic form factors of the nucleon based on lattice QCD. Our result, an order of magnitude smaller than model predictions, opens the door for more precise experimental measurements of the strange proton form factors using existing methods.

7.1 Dirac, Pauli and Sachs Form Factors

The electromagnetic form factors are formally defined in terms of the matrix element of the electromagnetic current density operator, j_μ, between baryon states. The standard decomposition of this matrix element into distinct Dirac structures, restricted by the requirement of covariance under the improper Lorentz group, charge conservation, and symmetry under spatial reflections, yields the Dirac and Pauli form factors $F_1(Q^2)$ and $F_2(Q^2)$ [249]:

$$\langle B(p',s')|j_\mu(q)|B(p,s)\rangle = \overline{u}(p',s')\left[\gamma_\mu F_1^B\big(Q^2\big) + \frac{i\sigma_{\mu\nu}q^\nu}{2M_B}F_2^B\big(Q^2\big)\right]u(p,s). \qquad (7.1)$$

Here $u(p,s)$ is a Dirac spinor with momentum p and spin polarisation s, $q = p' - p$ is the momentum transferred to the baryon, $Q^2 = -q^2$, and M_B is the mass of the baryon B. For a classical point particle, both form factors are independent of Q^2; deviations from this expectation thus give insight into the extended nature of the baryon as seen by an electromagnetic probe.

Throughout this chapter, we use an alternative standard basis for the form factors, namely linear combinations of F_1 and F_2 named the electric and magnetic

Sachs form factors:

$$G_E^B(Q^2) = F_1^B(Q^2) - \frac{Q^2}{4M_B^2} F_2^B(Q^2), \tag{7.2}$$

$$G_M^B(Q^2) = F_1^B(Q^2) + F_2^B(Q^2). \tag{7.3}$$

This choice is convenient for the interpretation of electron scattering experiments because the (unpolarised) cross section may be expressed as a linear combination of the squares of G_E and G_M, with no interference term. The Sachs form factors also have simple physical interpretations: in the Breit frame, where the scattered electron transfers momentum but no energy, and in the non-relativistic limit, the three-dimensional Fourier transform of $G_E^B(Q^2)$ describes the electric charge density distribution within the baryon B, while that of $G_M^B(Q^2)$ encodes the magnetic current density distribution. Electric and magnetic mean-square radii are defined based on this straightforward interpretation:

$$\langle r^2 \rangle_{E/M}^B = -\frac{6}{G_{E/M}^B(0)} \frac{d}{dQ^2} G_{E/M}^B(Q^2) \bigg|_{Q^2=0}. \tag{7.4}$$

At zero momentum transfer, the electric form factor $G_E^B(0)$ simply gives the charge of baryon B. Moreover, $G_M^B(0) = \big(G_E^B(0) + \kappa_B\big) = \mu_B$ defines the baryon magnetic moment, where $\kappa_B = F_2^B(0)$ is the anomalous magnetic moment. Should $G_{E/M}(0) = 0$, this normalising factor is omitted from Eq. (7.4).

7.2 Lattice QCD Simulation

In this section we describe our lattice setup and summarise the standard methods used to calculate the octet baryon electromagnetic form factors. Because of the limitations of computation time, the simulations presented here are performed not only at larger-than-physical pseudoscalar masses, but omit operator self-contractions (quark-line–disconnected diagrams) which require the notoriously noisy and expensive 'all-to-all' quark propagators to be calculated.

In later sections we develop and apply a formalism based on connected chiral perturbation theory [72, 250–252] to correct for finite-volume effects and to extrapolate each baryon form factor to the physical pseudoscalar masses. While the omission of disconnected terms restricts the explicit calculation of full-QCD results from our simulations to quantities for which the omitted contributions vanish (e.g., isovector observables, up to CSV effects), the comparison of experimental numbers with the chirally-extrapolated lattice results for connected-only observables gives insight into the significance of disconnected quark-loop contributions at the physical point. This is the method by which we access the strange electromagnetic form factors (Section 7.7); the technique is complementary to direct lattice studies of disconnected terms [28, 246–248].

	β	κ_0	κ_l	κ_s	m_π (MeV)	m_K (MeV)	$m_\pi L$
1	5.5	0.120900	0.120900	0.120900	465	465	5.6
2			0.121040	0.120620	360	505	4.3
3			0.121095	0.120512	310	520	3.7
4	5.5	0.120920	0.120920	0.120920	440	440	5.3
5	5.5	0.120950	0.120950	0.120950	400	400	4.8
6			0.121040	0.120770	330	435	4.0
7	5.8	0.122810	0.122810	0.122810	305	405	6.1
8			0.122880	0.122670	340	430	5.1
9			0.122940	0.122551	265	450	4.1
10	5.5	0.120900	0.121166	0.120371	220	540	4.0

Table 7.1: Details of the lattice simulation parameters. Simulations 1–6 constitute data set I, with $\beta = 5.5$ corresponding to $a = 0.074(2)$ fm and $L^3 \times T = 32^3 \times 64$. Simulations 7–9 constitute set II, with $L^3 \times T = 48^3 \times 96$ and $\beta = 5.8$ corresponding to $a = 0.062(2)$ fm. Simulation 10 stands alone and has the same lattice scale as set I (corresponding to $\beta = 5.5$), but a larger lattice volume: $L^3 \times T = 48^3 \times 96$. The parameter κ_0 denotes the value of $\kappa_l = \kappa_s$ at the SU(3)-symmetric point.

7.2.1 Simulation Parameters

We use gauge field configurations with $2 + 1$ flavours of nonperturbatively $\mathcal{O}(a)$-improved Wilson fermions. The clover action consists of the tree-level Symanzik improved gluon action (described in Section 2.2.1) together with a mild 'stout' smeared fermion action [253]. We generate two sets of simulations, on ensembles with lattice volumes $L^3 \times T = 32^3 \times 64$ and $48^3 \times 96$, with lattice scales $a = 0.074(2)$ fm and $0.062(2)$ fm (set using various singlet quantities [24, 253, 254]), respectively. Details are given in Table 7.1.

The data set generated on each ensemble consists of the individual (quark-line–connected) quark contributions to the electric and magnetic form factors of the outer-ring octet baryons: $G_{E/M}^{p,u}$, $G_{E/M}^{p,d}$, $G_{E/M}^{\Sigma,u}$, $G_{E/M}^{\Sigma,s}$, $G_{E/M}^{\Xi,s}$, and $G_{E/M}^{\Xi,u}$, at six (simulation set I) or seven (set II) discrete values of the momentum transfer. These are the lowest six or seven momentum-transfers accessible on our particular lattices, where the simulations are performed with zero sink momentum. The three-momenta $\vec{q}^2$ are given by

$$\vec{q}^2 = \left(n_x^2 + n_y^2 + n_z^2\right) \times \left(\frac{2\pi}{La}\right)^2, \tag{7.5}$$

where $n_{x,y,z}$ are integers, L is the (dimensionless) spatial extent of the lattice (so $-L/2 < n_{x,y,z} \leq L/2$), and a is the lattice spacing. The values of the four-

momentum transfer q^2 vary with baryon mass M_B by the dispersion relation

$$q^2 = \left(\sqrt{M_B^2 + \vec{q}^{\,2}} - M_B\right)^2 - \vec{q}^{\,2}, \tag{7.6}$$

since the sink momentum is held fixed at 0. The values of q^2 for our simulations are shown graphically in Fig. 7.1.

A particular feature of the gauge configurations used here is that the primary simulation trajectory in quark-mass space, illustrated in Fig. 7.2, follows a line of constant singlet mass: $m_q = (m_u + m_d + m_s)/3 = (2m_l + m_s)/3$. This is achieved by first finding the SU(3)-flavour–symmetric point where flavour-singlet quantities take their physical values, then varying the individual quark masses about that point [24,253]. It is clear from Fig. 7.2 that this primary trajectory at $\kappa_0 = 0.120900$ (where the parameter κ_0 denotes the value of $\kappa_l = \kappa_s$ at the SU(3)-symmetric point) does not quite match the physical singlet-mass line [24]. Extrapolation to the physical point thus requires a shift not only along the simulation trajectory, but in a direction perpendicular to it. To constrain the quark-mass dependence in this perpendicular direction we include additional lattice simulations at several singlet masses (i.e., values of κ_0). These are listed as simulations 4–6 in Table 7.1 and are shown in Fig. 7.2.

In addition to our two primary simulation sets, we have a single ensemble at the same lattice scale as simulation set I ($\beta = 5.5$ corresponding to $a = 0.072(2)\,\mathrm{fm}$) but on a larger lattice volume, $L^3 \times T = 48^3 \times 96$, and at a pion mass of 220 MeV, about 100 MeV lighter than the lightest ensemble of data set I. Comparison of chirally-extrapolated set I (smaller volume) results with this additional point provides a test that both finite-volume effects and the extrapolation are under control. Raw lattice results for all simulations are tabulated in Appendix I.

7.2.2 Lattice Method

On the lattice, the Dirac and Pauli form factors $F_1(Q^2)$ and $F_2(Q^2)$ are obtained from the standard decomposition of the matrix element of the electromagnetic current j_μ between baryon states (see Eq. (7.1)). This quantity, $\langle B(p',s')|j_\mu(q)|B(p,s)\rangle$, is calculated in the usual way from the ratio of three-point and two-point correlation functions:

$$R(t,\tau;\vec{p}\,',\vec{p}\,) = \frac{C_{3\mathrm{pt}}(t,\tau;\vec{p}\,',\vec{p}\,)}{C_{2\mathrm{pt}}(t,\vec{p}\,')}\left[\frac{C_{2\mathrm{pt}}(\tau,\vec{p}\,')C_{2\mathrm{pt}}(\tau,\vec{p}\,')C_{2\mathrm{pt}}(t-\tau,\vec{p}\,)}{C_{2\mathrm{pt}}(\tau,\vec{p}\,)C_{2\mathrm{pt}}(t,\vec{p}\,)C_{2\mathrm{pt}}(t-\tau,\vec{p}\,')}\right]^{\frac{1}{2}},$$

where t denotes the Euclidean-time position of the sink and τ the operator insertion time. In order to ensure that excited-state contributions to the correlation functions are suppressed, we employ quark smearing at the source and sink and use a generous source-sink separation of 1–1.15 fm [237].

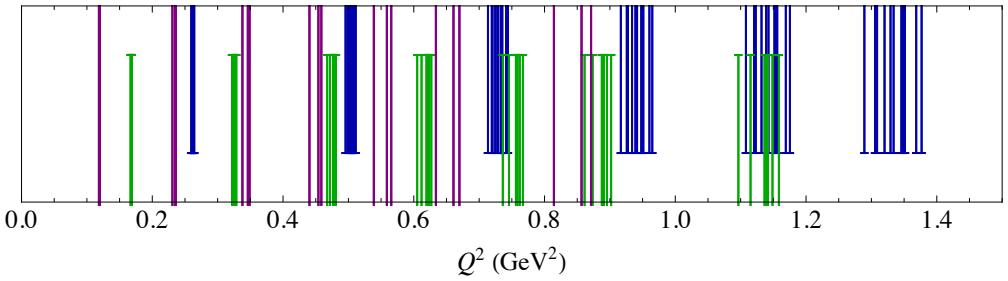

Figure 7.1: Distribution of four-momenta $Q^2 = -q^2$ for lattice simulation sets I (blue), II (green), and simulation 10 (purple) (see Table 7.1). The values of Q^2 corresponding to each fixed three-momentum vary slightly because of the different baryon masses feeding into the dispersion relation (Eq. (7.6)).

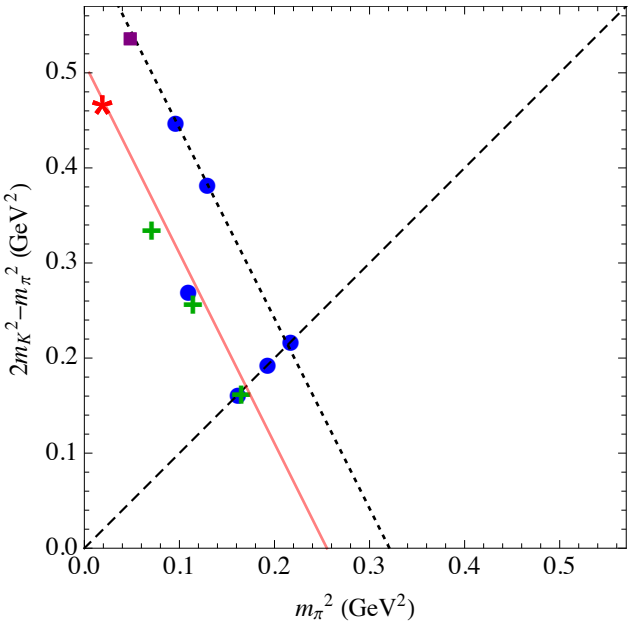

Figure 7.2: Locations of the lattice ensembles in the m_l–m_s plane. Blue circles and green crosses correspond to simulation sets I and II, respectively, while the purple square shows the location of simulation 10 (see Table 7.1). The red star denotes the physical point and the dashes indicate the flavour-symmetric line where $m_l = m_s$. Our primary simulation trajectory, illustrated by the dotted line, corresponds to the line of constant singlet quark mass, $(2m_K^2 + m_\pi^2)$, at $\kappa_0 = 0.120900$ (simulations 1–3 in Table 7.1). The solid red line indicates the physical value of the singlet mass.

The two-point and three-point functions are given, as in Ref. [237], by

$$C_{\text{2pt}}(\tau, \vec{p}) = \text{Tr}\left[\frac{1}{2}(1+\gamma_4)\langle B(\tau,\vec{p})\overline{B}(0,\vec{p})\rangle\right], \tag{7.7a}$$

$$C_{\text{3pt}}(t,\tau,\vec{p}\,',\vec{p},\mathcal{O}) = \text{Tr}\big[\Gamma\langle B(t,\vec{p}\,')\mathcal{O}(\vec{q},\tau)\overline{B}(0,\vec{p})\rangle\big], \tag{7.7b}$$

where 'Tr' denotes a trace in spinor space and the local vector current $\mathcal{O}$ is

$$\mathcal{O}_\mu(\vec{q},\tau) = \sum_{\vec{x}} e^{i\vec{q}\cdot\vec{x}}\,\overline{q}(\vec{x},\tau)\,\gamma_\mu\,q(\vec{x},\tau). \tag{7.8}$$

Here $q(\vec{x},\tau)$ is a quark field and $\vec{q}$ is the three-momentum transfer. The Dirac operator Γ represents a polarisation projection. For example, we use

$$\Gamma_{\text{unpol.}} = \frac{1}{2}(1+\gamma_4), \tag{7.9a}$$

$$\Gamma_3 = \frac{1}{2}(1+\gamma_4)i\gamma_5\gamma_3, \tag{7.9b}$$

for an unpolarised baryon or one polarised in the z-direction, respectively. As the current $\mathcal{O}$ is not strictly conserved at finite lattice spacings, we enforce charge conservation by using $2/F_1^{p,u}(0)$ as a multiplicative renormalisation on each ensemble (as explained later, the quark-level form factors are defined for quarks of unit charge). The values of these constants are approximately 0.86 and 0.88 for simulation ensembles with $\beta = 5.5$ and $\beta = 5.8$, respectively. Disconnected quark-line contributions to the three-point function of Eq. (7.7b) are neglected in these simulations. The effect of this omission will be discussed further in the following sections. As detailed in the previous section, simulations are performed with zero sink momentum and six or seven different values of the momentum transfer $\vec{q} = \vec{p}\,' - \vec{p}$ for each ensemble, corresponding to Q^2 values up to approximately $1.3\,\text{GeV}^2$.

7.2.3 Lattice Results for F_1 and F_2

Although the primary goal of this work is to determine the values of the electric and magnetic Sachs form factors at the physical quark masses, with details of the chiral and infinite-volume extrapolation presented in the following sections, we display here a sample typical of the raw lattice simulation results for F_1 and F_2. Numerical results are tabulated in their entirety in Appendix I. We also give the results of a naive extraction of the Dirac and Pauli mean-squared radii and the anomalous magnetic moment, based on dipole-like fit forms.

The raw lattice simulation results for the Dirac and Pauli form factors at the lightest simulation pion mass from data set I, $(m_\pi, m_K) = (310, 520)$ MeV, are shown in Figs. 7.3 and 7.4. The figures have been organised as doubly and singly-represented quark contributions. This grouping shows most clearly the environmental sensitivity of the quark contributions to the form factors; for example, any difference between the u-quark contributions to the proton and sigma baryon factors

must arise from the different masses of the spectator (d and s) quarks. For F_1 this sensitivity increases with Q^2. The apparent sensitivity of F_2 is largely the result of the baryon-dependence of the natural magneton units. The fits shown use the 2-parameter ansätze:

$$F_1(Q^2) = \frac{F_1(0)}{1 + c_{12}Q^2 + c_{14}Q^4}, \tag{7.10a}$$

$$F_2(Q^2) = \frac{F_2(0)}{(1 + c_{22}Q^2)^2}, \tag{7.10b}$$

where the c_{ij} and the anomalous magnetic moment $F_2^{B,q}(0) = \kappa^{B,q}$ are fit parameters, while $F_1(0)$ is fixed by charge conservation. As we consider quarks of unit charge, $F_1(0) = 2, 1$ for the doubly and singly-represented quarks, respectively. Clearly, the functional forms chosen provide excellent fits to the lattice simulation results; the particular pion-kaon mass point selected for display is typical of the entire data set.

Mean-squared radii are extracted from the Q^2-derivatives of the fit ansätze by

$$\langle r^2 \rangle_i = -\frac{6}{F_i(0)} \frac{d}{dQ^2} F_i(Q^2) \bigg|_{Q^2=0}. \tag{7.11}$$

The isovector radii for the nucleon are shown in Fig. 7.5. These results are in line with those based on other recent $2 + 1$ and $2 + 1 + 1$–flavour lattice simulations [236, 255–258]. We note that the results displayed from other collaborations were determined from simulations performed at a range of values of m_K. Moreover, although most were extracted using dipole or dipole-like forms to parameterise the Q^2-dependence, some include a systematic uncertainty arising from that choice while others do not. This partially accounts for the large variation in the quoted errors. Tables of results for all $\langle r^2 \rangle_{1,2}^{B,q}$ and $\kappa^{B,q}$ extracted from our fits are given in Appendix I.

7.3 Connected Chiral Perturbation Theory

The lattice simulations considered here, although fully dynamical, include only contributions from 'connected' insertions of the current operator. For this reason we extrapolate the simulation results from unphysically large pseudoscalar meson masses to the physical point using a formalism based on 'connected chiral perturbation theory' [250–252]. This is a special case of partially-quenched chiral perturbation theory [252, 259–265].

Partially-quenched lattice simulations traditionally employ different values for the sea and valence quark masses. As a result the distinguishing feature of the partially-quenched perturbation theory formalism, developed to extrapolate such simulations, is that it allows one to treat the sea and valence quarks separately. This is precisely what is needed to extrapolate connected lattice results; the 'quenching' effect is that the charges of the sea quarks are set to zero, removing the dis-

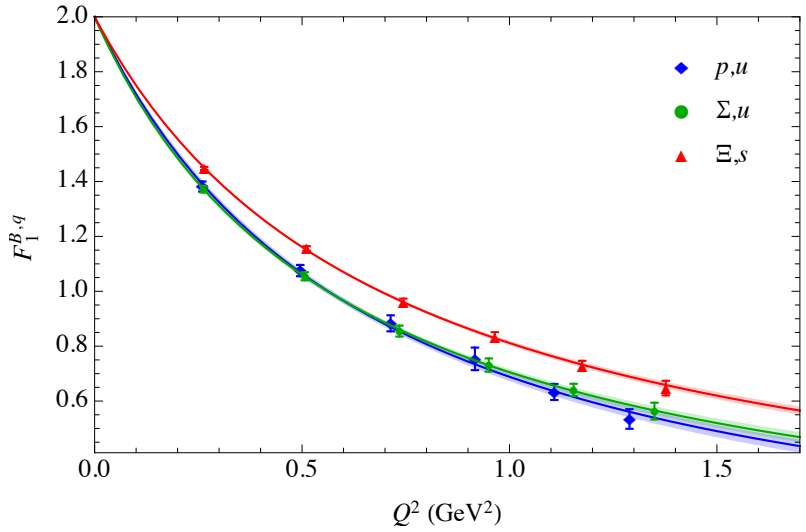

(a) Doubly-represented quark contributions.

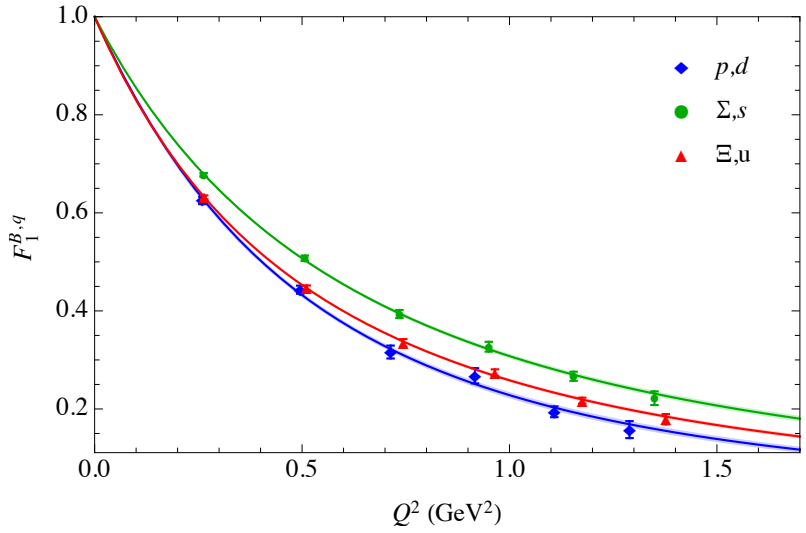

(b) Singly-represented quark contributions.

Figure 7.3: Quark contributions to the Dirac form factor F_1 of the octet baryons at the lightest pion mass from simulation set I, $(m_\pi, m_K) = (310, 520)\,\text{MeV}$. The charges of the relevant quarks have been set to one. The lines show dipole-like fits using Eq. (7.10a).

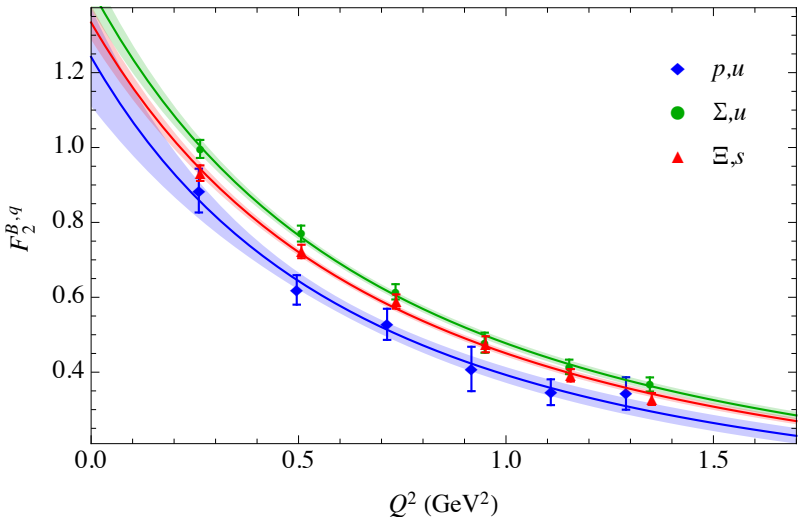

(a) Doubly-represented quark contributions.

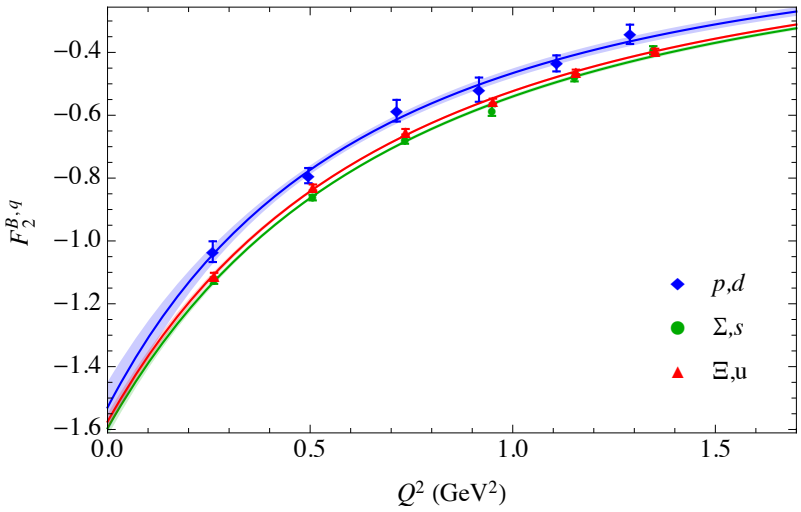

(b) Singly-represented quark contributions.

Figure 7.4: Quark contributions to the Pauli form factor F_2 of the octet baryons at the lightest pion mass from simulation set I, $(m_\pi, m_K) = (310, 520)\,\text{MeV}$. The charges of the relevant quarks have been set to one. The lines show dipole fits using Eq. (7.10b).

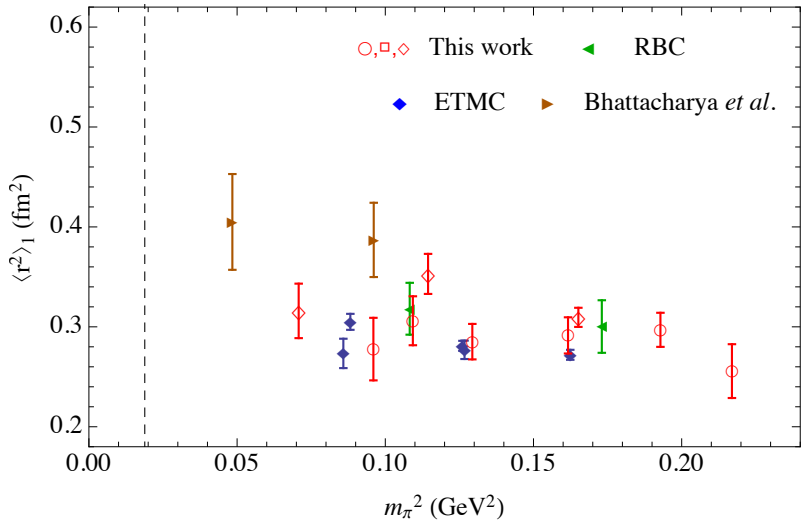

(a) Isovector Dirac radius of the nucleon.

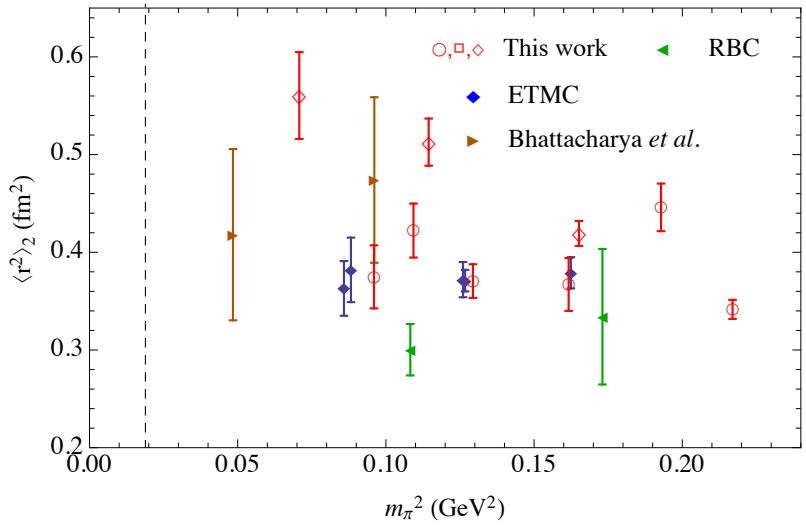

(b) Isovector Pauli radius of the nucleon.

Figure 7.5: Dirac and Pauli radii for the nucleon from recent $2+1$ and $2+1+1$–flavour lattice simulations [236, 255–258], compared with the results of this work. Empty circles, diamonds and squares denote our simulation sets I, II, and the stand-alone ensemble 10 (see Table 7.1), respectively. Note that the results displayed were generated from simulations performed using a range of values of m_K.

connected diagrams which are omitted from the lattice simulations. Here we use the heavy-baryon chiral perturbation theory expansion pioneered by Jenkins and Manohar [56, 266–269] which has been applied throughout this body of work. This section summarises our adaptation of this formalism and presents the resulting chiral extrapolation expressions for the Sachs form factors of the octet baryons.

7.3.1 Partially-Quenched Chiral Perturbation Theory

Details of partially-quenched chiral perturbation theory may be found in Refs. [252, 259–265]. Here we outline the special case of this formalism termed connected chiral perturbation theory [250].

Partially-quenched QCD includes nine quarks, which appear in the fundamental representation of the graded symmetry group SU(6|3):

$$\psi^T = \left(u, d, s, j, l, r, \tilde{u}, \tilde{d}, \tilde{s}\right). \tag{7.12}$$

In addition to the three usual light quarks (u, d, s), there are three light fermionic sea quarks (j, l, r) and three spin-$\frac{1}{2}$ bosonic ghost quarks $\left(\tilde{u}, \tilde{d}, \tilde{s}\right)$. When the ghost quarks are made pairwise mass and charge-degenerate with (u, d, s), their bosonic statistics ensure that closed q and $\tilde{q}$ quark-loop contributions cancel and hence such loops do not contribute to observables. Thus, if only (u, d, s) are used in hadronic interpolating fields, these quarks truly represent valence quarks, while (j, l, r) appear only in disconnected loops and are therefore interpreted as sea quarks.

For our application, the sea and ghost quarks are mass-degenerate with their corresponding valence partners. The quark-mass matrix is thus

$$M_\psi = \mathrm{diag}(m_u, m_d, m_s, m_u, m_d, m_s, m_u, m_d, m_s). \tag{7.13}$$

As we wish to exclude all diagrams with closed quark-loops from contributing to hadronic observables, we set the sea quark charges to zero. As the ghost quarks $\left(\tilde{u}, \tilde{d}, \tilde{s}\right)$ must have the same charges, pairwise, as (u, d, s), the general form of the quark-charge matrix is

$$Q = \mathrm{diag}(q_u, q_d, q_s, 0, 0, 0, q_u, q_d, q_s). \tag{7.14}$$

Individual quark contributions may be extracted by setting all but one charge to zero, for example by taking $q_u \to 1$, $q_d \to 0$, $q_s \to 0$ to isolate the u-quark contribution. Of course, reinstating the sea quark charges[1] yields a formalism which reproduces full chiral perturbation theory exactly [262].

The dynamics of the 80 pseudo-Goldstone mesons (both bosonic and fermionic) which emerge from the spontaneous breaking of the symmetry group:

$$\mathrm{SU}(6|3)_L \otimes \mathrm{SU}(6|3)_R \otimes \mathrm{U}(1)_V \to \mathrm{SU}(6|3)_V \otimes \mathrm{U}(1)_V \tag{7.15}$$

[1] This can be achieved by setting $Q \to \mathrm{diag}(q_u, q_d, q_s, q_u, q_d, q_s, q_u, q_d, q_s)$.

are described at lowest order by the Lagrangian

$$\mathcal{L} = \frac{f_\pi^2}{4}\,\mathrm{Str}\big(D^\mu\Sigma^\dagger D_\mu\Sigma\big) + \lambda\,\mathrm{Str}\,M_\psi\big(\Sigma+\Sigma^\dagger\big), \tag{7.16}$$

where

$$\Phi = \begin{pmatrix} \phi & \chi^\dagger \\ \chi & \widetilde{\phi} \end{pmatrix}, \quad \Sigma = \xi^2 = \exp\!\left(\frac{2i\Phi}{f_\pi}\right). \tag{7.17}$$

This is entirely analogous to the standard leading-order Lagrangian which is given in Eq. (3.14). Here ϕ and $\widetilde{\phi}$ are matrices of pseudo-Goldstone bosons with the quantum numbers of $q\overline{q}$ and $\tilde{q}\overline{\tilde{q}}$ pairs respectively, and χ contains pseudo-Goldstone fermions with the quantum numbers of $\tilde{q}\,\overline{q}$ pairs. With our conventions, Φ is normalised such that $\Phi_{12} = \pi^+/\sqrt{2}$. In this way, the upper 3×3 block of the matrix ϕ matches precisely the usual octet of pseudoscalar mesons. The standard naming of the mesons formed with sea and ghost quarks is made explicit in Ref. [263] (where the conventions for f_π and Φ differ from ours by a factor of $\sqrt{2}$). The symbol Str denotes the supertrace, and the gauge-covariant derivative is given by $D_\mu\Sigma = \partial_\mu\Sigma + ie\mathcal{A}_\mu[Q,\Sigma]$.

While the complete partially-quenched theory includes baryons composed of all types (and all mixtures of types) of quarks, for our application we need only predominantly valence states with at most one ghost or sea quark. These are constructed explicitly in Ref. [263]. In general terms, the baryon field B_{ijk} is constructed using an interpolating field

$$B^\gamma_{ijk} \sim \Big(\psi_i^{\alpha,a}\psi_j^{\beta,b}\psi_k^{\gamma,c} - \psi_i^{\alpha,a}\psi_j^{\gamma,c}\psi_k^{\beta,b}\Big)\epsilon_{abc}(C\gamma_5)_{\alpha\beta}. \tag{7.18}$$

The usual spin-$\frac{1}{2}$ baryon octet is embedded in B_{ijk}, for i,j,k restricted to 1–3, as

$$B_{ijk} = \frac{1}{\sqrt{6}}(\epsilon_{ijl}\mathbf{B}_{lk} + \epsilon_{ikl}\mathbf{B}_{lj}), \tag{7.19}$$

where $\mathbf{B}$ is the standard matrix of baryon fields introduced in Section 3.3.2 (see Eq. (3.25)). Similarly, the spin-$\frac{3}{2}$ decuplet baryons may be constructed as

$$T^{\alpha,\mu}_{ijk} \sim \Big(\psi_i^{\alpha,a}\psi_j^{\beta,b}\psi_k^{\gamma,c} + \psi_i^{\beta,b}\psi_j^{\gamma,c}\psi_k^{\alpha,a} + \psi_i^{\gamma,c}\psi_j^{\alpha,a}\psi_k^{\beta,b}\Big)\epsilon_{abc}(C\gamma^\mu)_{\beta,\gamma},$$

where, for i,j,k =1–3, T_{ijk} is simply the usual totally-symmetric tensor containing the decuplet of valence baryon resonances (see Eq. (3.32)).

The covariant derivative takes the same form for both the octet and decuplet baryons:

$$\begin{aligned}(D^\mu B)_{ijk} =& \partial^\mu B_{ijk} + (V^\mu)_{li}B_{ljk} \\ &+ (-1)^{\eta_i(\eta_j+\eta_m)}(V^\mu)_{jm}B_{imk} \\ &+ (-1)^{(\eta_i+\eta_j)(\eta_k+\eta_n)}(V^\mu)_{kn}B_{ijn}.\end{aligned} \tag{7.20}$$

Here the grading factor η_k tracks the statistics of the bosonic ghost quark sector:

$$\eta_k = \begin{cases} 1 & \text{for } k = 1\text{–}6 \\ 0 & \text{for } k = 7\text{–}9, \end{cases} \tag{7.21}$$

and the vector field V^μ is defined in analogy with that in QCD:

$$V^\mu = \frac{1}{2}\big(\xi\partial^\mu\xi^\dagger + \xi^\dagger\partial^\mu\xi\big). \tag{7.22}$$

The coupling of the 80 pseudo-Goldstone mesons to the baryons is described by

$$\begin{aligned}\mathcal{L} =& 2\alpha\big(\overline{B}S^\mu BA_\mu\big) + 2\beta\big(\overline{B}S^\mu A_\mu B\big) + 2\gamma\big(\overline{B}S^\mu B\big)\,\mathrm{Str}(A_\mu) + 2\mathcal{H}\big(\overline{T}^\nu S^\mu A_\mu T_\nu\big) \\ &+ \sqrt{\frac{3}{2}}\,\mathcal{C}\big[\big(\overline{T}^\nu A_\nu B\big) + \big(\overline{B}A_\nu T^\nu\big)\big] + 2\gamma'\big(\overline{T}^\nu S^\mu T_\nu\big)\,\mathrm{Str}(A_\mu),\end{aligned} \tag{7.23}$$

where, again in analogy with QCD,

$$A^\mu = \frac{i}{2}\big(\xi\partial^\mu\xi^\dagger - \xi^\dagger\partial^\mu\xi\big). \tag{7.24}$$

The brackets in Eq. (7.23) are a shorthand for field bilinear invariants, originally employed in Ref. [270], which are summarised in Appendix B, and S^μ is the covariant spin-vector. By matching to the usual QCD Lagrangian (Eq. (3.29)) for i, j, k restricted to 1–3, we make the identifications

$$\alpha = \frac{2}{3}D + 2F, \quad \beta = -\frac{5}{3}D + F, \tag{7.25}$$

while $\mathcal{C}$ and $\mathcal{H}$ map directly to their QCD values.

The heavy-baryon and off-diagonal meson propagators are the same as those which arise in the standard formalism; these are given in Eq. (3.40). For the mesons occupying the diagonal of Φ, however, the two-point functions deviate from the usual simple, single-pole form. As these mesons are by definition both flavour and charge-neutral, this subtlety can be avoided in the current context of the electromagnetic form factors; we leave the details to Ref. [263].

7.3.2 Electromagnetic Form Factors of the Octet Baryons

In the heavy-baryon formalism, the electromagnetic Sachs form factors G_E and G_M are defined by

$$\langle B(p')|j_\mu|B(p)\rangle = \overline{u}(p')\left[v_\mu G_E^B\big(Q^2\big) + \frac{i\epsilon_{\mu\nu\alpha\beta}v^\alpha S^\beta q^\nu}{M_N}G_M^B\big(Q^2\big)\right]u(p), \tag{7.26}$$

where, as before, $q = p' - p$ and $Q^2 = -q^2$. Here we take the magnetic form factor to be expressed in units of physical nuclear magnetons rather than the natural (baryon-

dependent) magnetons used in Eq. (7.1); this explains the presence of the nucleon mass M_N, rather than M_B, in this expression.

We focus in particular on developing chiral extrapolation formulae for the Sachs form factors at fixed, finite, values of Q^2. As our lattice simulations include results at values of Q^2 up to approximately $1.3\,\mathrm{GeV}^2$, it is not appropriate to our purposes to expand perturbatively in this momentum scale[2]. The following sections summarise our approach.

Magnetic Sachs Form Factor

In the familiar formulation of chiral perturbation theory, the magnetic moments of the octet baryons in the chiral limit are encoded in the coefficients of the 'magnetic Lagrangian density' [269]:

$$\mathcal{L}^M = \frac{e}{4M_N} F_{\mu\nu}\sigma^{\mu\nu}\big[\mu_\alpha\big(\overline{B}BQ\big) + \mu_\beta\big(\overline{B}QB\big) + \mu_\gamma\big(\overline{B}B\big)\,\mathrm{Str}(Q)\big]. \tag{7.27}$$

By comparison with the standard QCD Lagrangian (Eq. (3.29)), we make the identifications

$$\mu_\alpha = \frac{2}{3}\mu_D + 2\mu_F, \quad \mu_\beta = -\frac{5}{3}\mu_D + \mu_F. \tag{7.28}$$

The μ_γ term in Eq. (7.27) vanishes unless the quark charge matrix Q (Eq. (7.14)) is defined such that $\mathrm{Str}(Q) \neq 0$, for example when considering individual quark contributions to the form factors (e.g., setting $q_u \to 1$, $q_d \to 0$, $q_s \to 0$ to obtain the u-quark contribution). Terms describing the explicit symmetry-breaking at leading order in the quark masses are generated by

$$\begin{aligned}
\mathcal{L}^M_{\text{lin.}} = \mathcal{B}\frac{e}{2M_N}\Big[& c_1^M\big(\overline{B}M_\psi B\big)\,\mathrm{Str}(Q) + c_2^M\big(\overline{B}BM_\psi\big)\,\mathrm{Str}(Q) + c_3^M\big(\overline{B}QB\big)\,\mathrm{Str}(M_\psi) \\
& + c_4^M\big(\overline{B}BQ\big)\,\mathrm{Str}(M_\psi) + c_5^M\big(\overline{B}QM_\psi B\big) + c_6^M\big(\overline{B}BQM_\psi\big) \\
& + c_7^M\big(\overline{B}B\big)\,\mathrm{Str}(QM_\psi) + c_8^M\big(\overline{B}B\big)\,\mathrm{Str}(Q)\,\mathrm{Str}(M_\psi) \\
& + c_9^M(-1)^{\eta_l(\eta_j+\eta_m)}\Big(\overline{B}^{kji}(M_\psi)_i^l Q_j^m B_{lmk}\Big) \\
& + c_{10}^M(-1)^{\eta_j\eta_m+1}\Big(\overline{B}^{kji}(M_\psi)_i^m Q_j^l B_{lmk}\Big) \\
& + c_{11}^M(-1)^{\eta_l(\eta_j+\eta_m)}\Big(\overline{B}^{kji}Q_i^l(M_\psi)_j^m B_{lmk}\Big) \\
& + c_{12}^M(-1)^{\eta_j\eta_m+1}\Big(\overline{B}^{kji}Q_i^m(M_\psi)_j^l B_{lmk}\Big)\Big] F_{\mu\nu}\sigma^{\mu\nu},
\end{aligned} \tag{7.29}$$

where $\mathcal{B} = 4\lambda/f_\pi^2$ (see Eq. (7.16)). The one-loop diagrams displayed in Fig. 7.6 give rise to the leading chiral non-analyticities of the quark-mass expansion.

[2]For example, the proton electric form factor can be approximated by a dipole: $G_E^p(Q^2) \approx 1/\Big(1+\frac{Q^2}{0.71}\Big)^2$. This form has a pole at $Q^2 = -0.71\ \mathrm{GeV}^2$, which limits the radius of convergence of any expansion to $Q^2 = 0.71\,\mathrm{GeV}^2$.

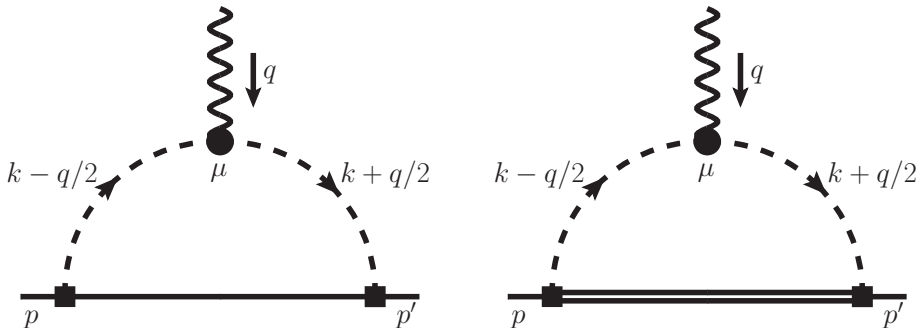

Figure 7.6: Loop diagrams which contribute to G_M at leading non-analytic order. Single, double, dashed, and wavy lines represent octet baryons, decuplet baryons, mesons, and photons, respectively.

For small values of the momentum transfer, the standard perturbative approach would be to generate extensions of Eqs. (7.27) and (7.29), with additional derivatives, to form a series expansion in Q^2. In the present work we are interested in the form factors over a much larger range of Q^2 than can be explored perturbatively. For this reason we consider independent chiral extrapolations at *fixed* values of Q^2. To do this, we take a model that maintains the SU(3) flavour structure of Eqs. (7.27) and (7.29). The parameters $\mu_{\alpha,\beta,\gamma}$ appearing in Eq. (7.27) are now interpreted as chiral-limit form factors at fixed Q^2; their numerical values may be different at each value of Q^2 considered [239, 271]. Similarly, the terms of Eq. (7.29) are associated with the symmetry-breaking at fixed Q^2. Given this interpretation, we can write down chiral extrapolation formulae which have independent sets of free coefficients at each value of Q^2. A particular advantage of this approach is that there is no need to impose a phenomenological constraint on the shape of the variation of the form factors with Q^2. Of course, a disadvantage is that the chiral extrapolation expressions which we generate must be fit to the lattice simulation results at each value of the momentum transfer independently.

The resulting expressions for the magnetic form factors as a function of quark mass—at some fixed finite value of Q^2—may be summarised as

$$G_M^{B,q}(Q^2) = \alpha^{Bq} + \sum_{q'} \overline{\alpha}^{Bq(q')} \mathcal{B}m_{q'} \tag{7.30}$$

$$+ \frac{M_N}{16\pi^3 f_\pi^2} \sum_{\phi} \Big(\beta_O^{Bq(\phi)} I_O^M(m_\phi, Q^2) + \beta_D^{Bq(\phi)} I_D^M(m_\phi, Q^2) \Big), \tag{7.31}$$

defined in units of physical nuclear magnetons μ_N. Here $\mathcal{B}m_q$ denotes the mass of the quark q, identified with the meson masses via the appropriate Gell-Mann–Oakes–Renner relation, e.g., $\mathcal{B}m_l = m_\pi^2/2$. The physical mass of the nucleon is given by M_N and ϕ stands for any of the 80 pseudo-Goldstone mesons of our theory. The contributions from Figs. 7.6(a) and 7.6(b) may be expressed in terms of the integrals

$$I_O^M = \int d\vec{k}\, \frac{k_y^2\, u(\vec{k}+\vec{q}/2)\, u(\vec{k}-\vec{q}/2)}{2\omega_+^2\omega_-^2}, \tag{7.32a}$$

$$I_D^M = \int d\vec{k}\, \frac{k_y^2\, (\omega_- + \omega_+ + \delta)\, u(\vec{k}+\vec{q}/2)\, u(\vec{k}-\vec{q}/2)}{2(\omega_+ + \delta)(\omega_- + \delta)\omega_+\omega_-(\omega_+ + \omega_-)}, \tag{7.32b}$$

where

$$\omega_\pm = \sqrt{(\vec{k} \pm \vec{q}/2)^2 + m^2}, \tag{7.33}$$

δ denotes the average octet-baryon–decuplet-baryon mass splitting, and $u(\vec{k})$ is the ultraviolet regulator used in the finite-range regularisation scheme (which is discussed in detail in Section 3.5). Just as was done in Chapter 6, we choose a dipole regulator, $u(k) = \left(\frac{\Lambda^2}{\Lambda^2+k^2}\right)^2$, with a regulator mass $\Lambda = 0.8 \pm 0.1\,\text{GeV}$. The dipole form is suggested by a comparison of the nucleon's axial and induced pseudoscalar form factors [78] and the choice of Λ is informed by a lattice analysis of nucleon magnetic moments [99]. Different regulator forms, for example monopole, Gaussian or sharp cutoff, yield fit parameters (and extrapolated results) which are consistent within the quoted uncertainties. The coefficients α^{Bq}, $\overline{\alpha}^{Bq(q')}$, $\beta_O^{Bq(\phi)}$, and $\beta_D^{Bq(\phi)}$ are given explicitly in terms of the chiral-limit form factors c_i^M and $\mu_{\alpha/\beta/\gamma}$ in Appendix F.

Electric Sachs Form Factor

The leading-order contribution to the electric form factor is generated by the following term in the Lagrangian:

$$\mathcal{L}^E = -ev^\mu(D^\nu F_{\mu\nu})\big[b_\alpha\big(\overline{B}BQ\big) + b_\beta\big(\overline{B}QB\big) + b_\gamma\big(\overline{B}B\big)\,\text{Str}(Q)\big]. \tag{7.34}$$

In analogy with the μ_γ term in Eq. (7.27) for the magnetic form factor, the b_γ term is relevant only when considering individual quark contributions to the electric form factor. In line with the notation used for the magnetic form factor (Eq. (7.28)), we define

$$b_\alpha = \frac{2}{3}b_D + 2b_F, \quad b_\beta = -\frac{5}{3}b_D + b_F. \tag{7.35}$$

Terms linear in the quark masses are generated by a Lagrangian piece, $\mathcal{L}^E_{\text{lin.}}$, which is identical to $\mathcal{L}^M_{\text{lin.}}$ (Eq. (7.29)) under the replacements

$$\frac{e}{4M_N}F_{\mu\nu}\sigma^{\mu\nu} \to v^\mu(D^\nu F_{\mu\nu}), \qquad c_i^M \to c_i^E. \tag{7.36}$$

The loop diagrams which contribute to G_E at leading order are those depicted in Fig. 7.6, as well as the tadpole diagram shown in Fig. 7.7 (which does not contribute to the magnetic form factors). Just as was done in the magnetic case, the coefficients

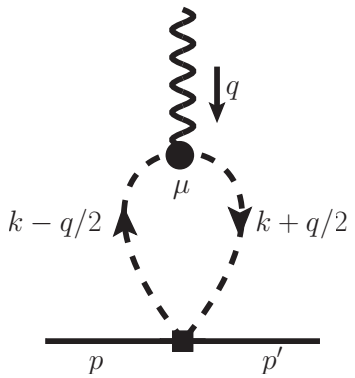

Figure 7.7: Tadpole loop diagram which contributes to G_E at leading order. Single, dashed, and wavy lines represent octet baryons, mesons, and photons, respectively.

in Eq. (7.34) are taken to be chiral-limit form factors at some fixed value of Q^2, with a similar interpretation for the c_i^E in $\mathcal{L}^E_{\text{lin.}}$ (see Eqs. (7.29) and (7.36)).

The leading-order loop contributions to G_E (Figs. 7.6 and 7.7) may be written in terms of the integrals

$$I_O^E = \int d\vec{k}\, \frac{(\vec{k}^2 - \vec{q}^{\,2}/4)\, u(\vec{k}+\vec{q}/2)\, u(\vec{k}-\vec{q}/2)}{\omega_+\omega_-(\omega_+ + \omega_-)}, \tag{7.37a}$$

$$I_D^E = \int d\vec{k}\, \frac{(\vec{k}^2 - \vec{q}^{\,2}/4)\, u(\vec{k}+\vec{q}/2)\, u(\vec{k}-\vec{q}/2)}{(\omega_+ + \delta)(\omega_- + \delta)(\omega_+ + \omega_-)}, \tag{7.37b}$$

$$I_T^E = \int d\vec{k}\, \frac{u(\vec{k}+\vec{q}/2)\, u(\vec{k}-\vec{q}/2)}{\omega_+ + \omega_-}, \tag{7.37c}$$

where $\omega_\pm$ is defined in Eq. (7.33). To prevent the baryon electric charges from being renormalised by contributions from the loop integrals we make the replacement

$$I(m,\vec{q}) \to \widetilde{I}(m,\vec{q}) = I(m,\vec{q}) - I(m,0) \tag{7.38}$$

for each of the integrals above.

Finally, the formulae for the chiral extrapolation of the electric form factors at some fixed, finite, value of Q^2 may be summarised as

$$\begin{aligned} G_E^{B,q}(Q^2) = {} & G_E^{B,q}(Q^2=0) + Q^2\alpha^{Bq} + Q^2 \sum_{q'} \overline{\alpha}^{Bq(q')} \mathcal{B}m_{q'} \\ & + \frac{1}{16\pi^3 f_\pi^2} \sum_\phi \Bigg(\frac{1}{2}\beta_O^{Bq(\phi)} \widetilde{I}_O^E(m_\phi, Q^2) - \beta_D^{Bq(\phi)} \widetilde{I}_D^E(m_\phi, Q^2) \\ & \qquad + \beta_T^{Bq(\phi)} \widetilde{I}_T^E(m_\phi, Q^2) \Bigg), \end{aligned} \tag{7.39}$$

where, again, $\mathcal{B}m_q$ is the mass of the quark q, identified with the meson masses through the appropriate Gell-Mann–Oakes–Renner relation. The term $G_E^{B,q}(Q^2=0)$

corresponds to the total charge of the quarks of flavour q in the baryon B. As these expressions apply to quarks of unit charge, $G_E^{B,q}(Q^2 = 0) = 2, 1$ for the doubly and singly-represented quarks, respectively.

The coefficients α^{Bq}, $\overline{\alpha}^{Bq(q')}$, $\beta_O^{Bq(\phi)}$, and $\beta_D^{Bq(\phi)}$ in Eq. (7.39) take the same form in terms of the undetermined chiral coefficients (e.g., $c_i^{E/M}$) as those named identically in the case of the magnetic form factor (under the replacements $\mu_F \to b_F$ and $\mu_D \to b_D$). These, as well as $\beta_T^{Bq(\phi)}$, are given explicitly in Appendix F. We point out that, while these parameters may have the same structure for the electric and magnetic form factors, the values of the undetermined chiral coefficients are different in each case.

7.4 Fits to Lattice Simulation Results

Here we describe the application of the chiral extrapolation formalism developed in the previous section to the lattice simulation results presented in Section 7.2. Before fitting the chiral expressions (Eqs. (7.30) and (7.39)) to the lattice results, we perform several corrections to the raw lattice data. First, we shift the raw numbers to correct for small finite-volume effects, estimated using the leading one-loop results of the chiral EFT (see Section 7.4.1). As the chiral extrapolation functions summarised in Section 7.3.2 are defined for fixed finite values of Q^2, we also analyse the lattice results in fixed-Q^2 bins; to facilitate this we interpolate the form factors to common points in Q^2.

For the magnetic form factors the entire analysis is performed in units of physical nuclear magnetons. This choice simplifies the extrapolation procedure as there is no need to consider a quark-mass dependent magneton, although an extrapolation using such units is possible and equivalent. The conversion from lattice natural magnetons to physical nuclear magnetons is performed on the simulation results at the bootstrap level.

7.4.1 Finite-Volume Corrections

As described in detail in Section 3.7, finite-volume corrections are performed using the difference between the infinite-volume integrals and corresponding finite-volume sums for the loop integrals which appear in the chiral expressions (Eqs. (7.30) and (7.39)). Because momentum is quantised on the lattice, the finite-volume sums must be calculated with the integrands in Eqs. (7.37) and (7.32) shifted from being symmetric (meson lines with momenta $k - q/2$ and $k + q/2$, as illustrated in Fig. 7.6) to what is more natural for the lattice, namely meson lines with momenta k and $k + q$.

The finite-volume corrections are small: for our smallest volume (data set I) they contribute approximately 2–4% of the nucleon magnetic form factor at the lowest value of Q^2 ($0.26\,\mathrm{GeV}^2$) and 0.03–0.06% at the largest ($1.35\,\mathrm{GeV}^2$), where the variation in each range is a result of the different pion and kaon mass points

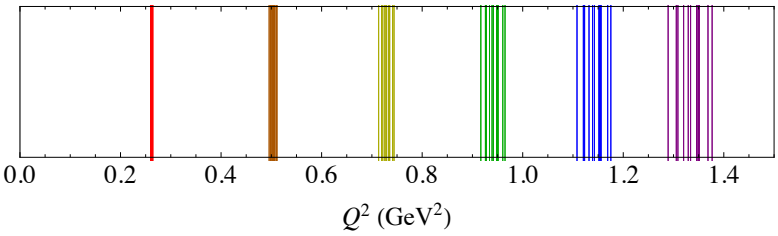

Figure 7.8: Four-momenta, Q^2, corresponding to the lattice simulation results in data set I. Colours indicate the Q^2-bin groupings; each bin corresponds to a single value of the three-momentum transfer in lattice units.

considered. For the electric form factor the corrections are in the range 1–2% at all values of Q^2. An artefact in this estimate is that the naive enforcement of charge-nonrenormalisation by Eq. (7.38) may lead to an overestimate of the corrections to the electric form factor at large values of the momentum transfer Q^2. While the higher-order diagrams (not included here) which would naturally prevent the renormalisation of charge would contribute progressively less at larger values of Q^2, the constant subtraction used here does not have that feature. As the finite-volume corrections are nevertheless small—neglecting them yields results for all relevant observables which are consistent within uncertainties with those presented here—this is not a significant effect.

7.4.2 Binning in Q^2

As the chiral extrapolation expressions used here (Eqs. (7.30) and (7.39)) are applicable for fixed finite values of the four-momentum transfer, we bin the lattice simulation results in Q^2 before performing independent fits to the data in each bin. The bin groupings are illustrated for data set I in Fig. 7.8; the binning (and fitting) procedure is performed separately for each data set. Each bin corresponds to a single value of the three-momentum transfer in lattice units. The corresponding physical values of Q^2 vary slightly because of the different baryon masses feeding into the dispersion relation (Eq. (7.6)). The largest variation is 1.29–1.37 GeV^2 for the bin with the highest value of Q^2.

To account for the small variation in Q^2 within each bin, all simulation results are shifted to the average Q^2-value of their respective bin. This shift is performed using a dipole-like fit to the (finite-volume–corrected) simulation results. The functional forms used for the magnetic and electric form factors are

$$G_M^{\text{fit}}(Q^2) = \frac{\mu}{1 + d_{M1}Q^2 + d_{M2}Q^4}, \tag{7.40a}$$

$$G_E^{\text{fit}}(Q^2) = \frac{G_E(Q^2 = 0)}{1 + d_{E1}Q^2 + d_{E2}Q^4}, \tag{7.40b}$$

where μ and $d_{E/M,i}$ are free parameters, and $G_E(Q^2 = 0) = 1, 2$ for the singly and doubly-represented quarks (of unit charge) respectively. These particular functional forms are chosen as they provide good fits to the lattice simulation results; as illustrated later, standard dipole forms perform poorly. Several examples of the fits are shown in Fig. 7.9.

After the fits have been performed, the raw lattice simulation results are shifted by $G^{\text{fit}}(Q^2_{\text{average}}) - G^{\text{fit}}(Q^2_{\text{simulation}})$. As these shifts are small, particularly at low values of Q^2 where the fit functions have larger slopes, there is no dependence, within uncertainties, on the functional form chosen for G^{fit}.

7.4.3 Fits

After the lattice simulation results have been finite-volume corrected and binned in Q^2 we perform an independent bootstrap-level fit, using Eqs. (7.30) and (7.39) for G_M and G_E, respectively, to the variation with m_π for the results in each Q^2-bin. An advantage of this approach [239, 271] is that it allows the fit parameters, which are the undetermined chiral coefficients, to vary with Q^2 without the need to impose some phenomenological expectation on the shape of their variation. The best values of the fit parameters are tabulated in Appendix J.1. The quality of fit is good, with the χ^2/d.o.f. in the range 0.5–1.4 for each bin. An illustration of the fit quality for data set I in representative bins, for both G_M and G_E, is given in Fig. 7.10. That figure shows the ratio of the fit function to the lattice simulation result for each data point; the 24 data points include 6 at each set of pseudoscalar masses where $m_\pi \neq m_K$ (i.e., $G_M^{p,u}$, $G_M^{p,d}$, $G_M^{\Sigma,u}$, $G_M^{\Sigma,s}$, $G_M^{\Xi,s}$, and $G_M^{\Xi,u}$) and 2 at each SU(3)-symmetric point. We recall that while each Q^2-set is treated as independent (as are G_E and G_M), the form factors for the different octet baryons are fit simultaneously.

Using these fits, the baryon Sachs form factors may be extrapolated to the physical pseudoscalar masses at each bin value of Q^2. For example, Fig. 7.11 shows results for the u-quark contribution to the proton form factors, plotted along a trajectory which holds the singlet pseudoscalar mass $(m_K^2 + m_\pi^2/2)$ fixed to its physical value. The results display the expected qualitative behaviour for the magnetic form factor; as Q^2 increases (moving down the figure), the extrapolation in m_π^2 decreases in curvature. This implies that the magnetic radius of the proton increases in magnitude as we approach the physical pion mass from above. Magnetic radii are discussed further in Section 7.5.3.

We note that any uncertainty in the value of the lattice scale, a, affects both the form factors themselves and the simulation values of Q^2 in physical units. At low Q^2 the shift in the form factors, and at high Q^2 the shift in Q^2 itself, is not negligible when varying $a = 0.074(2)$ fm or $a = 0.062(2)$ fm within the quoted uncertainties. Nevertheless, repeating the analysis presented in the following sections for a values at the extremities of the quoted ranges yields fits which are almost indistinguishable from those presented for the central value—essentially the points are shifted a short distance along lines interpolating the form factors in Q^2—and give entirely consistent

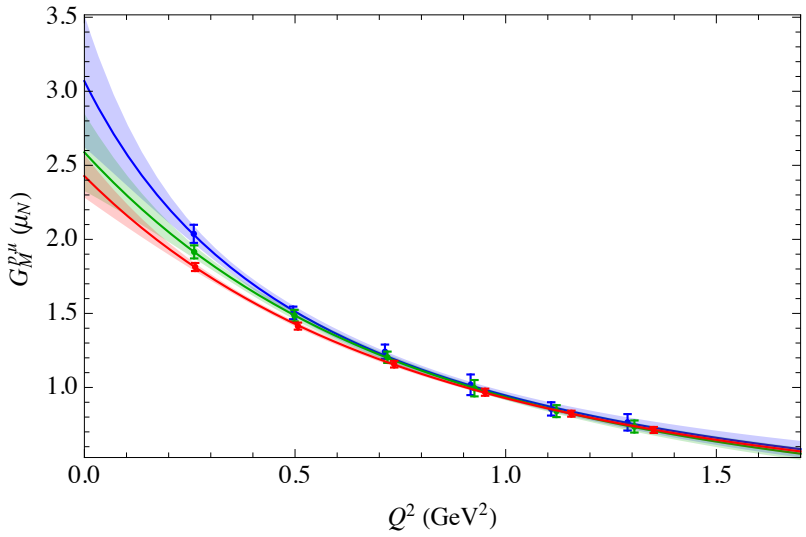

(a) Up-quark contribution to the proton magnetic form factor.

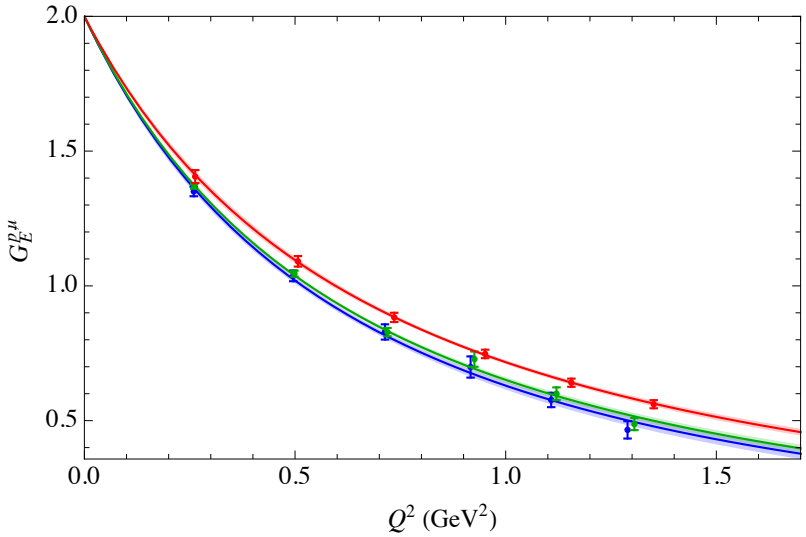

(b) Up-quark contribution to the proton electric form factor.

Figure 7.9: Generalised dipole fits (Eq. (7.40)) upon which the binning corrections are based. The three fits shown in each figure correspond to the three different pseudoscalar mass points along the primary simulation trajectory for simulation set I (red, green and blue points denote simulation ensembles 1, 2, and 3 in Table 7.1). Quarks have unit charge.

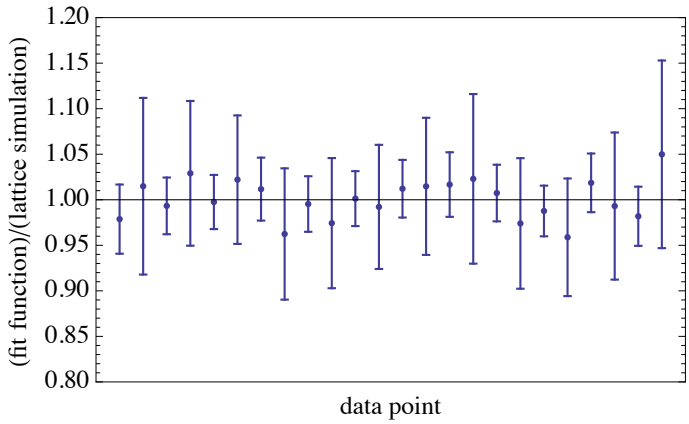

(a) G_M, $Q^2 \approx 0.26\,\mathrm{GeV}^2$.

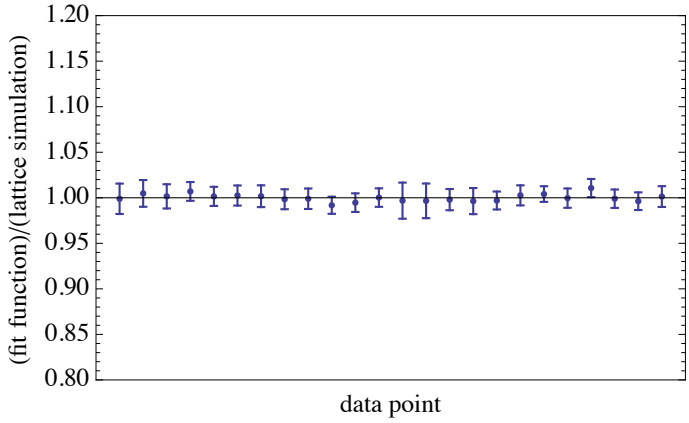

(b) G_E, lowest Q^2-bin: $Q^2 \approx 0.26\,\mathrm{GeV}^2$.

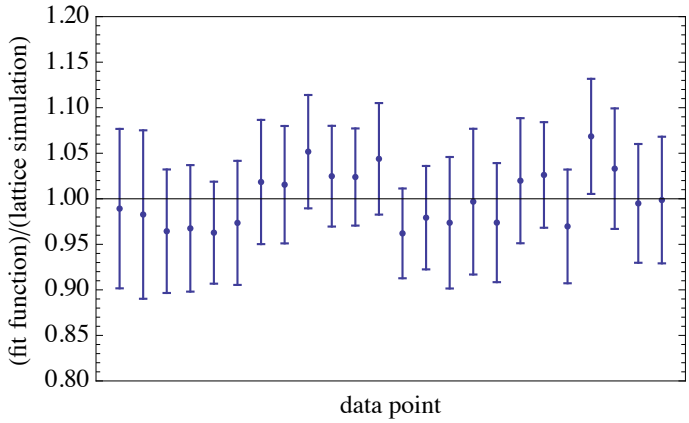

(c) G_E, highest Q^2-bin: $Q^2 \approx 1.35\,\mathrm{GeV}^2$.

Figure 7.10: Illustration of the quality of fit for data set I in representative Q^2-bins. Each point denotes one of the lattice simulation results e.g., $G_M^{p,u}$, $G_M^{p,d}$ ..., at one of the sets of pseudoscalar masses. For the electric form factor the comparison of Figs. 7.10(b) and 7.10(c) shows the expected increase in uncertainty as Q^2 increases (i.e., as one moves further from $Q^2 = 0$ where the value of G_E is fixed). Because of correlations between the lattice data points the χ^2/d.o.f. of the fit cannot be read trivially from these figures.

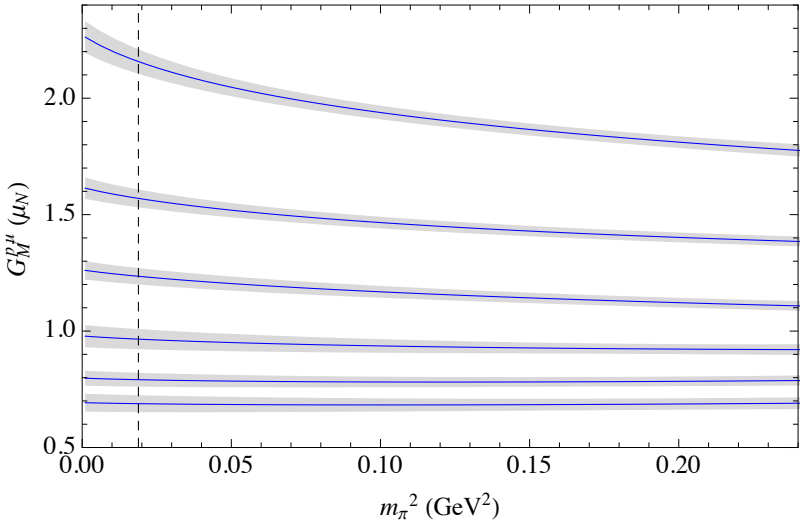

(a) Up-quark contribution to the proton magnetic form factor.

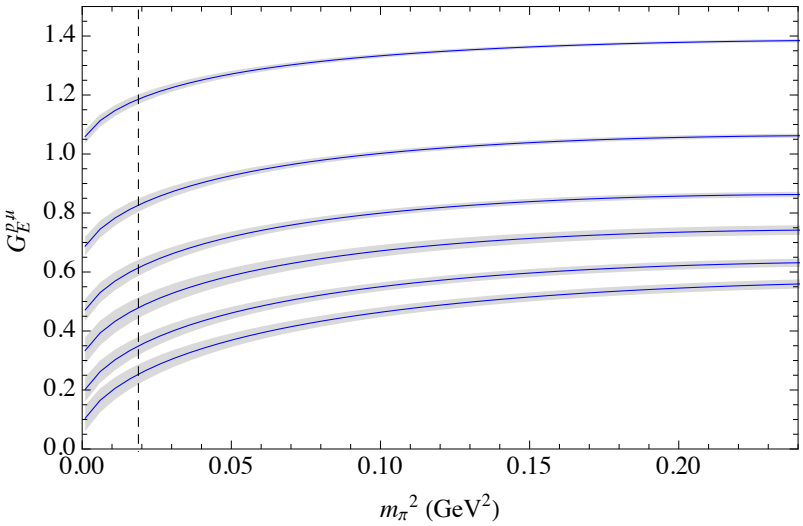

(b) Up-quark contribution to the proton electric form factor.

Figure 7.11: Up-quark (connected) contribution to the electromagnetic form factors of the proton for quarks with unit charge. Each line (top to bottom) shows the fit to data set I at a different (increasing) value of Q^2. The fits have been evaluated along the trajectory which holds the singlet pseudoscalar mass $(m_K^2 + m_\pi^2/2)$ fixed to its physical value.

results for each quantity, even when extrapolated to $Q^2 = 0$ using some functional form.

7.4.4 Test of Finite-Volume Effects

One limitation of the analysis presented in the previous sections is that it is difficult to quantify finite-volume effects beyond the corrections we perform based on chiral perturbation theory; all of the lattice simulations at a given value of the lattice scale were performed on a single volume. Simulation set I was performed at $\beta = 5.5$ corresponding to $a = 0.074(2)$ fm, on a $L^3 \times T = 32^3 \times 64$ volume. In physical units, this lattice has an extent of approximately 2.4 fm in the spatial direction. Simulation set II was performed at $\beta = 5.8$ corresponding to $a = 0.062(2)$ fm, on a larger $48^3 \times 96$ volume; this lattice has a spatial extent of approximately 3.0 fm in physical units. While comparing the results of these two simulation sets is a valuable consistency-check, any discrepancy between the two data sets cannot be conclusively categorised as a lattice-scale or finite-volume effect.

To facilitate an explicit check of the volume-dependence of our results, we have performed an additional simulation at the lattice scale of simulation set I, $\beta = 5.5$ corresponding to $a = 0.074(2)$ fm, on a larger $48^3 \times 96$ (3.6 fm) volume. This simulation is also performed at a lighter pion mass: $m_\pi = 220\,\mathrm{MeV}$. Details of this ensemble are given as simulation 10 in Table 7.1; raw lattice results for F_1 and F_2 are given in Appendix I.

As there is only one new simulation on the larger volume, and the discrete Q^2-values in physical units differ substantially between volumes, we do not include this new simulation into the chiral perturbation theory fits. Instead we compare the results of the fits to simulation set I, extrapolated *to the pseudoscalar masses of the new point* (with a pion mass about 100 MeV lighter than the lightest pion mass of set I), with the larger-volume results. We note that finite-volume corrections, as described in Section 7.4.1, have been applied to the new results.

Figures 7.12 and 7.13 show the excellent agreement between the chirally extrapolated small-volume results and the larger-volume results, in particular for the charged baryons. For the neutral-baryon electric form factors there is a systematic shift between the results on the two volumes, although we point out that the absolute magnitude of this shift is small—of order 5% of the proton form factor. This is comparable to the size of the discrepancies between the charged baryon form factors on the two volumes. The shift may be evidence of excited-state contamination in either set of results—which cannot be estimated quantitatively as only one value of the source-sink separation is used here—or the effect of some other yet-to-be-understood systematic. Nevertheless, the comparison is extremely encouraging and suggests that both the systematic finite-volume effect and the extrapolation in pion mass are well under control for the charged baryon form factors.

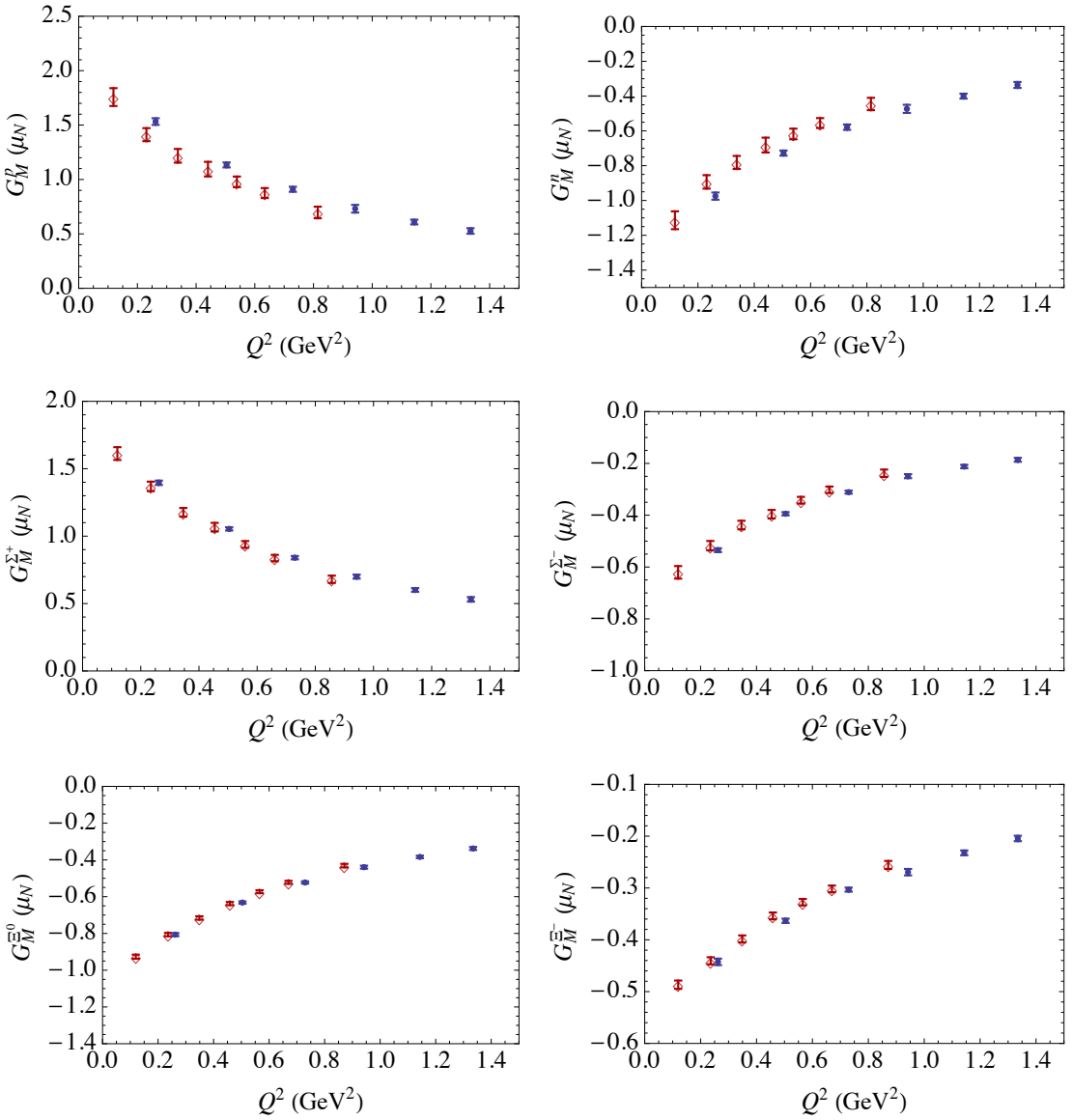

Figure 7.12: Connected part of the octet baryon magnetic form factors at the pseudoscalar masses of simulation 10 in Table 7.1, $(m_\pi, m_K) = (220, 540)$ MeV. Results calculated on ensemble 10 are represented by the empty red diamonds, while the solid blue circles denote the results of the chiral extrapolation of the set I ($32^3 \times 64$ volume) lattice simulation results to the same pseudoscalar meson masses. Finite-volume corrections, based on leading-order perturbation theory, have been applied to all results.

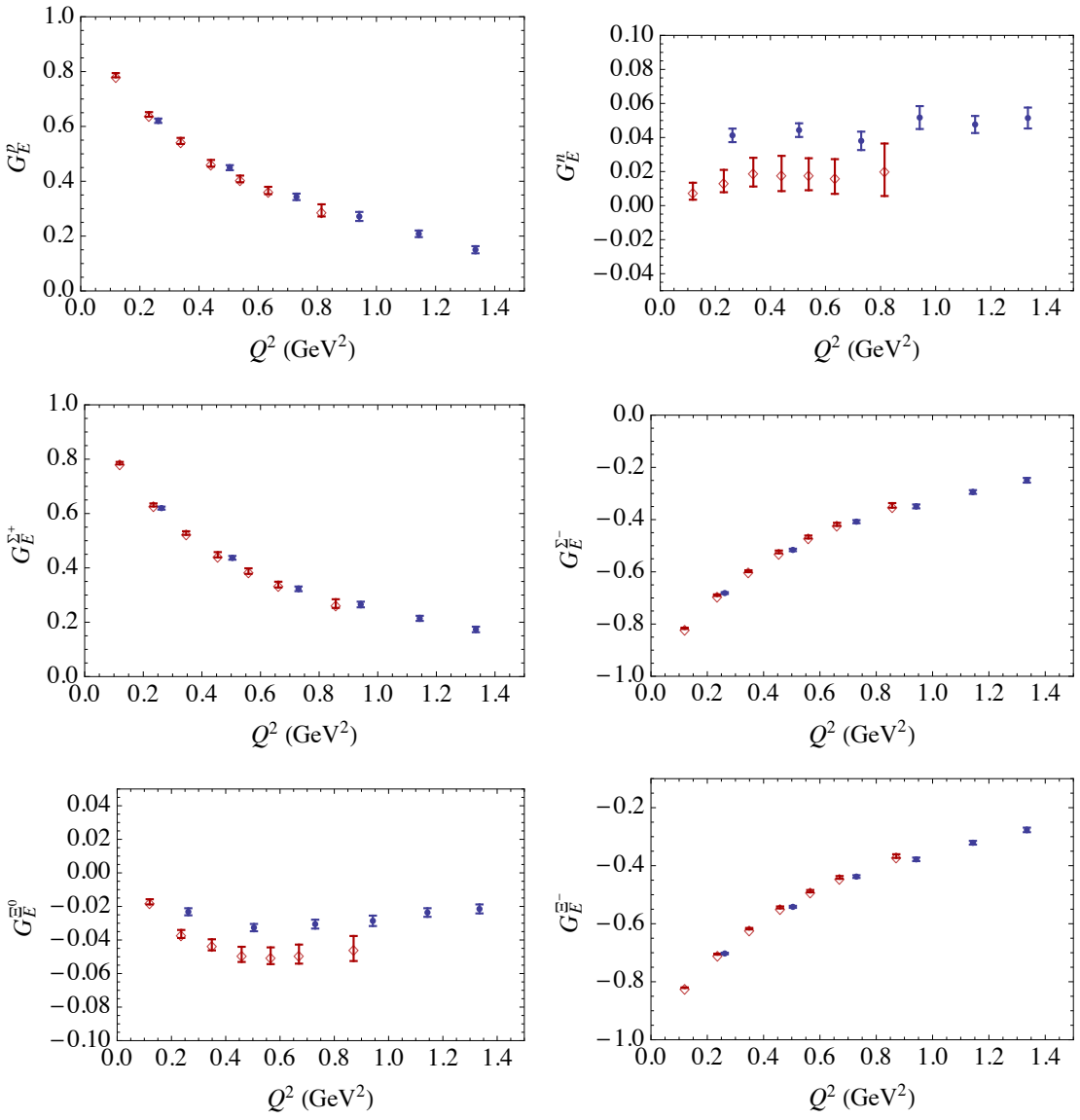

Figure 7.13: As in Fig. 7.12, for the electric Sachs form factors.

7.5 Electromagnetic Form Factors at the Physical Point

The following subsections present infinite-volume, chirally-extrapolated, results at the physical pseudoscalar masses for some electromagnetic form factor observables of interest. In particular, we focus on the isovector form factors which do not suffer from corrections associated with the omitted disconnected quark-loops (Section 7.5.1), as well as connected quantities such as the octet baryon magnetic moments (Section 7.5.2) and magnetic and electric radii (Section 7.5.3). An investigation of the individual quark contributions to the form factors gives insight into the environmental sensitivity of the distribution of quarks inside a baryon (Section 7.5.4). We also apply the methods developed in previous chapters to isolate the charge symmetry violating form factors (Section 7.6), which are essential inputs to experimental measurements of the strange form factors of the nucleon (Section 7.7).

7.5.1 Isovector Quantities

Isovector combinations of observables are of particular interest in this study as they can be determined from the connected-only lattice results with the smallest systematic uncertainty. Because disconnected quark-loop terms cancel in isovector combinations, the extrapolated results may be directly compared with experimental numbers.

The agreement between the extrapolated isovector nucleon form factors and experimental determinations of these quantities is impressive. Figure 7.14 displays our numbers, for both data sets I and II, compared against the Kelly [272] parameterisation of experimental results. The consistency between the two determinations, for both G_E and G_M, is remarkable across the entire range of Q^2-values considered. We do note, however, that the uncertainties shown for the Kelly parameterisation may be overestimated as we were unable to take into account the effect of correlations between the fit parameters. It is notable that a dipole form does not provide a good description of the extrapolated results for the isovector electric form factor over the full range of simulation Q^2-values: the χ^2/d.o.f. > 3 for each dipole fit (to data sets I or II). As G_M is described acceptably by a dipole form in Q^2, this suggests qualitatively that $G_E/G_M \neq$ constant. This is discussed further in Section 7.5.5.

The isovector combinations of sigma and cascade baryon form factors are shown in Figs. 7.15 and 7.16. There is complete consistency, within uncertainties, between the extrapolated results based on data sets I and II. As no experimental numbers are available for the hyperon form factors away from $Q^2 = 0$, dipole-like fits (Eq. (7.40)) to the extrapolated simulation results, as well as the experimental isovector baryon magnetic moments, are shown. We find fair agreement with the experimentally-measured baryon magnetic moments, even with simple phenomenological fits parameterising the Q^2-dependence of the form factors. It is clear, however, that the point at a lower value of Q^2 which is included in data set II acts to increase the

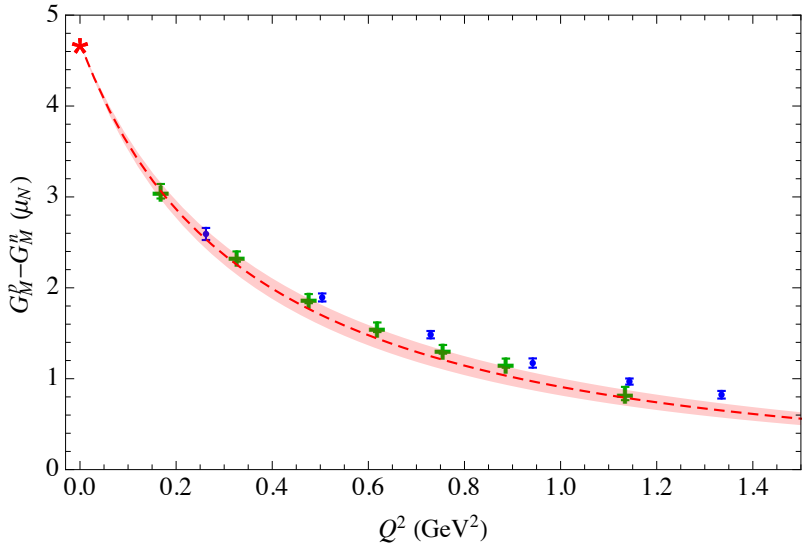

(a) Isovector nucleon magnetic form factor.

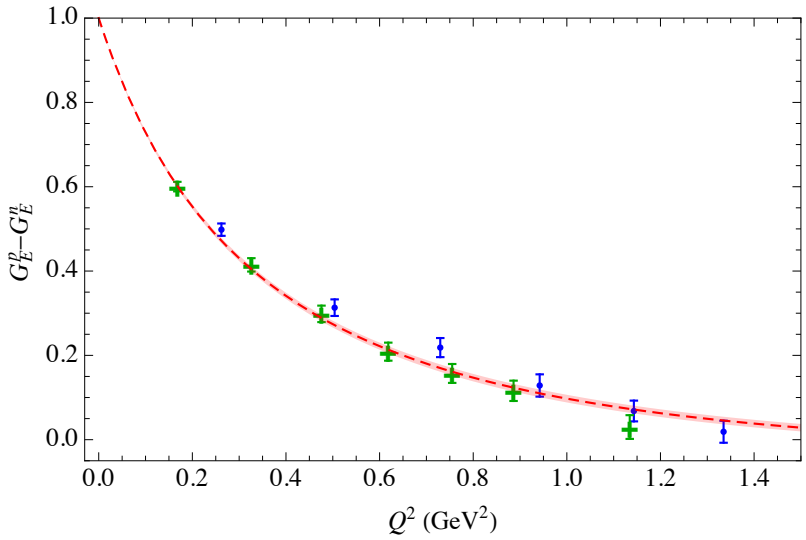

(b) Isovector nucleon electric form factor.

Figure 7.14: Isovector nucleon form factors extrapolated (at fixed Q^2-values) to infinite volume and the physical pseudoscalar masses. The dashed red band shows the Kelly parameterisation [272] of experimental results. The blue circles and green crosses denote results derived from simulation sets I ($a = 0.074(2)$ fm) and II ($a = 0.062(2)$ fm), respectively.

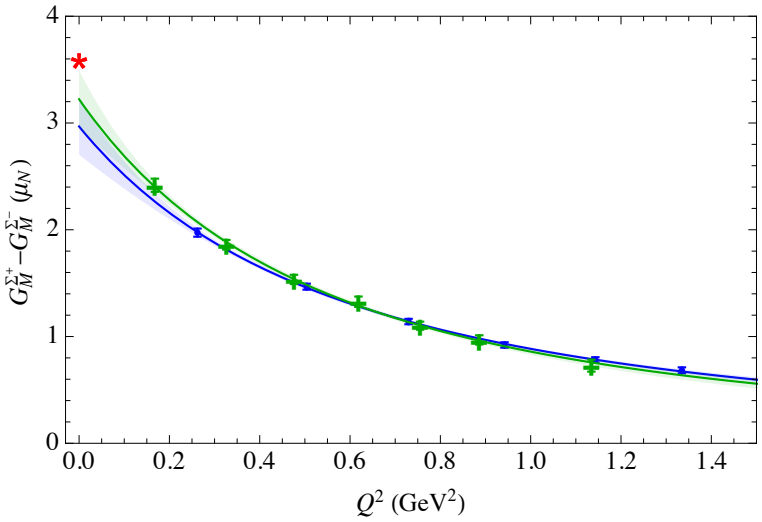

(a) Isovector sigma baryon magnetic form factor.

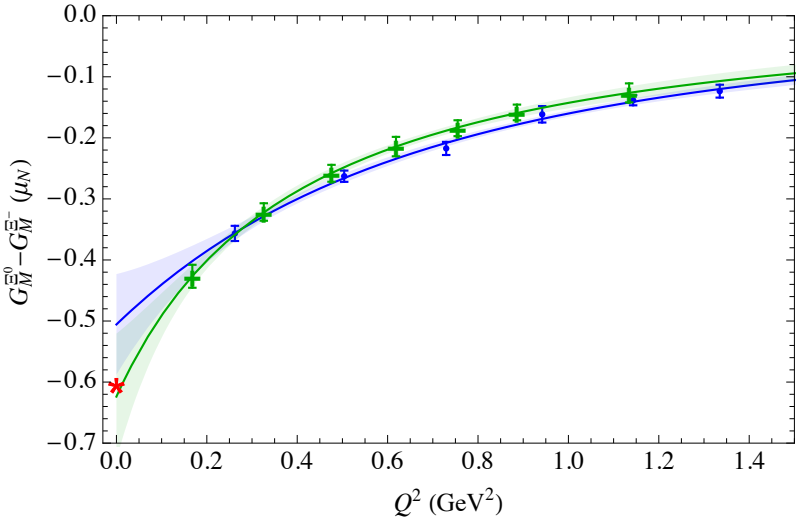

(b) Isovector cascade baryon magnetic form factor.

Figure 7.15: Isovector hyperon magnetic form factors extrapolated (at fixed Q^2-values) to infinite volume and the physical pseudoscalar masses. The bands show dipole-like fits in Q^2 using Eq. (7.40). The blue circles and green crosses denote results based on simulation sets I and II, respectively. The red stars indicate the experimental values of the isovector magnetic moments.

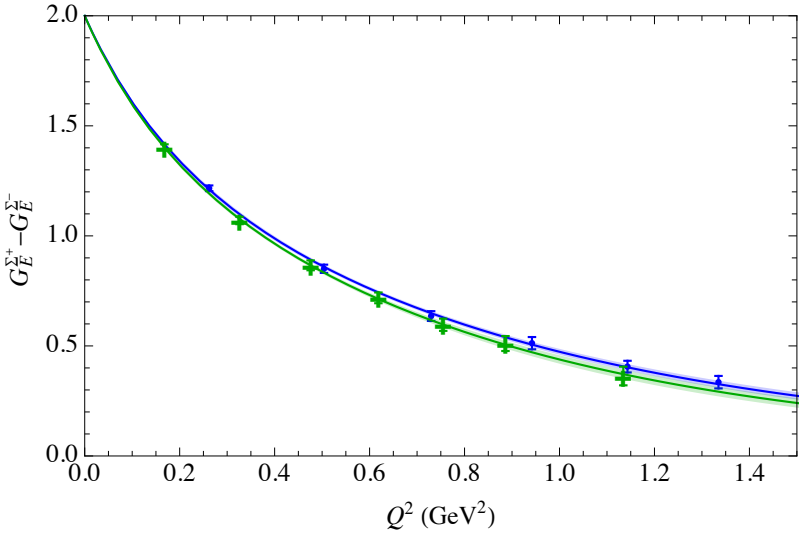

(a) Isovector sigma baryon electric form factor.

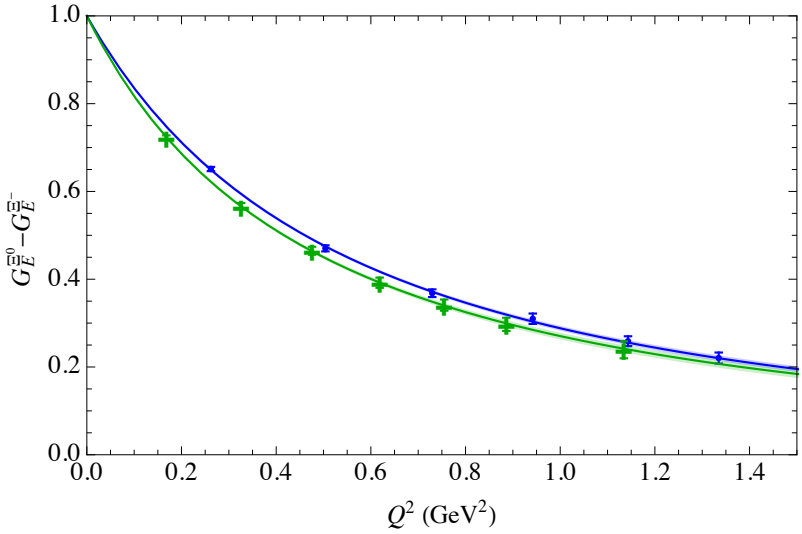

(b) Isovector cascade baryon electric form factor.

Figure 7.16: As in Fig. 7.15, for the isovector electric form factors of the hyperons.

	μ_B (μ_N)		
B	$p-n$	$\Sigma^+ - \Sigma^-$	$\Xi^0 - \Xi^-$
Extrapolated (set I)	3.8(4)	3.0(3)	−0.51(8)
Extrapolated (set II)	4.2(4)	3.2(3)	−0.62(10)
Experimental [30]	4.706	3.62(3)	−0.60(1)

Table 7.2: Isovector magnetic moments, based on sets I and II of chirally and infinite-volume extrapolated lattice simulation results. A dipole-like parameterisation (Eq. (7.40)) has been used to model the Q^2-dependence of the form factors.

curvature in the fit functions in Q^2, which improves the agreement with experiment in every case. Isovector magnetic moments, extracted using these fits, are given in Table 7.2.

We emphasise that the lattice simulation results away from the primary simulation trajectory for data set I (that is, simulations 1–3 in Table 7.1) are essential to tightly constrain the chiral extrapolation to the physical point. The effect of adding the additional off-trajectory points to the fit leads to a factor of 6 reduction in statistical uncertainty. This illustrates the importance for chiral extrapolations of performing lattice simulations which map out the m_l–m_s plane as we have done, rather than simply following a single trajectory in this space. For data set II we have simulation results along only one trajectory. However, as this lies very close to the physical singlet trajectory (as illustrated in Fig. 7.2), the extrapolation in a perpendicular direction to the physical point inflates the uncertainties only marginally.

7.5.2 Connected Baryon Form Factors

As well as the isovector quantities presented in the previous section, we can determine the 'quark-line–connected' part of all individual baryon form factors. Comparison of these quantities with experimental determinations is of particular interest—a systematic discrepancy between the lattice and experimental results could be a signal of significant disconnected contributions to the form factors.

Figures 7.17 and 7.18 show extrapolated results for the connected parts of the proton and neutron form factors, compared with the Kelly parameterisation [272] of experimental results. The level of agreement between the lattice and experiment across the entire range of simulation Q^2-values supports the conclusion of Ref. [28] that the omitted disconnected contributions are relatively small.

Figures displaying connected form factors for each of the octet baryons, including dipole-like fits in Q^2, are given in Appendix J.2. The magnetic moments extracted from the fits to the magnetic form factors, given in Table 7.3, are close to the experimental values, especially for data set II which includes a point at a lower value of Q^2. Once again, greater curvature in the functional form in Q^2 would improve the agreement with experiment in every case.

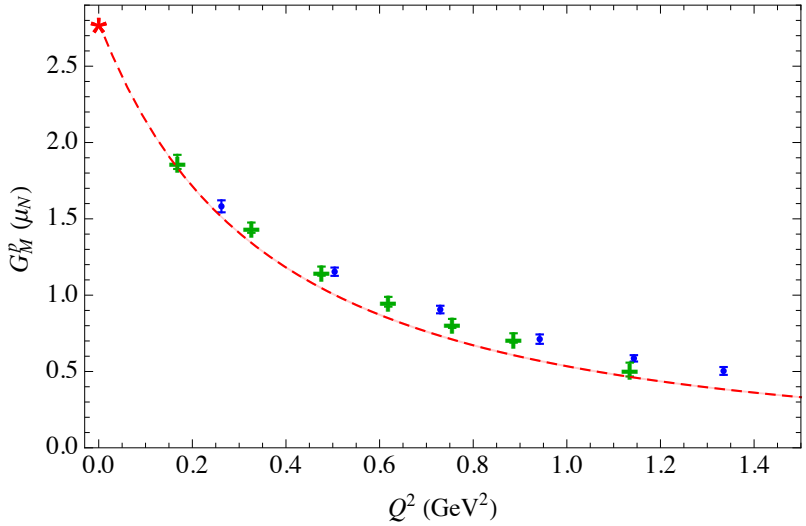

(a) Proton magnetic form factor.

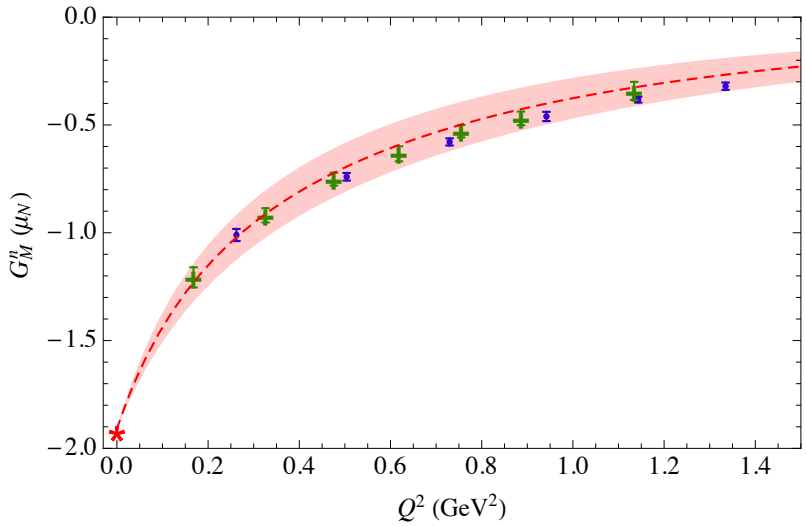

(b) Neutron magnetic form factor.

Figure 7.17: Extrapolated (connected part of the) proton and neutron magnetic form factors, compared with the Kelly parameterisation [272] of experimental measurements (dashed red band). The blue circles and green crosses denote extrapolated results based on simulation sets I and II, respectively.

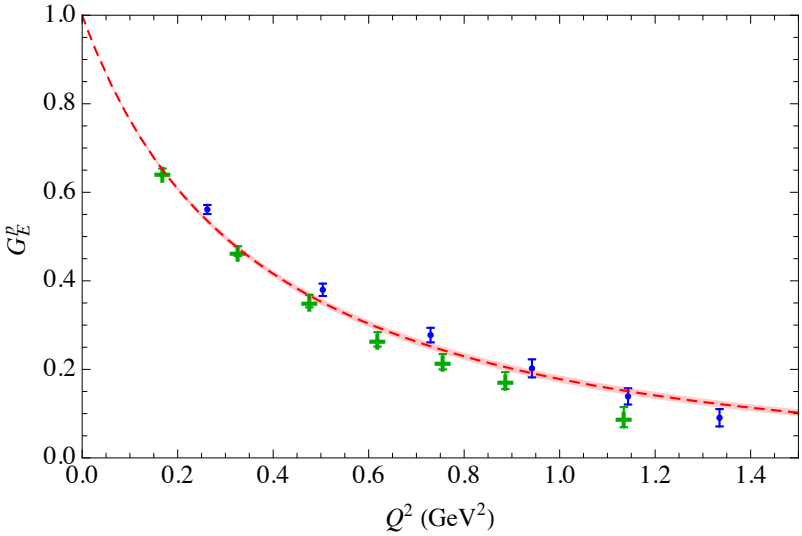

(a) Proton electric form factor.

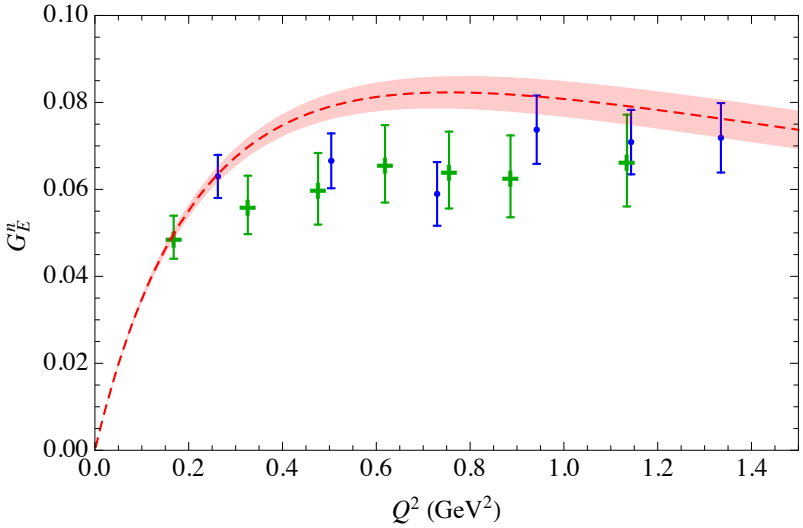

(b) Neutron electric form factor.

Figure 7.18: Extrapolated (connected part of the) proton and neutron electric form factors, compared with the Kelly parameterisation [272] of experimental measurements (dashed red band). The blue circles and green crosses denote extrapolated results based on simulation sets I and II, respectively.

	μ_B (μ_N)		
B	p	n	Σ^+
Extrapolated (set I)	2.3(3)	−1.45(17)	2.12(18)
Extrapolated (set II)	2.6(2)	−1.65(17)	2.27(18)
Experimental [30]	2.79	−1.913	2.458(10)
	Σ^-	Ξ^0	Ξ^-
Extrapolated (set I)	−0.85(10)	−1.07(7)	−0.57(5)
Extrapolated (set II)	−0.95(11)	−1.19(12)	−0.59(8)
Experimental [30]	−1.160(25)	−1.250(14)	−0.6507(25)

Table 7.3: Connected contribution to the octet baryon magnetic moments, based on a dipole-like fit (Eq. (7.40)) to the extrapolated lattice simulation results. Experimental values are taken from Ref. [30].

7.5.3 Magnetic and Electric Radii

The magnetic and electric radii of the octet baryons are defined by Eq. (7.4) in terms of the slopes of the Sachs form factors with respect to changes in the momentum scale Q^2, at $Q^2 = 0$. To determine these quantities from the lattice simulation results we again use dipole-like parameterisations of the Q^2-dependence of G_E and G_M.

It is clear that fitting the magnetic form factors with Eq. (7.40) will yield consistently smaller values for the magnetic radii than those determined experimentally (for the nucleon) or predicted in chiral quark models (for the octet baryons) [273, 274]; as noted in the previous sections, while our results are quite consistent with the experimental parameterisation of the nucleon form factors *where they are calculated*, the best-fit dipole-like function has slightly less curvature. This can be seen clearly from a comparison of Fig. 7.17 with Fig. 7.19.

To explore the model-dependence of this extraction of the magnetic radii we consider a second functional form in Q^2, inspired by the Kelly-style parameterisations of experimental results. This form has a more general polynomial in Q^2 in the denominator:

$$G_M^{\text{fit}}(Q^2) = \frac{\mu_B^{\text{exp.}}}{1 + c_{M1}Q^2 + c_{M2}Q^4 + c_{M3}Q^6}. \tag{7.41}$$

We now fix $\mu_B^{\text{exp.}}$ to the experimental magnetic moment (disregarding the omission of disconnected quark-line contributions in our simulations), so there are again three free parameters, c_{M1}, c_{M2}, and c_{M3}. As illustrated for the nucleon in Fig. 7.19 (and for the other octet baryons in Appendix J.2), the quality of fit using this functional form is entirely comparable with that using Eq. (7.40). The shift in the extracted value of the magnetic radius, however, is significant, as shown in Table 7.4. This example confirms that truly robust predictions for the hyperon magnetic radii

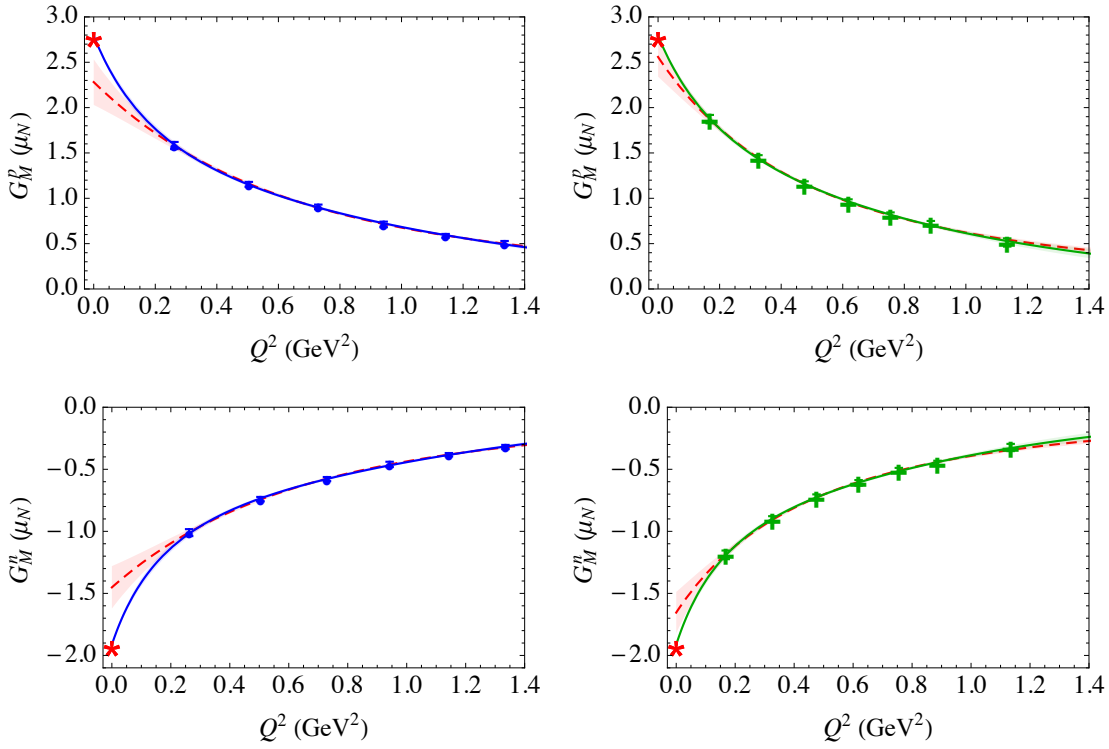

Figure 7.19: Connected part of the nucleon magnetic form factors. Blue circles (left-hand column) and green crosses (right-hand column) denote the results of simulation sets I and II, respectively, extrapolated to infinite volume and the physical pseudoscalar masses. The red stars indicate the experimental magnetic moments. The lines show dipole-like fits in Q^2 using Eq. (7.40) (dashed red) and Eq. (7.41) (solid blue or green).

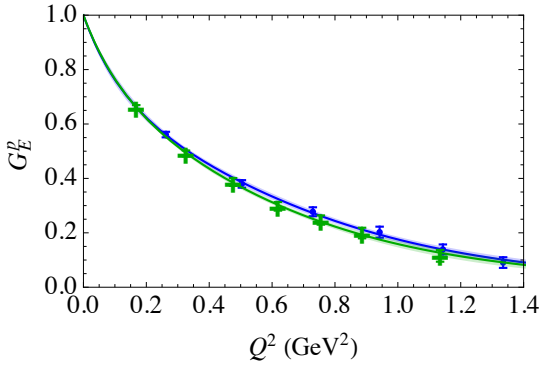

Figure 7.20: Connected part of the proton electric form factor. The symbols are as in Fig. 7.19. The lines shown correspond to dipole-like fits in Q^2 using Eq. (7.42).

	$\langle r_M^2 \rangle^B$ (fm^2)					
	p	n	Σ^+	Σ^-	Ξ^0	Ξ^-
Set I, free μ_B	0.35(11)	0.35(11)	0.39(9)	0.42(13)	0.27(8)	0.23(8)
Set II, free μ_B	0.47(14)	0.51(17)	0.42(13)	0.50(19)	0.34(14)	0.17(16)
Set I, general	0.71(8)	0.86(9)	0.66(5)	1.05(9)	0.53(5)	0.44(5)
Set II, general	0.69(8)	0.89(10)	0.62(7)	1.06(12)	0.48(8)	0.38(11)
Experimental [30]	0.777(16)	0.862(9)				

Table 7.4: Extrapolated results for the octet baryon magnetic radii, based on our fits to the lattice simulation results, compared with experimental values. Results labelled 'free μ_B' result from a dipole-like fit function in Q^2 (Eq. (7.40)), while those labelled 'general' use the ansatz given in Eq. (7.41) with μ_B fixed to the experimental values [30].

from lattice QCD will require results at much lower values of Q^2 to eliminate the significant dependence on the functional form chosen for the extrapolation in Q^2.

Nevertheless, by taking the experimental magnetic moments as additional input, we find an outstanding level of agreement between the extracted nucleon magnetic radii and the experimental values for these observables. Moreover, our results using simulation sets I and II, which have quite different sources of systematic uncertainty, are entirely consistent. Based on this, we conclude that we have achieved the first accurate calculation of the magnetic radii of the entire outer ring of the baryon octet from lattice QCD (extrapolated to the physical pseudoscalar masses).

To extract the electric radii we also use a more general dipole-like parameterisation of the Q^2-dependence of G_E, with three free parameters:

$$G_E^{\text{fit}}(Q^2) = \frac{G_E(Q^2 = 0)}{1 + c_{E1}Q^2 + c_{E2}Q^4 + c_{E3}Q^6}. \tag{7.42}$$

As was noted previously for the isovector nucleon form factor, the standard dipole form does not provide a good fit to the extrapolated lattice results; the χ^2/d.o.f. is as large as 4.0 for the Ξ^- and 1.7 for the proton. In contrast, the more general form of Eq. (7.42) yields fits with a χ^2/d.o.f. $\lesssim 1$ for each of the charged baryons. Fits using this ansatz are shown in Fig. 7.20 (for the proton) and Appendix J.2 (for the other octet baryons). Results for the radii of the charged baryons, compared with the available experimental numbers, are given in Table 7.5.

The electric radii determined by this method are consistently smaller than the corresponding experimental numbers for the proton and Σ^-. We point out that while this calculation omits any disconnected contributions to the form factors and therefore to the radii, the very close agreement of the extracted proton electric form factor with the experimental determination suggests that the effect of this omission is small, barring lattice artefacts as discussed in the previous section. It is clear that the simple dipole-like parameterisation used for the Q^2-dependence is not sufficient to extract accurate values of the electric radii from these simulations.

	$\langle r_E^2 \rangle^B$ (fm^2)			
	p	Σ^+	Σ^-	Ξ^-
Dipole ansatz, set I	0.601(14)	0.599(12)	0.414(5)	0.352(3)
Dipole ansatz, set II	0.718(15)	0.738(15)	0.505(10)	0.439(9)
Eq. (7.42) ansatz, set I	0.76(10)	0.61(8)	0.45(3)	0.39(2)
Eq. (7.42) ansatz, set II	0.76(10)	0.68(8)	0.52(4)	0.45(3)
Experimental [30]	0.878(5)		0.780(10)	

Table 7.5: Octet baryon electric radii based on a dipole or dipole-like (Eq. (7.42)) fit to the extrapolated lattice simulation results, compared with the available experimental values [30].

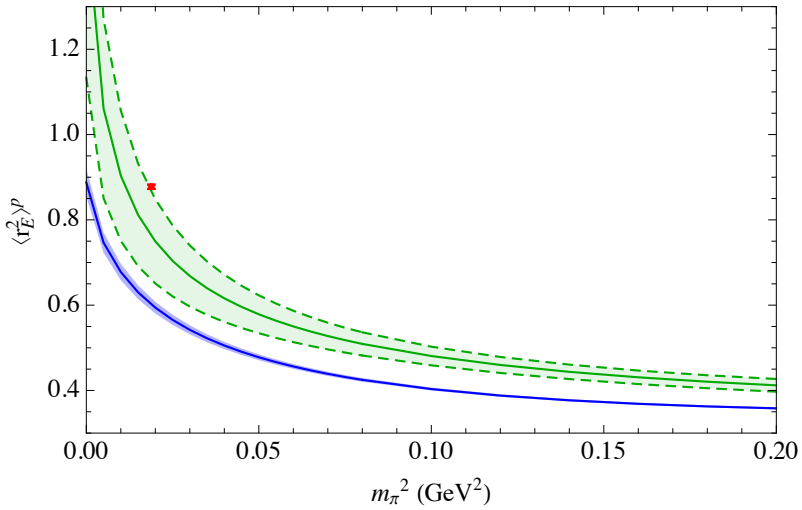

Figure 7.21: Electric radius of the proton from the chiral extrapolation of data set I, with a dipole (blue band) or dipole-like (green dashed band) ansatz (Eq. (7.42)) parameterising the Q^2-dependence. The singlet pseudoscalar mass ($m_K^2 + m_\pi^2/2$) is held fixed at its physical value. The red point indicates the experimental value [30].

Robust predictions of the electric radii from lattice QCD will require simulations with a similar level of precision to the results of this work, but at much lower values of Q^2. We note that the electric radius of the proton extracted as described above does display the expected behaviour with pion mass, increasing quite rapidly as one approaches the physical pseudoscalar masses from above. This is illustrated in Fig. 7.21.

7.5.4 Quark Form Factors

We investigate the environmental sensitivity of the distribution of quarks inside a hadron by inspecting the individual (connected) quark contributions to the form factors of the octet baryons. These contributions, evaluated using the chiral extrapolation described in previous sections, are illustrated in Figs. 7.22 and 7.23. The figures show the lowest-Q^2 result from the fit to data set I, at approximately $0.26\,\mathrm{GeV}^2$. We recall that the lines shown on each plot are not independent as the chiral extrapolation expressions are simultaneously fit to all of the octet baryon form factors.

Comparison of the u quark contributions to the proton and Σ^+ magnetic form factors, illustrated in Fig. 7.22(a), shows the relative suppression of $G_M^{\Sigma,u}$ caused by the heavier spectator quark in the sigma. This effect is replicated, and is more significant, when probing the singly-represented quark, as can be seen by the relative suppression (in magnitude) of the u contribution to the cascade baryon compared to the d in the proton in Fig. 7.22(b). Changing the mass of the probed quark—doubly-represented in the proton compared with the cascade, or singly-represented in the proton compared with the sigma—causes a similar effect.

The doubly-represented quark contributions to the electric form factors are illustrated in Fig. 7.23(a). While the u contribution to the proton and the u contribution to the sigma baryon are very similar—again, the only difference is the mass of the single spectator (d or s) quark—the s contribution to the cascade baryon has a different shape. As in the magnetic case, that form factor has significantly less curvature with m_π^2 below the SU(3)-symmetric point as a result of the heavier mass of the probed s quark.

The singly-represented quark contributions to the electric form factors are shown in Fig. 7.23(b). Here the difference between the d quark contribution to the proton and the s quark contribution to the sigma baryon illustrates the effect of changing the mass of the single probed quark. While the effect of changing the mass of the spectator quark is small for the doubly-represented form factors, it is far more significant here as there are now two spectator quarks. This may be seen by comparing the d quark contribution to the proton with the u in the cascade baryon.

We also notice that the u quark contribution to the cascade baryon electric form factor is considerably more suppressed in the light quark-mass region than the corresponding d quark contribution to the proton. That is, the magnitude of $\langle r^2 \rangle_u^\Xi$ is enhanced relative to $\langle r^2 \rangle_d^p$. This can be explained by the meson-dressing effects; the connected d in the proton prefers to form a π^+ with one of the valence u quarks

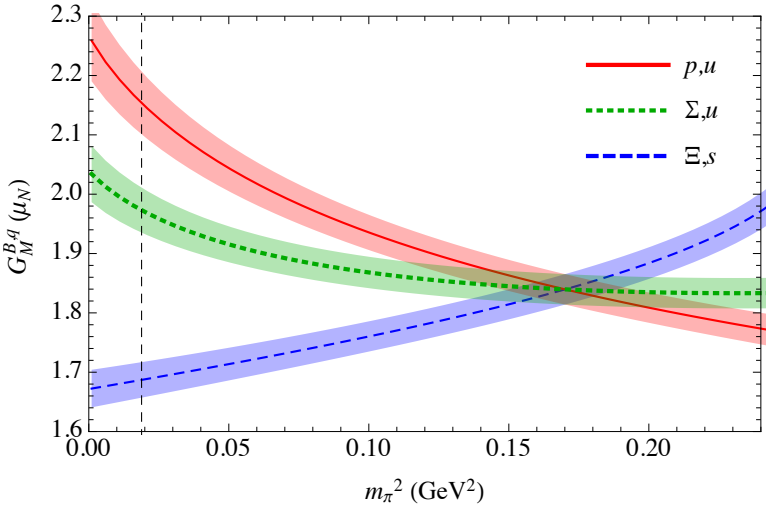

(a) Doubly-represented quark contributions.

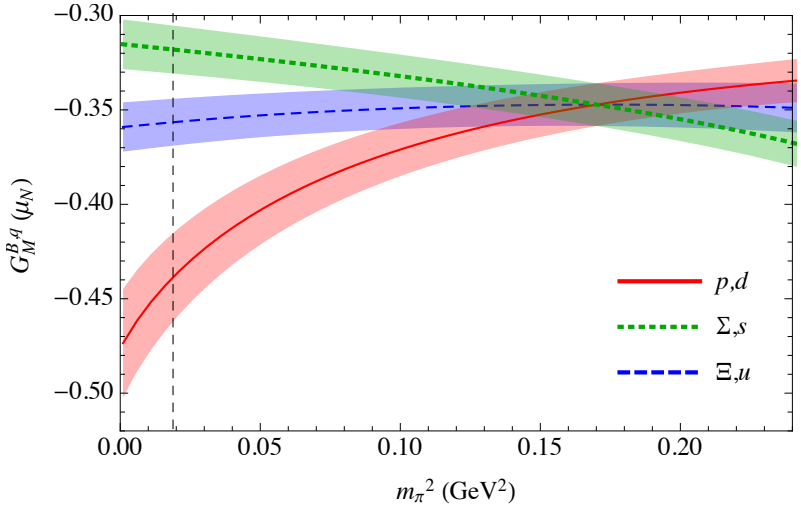

(b) Singly-represented quark contributions.

Figure 7.22: Connected part of the doubly and singly-represented quark contributions to the baryon magnetic form factors for data set I at $Q^2 \approx 0.26$ GeV^2. The singlet pseudoscalar mass $(m_K^2 + m_\pi^2/2)$ is held fixed at its physical value. The charges of the relevant quarks have been set to one.

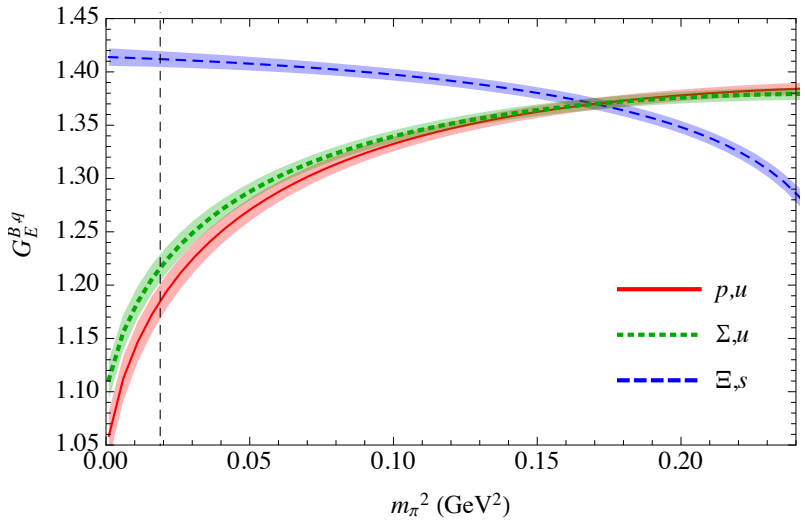

(a) Doubly-represented quark contributions.

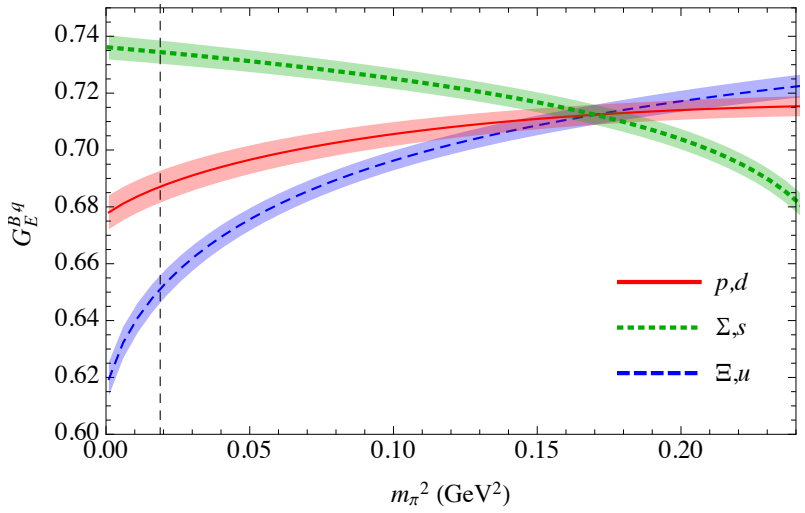

(b) Singly-represented quark contributions.

Figure 7.23: As in Fig. 7.22, for the electric form factors.

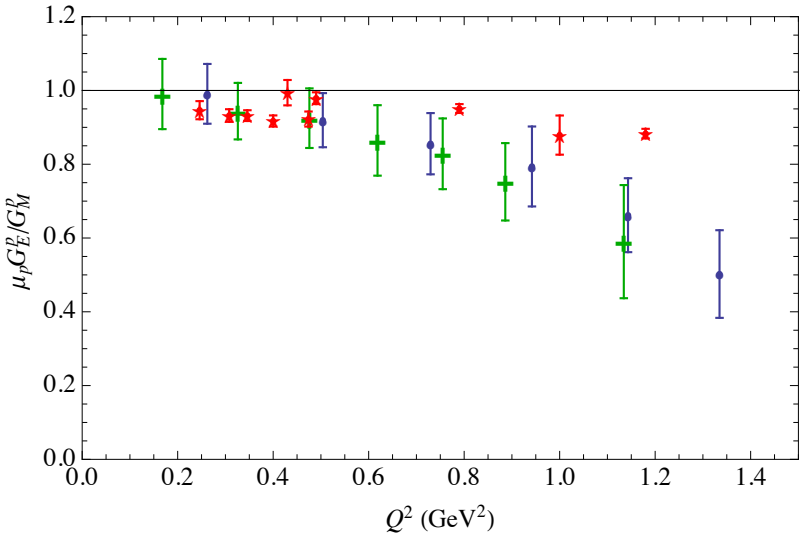

Figure 7.24: Ratio of the electric and magnetic form factors of the proton based on the chiral extrapolations of data sets I (blue circles) and II (green crosses). The red stars denote the experimental results of Refs. [225, 275, 276].

in the proton, giving rise to a substantial negative contribution to $\langle r^2 \rangle_d^p$ in the light quark-mass region. In contrast, the connected u in the cascade baryon can only form a pion state by coupling to a sea quark, from which the resulting enhancement is always positive.

7.5.5 Ratio of Electric and Magnetic Form Factors

By combining the chirally-extrapolated values of the octet baryon electric and magnetic form factors, we deduce the ratios $\mu_B G_E^B/G_M^B$ at each of the discrete values of Q^2 for which we have results. As with the chiral extrapolations themselves, the entire analysis of these ratios is performed at the bootstrap level.

Figure 7.24 shows the proton form factor ratio $\mu_p G_E^p/G_M^p$, where the experimental value is used for the magnetic moment μ_p [30]. While the results are qualitatively consistent with a linear decrease of that ratio with Q^2, as concluded from polarisation transfer experiments (e.g., see the results from Refs. [225, 275, 276], illustrated on the figure), this decrease is more pronounced in our results than in the experimental data, with the exception of the results of Ref. [223] which display a similarly steep trend. In our work this trend is explained by the observation that the lattice simulation results for G_M fall off less rapidly in Q^2 than the Kelly parameterisation of experimental results, while the lattice results for G_E are consistent with experiment.

Figure 7.25 shows the absolute value of $\mu_B G_E^B/G_M^B$ for each of the outer-ring octet baryons. The large value of this ratio for the Σ^- baryon is a result of the choice of normalisation; the magnetic moment of the Σ^- suggested by the lattice data was found to be significantly smaller than the experimental value [30] which is

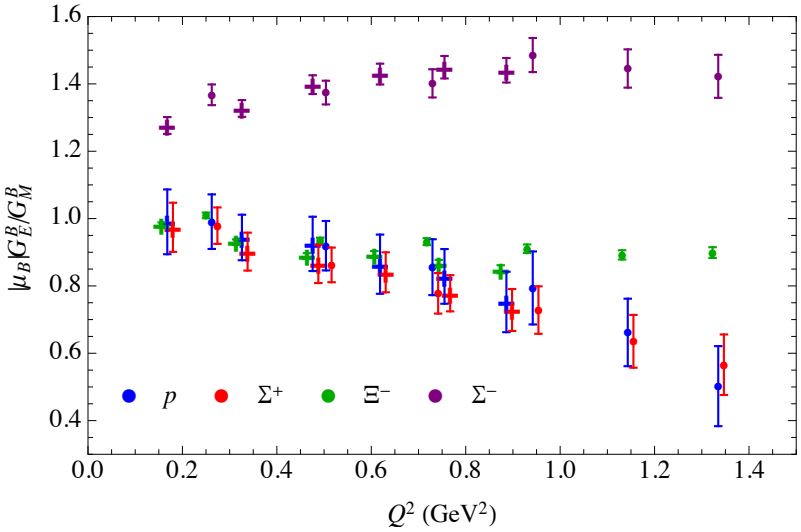

(a) Charged baryons.

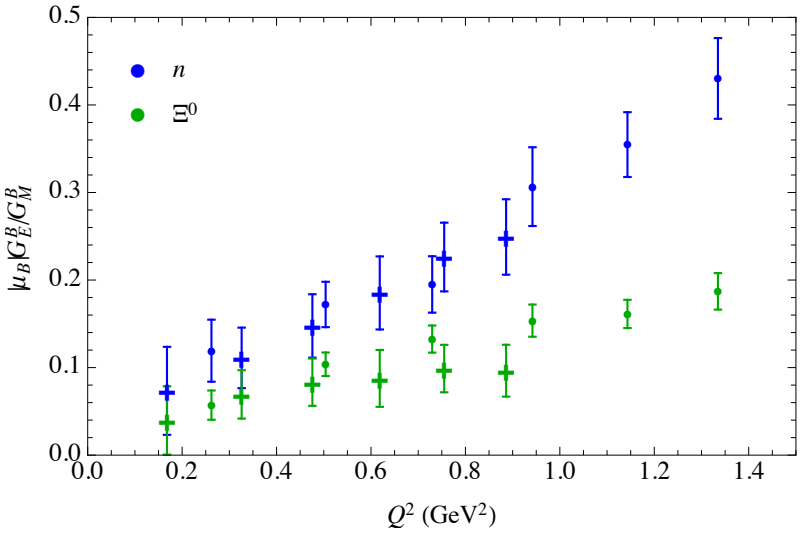

(b) Neutral baryons.

Figure 7.25: Ratios of the electric and magnetic form factors of the octet baryons. The points denoting the Σ^+ and Ξ^- baryons have been slightly offset on the Q^2-axis for clarity. The circles and crosses denote results based on simulation sets I and II, respectively.

used here. We note that if the trends displayed for $\mu_B G_E^B/G_M^B$ at the relatively low Q^2-values of this study continue to high Q^2, zero-crossings of this ratio for the Ξ^- and Σ^- baryons seem unlikely.

7.6 Charge Symmetry Violation

The assumption of good charge symmetry has been widely applied in studies of the electromagnetic structure of the nucleon, just as it has in investigations of sigma terms (Chapter 5) and in parton phenomenology (Chapter 6). In particular, the limiting factor in state-of-the-art experimental determinations of the strange-quark contribution to the nucleon electromagnetic form factors [277–281] is the poor theoretical constraint on the size of CSV effects.

Precisely, CSV form factors $G_{\rm CSV}$, if not accounted for, mimic the strange-quark contribution $G_{E/M}^s$ in the combination of form factors accessible through parity-violating electron scattering experiments [282–284]: the measured neutral weak current matrix elements $G_{E/M}^{p,Z}$ may be expressed as

$$G_{E/M}^{p,Z} = \left(1 - 4\sin^2\theta_W\right) G_{E/M}^{p,\gamma} - G_{E/M}^{n,\gamma} - G_{E/M}^{s} + G_{\rm CSV}, \tag{7.43}$$

where the weak mixing-angle θ_W and the total electromagnetic form factors $G_{E/M}^{p/n,\gamma}$ are precisely determined from other experimental studies.

With theoretical predictions of the size of $G_{\rm CSV}$ varying through several orders of magnitude [27, 285, 286], this uncertainty (along with the remarkable experimental challenges) has halted experimental parity-violating electron scattering programs [281]. Using the chiral extrapolations of lattice simulation results presented in the previous sections, we perform the first *ab-initio* calculation of the relevant CSV quantities. With the discovery that the CSV form factors are an order of magnitude smaller than the precision of existing parity-violating electron scattering studies, this calculation opens the door for a new generation of experiments to challenge the predictions of QCD.

7.6.1 CSV Form Factor Formalism

In terms of individual u and d quark contributions to the Sachs electric and magnetic form factors of the proton and neutron, the CSV form factors which we calculate are defined as

$$\delta_{E/M}^u = G_{E/M}^{p,u} - G_{E/M}^{n,d}, \qquad \delta_{E/M}^d = G_{E/M}^{p,d} - G_{E/M}^{n,u}, \tag{7.44}$$

where we explicitly calculate $G_{E/M}^{p/n,u/d}$ and perform the subtractions indicated. The combination relevant to experimental determinations of nucleon strangeness using

Eq. (7.43) is

$$G_{\rm CSV} = \left(\frac{2}{3}\delta^d_{E/M} - \frac{1}{3}\delta^u_{E/M}\right). \tag{7.45}$$

We express $G_{\rm CSV}$ as a function of pseudoscalar mass using the chiral formalism developed in the previous sections. Of course, this formalism must now incorporate the breaking of SU(2) symmetry; we allow for non-equal light quark masses $m_u \neq m_d$. Precisely as described in earlier chapters, where we investigated the mass splittings among members of baryon isospin multiplets (Chapter 4), the CSV sigma terms (Chapter 5), and CSV parton distribution moments (Chapter 6), this is a simple extension of the formalism which we have already described. Moreover, the low-energy parameters which appear in the SU(2)-breaking terms in the chiral extrapolation expressions for the electromagnetic form factors also appear in the isospin-averaged expressions. These parameters may thus be fixed by the previously-described fits to our $N_f = 2+1$ lattice QCD simulations on the baryon octet.

Explicitly, using the formalism presented in Section 7.3.2, chiral extrapolation expressions for the CSV electric and magnetic form factors can be written as

$$\begin{aligned}\delta^u_M =& \frac{1}{6}\big(2c_1^M - 3c_{10}^M - 3c_{12}^M - 4c_2^M - 2c_5^M - 5c_6^M - 54c_7^M + 3c_9^M\big)\mathcal{B}(m_d - m_u) \\ &+ \frac{M_N}{16\pi^3 f_\pi^2}\frac{1}{9}\big[\mathcal{C}^2\big(I_D^M(m_{K^0}) - I_D^M(m_{K^\pm})\big) \\ &\qquad -12\big(D^2+3F^2\big)\big(I_O^M(m_{K^0}) - I_O^M(m_{K^\pm})\big)\big],\end{aligned} \tag{7.46a}$$

$$\begin{aligned}\delta^d_M =& \frac{1}{6}\big(2c_1^M + 2c_{10}^M - 4c_{11}^M + 2c_{12}^M - 4c_2^M + 4c_5^M + c_6^M + 54c_7^M - c_9^M\big)\mathcal{B}(m_d - m_u) \\ &- \frac{M_N}{16\pi^3 f_\pi^2}\frac{2}{9}\big[\mathcal{C}^2\big(I_D^M(m_{K^0}) - I_D^M(m_{K^\pm})\big) - 9(D-F)^2\big(I_O^M(m_{K^0}) - I_O^M(m_{K^\pm})\big)\big],\end{aligned} \tag{7.46b}$$

$$\begin{aligned}\delta^u_E =& \frac{1}{6}\big(2c_1^E - 3c_{10}^E - 3c_{12}^E - 4c_2^E - 2c_5^E - 5c_6^E - 54c_7^E + 3c_9^E\big)Q^2\mathcal{B}(m_d - m_u) \\ &- \frac{1}{16\pi^3 f_\pi^2}\frac{1}{9}\big[\mathcal{C}^2\big(I_D^E(m_{K^0}) - I_D^E(m_{K^\pm})\big) + 6\big(D^2+3F^2\big)\big(I_O^E(m_{K^0}) - I_O^E(m_{K^\pm})\big) \\ &\qquad +18\big(I_T^E(m_{K^0}) - I_T^E(m_{K^\pm})\big)\big],\end{aligned} \tag{7.46c}$$

$$\begin{aligned}\delta^d_E =& \frac{1}{6}\big(2c_1^E + 2c_{10}^E - 4c_{11}^E + 2c_{12}^E - 4c_2^E + 4c_5^E + c_6^E + 54c_7^E - c_9^E\big)Q^2\mathcal{B}(m_d - m_u) \\ &+ \frac{1}{16\pi^3 f_\pi^2}\frac{1}{9}\big[2\mathcal{C}^2\big(I_D^E(m_{K^0}) - I_D^E(m_{K^\pm})\big) + 9(D-F)^2\big(I_O^E(m_{K^0}) - I_O^E(m_{K^\pm})\big) \\ &\qquad +9\big(I_T^E(m_{K^0}) - I_T^E(m_{K^\pm})\big)\big],\end{aligned} \tag{7.46d}$$

where the low-energy parameters $c_i^{E/M}$ are defined in Eqs. (7.29) and (7.36). All of these constants, other than $c_1^{E/M}$, $c_2^{E/M}$, and $c_7^{E/M}$, are determined from the chiral fits to the connected contribution to the isospin-averaged electromagnetic

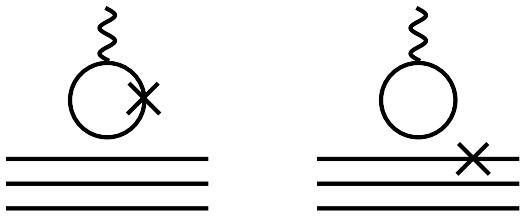

Figure 7.26: Diagrammatic quark-line skeleton representation of omitted contributions to the CSV form factors. Solid and wavy lines represent quarks and photons, respectively. The crosses denote quark mass insertions, i.e., the figures represent the contribution from disconnected quark-loops to the CSV arising from the different (u and d quark) masses of: (a): the struck sea quark; (b): spectator quarks. These contributions are proportional to $\mathcal{B}(m_d - m_u)$.

form factors which are described in Section 7.4. The parameters $c_1^{E/M}$, $c_2^{E/M}$, and $c_7^{E/M}$ do not appear in the previous fit expressions, and thus cannot be determined from the lattice simulations which we consider here. Bounds on these contributions to the CSV are estimated within the framework of a model which is described in Section 7.6.2.

7.6.2 Disconnected Contributions to the CSV

While some of the disconnected contribution to the CSV form factors can be systematically included by the method described in the previous section, other disconnected terms—those which are linear in $\mathcal{B}(m_d - m_u)$ and not generated by chiral logarithms from meson loops—cannot be determined in that way. Precisely, the terms which are generated by the Lagrangian pieces with coefficients $c_1^{E/M}$, $c_2^{E/M}$, and $c_7^{E/M}$ (defined in Eqs. (7.29) and (7.36)) cannot be determined from the present lattice simulations. Physically, they arise from the diagrams illustrated and described in Fig. 7.26. These contributions are anticipated to be small based on the success of valence quark models. This is supported by the results of direct lattice QCD calculations of $G_{E/M}$ which find that the disconnected contributions at small finite momentum transfer are consistent with zero and are bounded at the 1% level [28]. The terms which we seek to estimate here are only part of that disconnected contribution.

We choose to set contributions from the unknown terms $c_1^{E/M}$, $c_2^{E/M}$, and $c_7^{E/M}$ to 0, with an uncertainty taken to be twice the magnitude of the corresponding contributions from meson loop diagrams, evaluated with a dipole cutoff regulator with mass scale $\Lambda = 0.8(2)\,\mathrm{GeV}$. This is justified by the well-established and successful use of this model to relate full and partially-quenched lattice QCD calculations [287]. The loop diagram used to estimate the $c_{1,2}^{E/M}$ terms is represented in Fig. 7.27(b), where only the 'loop spectator' quark mass (i.e., the valence quark part of the meson mass) is changed. For the $c_7^{E/M}$ term, represented in Fig. 7.27(a), only the sea quark part of the loop meson mass is considered. These contributions are added in

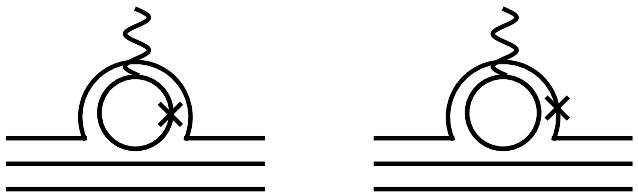

(a) (b)

Figure 7.27: Quark-line skeleton diagrams of the meson loops used to model the omitted contributions to the CSV form factors. Solid and wavy lines represent quarks and photons, respectively. The crosses denote quark mass insertions into: (a): the struck sea quark in the meson loop; (b): the meson loop spectator quark.

quadrature. The magnitude of this contribution to the total uncertainty varies with Q^2; it is largest at our lowest Q^2-values where it contributes 20–60% of the quoted uncertainty on the final result (depending which of $\delta_{E/M}^{u/d}$ one is considering), while at larger values of Q^2 it contributes 1–15%.

7.6.3 CSV Relevant to the Strange Electromagnetic Form Factors

Figure 7.28 shows the size of the CSV form factor combination, $G_{\rm CSV}$, as relevant to parity-violating electron scattering experiments probing the strange electromagnetic form factors of the nucleon by Eq. (7.43). The individual u and d quark contributions are shown in Fig. 7.29. The close agreement of the two sets of simulations (at different lattice spacings a and on different simulation volumes) confirms that the finite-volume corrections and chiral extrapolations are under control and that any discretisation effects resulting from the finite lattice spacing are small.

Our result gives quantitative confirmation that CSV effects in the electromagnetic form factors, for momentum transfers up to approximately $1.3\,\mathrm{GeV}^2$, are at the level of 0.2% of the relevant proton form factors—an order of magnitude smaller than the precision of existing parity-violating electron scattering studies. To put this in perspective, the level of CSV shown in Fig. 7.28(b) is equivalent to a CSV difference in charge radii of less than one attometer. These precise results open the door for a new generation of experiments to probe the structure of the quantum vacuum through the strange quark form factors. We turn to a deeper discussion of the strange electromagnetic form factors of the nucleon in the next section.

7.7 Strange Nucleon Form Factors

Recent years have seen extensive experimental efforts directed at measuring the strange quark contribution to the electromagnetic form factors of the nucleon. Probing a range of values of Q^2 up to approximately $0.94\,\mathrm{GeV}^2$, the combined data sets from programs at Jefferson National Lab (G0, HAPPEX) [279–281, 288–291], MIT-

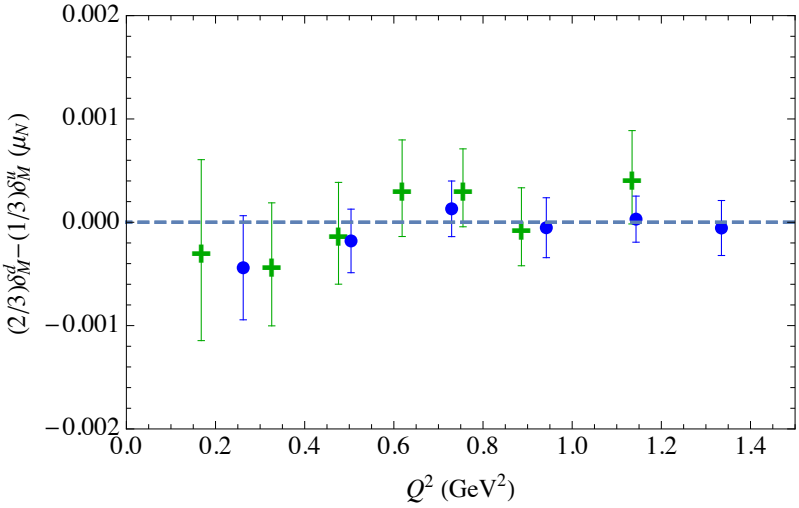

(a) Magnetic CSV form factors.

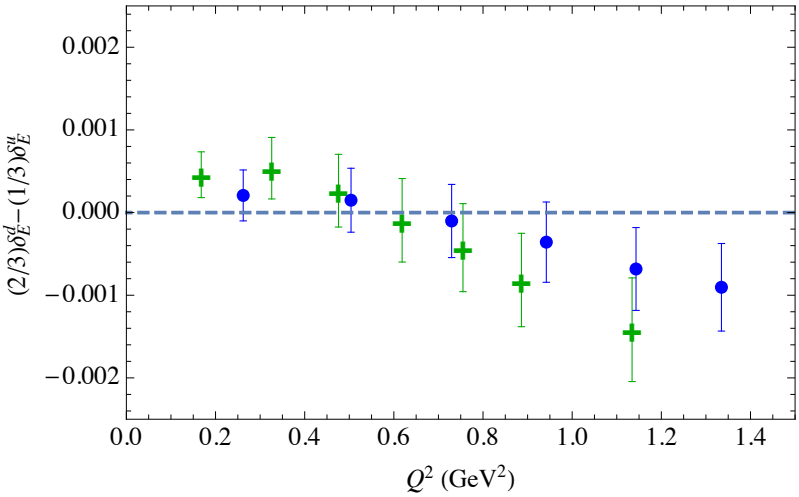

(b) Electric CSV form factors.

Figure 7.28: Magnetic and electric CSV form factors as relevant to experimental determinations of nucleon strangeness. The blue circles and green crosses denote our results based on simulation sets I ($a = 0.074(2)\,\mathrm{fm}$) and II ($a = 0.062(2)\,\mathrm{fm}$), respectively.

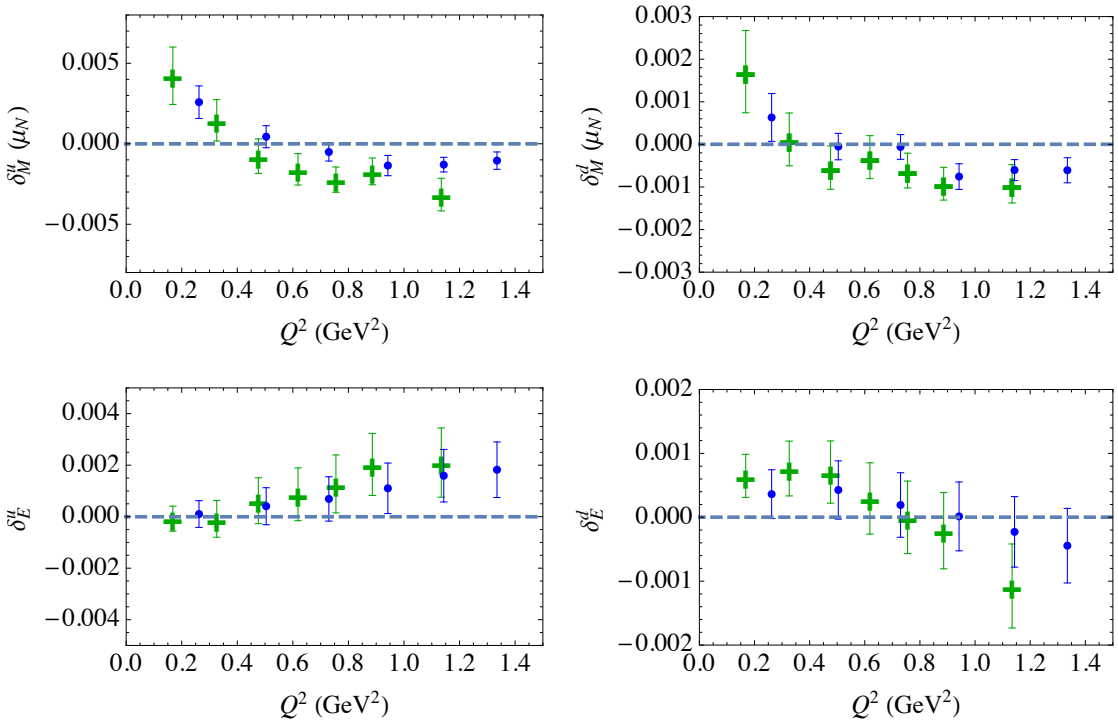

Figure 7.29: Individual up and down quark contributions to the CSV form factors. These terms are combined to give the total CSV form factors $G_{\text{CSV}} = \left(\frac{2}{3}\delta^d_{E/M} - \frac{1}{3}\delta^u_{E/M}\right)$. Blue points and green crosses show the results of data sets I and II extrapolated to the physical point, with corrections applied to model the omitted disconnected terms.

Bates (SAMPLE) [277,292], and Mainz (A4) [278,293,294] constrain these terms to be less than a few percent of the total form factors but all results are, at this stage, consistent with zero to within 2-sigma [295]. Our precise calculation of the CSV contributions to the electromagnetic form factors of the nucleon, presented in the last section, has opened the door for a new generation of parity-violating electron scattering experiments to improve on these determinations.

The status of the strange form factors from theory is less clear; predictions from various quark models cover a very broad range of values [296–301] and the large computational cost of all-to-all propagators has so far limited direct lattice QCD studies to large pion masses and single volumes [28, 29].

Using the connected lattice simulations of the octet baryon electromagnetic form factors presented in this chapter, we determine the strange quark contributions to the nucleon form factors indirectly over a range of values of Q^2 currently unattainable through direct experimental measurement. Our final result for the strange magnetic moment of the proton, $G_M^s(Q^2 = 0) = -0.07 \pm 0.03\,\mu_N$, is non-zero to 2-sigma and an order of magnitude more precise than the closest experimental results. It is also consistent with an earlier extraction using FRR to analyse quenched lattice data at relatively large quark masses [302]. The results reported at values of Q^2 above $0.6\,\mathrm{GeV}^2$ are the first determinations, experimental or based on lattice QCD, in that region. At present they cannot be distinguished from zero, but the uncertainties constrain their actual values to be very small.

7.7.1 Indirect Determination of the Strange Form Factors

We have shown in the last section that charge symmetry violation in the electromagnetic form factors of the nucleon is a small effect, with the CSV terms constrained to be smaller than approximately 0.2% of G_E and G_M over values of Q^2 up to $1.3\,\mathrm{GeV}^2$. Using this result—i.e., assuming good charge symmetry—we deduce the strange form factors [303–305] by combining experimental measurements of the total nucleon form factors with our lattice QCD determinations of the connected components. This method has been applied previously to determine the strange magnetic form factor at $Q^2 = \{0, 0.23\}\,\mathrm{GeV}^2$ [302,306] and the strange electric form factor at $Q^2 = 0.1\,\mathrm{GeV}^2$ [307] from quenched lattice QCD results.

Explicitly, under the assumption of charge symmetry, one may express the electromagnetic form factors of the proton and neutron as [303]

$$p = e^u u^p + e^d d^p + O_N, \tag{7.47a}$$

$$n = e^d u^p + e^u d^p + O_N. \tag{7.47b}$$

Here, p and n denote the physical (electric or magnetic) form factors of the proton and neutron and u^p and d^p represent the connected u and d quark contributions to the proton form factor. The disconnected quark-loop term, O_N, may be decomposed

into individual quark contributions:

$$O_N = \frac{2}{3}\,{}^{\ell}G^u - \frac{1}{3}\,{}^{\ell}G^d - \frac{1}{3}\,{}^{\ell}G^s, \tag{7.48a}$$

$$= \frac{{}^{\ell}G^s}{3}\left(\frac{1-{}^{\ell}R_d^s}{{}^{\ell}R_d^s}\right), \tag{7.48b}$$

where charge symmetry has been used to equate ${}^{\ell}G^u = {}^{\ell}G^d$ and the ratio of s to d disconnected quark-loops is denoted by ${}^{\ell}R_d^s = {}^{\ell}G^s/\,{}^{\ell}G^d$.

Rearranging Eqs. (7.47) and (7.48b) to isolate the strange quark loop contribution, ${}^{\ell}G^s$, yields two independent expressions which are rigorous consequences of QCD under the assumption of charge symmetry:

$${}^{\ell}G^s = \left(\frac{{}^{\ell}R_d^s}{1-{}^{\ell}R_d^s}\right)[2p+n-u^p], \tag{7.49a}$$

$${}^{\ell}G^s = \left(\frac{{}^{\ell}R_d^s}{1-{}^{\ell}R_d^s}\right)[p+2n-d^p]. \tag{7.49b}$$

In principle, given a suitable estimate of ${}^{\ell}R_d^s$, these expressions may be simply evaluated; the total form factors p and n are well known experimentally and the connected contributions u^p and d^p may be calculated on the lattice.

This procedure relies on the assumption that the difference between the experimental numbers and the connected lattice simulation results for the form factors may be entirely attributed to contributions from disconnected quark loops, i.e., that all other systematic effects are under control. In order to be able to estimate any as-yet undetermined lattice systematics, we average Eqs. (7.49a) and (7.49b) resulting in a form where only the connected contribution to the isoscalar combination, $(u^p + d^p)_{\text{conn.}}$, needs to be determined from the lattice simulations:

$${}^{\ell}G^s = \left(\frac{{}^{\ell}R_d^s}{1-{}^{\ell}R_d^s}\right)\left[\frac{3}{2}(p+n) - \frac{1}{2}(u^p+d^p)_{\text{conn.}}\right]. \tag{7.50}$$

Relaxing the assumption of exact charge symmetry in the valence sector would result in an additional term $+\frac{3}{2}G_{\text{CSV}}$ (where G_{CSV}, defined in Eq. (7.43), is the systematic CSV uncertainty affecting experimental determinations of the strange form factors) appearing within the square brackets of Eq. (7.50). For low values of Q^2, in particular where $\left({}^{\ell}R_d^s/(1-{}^{\ell}R_d^s)\right)$ is small, this systematic error thus affects our extraction of the strange form factors considerably less than it impacts on experimental determinations of these quantities, where the assumption of good charge symmetry is also standard.

From our analysis of the CSV form factors in Section 7.6 it is clear that contributions from G_{CSV} are negligible for this calculation of the strange form factors across the entire Q^2-range of relevance. If we disregard our own calculation, which constrains CSV to be an order of magnitude smaller than suggested by previous

studies, and instead take values of $G_{\rm CSV}$ from Ref. [286] (for $Q^2 < 0.3\,{\rm GeV}^2$ where the calculation is valid) as a systematic uncertainty, our error bands increase by less than 10%. A recent re-evaluation of $G_{\rm CSV}$ using relativistic chiral perturbation theory with a more realistic ω-nucleon coupling [285] found a significant reduction in $G_{\rm CSV}$ over the values in Ref. [286]. This confirms that the assumption of good charge symmetry has a negligible effect on our results.

We discuss in turn each of the three inputs into Eq. (7.50):

- The lattice values for $(u^p + d^p)_{\rm conn.}$.
- The experimental p and n form factors.
- The ratio ${}^\ell R_d^s = {}^\ell G^s / {}^\ell G^d$.

Lattice Determinations of u^p and d^p

The connected quark-line contributions to the proton electric and magnetic form factors are obtained as described in Section 7.4. Both statistical uncertainties and systematic effects resulting from the chiral and infinite-volume extrapolations, including an estimate of the model-dependence, are included. Additionally, we allow for any unknown systematics on the combination $(u^p + d^p)_{\rm conn.}$ by estimating that such effects will be similar in magnitude for the isovector combination $(u^p - d^p)_{\rm conn.}$, which may be directly compared with experiment. Because disconnected contributions in the total form factors cancel in the combination $(p - n)$, the difference $(u^p - d^p)_{\rm latt.} - (p - n)_{\rm exp.}$ provides an estimate of any unaccounted-for uncertainty in the lattice simulation results. We take the largest value of this difference, evaluated over the entire range of discrete simulation Q^2-values, as a conservative estimate.

This procedure is followed for both the electric and magnetic form factors. The additional uncertainty included in this fashion is significant and larger than the statistical uncertainty in the determination of the strange magnetic form factor. For the electric form factor it is a modest contribution of a size similar to, or smaller than, the statistical uncertainty (see Table 7.6 in Section 7.7.2).

Experimental p and n Form Factors

The total proton and neutron electromagnetic form factors p and n are taken from the parameterisations of experimental results by Kelly [272] and Arrington and Sick [308] (the latter is used only on its quoted range of validity, $Q^2 < 1\,{\rm GeV}^2$). The entire calculation, including the additional estimate of lattice systematics, is performed using each parameterisation. The average central value of the two sets of results is taken as the best-estimate of the strange form factors. Half of the difference between the two central values is included as an estimate of the parameterisation-dependent uncertainty. As shown in Table 7.6 in Section 7.7.2, this contribution to the uncertainty is small.

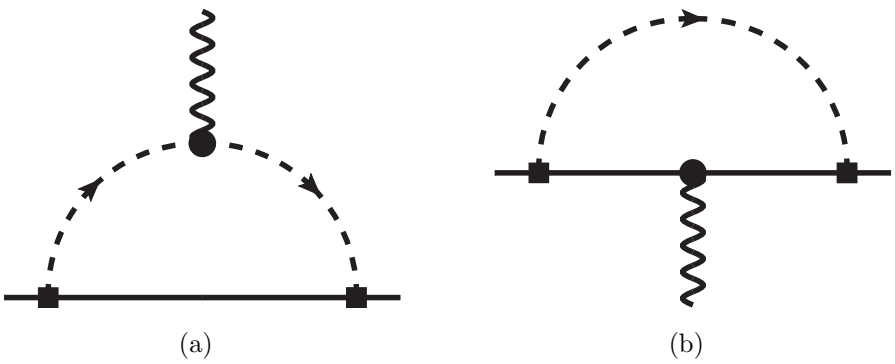

Figure 7.30: Loop diagrams which are included in the estimate of ${}^{\ell}R_d^s$ from effective field theory. Fig. 7.30(b) is included for the electric form factor only. The solid, dashed, and wavy lines denote octet baryons, mesons, and photons, respectively.

Estimate of the Ratio ${}^{\ell}R_d^s$

We derive an estimate for the disconnected quark-loop ratio ${}^{\ell}R_d^s = {}^{\ell}G^s/{}^{\ell}G^d$ using a model based on chiral effective field theory, as was also done in Refs. [302, 306, 307]. In that formalism ${}^{\ell}R_d^s$ is given by the ratio of loop diagram contributions to the electromagnetic form factors, where the relevant loop integrals are weighted by the appropriate 'disconnected' chiral coefficients for the s and d quarks [252, 306, 307].

The primary loop diagram relevant to this calculation is depicted in Fig. 7.6(a). For the electric form factor in particular, a higher-order diagram (Fig. 7.30(b)) is important as it makes a significant contribution of the opposite sign to that of Fig. 7.6(a), resulting in a large cancellation. While to the order of our chiral extrapolation this term contributes a constant to $G_E(Q^2)$ (enforcing charge conservation at $Q^2 = 0$), this is not a good approximation for the large values of Q^2 considered in this work.

For this reason we include Fig. 7.30(b), with an estimate of its Q^2-dependence, explicitly in our calculation of ${}^{\ell}R_d^s$ for the electric form factor. This is achieved by calculating the diagram in heavy-baryon chiral perturbation theory and modelling the Q^2-dependence of the photon-baryon vertex based on the lattice results described in previous sections. Further details are given in Appendix J.3.

For both the electric and magnetic form factors the effect of additionally including loops with decuplet baryon intermediate states is taken as an estimate of the uncertainty in the ratio ${}^{\ell}R_d^s$. The errors quoted for the numerical results in Table 7.6 in Section 7.7.2 combine this estimate in quadrature with that given by allowing the dipole mass-parameter Λ used in the finite-range regularisation scheme to vary in the range 0.6–1.0 GeV. The final values for ${}^{\ell}R_d^s$ are shown in Fig. 7.31.

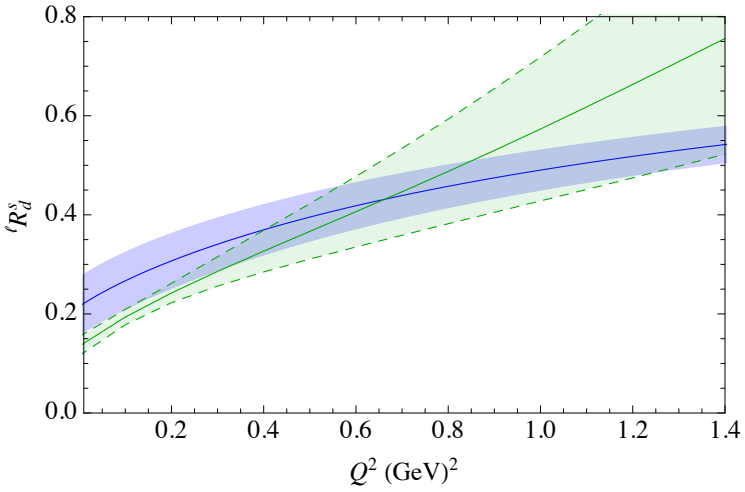

Figure 7.31: Estimate of ${}^{\ell}R_d^s$ from effective field theory with finite-range regularisation, for the electric (dashed green) and magnetic (solid blue) form factors. Details are given in Section 7.7.1.

7.7.2 Strange Form Factors at $Q^2 > 0$

The results of this analysis (using Eq.(7.50)) for the strange electric and magnetic form factors of the proton are summarised in Table 7.6 and are displayed in Fig. 7.32 alongside the latest experimental determinations of those quantities. All results (away from $Q^2 = 0$) are consistent with zero to within 2-sigma. The results for the strange magnetic form factor favour negative values which are consistent with recent experimental results. For the electric form factor, the two independent analyses based on the two sets of lattice QCD simulations at different lattice spacings and volumes are inconsistent at 1-sigma. As a result, simple estimates of the strange electric charge radius of the proton using a straight-line fit in Q^2 to the lowest-Q^2 result for G_E^s give results with opposite signs for the two analyses:

$$\langle r_E^2 \rangle^s = \begin{cases} 0.0086(79)\ \text{fm}^2, & \text{Set I,} \\ -0.0114(88)\ \text{fm}^2, & \text{Set II.} \end{cases} \tag{7.51}$$

Although we cannot make a conclusive statement without additional simulation results, we expect that this difference is dominated by statistical fluctuations.

Since experimental determinations of the strange form factors are obtained as linear combinations of G_E^s and G_M^s we also display results at the lowest values of the momentum transfer, $Q^2 = 0.26\,\text{GeV}^2$ and $0.17\,\text{GeV}^2$ for simulation sets I and II, respectively, in the G_M^s–G_E^s plane in Fig. 7.33. The available experimental results for similar values of Q^2 appear on this figure as ellipses. Both of our calculations are consistent with experiment to within 2-sigma.

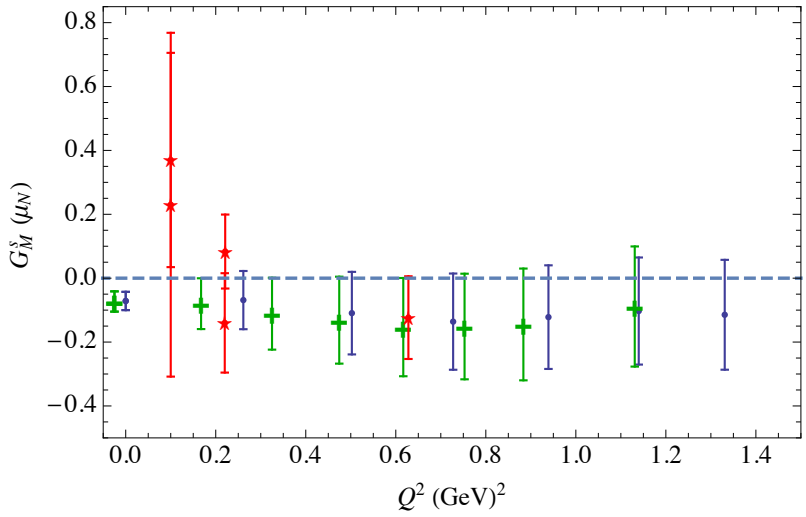

(a) Strange magnetic form factor.

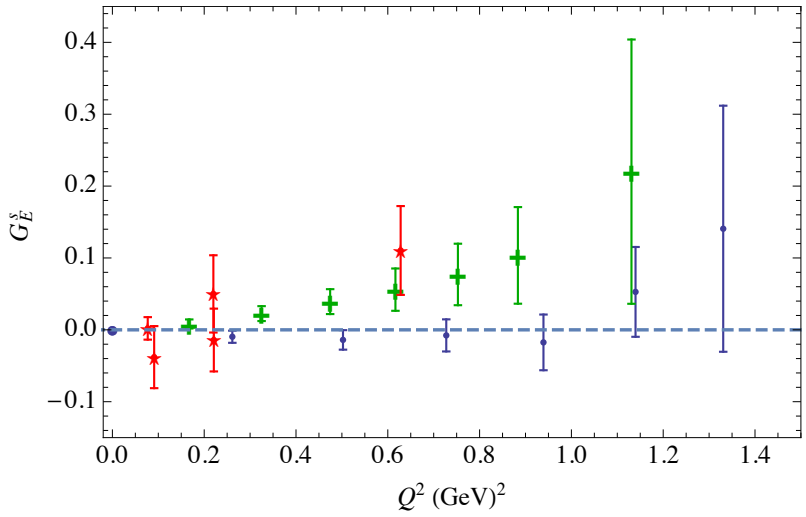

(b) Strange electric form factor.

Figure 7.32: Strange contribution to the magnetic and electric form factors of the proton, for strange quarks of unit charge. The blue circles and green crosses show the results of independent analyses based on lattice simulation sets I and II (with lattice scales $a = 0.074(2)\,\text{fm}$ and $0.062(2)\,\text{fm}$), respectively. The experimental results (red stars) are taken from Refs. [277, 280, 281, 289, 292, 294].

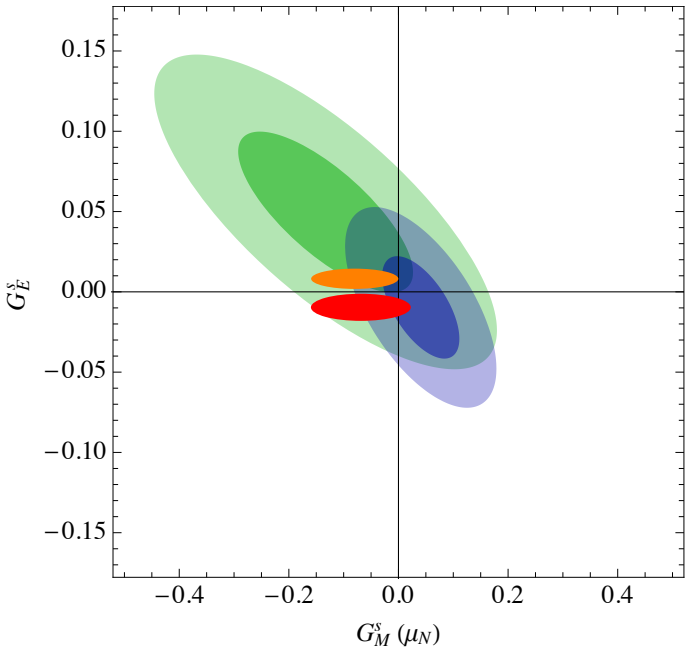

Figure 7.33: Comparison of the results of this work (to 1-sigma) at $Q^2 = 0.26\,\mathrm{GeV}^2$ for simulation set I (red ellipse), and at $Q^2 = 0.17\,\mathrm{GeV}^2$ for simulation set II (orange ellipse), with available experimental results at similar values of Q^2. The dark (pale) green ellipse shows 1-sigma (2-sigma) results from the A4 collaboration at $Q^2 = 0.23\,\mathrm{GeV}^2$ [293], while the blue ellipses show G0 collaboration results close to $Q^2 = 0.23\,\mathrm{GeV}^2$ [288, 289].

	Q^2 (GeV^2)	G_M^s (μ_N)	G_E^s
Set I	0.26	−0.069(12)(44)(15)(78)	−0.010(4)(5)(2)(6)
	0.50	−0.109(12)(59)(21)(112)	−0.014(8)(8)(3)(7)
	0.73	−0.136(15)(72)(24)(129)	−0.008(15)(11)(1)(13)
	0.94	−0.122(20)(83)(20)(136)	−0.017(28)(16)(3)(20)
	1.14	−0.103(16)(94)(17)(137)	0.053(34)(24)(40)(24)
	1.33	−0.115(20)(103)(18)(135)	0.141(57)(35)(153)(36)
Set II	0.17	−0.080(20)(48)(19)(56)	0.0081(31)(29)(4)(46)
	0.33	−0.111(20)(61)(24)(88)	0.023(7)(4)(3)(6)
	0.47	−0.131(23)(73)(26)(109)	0.039(12)(6)(9)(6)
	0.62	−0.153(28)(84)(29)(122)	0.056(20)(7)(18)(9)
	0.75	−0.151(28)(94)(28)(130)	0.077(27)(9)(30)(12)
	0.88	−0.145(35)(103)(25)(135)	0.104(40)(11)(50)(15)
	1.13	−0.089(47)(119)(14)(137)	0.220(78)(17)(164)(24)

Table 7.6: Results for the strange electric and magnetic form factors of the proton at the non-zero values of Q^2 investigated here. The first uncertainty quoted is propagated from the lattice values for the connected u and d quark contributions to the proton form factors, while the second is the additional systematic uncertainty included as described in Section 7.7.1. The third uncertainty is that propagated from the factor $\left({}^{\ell}R_d^s/(1-{}^{\ell}R_d^s)\right)$ (see Section 7.7.1). The last uncertainty is that from the Kelly parameterisation of the experimental p and n form factors [272], combined in quadrature with the parameterisation-uncertainty in those results for $Q^2 < 1$ GeV^2, where we use two parameterisations as described in Section 7.7.1.

7.7.3 Strange Magnetic Moment

Using the additional information available from experiment at $Q^2 = 0$, where the hyperon form factors have been measured [30], we also determine the strange quark contribution to the proton magnetic moment. We rearrange Eqs. (7.49a) and (7.49b), using the assumption of charge symmetry, to express the nucleon strange magnetic moment in terms of the hyperon moments [303, 305]:

$$ {}^{\ell}G^s = \left(\frac{{}^{\ell}R_d^s}{1 - {}^{\ell}R_d^s}\right)\left[2p + n - \frac{u^p}{u^\Sigma}\left(\Sigma^+ - \Sigma^-\right)\right], \tag{7.52a} $$

$$ {}^{\ell}G^s = \left(\frac{{}^{\ell}R_d^s}{1 - {}^{\ell}R_d^s}\right)\left[p + 2n - \frac{u^n}{u^\Xi}\left(\Xi^0 - \Xi^-\right)\right]. \tag{7.52b} $$

This rearrangement minimises the propagation of lattice systematics as only the ratios of form factors, not their absolute values, must be determined from lattice QCD.

The ratios u_M^p/u_M^Σ and u_M^n/u_M^Ξ of connected up quark contributions to the hyperon form factors, at a range of non-zero values of the momentum transfer Q^2, are taken from the lattice QCD analyses described earlier (see Section 7.4). We determine the $Q^2 = 0$ values needed here using a linear extrapolation in Q^2, with an additional experimental constraint provided by the equality of Eqs. (7.52a) and (7.52b):

$$ \frac{u_M^p}{u_M^\Sigma} = \frac{u_M^n}{u_M^\Xi}\left(\frac{\mu_{\Xi^0} - \mu_{\Xi^-}}{\mu_{\Sigma^+} - \mu_{\Sigma^-}}\right) + \left(\frac{\mu_p - \mu_n}{\mu_{\Sigma^+} - \mu_{\Sigma^-}}\right), \tag{7.53} $$

where μ_B denotes the experimental magnetic moment of the baryon B [30]. The fit is performed to the lattice results where $Q^2 < 1\,\mathrm{GeV}^2$, which display qualitatively linear behaviour and for which the linear-fit χ^2/d.o.f. is acceptable given the constraint of Eq. (7.53). Fitting to one less data point does not change the results to the precision quoted. The extrapolation for data set I is illustrated in Fig. 7.34; the same procedure is followed (independently) for data set II.

The best estimates of the ratios of the connected contributions to the baryon magnetic form factors at $Q^2 = 0$ are

$$ \left[\frac{u_M^p}{u_M^\Sigma}, \frac{u_M^n}{u_M^\Xi}\right] = \begin{cases} [1.096(16), 1.239(90)], & \text{Set I}, \\ [1.095(17), 1.222(98)], & \text{Set II}, \end{cases} \tag{7.54} $$

where the two sets of results correspond to our two independent analyses using lattice QCD simulation results at different lattice spacings and volumes as described earlier. These full-QCD numbers align remarkably well with those determined in Ref. [302], given that that analysis was based on quenched lattice simulation results at rather large quark masses, after the application of a theoretical 'unquenching' formalism and FRR [309].

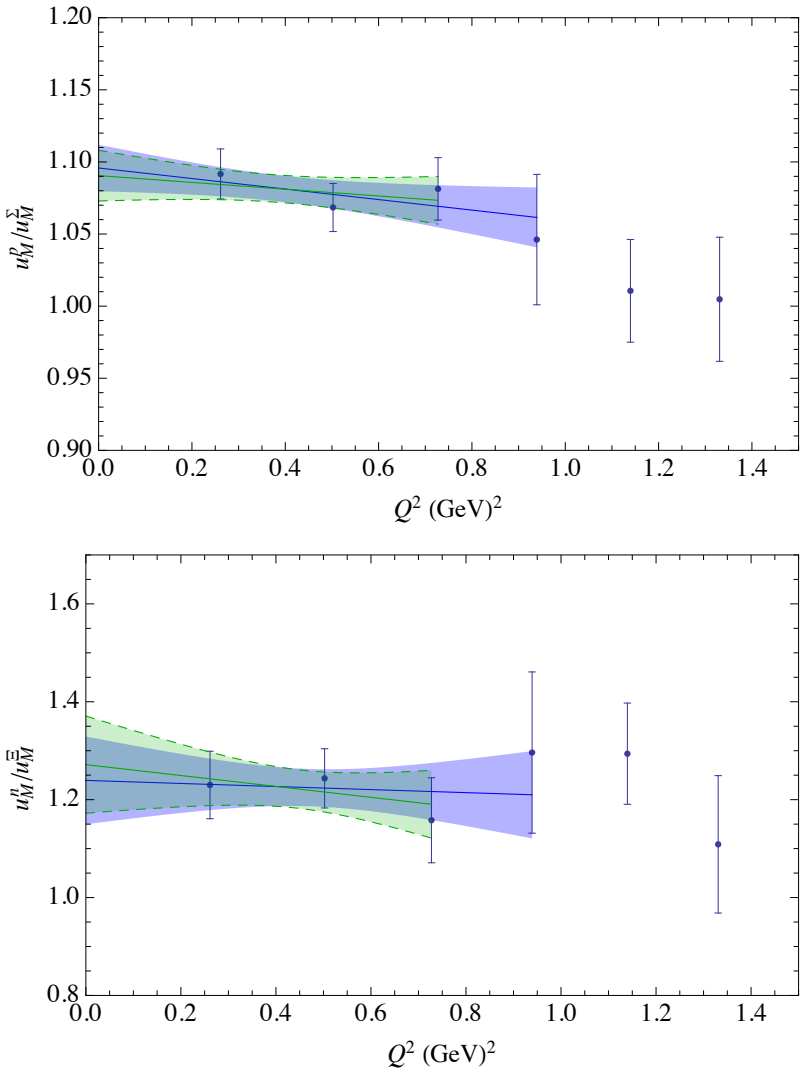

Figure 7.34: Results for the ratios u_M^p/u_M^Σ and u_M^n/u_M^Ξ of connected contributions to the baryon magnetic form factors for the simulations in data set I. The bands show simultaneous fits, linear in Q^2, to the lowest 4 (blue solid band) or 3 (green dashed band) data points, constrained by Eq. (7.53) at $Q^2 = 0$.

The resulting values for the strange magnetic moment (from Eqs. (7.52a) and (7.52b)), conventionally defined without the charge factor, are

$$G_M^s\big(Q^2=0\big) = \begin{cases} -0.071(13)(25)(4)\,\mu_N, & \text{Set I,} \\ -0.073(14)(26)(4)\,\mu_N, & \text{Set II.} \end{cases} \tag{7.55}$$

The first uncertainty is propagated from the lattice simulation results, the second, dominant, contribution comes from the ratio ${}^{\ell}R_d^s$, and the last is that from the experimental determination of the magnetic moments [30]. Clearly, the results of our analysis using the two independent calculations performed at different lattice spacings and volumes are in excellent agreement. Our final result, $G_M^s(Q^2=0) = -0.07 \pm 0.03\,\mu_N$, is non-zero to 2-sigma and an order of magnitude more precise than the closest experimental results.

7.8 Summary and Discussion

In this chapter we have presented a 2+1–flavour lattice QCD study of the electromagnetic form factors of the octet baryons. The results are based on two independent sets of simulations, with different lattice spacings and volumes, at a total of 13 discrete values of the momentum transfer in the range 0.17–1.3 GeV^2.

By performing simulations on configurations which 'map out' the m_l–m_s plane, rather than following a single trajectory in this space, we are able to robustly constrain chiral extrapolations of the Sachs form factors to the physical pseudoscalar masses. Independent extrapolations are performed at each simulation value of Q^2 using a formalism based on connected heavy-baryon chiral perturbation theory. An advantage of this method is that it requires no phenomenological input regarding the Q^2-dependence of the form factors. Systematic uncertainties are controlled by evaluating finite-volume corrections using the same formalism. The uncertainties inherent in the determination of the lattice scale a, the shape of the ultraviolet cutoff, and the value of the cutoff parameter Λ in the finite-range regularisation scheme, are found to be negligible. Moreover, both sets of simulations, which one would expect to suffer from different systematic finite-volume and finite-a effects, are entirely consistent after extrapolation to the physical point. It is notable that, even after extrapolation, the precision of these results rivals experimental measurements of the nucleon form factors.

It is particularly notable that a pure dipole form in Q^2 does not, in general, provide a good fit to the extrapolated lattice simulation results for G_E or G_M. A dipole-like fit function, with a more general polynomial in the denominator, fares significantly better. In fact, by using a dipole-like fit form and taking the experimental values for the baryon magnetic moments as additional input in Q^2-extrapolations of G_M, we are able to perform the first accurate extraction of the magnetic radii of the entire outer-ring baryon octet. Our analysis suggests that meaningful determinations of the magnetic moments and radii from lattice QCD alone requires a

more careful analysis than the standard procedure using a pure dipole form in Q^2 allows, unless simulations are performed for very small Q^2-values much less than $0.2\,\mathrm{GeV}^2$. Analyses similar to that performed here may reveal that other existing lattice simulations are in fact more compatible with experiment than the results of the standard calculations indicate.

The connected proton and neutron form factors, extrapolated to the physical pseudoscalar masses, agree remarkably well with the experimental determinations of these quantities at all values of Q^2 considered. This gives a good indication that disconnected quark-loop contributions to the nucleon form factors are small relative to the uncertainties of this calculation. By combining our lattice simulation results with experimental input, we are able to quantify this claim; we deduce values for the strange electromagnetic form factors of the proton which are consistent with available direct measurements of these quantities but span a far larger range of values of Q^2. At Q^2 above about $0.6\,\mathrm{GeV}^2$ our results are the first determinations of the strange form factors, experimental or based on lattice QCD. Our calculation of the strange magnetic moment is an order of magnitude more precise than the closest experimental result and is non-zero to 2-sigma: $G_M^s(Q^2 = 0) = 0.07(3)\mu_N$.

We also determine the CSV electromagnetic form factors of the nucleon based on our chiral extrapolations and a best value for the light-quark mass ratio m_u/m_d. Our results reveal that these quantities are at most 0.2% of the relevant proton form factors to 1-sigma—an order of magnitude smaller than suggested by previous work. Until now, the dominant uncertainty in experimental determinations of the strange proton form factors has come from the assumption that the CSV form factors are small; by quantifying this assumption, our precise results open the door for a new generation of experimental tests of QCD through the proton's strange form factors.

Chapter 8

Summary and Outlook

The strong-interaction properties of the nucleon are of broad interest; they directly reveal the structure and interactions of hadrons, inform astrophysics, and are necessary input into models of the evolution of the universe. Moreover, achieving percent-level precision in Standard Model (SM) expectations for nucleon observables has become essential in order to interpret modern direct and indirect experimental searches for new physics. We have investigated the strong-interaction properties of hadrons, in particular the nucleon, using lattice QCD and chiral effective field theory. Our focus has been on nucleon strangeness and charge symmetry violation (CSV), both associated with small deviations from approximate features of the nucleon in QCD.

Strange-quark effects in the nucleon provide a unique probe of the vacuum; as the nucleon has no net strangeness, $s\bar{s}$ pairs can only appear through quantum fluctuations. The contribution of s quarks to the mass of the nucleon—encoded in the strange sigma term—is also relevant to searches for particle dark matter by direct detection. Our precise new determination of this quantity using the Feynman-Hellmann relation, $\sigma_{Ns} = 20(6)$ MeV, is in line with results from direct lattice QCD simulations. We have also deduced values for the strange electromagnetic form factors of the proton based on a comprehensive new lattice study of the octet baryon Sachs form factors. Our results are consistent with available experimental measurements of these quantities but span a far larger range of values of the probing momentum scale, Q^2. At Q^2 above about $0.6\,\mathrm{GeV}^2$ ours are the first determinations of the strange form factors, experimental or based on lattice QCD. Our calculation of the strange magnetic moment is an order of magnitude more precise than the closest experimental result and is non-zero to 2-sigma: $G_M^s(Q^2 = 0) = 0.07(3)\mu_N$. These investigations present a coherent picture; contributions from strange quarks to both the mass and electromagnetic form factors of the nucleon appear at the percent-level.

CSV effects are smaller still and affect observables at a scale which is typically a fraction of a percent. Nevertheless, precise determinations of these quantities are essential at the level of precision of current experiments searching for physics beyond the SM. For example, our results reveal that the CSV contributions to the electromagnetic form factors of the nucleon are at most 0.2% at 1-sigma—an order of magnitude smaller than suggested by previous work. This revelation has removed the dominant uncertainty in experimental determinations of the proton's strange

form factors and has hence opened the door for a new generation of tests of QCD. Moreover, we have resolved CSV in the low spin-dependent and spin-independent Mellin moments of parton distribution functions to be non-zero to 3-sigma, but, again, these contributions appear only at the level of a fraction of a percent of the total moments. In particular, CSV corrections to the Bjorken sum rule are approximately 0.5%. This is an order of magnitude smaller than the uncertainty of the current best experimental determination but will nevertheless be significant in connection with proposed measurements at a future electron-ion collider. Proper consideration of the small CSV effects in the spin-independent Mellin moments may reduce the 3-sigma discrepancy with the SM reported by the NuTeV collaboration, in neutrino-nucleus deep inelastic scattering experiments, by up to 1-sigma.

Our investigation of nucleon CSV effects proceeded using a novel formalism combining the symmetries of QCD, encoded in the low-energy chiral effective field theory, with the information gained from studying the entire baryon octet in isospin-averaged 2+1–flavour lattice QCD simulations. In principle this method could constrain the light-quark mass ratio $R = m_u/m_d$, if the strong and electromagnetic mass-splittings among members of the baryon isospin multiplets were precisely known. Even at the level of precision of current determinations of these quantities our analysis favours $R = 0.553(43)$ over the slightly smaller number, $R = 0.47(4)$, obtained from a world-average of lattice simulation results. Clearly, more precise determinations of the strong and electromagnetic CSV effects in the baryon masses are of considerable interest.

In the course of our study we were also able to calculate a number of other observables relevant to nucleon and hyperon structure which are of phenomenological importance in their own right. Through a detailed analysis of the octet baryon masses, based on several independent sets of lattice simulations, we determined the pion-nucleon sigma term: $\sigma_{\pi N} = 46(7)\,\text{MeV}$. This result is in complete agreement with the benchmark experimental value, 45(8) MeV, from an analysis by Gasser, Leutwyler and Sainio in the early 1990s. Clearly, lattice simulations will be able to rival experimental precision for this quantity in the near future. Furthermore, our investigation of the lowest spin-dependent parton distribution moment can give some insight into the resolution of the proton spin puzzle: we have revealed that the fraction of spin carried by the quarks in the octet baryons varies, that is, that the quark spin-fraction is structure-dependent. This result suggests that the spin-suppression observed in the proton cannot be explained by the axial anomaly alone.

Our complete lattice study of the octet baryon electromagnetic form factors—including careful consideration of meson mass, finite-volume, and lattice discretisation effects—allowed a detailed investigation of the hyperon form factors, which have received little attention in the literature to date. These quantities are of interest both in their own right and because they provide valuable insight into the environmental sensitivity of the distribution of quarks inside a hadron. Importantly, we performed the first accurate extraction of the magnetic radii of the entire outer-ring baryon octet from lattice QCD. It is also notable that the precision of our results

for the nucleon form factors, extrapolated to the physical point, rivals experimental measurements.

In summary, we have determined precise new SM values for a number of strong observables relevant to nucleon and hyperon structure. This investigation has been guided by experiment. Not only do our results set benchmark values for tests of QCD, but they provide input for direct searches for physics beyond the SM and inform the analysis of experimental measurements of poorly-known SM quantities. By combining lattice QCD simulations with chiral effective field theory techniques we have truly been able to probe QCD in the physically-relevant parameter space. We have carefully corrected systematic effects in our simulations, such as unphysically-large meson masses and finite lattice volumes, and have taken advantage of the information provided by the baryon octet to investigate SU(3)-flavour–breaking effects. Most notably, we have developed a formalism for determining nucleon CSV observables from isospin-averaged 2+1–flavour lattice simulations. A coherent picture has emerged; CSV effects typically appear at the level of a fraction of a percent—an order of magnitude smaller than most previous estimates. Our study of strange-quark contributions to nucleon observables has revealed that these are of order 1%.

Appendix A

Formal Details of Heavy Mass Techniques

In this appendix we explicitly derive the heavy-baryon Lagrangian for the interactions of the spin-$\frac{1}{2}$ baryon octet with the octet mesons from the familiar relativistic expression. For simplicity we omit electromagnetic terms and interactions with the spin-$\frac{3}{2}$ decuplet; as the effective theory is represented by the most general Lagrangian consistent with the broken chiral symmetry, it is in most cases simplest to construct this directly in terms of the heavy-baryon fields. This is the approach which is taken in Chapter 3.

Representing the octet baryons in matrix form, as in Section 3.3.2, the standard relativistic Lagrangian for baryon-meson interactions is

$$\mathcal{L} = \overline{B}(i\not{D} - M_B) + D\overline{B}\gamma_\mu\gamma_5\{A^\mu, B\} + F\overline{B}\gamma_\mu\gamma_5[A^\mu B]. \tag{A.1}$$

Considering the baryons to be heavy, their four-momenta are expressed as $p_\mu = M_B v_\mu + k_\mu$, where v_μ is a four-velocity satisfying $v^2 = 1$, and k_μ is a soft momentum with $v \cdot k \ll \{M_B, \Lambda_\chi\}$. One can then construct eigenstates of operators which project the upper and lower components of the Dirac wavefunction, so that

$$B(x) = e^{-iM_B v\cdot x}(H(x) + h(x)), \tag{A.2}$$

where

$$H(x) = e^{iM_B v\cdot x} P_+ B(x), \tag{A.3a}$$
$$h(x) = e^{iM_B v\cdot x} P_- B(x), \tag{A.3b}$$

and

$$P_\pm = \frac{1}{2}(1 \pm \not{v}). \tag{A.4}$$

In terms of these new fields, the Lagrangian of Eq. (A.1) assumes the form

$$\mathcal{L} = \overline{H}\mathcal{A}H + \overline{h}\mathcal{B}H + \overline{H}\gamma_0\mathcal{B}^\dagger\gamma_0 h - \overline{h}\mathcal{C}h. \tag{A.5}$$

Using the projection operator identities

$$P_\pm P_\mp = 0, \quad P_\pm P_\pm = P_\pm, \quad P_\pm \not{D} P_\pm = \pm v\cdot D P_\pm, \quad P_\pm \not{D} P_\mp = \not{D} - \not{v} v\cdot D, \quad \text{(A.6)}$$

one finds the explicit low-energy expansions

$$\mathcal{A} = iv\cdot D + 2D\overline{B}\mathbf{S}_\mu\{A^\mu, B\} + 2F\overline{B}\mathbf{S}_\mu[A^\mu, B] + \ldots, \quad \text{(A.7a)}$$

$$\mathcal{B} = i(\not{D} - \not{v} v\cdot D) - D\overline{B}\gamma_5 v_\mu\{A^\mu, B\} - F\overline{B}\gamma_5 v_\mu[A^\mu, B] + \ldots, \quad \text{(A.7b)}$$

$$\mathcal{C} = \mathcal{A} + 2M_B + \ldots. \quad \text{(A.7c)}$$

Clearly the two field components H and h are coupled in the Lagrangigan of Eq. (A.5). This can be resolved via the field-redefinition

$$h' = h - \mathcal{C}^{-1}\mathcal{B}H. \quad \text{(A.8)}$$

In path-integral language it is clear that the 'heavy' field h, with a mass parameter of twice the baryon mass, can be integrated out: the generating functional $Z[\text{sources}]$ is given by

$$\begin{aligned} e^{iZ[\text{sources}]} &= \text{const.} \int \delta H\, \delta\overline{H}\, \delta h\, \delta\overline{h} \exp\left(i \int d^4x \, (\mathcal{L} + \text{source terms}) \right) \\ &= \text{const.} \int \delta H\, \delta\overline{H}\, \delta h\, \delta\overline{h} \exp\left(i \int d^4x \, \Big(\overline{H}\big(\mathcal{A} + \gamma_0\mathcal{B}\gamma_0\mathcal{C}^{-1}\mathcal{B}\big)H \right. \\ &\qquad \left. - \overline{h}'\mathcal{C}h' + \text{source terms} \Big) \right) \\ &= \text{const.} \int \delta H\, \delta\overline{H}\, \det(\mathcal{C}) \exp\left(i \int d^4x \, \Big(\overline{H}\big(\mathcal{A} + \gamma_0\mathcal{B}\gamma_0\mathcal{C}^{-1}\mathcal{B}\big)H \right. \\ &\qquad \left. + \text{source terms} \Big) \right), \end{aligned} \quad \text{(A.9)}$$

where the integrated determinant generates an (uninteresting) overall constant. Finally, we have derived an effective Lagrangian in terms of the 'light' field components H only:

$$\mathcal{L}_{\text{eff.}} = \overline{H}\big(\mathcal{A} + \big(\gamma_0\mathcal{B}^\dagger\gamma_0\big)\mathcal{C}^{-1}\mathcal{B}\big)H. \quad \text{(A.10)}$$

Expanding $\mathcal{C}^{-1}$ in a power series in $1/M_B$, to leading order, gives the Lagrangian presented in Eq. (3.29). The first $1/M_B$ corrections are generated by

$$\mathcal{L}^{(1/M_B)} = \overline{H}\,\frac{\gamma_0\mathcal{B}^\dagger\gamma_0\mathcal{B}}{2M_B}\,H. \quad \text{(A.11)}$$

Of course, when loop contributions are calculated, a set of counterterms is required to absorb the various divergences which arise. These are constructed in the heavy-baryon formalism just as they are in the relativistic framework: by considering all possible local terms allowed by the symmetry requirements of parity transforma-

tions, charge conjugation, hermitean conjugation, overall Lorentz-invariance, and invariance under chiral vector and axial-vector transformations.

Appendix B

Definitions and Identities

Here we collate a number of identities and relations which were used to simplify the expressions which arose in the derivation of the results presented in Chapters 4, 6, and 7. As defined in Chapter 3, v^μ denotes the four-velocity of a heavy baryon, Pauli-Lubanski spin operators are denoted by $\mathbf{S}^\mu$, and $P^{\mu\nu}$ is a spin-polarisation projector that acts on the decuplet baryon field tensor T^μ to project out the positive spin-$\frac{1}{2}$ solutions to the equation of motion.

$$v\cdot\mathbf{S}=0, \qquad \mathbf{S}^2 B=-\frac{3}{4}B, \tag{B.1}$$

$$v^\mu T_\mu=0, \qquad \mathbf{S}^\mu T_\mu=0, \tag{B.2}$$

$$P^{\mu\nu}P_\nu{}^\lambda=-P^{\mu\lambda}, \qquad P^{\mu\nu}g_{\mu\nu}=-2, \tag{B.3}$$

$$P^{\mu\nu}\mathbf{S}_\mu=-\frac{4}{3}\mathbf{S}^\nu, \qquad \mathbf{S}_\nu P^{\mu\nu}=-\frac{4}{3}\mathbf{S}^\mu, \tag{B.4}$$

$$\{\mathbf{S}^\lambda,\mathbf{S}^\sigma\}=\frac{1}{2}\big(v^\lambda v^\sigma-g^{\lambda\sigma}\big), \qquad P^{\mu\nu}=(v^\mu v^\nu-g^{\mu\nu})-\frac{4}{3}\mathbf{S}^\mu\mathbf{S}^\nu, \tag{B.5}$$

$$P^{\mu\nu}v_\nu=P^{\mu\nu}v_\mu=0, \qquad P^{\mu\nu}\mathbf{S}_\nu=\mathbf{S}_\mu P^{\mu\nu}=0. \tag{B.6}$$

Throughout this work we employ a compact notation for field bilinear invariants which was originally employed by Labrenz and Sharpe in Ref. [270]. In the following expressions, A is an operator with the transformation properties of the axial current A_μ, while Γ is an arbitrary Dirac matrix, e.g., the spin operator $\mathbf{S}^\mu$. The octet and decuplet baryon tensors B_{ijk} and T^μ_{ijk} are as defined in Eqs. (3.39) and (3.32).

$$\big(\overline{B}\Gamma B\big)\equiv\overline{B}^\alpha_{kji}\Gamma^\beta_\alpha B_{ijk,\beta}, \tag{B.7}$$

$$\big(\overline{B}\Gamma AB\big)\equiv\overline{B}^\alpha_{kji}\Gamma^\beta_\alpha A_{ii'}B_{i'jk,\beta}, \tag{B.8}$$

$$\big(\overline{B}\Gamma BA\big)\equiv\overline{B}^\alpha_{kji}\Gamma^\beta_\alpha A_{kk'}B_{ijk',\beta}\times(-1)^{(i+j)(k+k')}, \tag{B.9}$$

$$\big(\overline{B}\Gamma A^\mu T_\mu\big)\equiv\overline{B}^\alpha_{kji}\Gamma^\beta_\alpha A^\mu_{ii'}T^\beta_{\mu,i'jk}, \tag{B.10}$$

$$\big(\overline{T}^\mu\Gamma T_\mu\big)\equiv\overline{T}^\mu_{kji,\alpha}\Gamma^\alpha_\beta T^\beta_{\mu,ijk}, \tag{B.11}$$

$$\big(\overline{T}^\mu\Gamma A^\nu T_\mu\big)\equiv\overline{T}^\mu_{kji,\alpha}\Gamma^\alpha_\beta A^\nu_{ii'}T^\beta_{\mu,i'jk}. \tag{B.12}$$

Appendix C

Derivations for Chapter 3

In this appendix we give the details of several derivations relevant to the discussion of Chapter 3.

C.1 Loop Integral Transform

Here we show the simplification of a loop integral required in Section 3.6.

$$\begin{aligned}
\overline{I} &= \int \frac{d^4k}{(2\pi)^4} \frac{k_i k_j}{(k_0 - i\epsilon)(k^2 - m^2 + i\epsilon)} \\
&= \int \frac{d^3\vec{k}}{(2\pi)^4} \int dk_0 \frac{k_i k_j}{(k_0 - i\epsilon)(k^2 - m^2 + i\epsilon)} \\
&= \int \frac{d^3\vec{k}}{(2\pi)^4} \int dk_0 \frac{k_i k_j}{(k_0 - i\epsilon)(k_0 - \omega + i\epsilon)(k_0 + \omega - i\epsilon)}, \qquad \text{where } \omega = \sqrt{\vec{k}^2 + m^2}, \\
&= -(2\pi i) \int \frac{d^3\vec{k}}{(2\pi)^4} \left\{ \frac{k_i k_j}{k_0(k_0 + w)} \bigg|_{k_0 = \omega} \right\} \\
&= -(2\pi i) \int \frac{d^3\vec{k}}{(2\pi)^4} \left\{ \frac{k_i k_j}{2\omega^2} \right\} \\
&= -i \int \frac{d^3\vec{k}}{(2\pi)^3} \left\{ \frac{k_i k_j}{2(\vec{k}^2 + m^2)} \right\} \\
&= -i \frac{\delta_{ij}}{6} \int \frac{d^3\vec{k}}{(2\pi)^3} \frac{\vec{k}^2}{\vec{k}^2 + m^2} \\
&= -i \frac{2\pi\delta_{ij}}{3} \int_0^\infty \frac{dk}{(2\pi)^3} \frac{k^4}{k^2 + m^2}.
\end{aligned} \tag{C.1}$$

C.2 Example of Finite-Volume Correction

Here we explicitly derive the finite-volume correction expression presented in Section 3.6. We consider the integral of Eq. (3.55), with a dipole regulator in the FRR

scheme:

$$I_\pi^{\text{dip.}} = \frac{2}{\pi}\int dk \frac{k^4}{k^2+m^2}\left(\frac{\Lambda^2}{\Lambda^2+k^2}\right) = \frac{1}{2\pi^2}\int d^3k \frac{k^2}{k^2+m^2}\left(\frac{\Lambda^2}{\Lambda^2+k^2}\right). \tag{C.2}$$

The finite-volume correction to the associated loop-integral expression can be modeled as

$$\begin{aligned}
\delta_L\big(I_\pi^{\text{dip.}}\big) =& \frac{1}{2\pi^2}\left[\frac{(2\pi)^3}{L^3}\sum_{\vec{k}} \frac{k^2}{k^2+m^2}\left(\frac{\Lambda^2}{\Lambda^2+k^2}\right)^4 - \int d^3k \frac{k^2}{k^2+m^2}\left(\frac{\Lambda^2}{\Lambda^2+k^2}\right)^4\right] \\
=& \frac{1}{2\pi^2}\left[\frac{(2\pi)^3}{L^3}\sum_{\vec{k}} \left(\frac{\Lambda^2}{\Lambda^2+k^2}\right)^4 - \int d^3k \left(\frac{\Lambda^2}{\Lambda^2+k^2}\right)^4\right] \\
&+ \frac{1}{2\pi^2}\left[\frac{(2\pi)^3}{L^3}\sum_{\vec{k}} \frac{-m^2}{k^2+m^2}\left(\frac{\Lambda^2}{\Lambda^2+k^2}\right)^4 - \int d^3k \frac{-m^2}{k^2+m^2}\left(\frac{\Lambda^2}{\Lambda^2+k^2}\right)^4\right] \\
=& 4\pi\Lambda^8\left[\frac{1}{L^3}\sum_{\vec{k}} \left(\frac{1}{k^2+\Lambda^2}\right)^4 - \int \frac{d^3k}{(2\pi)^3}\left(\frac{1}{k^2+\Lambda^2}\right)^4\right] \\
&- 4\pi m^2\Lambda^8\left[\frac{1}{L^3}\sum_{\vec{k}} \frac{1}{(k^2+m^2)(k^2+\Lambda^2)^4} - \int \frac{d^3k}{(2\pi)^3}\frac{1}{(k^2+m^2)(k^2+\Lambda^2)^4}\right].
\end{aligned} \tag{C.3}$$

The final step is to use Feynman parameters to express the second term in the expression in the standard form:

$$\begin{aligned}
\frac{1}{(k^2+m^2)(k^2+\Lambda^2)^4} &= 4\int_0^1 dx \frac{(1-x)^3}{\left(x(k^2+m^2)+(1-x)(k^2+\Lambda^2)\right)^5} \\
&= 4\int_0^1 dx \frac{(1-x)^3}{\left(k^2+xm^2+(1-x)\Lambda^2\right)^5},
\end{aligned} \tag{C.4}$$

giving the result stated in Section 3.7:

$$\delta_L\big(I_\pi^{\text{dip.}}\big) = 4\pi\Lambda^8\delta_L(\Lambda,4) - 16\pi m^2\Lambda^8\int_0^1 dx(1-x)^3\delta_L\Big(\sqrt{xm^2+(1-x)\Lambda^2},5\Big). \tag{C.5}$$

Appendix D

Additional Figures for Chapter 4

In this appendix we display several additional figures relevant to the discussion of Chapter 4.

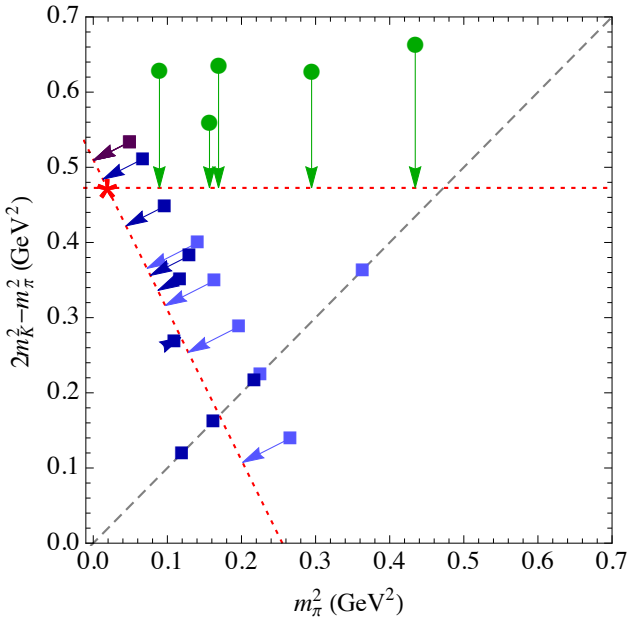

Figure D.1: Locations of the lattice simulations in the m_l–m_s plane. The symbols are as in Fig. 4.1. The arrows show the chosen projection of the lattice simulation results onto the trajectories plotted in Figs. 4.2 and 4.3.

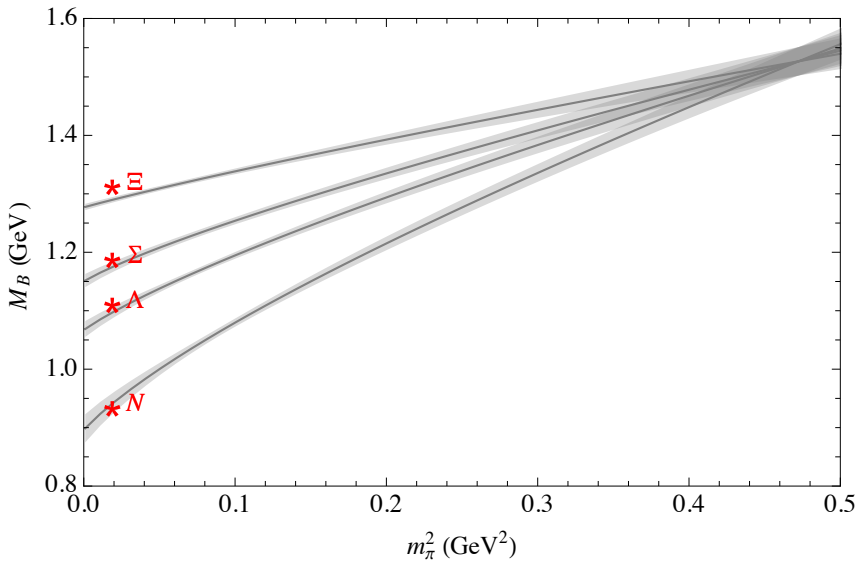

Figure D.2: Fit to the QCDSF-UKQCD collaboration baryon octet data (also shown in Fig. 4.3), plotted along the trajectory of fixed (physical) strange quark mass. The error bands are as in Fig. 4.3. The red stars show the experimental values of the baryon masses [30]. This figure may be directly compared with Fig. 4.2, which shows the fit to the PACS-CS collaboration lattice results along the same trajectory in m_π–m_K space.

Appendix E

Additional Results for Chapter 5

In this appendix we give some additional results of the work presented in Section 5.3.

	σ_{Bq} (MeV)		
B	u	d	s
p	19(3)	24(4)	53(8)
n	13(2)	35(5)	50(8)
Λ	11(2)	20(3)	185(11)
Σ^0	9(1)	16(2)	227(14)
Σ^+	16(2)	3(1)	231(14)
Σ^-	2(1)	30(4)	224(13)
Ξ^0	9(1)	1.15(41)	339(16)
Ξ^-	0.78(23)	16(2)	335(15)

Table E.1: Octet baryon sigma terms, derived using the Feynman-Hellmann relation applied to the chiral extrapolation of PACS-CS collaboration lattice simulation results described in Chapter 5, with the lattice scale set using the mass-independent prescription (c.f., Table 5.3).

	σ_{Bq} (MeV)		
B	u	d	s
p	17(3)	21(4)	27(15)
n	11(2)	30(5)	25(15)
Λ	10(2)	17(3)	163(14)
Σ^0	8(1)	14(2)	234(14)
Σ^+	15(2)	1(1)	236(14)
Σ^-	1(2)	27(3)	231(14)
Ξ^0	9(1)	0.00(81)	336(14)
Ξ^-	0.11(44)	16(2)	332(14)

Table E.2: As in Table E.2, based on the extrapolation of QCDSF-UKQCD collaboration lattice simulations of the octet baryon masses.

Appendix F

Tables of Chiral Coefficients

The tables in this appendix give explicit expressions for the various chiral coefficients used in this body of work, particularly in Chapters 6 and 7. Coefficients which vanish are either omitted from the tables, or their positions are left blank.

F.1 Strong Interaction Vertices

Tables F.1–F.14 give the Clebsch-Gordan coefficients $C_{BB'\phi}$ and $C_{BT\phi}$ (defined in Eqs. (3.40d) and (3.40e)), which correspond to leading-order strong interaction vertices coupling an octet-baryon to octet-baryon or octet-baryon to decuplet-baryon through the emission of a meson. These vertices are illustrated in Figs. 3.1(a) and 3.1(b). The coefficients are expressed in terms of the parameters D, F, and $\mathcal{C}$, which are defined in the Lagrangians of Eq. (3.29) and (3.37) in Chapter 3.

F.2 Twist-Two Operator Insertion Vertices

The Clebsch-Gordan coefficients corresponding to insertions of the twist-two operators relevant to our exploration of parton distribution moments in Chapter 6 are given in Tables F.15–F.24. The coefficients are defined in Eqs. (6.17) and (6.18), and the associated vertices are illustrated in Fig. 6.1. Superscripts (n) on every coefficient C and on every unknown parameter α, β, σ, and b_i (defined in the Lagrangians derived in Section 6.2) have been suppressed for clarity of notation. We have displayed the coefficient tables for the spin-independent case only; the spin-dependent coefficients are recovered by the trivial re-labelling $\alpha^{(n)} \to \Delta\alpha^{(n)}$ etc. The labels 'Doubly', 'Singly', 'Triply', and 'Other' denote the status of the indicated quark flavour in the baryon B or T, i.e., whether it is the doubly, singly or triply-represented quark, or does not appear at all.

F.3 Electromagnetic Form Factor Extrapolation

In Tables F.25–F.37 we present expressions for the coefficients α^{Bq}, $\overline{\alpha}^{Bq(q')}$, and $\beta_{O/D/T}^{Bq(\phi)}$ which appear in the chiral extrapolation expressions for the magnetic and electric Sachs form factors, Eqs. (7.30) and (7.39), derived in Chapter 7. These

parameters take the same form in terms of the undetermined chiral-limit form factors $c_i^{E/M}$ and $\mu_{\alpha/\beta/\gamma}$ (defined in Section 7.3.2) for the magnetic and electric form factors (under the replacements $\mu_F \to b_F$ and $\mu_D \to b_D$ for G_E). Of course, the numerical values of the chiral-limit form factors differ not only for the electric and magnetic cases, but at each fixed value of Q^2 at which the extrapolation is applied. As above, the labels 'Doubly', 'Singly', and 'Other' indicate whether the quark q' or q is doubly-represented, singly-represented, or not at all represented in the baryon B.

	$C_{BB'\pi^+}$				
B' \ B	p	Λ	Σ^0	Σ^+	Ξ^0
n	$2(D+F)$				
Λ				$2\sqrt{\frac{2}{3}}D$	
Σ^0				$-2\sqrt{2}F$	
Σ^-		$2\sqrt{\frac{2}{3}}D$	$2\sqrt{2}F$		
Ξ^-					$2(D-F)$

Table F.1: Clebsch-Gordan coefficients for the leading-order strong coupling of octet baryons B and B' through the emission of the pseudoscalar meson π^+.

	$C_{BB'\pi^-}$				
B' \ B	n	Λ	Σ^0	Σ^-	Ξ^-
p	$2(D+F)$				
Λ				$2\sqrt{\frac{2}{3}}D$	
Σ^0				$2\sqrt{2}F$	
Σ^+		$2\sqrt{\frac{2}{3}}D$	$-2\sqrt{2}F$		
Ξ^0					$2(D-F)$

Table F.2: Clebsch-Gordan coefficients for the leading-order strong coupling of octet baryons B and B' through the emission of the pseudoscalar meson π^-.

B' \ B	$C_{BB'K^0}$				
	p	n	Λ	Σ^0	Σ^-
Λ		$-\sqrt{\frac{2}{3}}(D+3F)$			
Σ^0		$\sqrt{2}(F-D)$			
Σ^+	$2(D-F)$				
Ξ^0			$-\sqrt{\frac{2}{3}}(D-3F)$	$-\sqrt{2}(D+F)$	
Ξ^-					$2(D+F)$

Table F.3: Clebsch-Gordan coefficients for the leading-order strong coupling of octet baryons B and B' through the emission of the pseudoscalar meson K^0.

B' \ B	$C_{BB'K^+}$				
	p	n	Λ	Σ^0	Σ^+
Λ	$-\sqrt{\frac{2}{3}}(D+3F)$				
Σ^0	$\sqrt{2}(D-F)$				
Σ^-		$2(D-F)$			
Ξ^0					$2(D+F)$
Ξ^-			$-\sqrt{\frac{2}{3}}(D-3F)$	$\sqrt{2}(D+F)$	

Table F.4: Clebsch-Gordan coefficients for the leading-order strong coupling of octet baryons B and B' through the emission of the pseudoscalar meson K^+.

$C_{BB'K^-}$					
B' \ B	Λ	Σ^0	Σ^-	Ξ^0	Ξ^-
p	$-\sqrt{\frac{2}{3}}(D+3F)$	$\sqrt{2}(D-F)$			
n			$2(D-F)$		
Λ					$-\sqrt{\frac{2}{3}}(D-3F)$
Σ^0					$\sqrt{2}(D+F)$
Σ^+				$2(D+F)$	

Table F.5: Clebsch-Gordan coefficients for the leading-order strong coupling of octet baryons B and B' through the emission of the pseudoscalar meson K^-.

$C_{BB'\overline{K}^0}$					
B' \ B	Λ	Σ^0	Σ^+	Ξ^0	Ξ^-
p			$2(D-F)$		
n	$-\sqrt{\frac{2}{3}}(D+3F)$	$\sqrt{2}(F-D)$			
Λ				$-\sqrt{\frac{2}{3}}(D-3F)$	
Σ^0				$-\sqrt{2}(D+F)$	
Σ^-					$2(D+F)$

Table F.6: Clebsch-Gordan coefficients for the leading-order strong coupling of octet baryons B and B' through the emission of the pseudoscalar meson $\overline{K}^0$.

BB' \ ϕ	$C_{BB'\phi}$	
	π^0	η
pp	$\frac{1}{3}\sqrt{2}\big(3(D+F)\cos\epsilon - \sqrt{3}(D-3F)\sin\epsilon\big)$	$-\frac{1}{3}\sqrt{2}\big(\sqrt{3}(D-3F)\cos\epsilon + 3(D+F)\sin\epsilon\big)$
nn	$-\frac{1}{3}\sqrt{2}\big(3(D+F)\cos\epsilon + \sqrt{3}(D-3F)\sin\epsilon\big)$	$\sqrt{2}(D+F)\sin\epsilon - \sqrt{\frac{2}{3}}(D-3F)\cos\epsilon$
$\Lambda\Lambda$	$-2\sqrt{\frac{2}{3}}D\sin\epsilon$	$-2\sqrt{\frac{2}{3}}D\cos\epsilon$
$\Lambda\Sigma^0$	$2\sqrt{\frac{2}{3}}D\cos\epsilon$	$-2\sqrt{\frac{2}{3}}D\sin\epsilon$
$\Sigma^0\Sigma^0$	$2\sqrt{\frac{2}{3}}D\sin\epsilon$	$2\sqrt{\frac{2}{3}}D\cos\epsilon$
$\Sigma^+\Sigma^+$	$2\sqrt{2}F\cos\epsilon + 2\sqrt{\frac{2}{3}}D\sin\epsilon$	$2\sqrt{\frac{2}{3}}D\cos\epsilon - 2\sqrt{2}F\sin\epsilon$
$\Sigma^-\Sigma^-$	$2\sqrt{\frac{2}{3}}D\sin\epsilon - 2\sqrt{2}F\cos\epsilon$	$2\sqrt{\frac{2}{3}}D\cos\epsilon + 2\sqrt{2}F\sin\epsilon$
$\Xi^0\Xi^0$	$-\frac{1}{3}\sqrt{2}\big(3(D-F)\cos\epsilon + \sqrt{3}(D+3F)\sin\epsilon\big)$	$-\frac{1}{3}\sqrt{2}\big(\sqrt{3}(D+3F)\cos\epsilon + 3(F-D)\sin\epsilon\big)$
$\Xi^-\Xi^-$	$\frac{1}{3}\sqrt{2}\big(3(D-F)\cos\epsilon - \sqrt{3}(D+3F)\sin\epsilon\big)$	$-\frac{1}{3}\sqrt{2}\big(\sqrt{3}(D+3F)\cos\epsilon + 3(D-F)\sin\epsilon\big)$

Table F.7: Clebsch-Gordan coefficients for the leading-order strong coupling of octet baryons B and B' through the emission of the pseudoscalar mesons π^0 and η. The π^0–η mixing parameter ϵ is defined in Eq. (4.5).

$C_{BT\pi^+} \times \mathcal{C}^{-1}$						
T \ B	p	n	Λ	Σ^0	Σ^+	Ξ^0
Δ^0	$\frac{1}{\sqrt{3}}$					
Δ^-		1				
Σ^{*0}					$-\frac{1}{\sqrt{6}}$	
Σ^{*-}			$-\frac{1}{\sqrt{2}}$	$\frac{1}{\sqrt{6}}$		
Ξ^{*-}						$-\frac{1}{\sqrt{3}}$

Table F.8: Clebsch-Gordan coefficients for the leading-order strong coupling of an octet baryon B to a decuplet baryon T through the emission of the pseudoscalar meson π^+.

$C_{BT\pi^-} \times \mathcal{C}^{-1}$						
T \ B	p	n	Λ	Σ^0	Σ^-	Ξ^-
Δ^{++}	-1					
Δ^+		$-\frac{1}{\sqrt{3}}$				
Σ^{*0}					$\frac{1}{\sqrt{6}}$	
Σ^{*+}			$\frac{1}{\sqrt{2}}$	$\frac{1}{\sqrt{6}}$		
Ξ^{*0}						$\frac{1}{\sqrt{3}}$

Table F.9: Clebsch-Gordan coefficients for the leading-order strong coupling of an octet baryon B to a decuplet baryon T through the emission of the pseudoscalar meson π^-.

$C_{BTK^0} \times \mathcal{C}^{-1}$						
T \ B	p	n	Λ	Σ^0	Σ^-	Ξ^-
Σ^{*0}		$-\frac{1}{\sqrt{6}}$				
Σ^{*+}	$-\frac{1}{\sqrt{3}}$					
Ξ^{*0}			$\frac{1}{\sqrt{2}}$	$\frac{1}{\sqrt{6}}$		
Ξ^{*-}					$\frac{1}{\sqrt{3}}$	
Ω^-						1

Table F.10: Clebsch-Gordan coefficients for the leading-order strong coupling of an octet baryon B to a decuplet baryon T through the emission of the pseudoscalar meson K^0.

$C_{BTK^+} \times \mathcal{C}^{-1}$						
T \ B	p	n	Λ	Σ^0	Σ^+	Ξ^0
Σ^{*0}	$\frac{1}{\sqrt{6}}$					
Σ^{*-}		$\frac{1}{\sqrt{3}}$				
Ξ^{*0}					$-\frac{1}{\sqrt{3}}$	
Ξ^{*-}			$-\frac{1}{\sqrt{2}}$	$\frac{1}{\sqrt{6}}$		
Ω^-						-1

Table F.11: Clebsch-Gordan coefficients for the leading-order strong coupling of an octet baryon B to a decuplet baryon T through the emission of the pseudoscalar meson K^+.

$C_{BTK^-} \times \mathcal{C}^{-1}$					
T \ B	Σ^0	Σ^+	Σ^-	Ξ^0	Ξ^-
Δ^{++}		1			
Δ^+	$-\sqrt{\frac{2}{3}}$				
Δ^0			$-\frac{1}{\sqrt{3}}$		
Σ^{*0}					$-\frac{1}{\sqrt{6}}$
Σ^{*+}			$\frac{1}{\sqrt{3}}$		

Table F.12: Clebsch-Gordan coefficients for the leading-order strong coupling of an octet baryon B to a decuplet baryon T through the emission of the pseudoscalar meson K^-.

$C_{BT\overline{K}^0} \times \mathcal{C}^{-1}$					
T \ B	Σ^0	Σ^+	Σ^-	Ξ^0	Ξ^-
Δ^+		$\frac{1}{\sqrt{3}}$			
Δ^0	$-\sqrt{\frac{2}{3}}$				
Δ^-			-1		
Σ^{*0}				$\frac{1}{\sqrt{6}}$	
Σ^{*-}					$-\frac{1}{\sqrt{3}}$

Table F.13: Clebsch-Gordan coefficients for the leading-order strong coupling of an octet baryon B to a decuplet baryon T through the emission of the pseudoscalar meson $\overline{K}^0$.

	$C_{BT\phi} \times \mathcal{C}^{-1}$	
BT \ ϕ	π^0	η
$p\Delta^+$	$\sqrt{\frac{2}{3}}\cos\epsilon$	$-\sqrt{\frac{2}{3}}\sin\epsilon$
$n\Delta^0$	$\sqrt{\frac{2}{3}}\cos\epsilon$	$-\sqrt{\frac{2}{3}}\sin\epsilon$
$\Lambda\Sigma^{*0}$	$-\frac{1}{\sqrt{2}}\cos\epsilon$	$\frac{1}{\sqrt{2}}\sin\epsilon$
$\Sigma^0\Sigma^{*0}$	$\frac{1}{\sqrt{2}}\sin\epsilon$	$\frac{1}{\sqrt{2}}\cos\epsilon$
$\Sigma^+\Sigma^{*+}$	$-\frac{1}{\sqrt{6}}\big(\cos\epsilon+\sqrt{3}\sin\epsilon\big)$	$\frac{1}{\sqrt{6}}\big(\sin\epsilon-\sqrt{3}\cos\epsilon\big)$
$\Sigma^-\Sigma^{*-}$	$\frac{1}{\sqrt{6}}\big(\sqrt{3}\sin\epsilon-\cos\epsilon\big)$	$\frac{1}{\sqrt{6}}\big(\sqrt{3}\cos\epsilon+\sin\epsilon\big)$
$\Xi^0\Xi^{*0}$	$-\frac{1}{\sqrt{6}}\big(\cos\epsilon+\sqrt{3}\sin\epsilon\big)$	$\frac{1}{\sqrt{6}}\big(\sin\epsilon-\sqrt{3}\cos\epsilon\big)$
$\Xi^-\Xi^{*-}$	$\frac{1}{\sqrt{6}}\big(\sqrt{3}\sin\epsilon-\cos\epsilon\big)$	$\frac{1}{\sqrt{6}}\big(\sqrt{3}\cos\epsilon+\sin\epsilon\big)$

Table F.14: Clebsch-Gordan coefficients for the leading-order strong coupling of an octet baryon B to a decuplet baryon T through the emission of the pseudoscalar meson π^0 or η. The π^0–η mixing parameter ϵ is defined in Eq. (4.5).

C_{BBO_q}		
Doubly	Singly	Other
$\frac{1}{6}(5\alpha+2\beta+6\sigma)$	$\frac{1}{6}(\alpha+4\beta+6\sigma)$	σ

Table F.15: Clebsch-Gordan coefficients for the leading-order interaction of the twist-two operator defined in Eq. (6.4a) with an outer-ring octet baryon B. Labels 'Doubly', 'Singly', and 'Other' indicate whether the quark flavour q is doubly, singly, or not at all represented in B.

	$C_{BB'O_q}$		
BB' \ q	u	d	s
$\Lambda\Lambda$	$\frac{1}{4}(\alpha+2\beta+4\sigma)$	$\frac{1}{4}(\alpha+2\beta+4\sigma)$	$\frac{1}{2}(\alpha+2\sigma)$
$\Lambda\Sigma^0$	$\frac{1}{4\sqrt{3}}(\alpha-2\beta)$	$-\frac{1}{4\sqrt{3}}(\alpha-2\beta)$	
$\Sigma^0\Sigma^0$	$\frac{1}{12}(5\alpha+2\beta+12\sigma)$	$\frac{1}{12}(5\alpha+2\beta+12\sigma)$	$\frac{1}{6}(\alpha+4\beta+6\sigma)$

Table F.16: Clebsch-Gordan coefficients for the leading-order interaction of the twist-two operator defined in Eq. (6.4a) with the Λ and Σ^0 baryons.

$C_{BBO_qM} \times m_{q'}^{-1}$	
q' \ q	Doubly
Doubly	$-b_1 + b_2 - b_3 + b_4 + b_5 + b_7 + b_9$
Singly	b_7
Other	$b_1 + b_2 + b_3 + b_4 + b_7 + b_8$
	Singly
Doubly	b_9
Singly	b_5
Other	b_8
	Other
Doubly	$b_1 - b_2 - b_3 + b_4 + b_6 + b_9$
Singly	b_6
Other	$-b_1 - b_2 + b_3 + b_4 + b_5 + b_6 + b_8$

Table F.17: Clebsch-Gordan coefficients for the $\mathcal{O}(m_q)$ counterterms relevant to effective matrix elements of the twist-two operator defined in Eq. (6.4a). Labels 'Doubly', 'Singly', and 'Other' indicate whether the quark flavours q and q' are doubly, singly, or not at all represented in the outer-ring octet baryon B.

$C_{\Lambda\Lambda O_q M} \times m_{q'}^{-1}$		
q' \ q	u	d
u	$\frac{1}{6}(b_{10}+4b_4+6b_5+b_6+b_7+b_8+b_9)$	$\frac{1}{6}(b_{10}+b_6+b_7+b_8+b_9)$
d	$\frac{1}{6}(b_{10}+b_6+b_7+b_8+b_9)$	$\frac{1}{6}(b_{10}+4b_4+6b_5+b_6+b_7+b_8+b_9)$
s	$\frac{1}{6}(-2b_{10}+b_6+b_7+4b_8+4b_9)$	$\frac{1}{6}(-2b_{10}+b_6+b_7+4b_8+4b_9)$
	s	
u	$\frac{1}{6}(-2b_{10}+4b_6+4b_7+b_8+b_9)$	
d	$\frac{1}{6}(-2b_{10}+4b_6+4b_7+b_8+b_9)$	
s	$\frac{1}{3}(2b_{10}+8b_4+3b_5+2b_6+2b_7+2b_8+2b_9)$	

Table F.18: Clebsch-Gordan coefficients for the $\mathcal{O}(m_q)$ counterterms relevant to effective matrix elements of the twist-two operator defined in Eq. (6.4a) in Λ baryon external states.

$C_{\Sigma^0\Sigma^0 O_q M} \times m_{q'}^{-1}$			
q' \ q	u	d	s
u	$\frac{1}{2}(b_{10}+4b_4+2b_5+b_6+b_7+b_8+b_9)$	$\frac{1}{2}(-b_{10}+b_6+b_7+b_8+b_9)$	$\frac{1}{2}(b_8+b_9)$
d	$\frac{1}{2}(-b_{10}+b_6+b_7+b_8+b_9)$	$\frac{1}{2}(b_{10}+4b_4+2b_5+b_6+b_7+b_8+b_9)$	$\frac{1}{2}(b_8+b_9)$
s	$\frac{1}{2}(b_6+b_7)$	$\frac{1}{2}(b_6+b_7)$	b_5

Table F.19: Clebsch-Gordan coefficients for the $\mathcal{O}(m_q)$ counterterms relevant to effective matrix elements of the twist-two operator defined in Eq. (6.4a) in Σ^0 baryon external states.

B \ $\phi\phi'$	$C_{BB\phi\phi' O_u}$ $\pi^+\pi^-$	K^+K^-
p	$\frac{1}{3}(\beta - 2\alpha)$	$\frac{1}{6}(-5\alpha - 2\beta)$
n	$\frac{1}{3}(2\alpha - \beta)$	$\frac{1}{6}(-\alpha - 4\beta)$
Λ		$\frac{1}{4}(\alpha - 2\beta)$
Σ^0		$\frac{1}{4}(2\beta - \alpha)$
Σ^+	$\frac{1}{6}(-5\alpha - 2\beta)$	$\frac{1}{3}(\beta - 2\alpha)$
Σ^-	$\frac{1}{6}(5\alpha + 2\beta)$	$\frac{1}{6}(\alpha + 4\beta)$
Ξ^0	$\frac{1}{6}(-\alpha - 4\beta)$	$\frac{1}{3}(2\alpha - \beta)$
Ξ^-	$\frac{1}{6}(\alpha + 4\beta)$	$\frac{1}{6}(5\alpha + 2\beta)$

Table F.20: Clebsch-Gordan coefficients for the coupling of the u-quark twist-two operator defined in Eq. (6.4a) to the octet baryon B through the emission of two mesons.

B \ $\phi\phi'$	$C_{BB\phi\phi' O_d}$ $\pi^+\pi^-$	$K^0\overline{K}^0$
p	$\frac{1}{3}(2\alpha - \beta)$	$\frac{1}{6}(-\alpha - 4\beta)$
n	$\frac{1}{3}(\beta - 2\alpha)$	$\frac{1}{6}(-5\alpha - 2\beta)$
Λ		$\frac{1}{4}(\alpha - 2\beta)$
Σ^0		$\frac{1}{4}(2\beta - \alpha)$
Σ^+	$\frac{1}{6}(5\alpha + 2\beta)$	$\frac{1}{6}(\alpha + 4\beta)$
Σ^-	$\frac{1}{6}(-5\alpha - 2\beta)$	$\frac{1}{3}(\beta - 2\alpha)$
Ξ^0	$\frac{1}{6}(\alpha + 4\beta)$	$\frac{1}{6}(5\alpha + 2\beta)$
Ξ^-	$\frac{1}{6}(-\alpha - 4\beta)$	$\frac{1}{3}(2\alpha - \beta)$

Table F.21: Clebsch-Gordan coefficients for the coupling of the d-quark twist-two operator defined in Eq. (6.4a) to the octet baryon B through the emission of two mesons.

B \ $\phi\phi'$	$C_{BB\phi\phi' O_s}$ $K^0\overline{K}^0$	K^+K^-
p	$\frac{1}{6}(\alpha+4\beta)$	$\frac{1}{6}(5\alpha+2\beta)$
n	$\frac{1}{6}(5\alpha+2\beta)$	$\frac{1}{6}(\alpha+4\beta)$
Λ	$\frac{1}{4}(2\beta-\alpha)$	$\frac{1}{4}(2\beta-\alpha)$
Σ^0	$\frac{1}{4}(\alpha-2\beta)$	$\frac{1}{4}(\alpha-2\beta)$
Σ^+	$\frac{1}{6}(-\alpha-4\beta)$	$\frac{1}{3}(2\alpha-\beta)$
Σ^-	$\frac{1}{3}(2\alpha-\beta)$	$\frac{1}{6}(-\alpha-4\beta)$
Ξ^0	$\frac{1}{6}(-5\alpha-2\beta)$	$\frac{1}{3}(\beta-2\alpha)$
Ξ^-	$\frac{1}{3}(\beta-2\alpha)$	$\frac{1}{6}(-5\alpha-2\beta)$

Table F.22: Clebsch-Gordan coefficients for the coupling of the s-quark twist-two operator defined in Eq. (6.4a) to the octet baryon B through the emission of two mesons.

	$C_{TTO_q} \times 3\left(\gamma - \frac{\gamma'}{3}\right)^{-1}$
Singly	1
Doubly	2
Triply	3

Table F.23: Clebsch-Gordan coefficients for the leading-order interaction of the twist-two operator defined in Eq. (6.4a) with a decuplet baryon T. Labels 'Doubly', 'Singly', and 'Triply' indicate whether the quark flavour q is doubly, singly, or triply-represented in T. The low-energy constants γ and γ' are defined in Eq. (6.11).

$C_{BTO_{\Delta q}} \times \omega^{-1}$			
BT \ q	u	d	s
$p\Delta^+$	$\frac{1}{\sqrt{3}}$	$-\frac{1}{\sqrt{3}}$	
$n\Delta^0$	$\frac{1}{\sqrt{3}}$	$-\frac{1}{\sqrt{3}}$	
$\Lambda\Sigma^{*0}$	$-\frac{1}{2}$	$\frac{1}{2}$	
$\Sigma^0\Sigma^{*0}$	$\frac{1}{2\sqrt{3}}$	$\frac{1}{2\sqrt{3}}$	$-\frac{1}{\sqrt{3}}$
$\Sigma^+\Sigma^{*+}$	$-\frac{1}{\sqrt{3}}$		$\frac{1}{\sqrt{3}}$
$\Sigma^-\Sigma^{*-}$		$\frac{1}{\sqrt{3}}$	$-\frac{1}{\sqrt{3}}$
$\Xi^0\Xi^{*0}$	$-\frac{1}{\sqrt{3}}$		$\frac{1}{\sqrt{3}}$
$\Xi^-\Xi^{*-}$		$\frac{1}{\sqrt{3}}$	$-\frac{1}{\sqrt{3}}$

Table F.24: Clebsch-Gordan coefficients for the transition between an octet baryon B and decuplet baryon T via an insertion of the twist-two operator defined in Eq. (6.4b). The low-energy constant ω is defined in Eq. (6.16).

α^{Bq}	
Doubly	Singly
$2\mu_F$	$\mu_F - \mu_D$

Table F.25: Expressions for the coefficients α^{Bq} which appear in the chiral expansion for the magnetic Sachs form factor G_M (Eq. (7.30)). The labels 'Doubly' and 'Singly' indicate whether the quark flavour q is doubly or singly-represented in the outer-ring octet baryon B.

α^{Bq}			
B \ q	u	d	s
Λ	$\mu_F - \frac{2\mu_D}{3}$	$\mu_F - \frac{2\mu_D}{3}$	$\frac{\mu_D}{3} + \mu_F$
Σ^0	μ_F	μ_F	$\mu_F - \mu_D$

Table F.26: Expressions for the chiral coefficients α^{Bq}, defined in Eq. (7.30), for the Λ and Σ^0 baryons.

	$\overline{\alpha}^{Bq(q')}$
$m_{q'}$ \ q	Doubly
m_{Doubly}	$\frac{1}{6}(c_{10}+c_{11}+c_{12}+18c_3+45c_4+2c_5+5c_6+c_9)$
m_{Singly}	$\frac{1}{6}(-2c_{10}+c_{11}-2c_{12}+18c_3+45c_4+4c_9)$
m_{Other}	$\frac{1}{2}(6c_3+15c_4)$
	Singly
m_{Doubly}	$\frac{1}{6}(-2c_{10}+4c_{11}-2c_{12}+36c_3+9c_4+c_9)$
m_{Singly}	$\frac{1}{6}(36c_3+9c_4+4c_5+c_6)$
m_{Other}	$\frac{3}{2}(4c_3+c_4)$

Table F.27: Coefficients of terms in the chiral expansion for the magnetic Sachs form factor G_M (Eq. (7.30)) which are linear in the quark masses. The labels 'Doubly', 'Singly', and 'Other' indicate whether the quark flavour q or q' is doubly, singly, or not at all represented in the outer-ring octet baryon B.

	$\overline{\alpha}^{\Lambda q(q')}$
$m_{q'}$ \ q	u
m_u	$\frac{1}{4}(18c_3+9c_4+2c_5+c_6)$
m_d	$\frac{1}{4}(-\text{c12}-c_{10}+c_{11}+18c_3+9c_4+c_9)$
m_s	$\frac{1}{4}(c_{11}+9(2c_3+c_4))$
	d
m_u	$\frac{1}{4}(-\text{c12}-c_{10}+c_{11}+18c_3+9c_4+c_9)$
m_d	$\frac{1}{4}(18c_3+9c_4+2c_5+c_6)$
m_s	$\frac{1}{4}(c_{11}+9(2c_3+c_4))$
	s
m_u	$\frac{1}{4}(18c_4+c_9)$
m_d	$\frac{1}{4}(18c_4+c_9)$
m_s	$\frac{1}{2}(9c_4+c_6)$

Table F.28: Coefficients of terms in the chiral expansion for the magnetic Sachs form factor of the Λ baryon (Eq. (7.30)) which are linear in the quark masses.

	$\overline{\alpha}^{\Sigma^0 q(q')}$
$m_{q'}$ \ q	u
m_u	$\frac{1}{12}(18c_3 + 45c_4 + 2c_5 + 5c_6)$
m_d	$\frac{1}{12}(c_{10} + c_{11} + c_{12} + 18c_3 + 45c_4 + c_9)$
m_s	$\frac{1}{12}(-2c_{10} + c_{11} - 2c_{12} + 18c_3 + 45c_4 + 4c_9)$
	d
m_u	$\frac{1}{12}(c_{10} + c_{11} + c_{12} + 18c_3 + 45c_4 + c_9)$
m_d	$\frac{1}{12}(18c_3 + 45c_4 + 2c_5 + 5c_6)$
m_s	$\frac{1}{12}(-2c_{10} + c_{11} - 2c_{12} + 18c_3 + 45c_4 + 4c_9)$
	s
m_u	$\frac{1}{12}(-2c_{10} + 4c_{11} - 2c_{12} + 72c_3 + 18c_4 + c_9)$
m_d	$\frac{1}{12}(-2c_{10} + 4c_{11} - 2c_{12} + 72c_3 + 18c_4 + c_9)$
m_s	$\frac{1}{6}(36c_3 + 9c_4 + 4c_5 + c_6)$

Table F.29: Coefficients of terms in the chiral expansion for the magnetic Sachs form factor of the Σ^0 baryon (Eq. (7.30)) which are linear in the quark masses.

	$\beta_O^{Bq(\phi)}$	
$\mathcal{B}^{-1}m_\phi$ \ q	Doubly	Singly
$m_{\text{Doubly}} + m_{\text{Singly}}$	$4(D^2 + F^2)$	$-\frac{2}{3}(D^2 + 6DF - 3F^2)$
$m_{\text{Singly}} + m_{\text{Other}}$		$2(D - F)^2$
$m_{\text{Doubly}} + m_{\text{Other}}$	$\frac{4}{3}(D^2 + 3F^2)$	
$2m_{\text{Doubly}}$	$\frac{4}{3}(D^2 + 3F^2)$	
$2m_{\text{Singly}}$		$2(D - F)^2$

Table F.30: Coefficients of terms in the chiral expansion for the magnetic Sachs form factor (Eq. (7.30)) corresponding to loop contributions with octet baryon intermediate states. The labels 'Doubly', 'Singly', and 'Other' indicate whether the quark flavour q is doubly, singly, or not at all represented in the outer-ring octet baryon B.

	$\beta_O^{\Lambda q(\phi)}$	
$\mathcal{B}^{-1}m_\phi$ \ q	u	d
$m_u + m_d$	$\frac{2}{9}(7D^2 - 12DF + 9F^2)$	$\frac{2}{9}(7D^2 - 12DF + 9F^2)$
$m_d + m_s$		$\frac{2}{9}(D^2 - 12DF + 9F^2)$
$m_u + m_s$	$\frac{2}{9}(D^2 - 12DF + 9F^2)$	
$2m_u$	$\frac{2}{9}(7D^2 - 12DF + 9F^2)$	
$2m_d$		$\frac{2}{9}(7D^2 - 12DF + 9F^2)$
	s	
$m_d + m_s$	$\frac{2}{9}(7D^2 + 6DF + 9F^2)$	
$m_u + m_s$	$\frac{2}{9}(7D^2 + 6DF + 9F^2)$	
$2m_s$	$\frac{2}{9}(D + 3F)^2$	

Table F.31: Coefficients of terms in the chiral expansion for the magnetic Sachs form factor of the Λ baryon (Eq. (7.30)) corresponding to loop contributions with octet baryon intermediate states.

	$\beta_O^{\Sigma^0 q(\phi)}$		
$\mathcal{B}^{-1}m_\phi$ \ q	u	d	s
$m_u + m_d$	$\frac{2}{3}(D^2 + 3F^2)$	$\frac{2}{3}(D^2 + 3F^2)$	
$m_d + m_s$		$2(D^2 + F^2)$	$\frac{2}{3}(D^2 - 6DF + 3F^2)$
$m_u + m_s$	$2(D^2 + F^2)$		$\frac{2}{3}(D^2 - 6DF + 3F^2)$
$2m_u$	$\frac{2}{3}(D^2 + 3F^2)$		
$2m_d$		$\frac{2}{3}(D^2 + 3F^2)$	
$2m_s$			$2(D - F)^2$

Table F.32: Coefficients of terms in the chiral expansion for the magnetic Sachs form factor of the Σ^0 baryon (Eq. (7.30)) corresponding to loop contributions with octet baryon intermediate states.

$\beta_D^{Bq(\phi)} \times \mathcal{C}^{-2}$ $\mathcal{B}^{-1}m_\phi$ \ q	Doubly	Singly
$m_{\text{Doubly}} + m_{\text{Singly}}$	$\frac{2}{9}$	$-\frac{5}{9}$
$m_{\text{Singly}} + m_{\text{Other}}$		$-\frac{2}{9}$
$m_{\text{Doubly}} + m_{\text{Other}}$	$-\frac{1}{9}$	
$2m_{\text{Doubly}}$	$-\frac{1}{9}$	
$2m_{\text{Singly}}$		$-\frac{2}{9}$

Table F.33: Coefficients of terms in the chiral expansion for the magnetic Sachs form factor (Eq. (7.30)) corresponding to loop contributions with decuplet baryon intermediate states. The labels 'Doubly', 'Singly', and 'Other' indicate whether the quark flavour q is doubly, singly, or not at all represented in the outer-ring octet baryon B.

$\beta_D^{\Lambda q(\phi)} \times \mathcal{C}^{-2}$ $\mathcal{B}^{-1}m_\phi$ \ q	u	d	s
$m_u + m_d$	$-\frac{1}{6}$	$-\frac{1}{6}$	
$m_d + m_s$		$-\frac{1}{3}$	$\frac{1}{6}$
$m_u + m_s$	$-\frac{1}{3}$		$\frac{1}{6}$
$2m_u$	$-\frac{1}{6}$		
$2m_d$		$-\frac{1}{6}$	

Table F.34: Coefficients of terms in the chiral expansion for the magnetic Sachs form factor of the Λ baryon (Eq. (7.30)) corresponding to loop contributions with decuplet baryon intermediate states.

$\beta_D^{\Sigma^0 q(\phi)} \times \mathcal{C}^{-2}$ $\mathcal{B}^{-1}m_\phi$ \ q	u	d	s
$m_u + m_d$	$-\frac{1}{18}$	$-\frac{1}{18}$	
$m_d + m_s$		$\frac{1}{9}$	$-\frac{7}{18}$
$m_u + m_s$	$\frac{1}{9}$		$-\frac{7}{18}$
$2m_u$	$-\frac{1}{18}$		
$2m_d$		$-\frac{1}{18}$	
$2m_s$			$-\frac{2}{9}$

Table F.35: Coefficients of terms in the chiral expansion for the magnetic Sachs form factor of the Σ^0 baryon (Eq. (7.30)) corresponding to loop contributions with decuplet baryon intermediate states.

m_ϕ \ $\beta_T^{Bq(\phi)}$ q	Doubly	Singly
$m_{\text{Doubly}} + m_{\text{Singly}}$	2	1
$m_{\text{Singly}} + m_{\text{Other}}$		1
$m_{\text{Doubly}} + m_{\text{Other}}$	2	
$2m_{\text{Doubly}}$	2	
$2m_{\text{Singly}}$		1

Table F.36: Coefficients of terms in the chiral expansion for the electric Sachs form factor (Eq. (7.39)) corresponding to tadpole-loop contributions. The labels 'Doubly', 'Singly', and 'Other' indicate whether the quark flavour q is doubly, singly, or not at all represented in the outer-ring octet baryon B.

m_ϕ \ $\beta_T^{Bq(\phi)}$ q	u	d	s
$m_u + m_d$	1	1	
$m_d + m_s$		1	1
$m_u + m_s$	1		1
$2m_u$	1		
$2m_d$		1	
$2m_s$			1

Table F.37: Coefficients of terms in the chiral expansion for the electric Sachs form factor of the Λ or Σ^0 baryon (Eq. (7.39)) corresponding to tadpole-loop contributions.

Appendix G

Deep Inelastic Scattering and the Operator Product Expansion

Here we sketch the connection between inclusive deep inelastic scattering (DIS), hadron structure functions, and parton distribution functions (PDFs). We focus in particular on the use of the operator product expansion to separate the hard (perturbative) and soft (nonperturbative) physics, and the relation of PDFs to matrix elements of local operators which is the result used in Chapter 6. Further details can be found in Ref. [30].

G.1 DIS and the Compton Forward Scattering Amplitude

At lowest order in perturbation theory, the double-differential cross section for DIS of polarised leptons on polarised nucleons can be factorised into leptonic and hadronic components:

$$\frac{d^2\sigma}{dx\,dy} = \frac{2\pi y\alpha^2}{Q^4}\sum_j \eta_j L_j^{\mu\nu} W_{\mu\nu}^j. \tag{G.1}$$

Here $x = Q^2/2M\nu$, where q is the four-momentum transferred to the nucleon through the virtual gauge boson with $Q^2 = -q^2 > 0$, ν is the lepton's energy loss in the nucleon's rest frame, and $y = \nu/E$. The summation in j is over the exchanged bosons (γ and Z for neutral-current processes, W for charged-current processes), and the factors η_j denote ratios of the corresponding propagators and couplings to the photon propagator and coupling (squared). The lepton tensor $L_{\mu\nu}$ encodes the coupling of the exchanged boson to the leptons and is explicitly calculable in electroweak theory. The hadronic tensor, on the other hand, encodes all of the internal structure of the nucleon that is probed by the electroweak currents. It may be expressed as

$$W_{\mu\nu}(q,p,S) = \frac{1}{4\pi}\int d^4z\, e^{iq\cdot z}\big\langle p,S\big|\big[J_\mu^\dagger(z), J_\nu(0)\big]\big|p,S\big\rangle, \tag{G.2}$$

where p and S denote the momentum and polarisation vector of the nucleon, respectively, and $p \cdot S = 0$. The hadronic currents, $J_\mu(z)$, are electromagnetic or weak quark currents which couple to the exchanged gauge boson. For example, the electromagnetic hadronic current is

$$J_\mu^{(\gamma)}(z) = \sum_q e_q \overline{\psi}_q(z)\, \gamma_\mu\, \psi_q(z), \tag{G.3}$$

where the sum runs over all quark flavours q.

The hadronic tensor can be decomposed into a sum of distinct Lorentz tensor structures multiplied by dimensionless quantities, known as structure functions, accompanied only by kinematic variables. This decomposition is given explicitly in Ref. [30]. Of interest to us here is the relationship between moments of these structure functions and a series of nucleon matrix elements of local operators composed of quark and gluon fields. To derive this relationship using the operator product expansion it is useful to consider the virtual Compton forward scattering amplitude, defined by the time-ordered product of hadronic currents:

$$T_{\mu\nu}(q,p,S) = i \int d^4z\, e^{iq\cdot z} \big\langle p,S \big| T J_\mu^\dagger(z) J_\nu(0) \big| p,S \big\rangle. \tag{G.4}$$

By the optical theorem, this quantity is related to the hadronic tensor by

$$W_{\mu\nu}(q,p,S) = \frac{1}{2\pi} \operatorname{Im} T_{\mu\nu}(q,p,S), \tag{G.5}$$

i.e., considered as a function of q^2 and $\omega = 1/x$, $W_{\mu\nu}$ is given by the discontinuity of $T_{\mu\nu}$ across the branch cuts in the complex plane for ω (which lie on the real axis where $-\infty < \omega \leq -1$ and $1 \leq \omega < \infty$). The operator product expansion described in the next section uses the result that the leading Q^2-behaviour of $W_{\mu\nu}$ is determined by the light-cone singularities of the time ordered product of currents in $T_{\mu\nu}$.

G.2 The Operator Product Expansion

Wilson's operator product expansion gives a factorisation of the hadronic tensor into hard and soft components by a formal expansion of the product of hadronic currents in coordinate space and a systematic analysis of its light-cone behaviour. Explicitly, the time-ordered product of hadronic currents can be expanded near the light-cone as

$$iTJ^\dagger(z)J(0) \overset{z^2 \to 0}{\approx} \sum_i C^{(i)}\big(z^2\big)\, \mathcal{O}^{(i)}(z,0), \tag{G.6}$$

where Lorentz indices have been suppressed for clarity. The Wilson coefficients $C^{(i)}(z^2)$ are complex-valued functions which are, in general, singular for $z^2 \to 0$. The sum runs over all bilocal operators $\mathcal{O}(z,0)$ with the same quantum numbers

and transformation properties as the product of currents on the left hand side. The expansion can be further re-written in terms of local operators by a Taylor expansion about $z^2 = 0$:

$$iTJ^\dagger(z)J(0) \overset{z^2\to 0}{\approx} \sum_i C_n^{(i)}\big(z^2\big) z^{\mu_1}\cdots z^{\mu_n}\mathcal{O}^{(i)}_{\mu_1\cdots\mu_n}(0). \tag{G.7}$$

Because components of z might be large even where $z^2 \to 0$, all higher-order terms in this expansion are important. The set of local operators chosen here is generally taken to be totally symmetric and traceless in the Lorentz indices, in order to project onto definite spin n. The singular behaviour of the coefficient functions $C^{(i)}(z^2)$ for $z^2 \to 0$ can be derived by naive dimensional counting to be

$$C^{(i)}\big(z^2\big) \overset{z^2\to 0}{\sim} \left(\frac{1}{|z|}\right)^{2d_J-\left(d_n^{(i)}-n\right)}. \tag{G.8}$$

Here $d_n^{(i)}$ denotes the mass-dimension of the local operators $\mathcal{O}$, and d_J that of the currents. Clearly, for a given product of currents, the singular behaviour of the coefficient functions $C^{(i)}(z^2)$ scales with the difference of the mass dimension and spin of the associated operators. This dimension is named twist: $\tau_n^{(i)} = d_n^{(i)} - n$, and the operators with the lowest twist are dominant in the Bjorken limit (where Q^2 and $\nu \to \infty$ with x fixed). As operators are at least bilinear in the parton fields, the smallest possible twist is two. Higher-twist contributions are suppressed by powers of Q^2.

Re-writing the Compton amplitude T (Eq. (G.4)) using the operator product expansion, the dominant contributions are thus

$$T \approx \sum_{i,n}\int d^4x\, q^{iq\cdot z}\, C_n^{(i)}\big(z^2\big)\, z^{\mu_1}\cdots z^{\mu_n}\big\langle p\big|\mathcal{O}^{(i)}_{\mu_1\cdots\mu_n}(0)\big|p\big\rangle \tag{G.9}$$

$$\approx \sum_{i,n}\left(\frac{2}{Q^2}\right)^n C_n^{(i)}\big(Q^2\big)\, q^{\mu_1}\cdots q^{\mu_n}\big\langle p\big|\mathcal{O}^{(i)}_{\mu_1\cdots\mu_n}(0)\big|p\big\rangle - \mathrm{Tr}\,. \tag{G.10}$$

Here we have simplified the notation by dropping Lorentz indices on the currents and suppressing any spin-dependence. The symbol Tr denotes trace terms proportional to $g_{\mu_i\mu_j}$. The coefficient functions $C_n^{(i)}(Q^2)$ are essentially Fourier transforms of the $C_n^{(i)}(z^2)$. Parameterising the matrix elements of the local operators as

$$\big\langle p\big|\mathcal{O}^{(i)}_{\mu_1\cdots\mu_n}(0)\big|p\big\rangle = 2O_n^{(i)}(p_{\mu_1}\cdots p_{\mu_n} - \mathrm{Tr}), \tag{G.11}$$

the Compton forward scattering amplitude thus becomes a Laurent series in $(1/x)$:

$$T = 2\sum_{i,n} C_n^{(i)}(Q^2)\, O_n^{(i)}\left(\frac{1}{x}\right)^n + \ldots, \tag{G.12}$$

where the ellipsis denotes the contributions from higher-twist terms. The reduced matrix elements $O_n^{(i)}$ generally depend on the renormalisation scale μ^2 of the corresponding operators.

Using the optical theorem (see discussion surrounding Eq. (G.5)), we thus reveal a relationship between the nth moments of the hadronic tensor, or equivalently the nth moments of the structure functions, and the nucleon matrix elements of the spin-n operators in the operator product expansion[1]:

$$\int_0^1 dx\, x^{n-1} W(x, Q^2) = \sum_i C_n^{(i)}(Q^2)\, O_n^{(i)} + \cdots . \tag{G.13}$$

Factorisation appears clearly here; the hadronic tensor has been separated into hard and soft parts. The Wilson coefficients $C_n^{(i)}(Q^2)$ encode the hard physics, are independent of the target state, and their dependence on Q^2 is perturbatively calculable. The reduced matrix elements $O_n^{(i)}(\mu^2)$ contain all of the information about the soft physics of the process and the internal structure of the target. These quantities are inherently nonperturbative, and, as we describe in the next section, may be identified with the PDFs of the QCD-improved parton model.

G.3 The QCD-Improved Parton Model

As outlined in the introduction to Chapter 6, a proton is described in the parton model as being composed of a number of point-like quark and gluon constituents named partons. Approaching the infinite-momentum frame of the proton, these partons behave as quasi-free, non-interacting particles with collinear momenta. The DIS structure functions can then be described as the incoherent sum of all virtual-photon–parton cross-sections, weighted by the probability of finding each parton in the proton with a given longitudinal momentum fraction x. The (nonperturbative) momentum distribution number-density functions are the PDFs. In general, a structure function F may thus be decomposed as

$$F(x) = \sum_q C_q(x)\, q(x), \tag{G.14}$$

where $q(x)$ generically denotes a combination of PDFs. In general one writes $q(x)$ for quarks, $\overline{q}(x)$ for antiquarks, and Δq for the spin-dependent combination (the difference of the distributions with the quark spin parallel and antiparallel to the proton spin) of flavour q.

This intuitive picture is modified by our understanding of QCD. In particular, the radiation of hard gluons from the quarks violates the assumption that the transverse momentum of the partons in the infinite-momentum frame of the proton is small.

[1] In fact, because of some details of the Cauchy integration in $\omega = 1/x$ in the derivation, this holds only for certain values of n (even or odd) depending on amplitude under consideration. Details are given in Ref. [30] or in standard textbooks.

This leads to logarithmic scaling violations (particularly at small x). That is, the structure functions in fact evolve with the probing scale and are not functions of x alone. In this 'QCD-improved' parton picture, the structure functions still factorise, but are now described in terms of scale-dependent PDFs $f(x,\mu^2)$, where f denotes the gluons g or some flavour of quark q, and μ is the scale of the probe[2].

From Eq. (G.13) applied to the structure functions it is clear that moments of the QCD-improved parton model PDFs may be directly identified with the scale-dependent reduced matrix elements of local operators. As an explicit example we consider the current $J_\mu = \overline{q}\gamma_\mu q$ for a single quark flavour q. At twist-two, the Lorentz structure of the operators that can contribute to the operator product expansion can be either $\overline{q}\gamma^\mu q$ or $\overline{q}\gamma^\mu\gamma_5 q$ (in the limit that light quark masses can be neglected), because the operator product $J^\mu J^\nu$ does not change chirality. The conventional basis of twist-two spin-n operators is

$$\mathcal{O}_q^{\mu_1\cdots\mu_n} = i^{n-1}\overline{q}\gamma^{\mu_1}\overleftrightarrow{D}^{\mu_2}\cdots\overleftrightarrow{D}^{\mu_n}q, \tag{G.15a}$$

$$\mathcal{O}_{\Delta q}^{\mu_0\cdots\mu_m} = i^{m}\overline{q}\gamma_5\gamma^{\mu_0}\overleftrightarrow{D}^{\mu_1}\cdots\overleftrightarrow{D}^{\mu_m}q. \tag{G.15b}$$

These operators basically assess the one-particle properties of the quarks in some state, e.g., in a baryon B. At $n=1$ they reduce to the usual vector and axial-vector currents which measure the coresponding baryon charges. Matrix elements of these operators:

$$\big\langle B(\vec{p})\big|[\mathcal{O}_q^{\{\mu_1\cdots\mu_n\}} - \mathrm{Tr}]\big|B(\vec{p})\big\rangle = 2\langle x^{n-1}\rangle_q^B\big[p^{\{\mu_1}\cdots p^{\mu_n\}} - \mathrm{Tr}\big], \tag{G.16a}$$

$$\big\langle B(\vec{p})\big|[\mathcal{O}_{\Delta q}^{\{\mu_0\cdots\mu_m\}} - \mathrm{Tr}]\big|B(\vec{p})\big\rangle = 2\langle x^{m}\rangle_{\Delta q}^B M_B\big[S^{\{\mu_0}p^{\mu_1}\cdots p^{\mu_m\}} - \mathrm{Tr}\big], \tag{G.16b}$$

are matched to moments of the spin-independent (q^B) and spin-dependent (Δq^B) quark distribution functions in B (where we have suppressed the dependence on the scale μ^2):

$$\langle x^{n-1}\rangle_q^B = \int_0^1 dx\, x^{n-1}(q^B(x) + (-1)^n\overline{q}^B(x)), \tag{G.17a}$$

$$\langle x^{m}\rangle_{\Delta q}^B = \int_0^1 dx\, x^{m}(\Delta q^B(x) + (-1)^m\Delta\overline{q}^B(x)). \tag{G.17b}$$

Higher-twist effects have no single-particle interpretation within the parton model. For example, twist-four (next-to-leading order) contributions are understood to originate from two sources: the influence of nonperturbative background gluon fields on the quark propagators, i.e., the correlation of a quark and gluon with total momentum fraction x, and four-quark operators.

[2]The generalisation of Eq. (G.14) in fact involves the convolution of the perturbatively-calculable hard scattering cross-section term and the PDFs.

Appendix H

Chiral Extrapolation Formulae for Moments of PDFs

In this appendix we give explicit expressions for the chiral extrapolation of several PDF-moment observables which were discussed in Chapter 6.

H.1 g_A and $\langle x \rangle^p_{u-d}$

To facilitate direct comparison with, and use of, the master expressions given in Eqs. (6.38) and (6.39), we write out the chiral expansions for the isovector observables $\langle 1 \rangle^p_{\Delta u - \Delta d} = g_A$ and $\langle x \rangle^p_{u-d}$ explicitly. These expressions match earlier work [171, 310] in the limit $\epsilon \to 0$. As outlined in Chapter 6, the integrals $\widetilde{J}$ correspond directly to logarithmic contributions of the form $m^2 \log(m^2)$ in DR. In matching with familiar notation, we identify $\Delta\gamma^{(0)} = 2\mathcal{H}$ and impose the SU(6) relation $\mathcal{H} = -3D$.

$$g_A = a + b_M + \frac{1}{16\pi^2 f_\pi^2}\big(d + d'\mathcal{C}^2\big), \tag{H.1}$$

$$a = D + F, \tag{H.2a}$$

$$\begin{aligned} b_M = \frac{1}{2}\Big[&\Big(-\Delta b_1^{(0)} + \Delta b_2^{(0)} - \Delta b_3^{(0)} + \Delta b_4^{(0)} + \Delta b_5^{(0)} + \Delta b_7^{(0)}\Big)\mathcal{B}m_u \\ &+ \Big(-\Delta b_5^{(0)} + \Delta b_7^{(0)}\Big)\mathcal{B}m_d \\ &+ \Big(\Delta b_1^{(0)} + \Delta b_2^{(0)} + \Delta b_3^{(0)} + \Delta b_4^{(0)} + \Delta b_7^{(0)}\Big)\mathcal{B}m_s\Big], \end{aligned} \tag{H.2b}$$

$$\begin{aligned} d = &-\frac{1}{9}(D+F)\Big[-3(D+F)\cos\epsilon + \sqrt{3}(D-3F)\sin\epsilon\Big]^2 \widetilde{J}\big(m^2_{\pi^0}\big) \\ &-(D+F)\Big[(D+F)^2\,\widetilde{J}\big(m^2_{\pi^\pm}\big) + \widetilde{J}_T\big(m^2_{\pi^\pm}\big)\Big] \\ &-\frac{1}{2}(D-F)\Big\{[2F+3(D+F)](D-F)\,\widetilde{J}\big(m^2_{K^0}\big) + \widetilde{J}_T\big(m^2_{K^0}\big)\Big\} \end{aligned}$$

$$
\begin{aligned}
&- \frac{1}{3}\left[2D^3 + D^2F + 12DF^2 + 9F^3\right] \widetilde{J}\left(m_{K^\pm}^2\right) - F\, \widetilde{J}_T\left(m_{K^\pm}^2\right) \\
&- \frac{1}{9}(D+F)\Big[3(D+F)\sin\epsilon + \sqrt{3}(D-3F)\cos\epsilon\Big]^2\, \widetilde{J}\left(m_\eta^2\right), \qquad \text{(H.2c)}
\end{aligned}
$$

$$
\begin{aligned}
d' =& \frac{30}{81} D\Big[(\cos^2\epsilon)\, \widetilde{J}_2\left(m_{\pi^0}^2, \delta\right) + 4\, \widetilde{J}_2\left(m_{\pi^\pm}^2, \delta\right) + \widetilde{J}_2\left(m_{K^0}^2, \delta\right) + (\sin^2\epsilon)\, \widetilde{J}_2\left(m_\eta^2, \delta\right)\Big] \\
&- \frac{1}{6}(D+F)\Big[4(\cos^2\epsilon)\, \widetilde{J}_2\left(m_{\pi^0}^2, \delta\right) + 8\, \widetilde{J}_2\left(m_{\pi^\pm}^2, \delta\right) + 2\, \widetilde{J}_2\left(m_{K^0}^2, \delta\right) + \widetilde{J}_2\left(m_{K^\pm}^2, \delta\right) \\
&\qquad + 4(\sin^2\epsilon)\, \widetilde{J}_2\left(m_\eta^2, \delta\right)\Big] \\
&+ \frac{2}{9}\Bigg\{4(\cos\epsilon)\left[(D+F)\cos\epsilon - \frac{1}{\sqrt{3}}(D-3F)\sin\epsilon\right] \widetilde{J}_1\left(m_{\pi^0}^2, \delta\right) \\
&\quad + 4(D+F)\, \widetilde{J}_1\left(m_{\pi^\pm}^2, \delta\right) + 2(D-F)\, \widetilde{J}_1\left(m_{K^0}^2, \delta\right) + (D+3F)\, \widetilde{J}_1\left(m_{K^\pm}^2, \delta\right) \\
&\quad + 4(\sin\epsilon)\left[(D+F)\sin\epsilon + \frac{1}{\sqrt{3}}(D-3F)\cos\epsilon\right] \widetilde{J}_1\left(m_{\pi^0}^2, \delta\right)\Bigg\}. \qquad \text{(H.2d)}
\end{aligned}
$$

$$
\langle x \rangle_{u-d}^p = \overline{a} + \overline{b}_M + \frac{1}{16\pi^2 f_\pi^2}\left(\overline{d} + \overline{d}'\mathcal{C}^2\right), \qquad \text{(H.3)}
$$

$$
\overline{a} = \frac{1}{3}\left(\alpha^{(2)} - \frac{1}{2}\beta^{(2)}\right), \qquad \text{(H.4a)}
$$

$$
\begin{aligned}
\overline{b}_M =& \frac{1}{2}\Big[\left(-b_1^{(2)} + b_2^{(2)} - b_3^{(2)} + b_4^{(2)} + b_5^{(2)} + b_7^{(2)}\right)\mathcal{B}m_u + \left(-b_5^{(2)} + b_7^{(2)}\right)\mathcal{B}m_d \\
&+ \left(b_1^{(2)} + b_2^{(2)} + b_3^{(2)} + b_4^{(2)} + b_7^{(2)}\right)\mathcal{B}m_s\Big], \qquad \text{(H.4b)}
\end{aligned}
$$

$$
\begin{aligned}
\overline{d} =& -\frac{1}{6}\left(2\alpha^{(2)} - \beta^{(2)}\right)\Big[3(D+F)^2\, \widetilde{J}\left(m_{\pi^\pm}^2\right) + \widetilde{J}_T\left(m_{\pi^\pm}^2\right)\Big] \\
&+ \frac{1}{24}\left(\alpha^{(2)} + 4\beta^{(2)}\right)\Big[3(D-F)^2\, \widetilde{J}\left(m_{K^0}^2\right) + 2\, \widetilde{J}_T\left(m_{K^0}^2\right)\Big] \\
&- \frac{1}{24}\Big\{\left[6DF\left(\alpha^{(2)} - 2\beta^{(2)}\right) + 3F^2\left(\alpha^{(2)} + 2\beta^{(2)}\right)\right. \\
&\qquad \left. + D^2\left(11\alpha^{(2)} - 10\beta^{(2)}\right)\right]\, \widetilde{J}\left(m_{K^\pm}^2\right) \\
&\qquad + \left(5\alpha^{(2)} + 2\beta^{(2)}\right)\, \widetilde{J}_T\left(m_{K^\pm}^2\right)\Big\}, \qquad \text{(H.4c)}
\end{aligned}
$$

$$
\begin{aligned}
\overline{d}' =& -\frac{1}{9}\left(\gamma^{(2)} - \gamma'^{(2)}\right)\Big[(\cos^2\epsilon)\, \widetilde{J}_2\left(m_{\pi^0}^2, \delta\right) + 4\, \widetilde{J}_2\left(m_{\pi^\pm}^2, \delta\right) + \widetilde{J}_2\left(m_{K^0}^2, \delta\right) \\
&\qquad + (\sin^2\epsilon)\, \widetilde{J}_2\left(m_\eta^2, \delta\right)\Big] \\
&- \frac{1}{36}\left(2\alpha^{(2)} - \beta^{(2)}\right)\Big[4(\cos^2\epsilon)\, \widetilde{J}_2\left(m_{\pi^0}^2, \delta\right) + 8\, \widetilde{J}_2\left(m_{\pi^\pm}^2, \delta\right) + 2\, \widetilde{J}_2\left(m_{K^0}^2, \delta\right) \\
&\qquad + \widetilde{J}_2\left(m_{K^\pm}^2, \delta\right) + 4(\sin^2\epsilon)\, \widetilde{J}_2\left(m_\eta^2, \delta\right)\Big]. \qquad \text{(H.4d)}
\end{aligned}
$$

H.2 Charge Symmetry Violation

This section gives formulae for the spin-dependent and spin-independent charge symmetry violating quark distributions as functions of quark and meson mass. The expression for $\delta\Delta u^m$ was presented as Eq. (6.50) in Chapter 6. All integrals and constants are defined in that chapter.

H.2.1 Spin-Dependent CSV PDFs

$$\delta\Delta d^m = \langle x^m \rangle^p_{\Delta d} - \langle x^m \rangle^n_{\Delta u} = \overline{a}^{(m)}_\Delta + \frac{1}{16\pi^2 f_\pi^2}\Big(\overline{b}^{(m)}_\Delta + \overline{d}^{(m)}_\Delta + \overline{g}^{(m)}_\Delta\Big), \tag{H.5}$$

$$\overline{a}^{(m)}_\Delta = \frac{1}{2}\Big(-\Delta n_3^{(m)} + \Delta n_6^{(m)}\Big) B(m_u - m_d), \tag{H.6a}$$

$$\begin{aligned}\overline{b}^{(m)}_\Delta =& \frac{1}{6\sqrt{3}}\big(D^2 - 2DF - 3F^2\big)\sin(2\epsilon)\big(\Delta\alpha^{(m)} + 4\Delta\beta^{(m)} + 6\Delta\sigma^{(m)}\big) \\ &\times \Big[\widetilde{J}\big(m^2_{\pi_0}\big) - \widetilde{J}\big(m^2_\eta\big)\Big] \\ &+ \frac{1}{24}\big[D^2\big(\Delta\alpha^{(m)} - 4\Delta\beta^{(m)} - 8\Delta\sigma^{(m)}\big) + 6DF\big(\Delta\alpha^{(m)} + 4\Delta\beta^{(m)} + 8\Delta\sigma^{(m)}\big) \\ &\qquad + F^2\big(5\Delta\alpha^{(m)} + 20\Delta\beta^{(m)} + 24\Delta\sigma^{(m)}\big)\big]\Big[\widetilde{J}\big(m^2_{K^0}\big) - \widetilde{J}\big(m^2_{K^\pm}\big)\Big] \\ &- \frac{1}{24}\big(\Delta\alpha^{(m)} + 4\Delta\beta^{(m)}\big)\Big[\widetilde{J}_T\big(m^2_{K^0}\big) - \widetilde{J}_T\big(m^2_{K^\pm}\big)\Big],\end{aligned} \tag{H.6b}$$

$$\begin{aligned}\overline{d}^{(m)}_\Delta =& -\frac{1}{72}\big(\Delta\alpha^{(m)} + 4\Delta\beta^{(m)} + 6\Delta\sigma^{(m)}\big)\mathcal{C}^2\Big[\widetilde{J}_2\big(m^2_{K^0},\delta\big) - \widetilde{J}_2\big(m^2_{K^\pm},\delta\big)\Big], \\ &+ \frac{1}{324}\big(5\Delta\gamma^{(m)} - \Delta\gamma'^{(m)}\big)\mathcal{C}^2\Big[\widetilde{J}_2\big(m^2_{K^0},\delta\big) - \widetilde{J}_2\big(m^2_{K^\pm},\delta\big)\Big]\end{aligned} \tag{H.6c}$$

$$\begin{aligned}\overline{g}^{(m)}_\Delta =& + \frac{4}{9\sqrt{3}}(D - 3F)\sin(2\epsilon)\Delta\omega^{(m)}\Big[\widetilde{J}_1\big(m^2_{\pi^0},\delta\big) + \widetilde{J}_1\big(m^2_\eta,\delta\big)\Big] \\ &+ \frac{4}{9}F\Delta\omega^{(m)}\Big[\widetilde{J}_1\big(m^2_{K^0},\delta\big) - \widetilde{J}_1\big(m^2_{K^\pm},\delta\big)\Big].\end{aligned} \tag{H.6d}$$

H.2.2 Spin-Independent CSV PDFs

$$\delta u^m = \langle x^m \rangle^p_u - \langle x^m \rangle^n_d = a^{(m)} + \frac{1}{16\pi^2 f_\pi^2}\big(b^{(m)} + d^{(m)}\big), \tag{H.7a}$$

$$\delta d^m = \langle x^m \rangle^p_d - \langle x^m \rangle^n_u = \overline{a}^{(m)} + \frac{1}{16\pi^2 f_\pi^2}\Big(\overline{b}^{(m)} + \overline{d}^{(m)}\Big), \tag{H.7b}$$

$$a^{(m)} = \frac{1}{2}\Big(-n_1^{(m)} + n_2^{(m)} + n_3^{(m)} + n_6^{(m)}\Big) B(m_u - m_d), \tag{H.8a}$$

$$
\begin{aligned}
b^{(m)} =& \frac{1}{24}\left[D^2\left(7\alpha^{(m)} - 2\beta^{(m)}\right) + 6DF\left(\alpha^{(m)} - 2\beta^{(m)}\right) + 3F^2\left(5\alpha^{(m)} + 2\beta^{(m)}\right)\right] \\
& \times \left[\widetilde{J}\left(m_{K^0}^2\right) - \widetilde{J}\left(m_{K^\pm}^2\right)\right] \\
& + \frac{1}{24}\left(5\alpha^{(m)} + 2\beta^{(m)}\right)\left[\widetilde{J}_T\left(m_{K^0}^2\right) - \widetilde{J}_T\left(m_{K^\pm}^2\right)\right], \qquad \text{(H.8b)}
\end{aligned}
$$

$$
\begin{aligned}
d^{(m)} =& -\frac{1}{72}\left(5\alpha^{(m)} + 2\beta^{(m)} + 6\sigma^{(m)}\right)\mathcal{C}^2\left[\widetilde{J}_2\left(m_{K^0}^2, \delta\right) - \widetilde{J}_2\left(m_{K^\pm}^2, \delta\right)\right] \\
& - \frac{1}{36}\left(3\gamma^{(m)} - \gamma'^{(m)}\right)\mathcal{C}^2\left[\widetilde{J}_2\left(m_{K^0}^2, \delta\right) - \widetilde{J}_2\left(m_{K^\pm}^2, \delta\right)\right]. \qquad \text{(H.8c)}
\end{aligned}
$$

$$
\overline{a}^{(m)} = \frac{1}{2}\left(-n_3^{(m)} + n_6^{(m)}\right)B(m_u - m_d), \qquad \text{(H.8d)}
$$

$$
\begin{aligned}
\overline{b}^{(m)} =& \frac{1}{24}\left[-D^2\left(7\alpha^{(m)} + 4\beta^{(m)}\right) + 6DF\left(\alpha^{(m)} + 4\beta^{(m)}\right) - 3F^2\left(\alpha^{(m)} + 4\beta^{(m)}\right)\right] \\
& \times \left[\widetilde{J}\left(m_{K^0}^2\right) - \widetilde{J}\left(m_{K^\pm}^2\right)\right] \\
& - \frac{1}{24}\left(\alpha^{(m)} + 4\beta^{(m)}\right)\left[\widetilde{J}_T\left(m_{K^0}^2\right) - \widetilde{J}_T\left(m_{K^\pm}^2\right)\right], \qquad \text{(H.8e)}
\end{aligned}
$$

$$
\begin{aligned}
\overline{d}^{(m)} =& -\frac{1}{72}\left(\alpha^{(m)} + 4\beta^{(m)} + 6\sigma^{(m)}\right)\mathcal{C}^2\left[\widetilde{J}_2\left(m_{K^0}^2, \delta\right) - \widetilde{J}_2\left(m_{K^\pm}^2, \delta\right)\right] \\
& + \frac{1}{108}\left(3\gamma^{(m)} - \gamma'^{(m)}\right)\mathcal{C}^2\left[\widetilde{J}_2\left(m_{K^0}^2, \delta\right) - \widetilde{J}_2\left(m_{K^\pm}^2, \delta\right)\right]. \qquad \text{(H.8f)}
\end{aligned}
$$

Appendix I

Lattice Simulation Results for the Electromagnetic Form Factors

This section presents tables of raw lattice simulation results, and basic derived quantities, for the electromagnetic form factors F_1 and F_2 for the simulation parameters tabulated in Section 7.2.1. The Dirac and Pauli mean-squared charge radii $\langle r^2\rangle_{1,2}^{B,q}$, and anomalous magnetic moments $\kappa^{B,q}$, extracted using naive dipole-like fits to the raw lattice data as discussed in Section 7.2.3, are shown in Tables I.1–I.7. The raw data for simulation set I is given in Tables I.8–I.10, that for simulation set II is presented in Tables I.11–I.13, and raw lattice results on the orphan 'ensemble 10' are given in Tables I.14–I.16.

B, q	$\langle r^2\rangle_1^{B,q}$ (fm^2)	$\langle r^2\rangle_2^{B,q}$ (fm^2)	$\kappa^{B,q}$ (μ_N)
p, u	0.467(16)	0.391(91)	0.0414(53)
p, d	0.558(19)	0.502(39)	−0.0616(27)
Σ, u	0.441(10)	0.374(40)	0.0615(37)
Σ, s	0.4008(69)	0.319(14)	−0.0598(11)
Ξ, s	0.3732(35)	0.283(16)	0.0482(11)
Ξ, u	0.5208(69)	0.450(13)	−0.0679(11)

Table I.1: Dirac and Pauli mean-squared charge radii and anomalous magnetic moments, extracted from dipole-like fits (Eqs. (7.10a) and (7.10b)) to ensemble 10 at $(m_\pi, m_K) = (220, 540)\,\text{MeV}$. Details are given in Section 7.2.3.

(m_π, m_K) (MeV)	$\langle r^2\rangle_1^{p,u}$ (fm^2)	$\langle r^2\rangle_1^{p,d}$	$\langle r^2\rangle_1^{\Sigma,u}$	$\langle r^2\rangle_1^{\Sigma,s}$	$\langle r^2\rangle_1^{\Xi,s}$	$\langle r^2\rangle_1^{\Xi,u}$
(465,465)	0.334(16)	0.387(22)	0.334(16)	0.387(22)	0.334(16)	0.387(22)
(360,505)	0.368(11)	0.420(12)	0.3639(87)	0.3630(60)	0.3218(58)	0.4260(84)
(310,520)	0.376(20)	0.437(24)	0.399(13)	0.382(10)	0.3329(65)	0.459(11)
(440,440)	0.3601(96)	0.405(12)	0.3601(96)	0.405(12)	0.3601(96)	0.405(12)
(400,400)	0.378(10)	0.438(15)	0.378(10)	0.438(15)	0.378(10)	0.438(15)
(330,435)	0.396(13)	0.445(25)	0.400(10)	0.412(14)	0.3650(74)	0.465(13)

Table I.2: Dirac mean-squared charge radii, extracted from generalised dipole fits to data set I—see Section 7.2.3.

(m_π, m_K) (MeV)	$\langle r^2\rangle_2^{p,u}$ (fm^2)	$\langle r^2\rangle_2^{p,d}$	$\langle r^2\rangle_2^{\Sigma,u}$	$\langle r^2\rangle_2^{\Sigma,s}$	$\langle r^2\rangle_2^{\Xi,s}$	$\langle r^2\rangle_2^{\Xi,u}$
(465,465)	0.337(18)	0.3434(79)	0.337(18)	0.3434(79)	0.337(18)	0.3434(79)
(360,505)	0.335(29)	0.405(18)	0.340(20)	0.3358(99)	0.292(15)	0.389(10)
(310,520)	0.364(59)	0.379(32)	0.331(29)	0.286(14)	0.282(15)	0.367(14)
(440,440)	0.491(51)	0.415(22)	0.491(51)	0.415(22)	0.491(51)	0.415(22)
(400,400)	0.377(48)	0.362(26)	0.377(48)	0.362(26)	0.377(48)	0.362(26)
(330,435)	0.429(51)	0.416(28)	0.413(37)	0.361(17)	0.369(26)	0.387(14)

Table I.3: Pauli mean-squared charge radii, extracted from generalised dipole fits to data set I—see Section 7.2.3.

(m_π, m_K) (MeV)	$\kappa^{p,u}$ (μ_N)	$\kappa^{p,d}$	$\kappa^{\Sigma,u}$	$\kappa^{\Sigma,s}$	$\kappa^{\Xi,s}$	$\kappa^{\Xi,u}$
(465,465)	0.0518(17)	−0.06113(95)	0.0518(17)	−0.06113(95)	0.0518(17)	−0.06113(95)
(360,505)	0.0456(24)	−0.0632(18)	0.0553(21)	−0.0619(10)	0.0500(14)	−0.0652(11)
(310,520)	0.0482(51)	−0.0594(31)	0.0576(32)	−0.0572(13)	0.0508(15)	−0.0629(14)
(440,440)	0.0526(42)	−0.0643(24)	0.0526(42)	−0.0643(24)	0.0526(42)	−0.0643(24)
(400,400)	0.0503(46)	−0.0570(26)	0.0503(46)	−0.0570(26)	0.0503(46)	−0.0570(26)
(330,435)	0.0513(44)	−0.0616(27)	0.0560(36)	−0.0606(16)	0.0514(24)	−0.0622(14)

Table I.4: Anomalous magnetic moments in nuclear magnetons, extracted from generalised dipole fits to data set I—see Section 7.2.3.

(m_π, m_K) (MeV)	$\langle r^2 \rangle_1^{p,u}$ (fm^2)	$\langle r^2 \rangle_1^{p,d}$	$\langle r^2 \rangle_1^{\Sigma,u}$	$\langle r^2 \rangle_1^{\Sigma,s}$	$\langle r^2 \rangle_1^{\Xi,s}$	$\langle r^2 \rangle_1^{\Xi,u}$
(405,405)	0.3994(52)	0.4692(75)	0.3994(52)	0.4692(75)	0.3994(52)	0.4692(75)
(340,430)	0.441(11)	0.514(12)	0.4389(95)	0.4552(91)	0.3960(59)	0.5140(93)
(265,450)	0.432(16)	0.528(20)	0.433(10)	0.4231(86)	0.3715(53)	0.5262(86)

Table I.5: Dirac mean-squared charge radii, extracted from generalised dipole fits to data set II—see Section 7.2.3.

(m_π, m_K) (MeV)	$\langle r^2\rangle_2^{p,u}$ (fm^2)	$\langle r^2\rangle_2^{p,d}$	$\langle r^2\rangle_2^{\Sigma,u}$	$\langle r^2\rangle_2^{\Sigma,s}$	$\langle r^2\rangle_2^{\Xi,s}$	$\langle r^2\rangle_2^{\Xi,u}$
(405,405)	0.401(22)	0.437(11)	0.401(22)	0.437(11)	0.401(22)	0.437(11)
(340,430)	0.546(44)	0.486(24)	0.532(38)	0.412(15)	0.478(27)	0.455(15)
(265,450)	0.623(93)	0.517(40)	0.543(46)	0.389(20)	0.416(23)	0.487(16)

Table I.6: Pauli mean-squared charge radii, extracted from generalised dipole fits to data set II—see Section 7.2.3.

(m_π, m_K) (MeV)	$\kappa^{p,u}$ (μ_N)	$\kappa^{p,d}$	$\kappa^{\Sigma,u}$	$\kappa^{\Sigma,s}$	$\kappa^{\Xi,s}$	$\kappa^{\Xi,u}$
(405,405)	0.0540(18)	−0.06240(98)	0.0540(18)	−0.06240(98)	0.0540(18)	−0.06240(98)
(340,430)	0.0558(31)	−0.0614(20)	0.0619(30)	−0.0618(12)	0.0556(19)	−0.0627(13)
(265,450)	0.0531(59)	−0.0629(31)	0.0643(39)	−0.0597(17)	0.0503(16)	−0.0660(14)

Table I.7: Anomalous magnetic moments in nuclear magnetons, extracted from generalised dipole fits to data set II—see Section 7.2.3.

(m_π, m_K) (MeV)	Q^2 (GeV^2)	$F_1^{p,u}$	$F_1^{p,d}$	$F_2^{p,u}$	$F_2^{p,d}$
(465,465)	0.26	1.434(24)	0.666(11)	0.932(20)	−1.113(11)
	0.51	1.134(19)	0.4873(94)	0.722(18)	−0.8298(94)
	0.73	0.936(17)	0.3744(88)	0.589(19)	−0.6525(88)
	0.95	0.804(16)	0.3014(75)	0.474(21)	−0.5547(75)
	1.15	0.697(15)	0.2491(72)	0.392(16)	−0.4621(72)
	1.35	0.616(15)	0.2058(73)	0.328(15)	−0.3956(73)
(360,505)	0.26	1.3982(91)	0.6425(40)	0.822(28)	−1.081(18)
	0.51	1.089(12)	0.4588(51)	0.651(23)	−0.792(12)
	0.72	0.884(17)	0.3412(66)	0.535(26)	−0.622(13)
	0.92	0.781(32)	0.284(11)	0.396(36)	−0.527(24)
	1.12	0.656(26)	0.2219(81)	0.341(22)	−0.426(17)
	1.3	0.551(26)	0.1719(81)	0.324(23)	−0.339(15)
(310,520)	0.26	1.382(18)	0.6253(75)	0.885(58)	−1.034(33)
	0.49	1.075(20)	0.4433(82)	0.620(39)	−0.792(24)
	0.71	0.883(29)	0.316(13)	0.528(41)	−0.586(34)
	0.91	0.754(41)	0.268(15)	0.409(59)	−0.519(38)
	1.1	0.633(29)	0.194(11)	0.346(34)	−0.435(25)
	1.29	0.535(36)	0.158(17)	0.343(43)	−0.342(30)
(440,440)	0.26	1.3994(79)	0.6540(40)	0.823(38)	−1.080(24)
	0.5	1.078(11)	0.4689(56)	0.590(31)	−0.804(20)
	0.73	0.871(15)	0.3548(79)	0.451(31)	−0.623(21)
	0.94	0.733(21)	0.2827(92)	0.336(32)	−0.479(20)
	1.14	0.616(19)	0.2264(89)	0.270(24)	−0.403(17)
	1.33	0.545(25)	0.189(11)	0.236(23)	−0.349(20)
(400,400)	0.26	1.3974(91)	0.6411(53)	0.854(56)	−1.027(29)
	0.5	1.084(12)	0.4564(62)	0.692(38)	−0.744(24)
	0.72	0.888(20)	0.3377(89)	0.506(33)	−0.596(25)
	0.93	0.787(28)	0.286(12)	0.412(47)	−0.533(28)
	1.13	0.668(20)	0.2299(85)	0.361(32)	−0.411(21)
	1.32	0.585(27)	0.184(10)	0.296(26)	−0.356(26)
(330,435)	0.26	1.367(11)	0.6303(80)	0.819(46)	−1.029(28)
	0.5	1.057(14)	0.437(10)	0.651(30)	−0.773(16)
	0.72	0.875(17)	0.324(13)	0.511(31)	−0.593(20)
	0.92	0.726(33)	0.267(16)	0.340(45)	−0.473(31)
	1.12	0.614(26)	0.207(13)	0.296(27)	−0.395(21)
	1.3	0.544(29)	0.170(13)	0.271(30)	−0.319(24)

Table I.8: Raw lattice simulation results for the nucleon: data set I.

(m_π, m_K) (MeV)	Q^2 (GeV^2)	$F_1^{\Sigma,u}$	$F_1^{\Sigma,s}$	$F_2^{\Sigma,u}$	$F_2^{\Sigma,s}$
(465,465)	0.26	1.434(24)	0.666(11)	0.932(20)	−1.113(11)
	0.51	1.134(19)	0.4873(94)	0.722(18)	−0.8298(94)
	0.73	0.936(17)	0.3744(88)	0.589(19)	−0.6525(88)
	0.95	0.804(16)	0.3014(75)	0.474(21)	−0.5547(75)
	1.15	0.697(15)	0.2491(72)	0.392(16)	−0.4621(72)
	1.35	0.616(15)	0.2058(73)	0.328(15)	−0.3956(73)
(360,505)	0.26	1.4008(72)	0.6829(21)	0.996(24)	−1.126(10)
	0.5	1.0839(97)	0.5058(31)	0.770(21)	−0.8620(89)
	0.73	0.871(13)	0.3882(43)	0.615(20)	−0.680(10)
	0.95	0.774(23)	0.3301(73)	0.479(27)	−0.587(15)
	1.15	0.646(20)	0.2611(60)	0.414(19)	−0.479(13)
	1.34	0.545(21)	0.2092(68)	0.367(18)	−0.393(13)
(310,520)	0.26	1.372(12)	0.6776(36)	1.062(38)	−1.095(14)
	0.51	1.055(14)	0.5074(56)	0.796(25)	−0.855(17)
	0.73	0.855(20)	0.3937(82)	0.657(29)	−0.681(24)
	0.95	0.731(24)	0.327(10)	0.507(35)	−0.592(21)
	1.15	0.641(22)	0.2667(94)	0.439(25)	−0.515(20)
	1.35	0.563(30)	0.222(14)	0.419(33)	−0.442(27)
(440,440)	0.26	1.3994(79)	0.6540(40)	0.823(38)	−1.080(24)
	0.5	1.078(11)	0.4689(56)	0.590(31)	−0.804(20)
	0.73	0.871(15)	0.3548(79)	0.451(31)	−0.623(21)
	0.94	0.733(21)	0.2827(92)	0.336(32)	−0.479(20)
	1.14	0.616(19)	0.2264(89)	0.270(24)	−0.403(17)
	1.33	0.545(25)	0.189(11)	0.236(23)	−0.349(20)
(400,400)	0.26	1.3974(91)	0.6411(53)	0.854(56)	−1.027(29)
	0.5	1.084(12)	0.4564(62)	0.692(38)	−0.744(24)
	0.72	0.888(20)	0.3377(89)	0.506(33)	−0.596(25)
	0.93	0.787(28)	0.286(12)	0.412(47)	−0.533(28)
	1.13	0.668(20)	0.2299(85)	0.361(32)	−0.411(21)
	1.32	0.585(27)	0.184(10)	0.296(26)	−0.356(26)
(330,435)	0.26	1.3678(86)	0.6557(48)	0.915(41)	−1.076(16)
	0.5	1.053(11)	0.4731(66)	0.714(24)	−0.815(13)
	0.73	0.864(13)	0.3598(81)	0.555(27)	−0.633(17)
	0.94	0.734(24)	0.297(11)	0.414(34)	−0.529(20)
	1.14	0.624(22)	0.238(10)	0.343(23)	−0.442(17)
	1.33	0.554(27)	0.198(11)	0.296(24)	−0.368(21)

Table I.9: Raw lattice simulation results for the sigma baryon: data set I.

(m_π, m_K) (MeV)	Q^2 (GeV^2)	$F_1^{\Xi,s}$	$F_1^{\Xi,u}$	$F_2^{\Xi,s}$	$F_2^{\Xi,u}$
(465,465)	0.26	1.434(24)	0.666(11)	0.932(20)	−1.113(11)
	0.51	1.134(19)	0.4873(94)	0.722(18)	−0.8298(94)
	0.73	0.936(17)	0.3744(88)	0.589(19)	−0.6525(88)
	0.95	0.804(16)	0.3014(75)	0.474(21)	−0.5547(75)
	1.15	0.697(15)	0.2491(72)	0.392(16)	−0.4621(72)
	1.35	0.616(15)	0.2058(73)	0.328(15)	−0.3956(73)
(360, 505)	0.26	1.4537(51)	0.6457(27)	0.940(18)	−1.129(10)
	0.51	1.1536(76)	0.4607(35)	0.747(15)	−0.8270(78)
	0.74	0.948(10)	0.3437(45)	0.616(14)	−0.6411(82)
	0.96	0.841(20)	0.2909(69)	0.481(18)	−0.531(13)
	1.17	0.712(19)	0.2278(58)	0.422(16)	−0.436(11)
	1.36	0.608(20)	0.1789(65)	0.376(16)	−0.354(11)
(310,520)	0.26	1.4475(58)	0.6317(38)	0.974(18)	−1.114(13)
	0.51	1.1557(86)	0.4468(51)	0.762(16)	−0.825(11)
	0.74	0.960(13)	0.3347(78)	0.630(18)	−0.640(14)
	0.96	0.834(17)	0.2742(66)	0.513(18)	−0.524(16)
	1.17	0.728(18)	0.2169(61)	0.442(17)	−0.449(17)
	1.37	0.647(26)	0.179(10)	0.403(21)	−0.376(20)
(440,440)	0.26	1.3994(79)	0.6540(40)	0.823(38)	−1.080(24)
	0.5	1.078(11)	0.4689(56)	0.590(31)	−0.804(20)
	0.73	0.871(15)	0.3548(79)	0.451(31)	−0.623(21)
	0.94	0.733(21)	0.2827(92)	0.336(32)	−0.479(20)
	1.14	0.616(19)	0.2264(89)	0.270(24)	−0.403(17)
	1.33	0.545(25)	0.189(11)	0.236(23)	−0.349(20)
(400,400)	0.26	1.3974(91)	0.6411(53)	0.854(56)	−1.027(29)
	0.5	1.084(12)	0.4564(62)	0.692(38)	−0.744(24)
	0.72	0.888(20)	0.3377(89)	0.506(33)	−0.596(25)
	0.93	0.787(28)	0.286(12)	0.412(47)	−0.533(28)
	1.13	0.668(20)	0.2299(85)	0.361(32)	−0.411(21)
	1.32	0.585(27)	0.184(10)	0.296(26)	−0.356(26)
(330,435)	0.26	1.4094(62)	0.6283(41)	0.892(28)	−1.082(14)
	0.5	1.1030(87)	0.4418(56)	0.684(18)	−0.795(11)
	0.73	0.911(11)	0.3313(63)	0.546(19)	−0.623(13)
	0.95	0.792(19)	0.273(10)	0.430(25)	−0.501(16)
	1.15	0.677(19)	0.2178(86)	0.352(18)	−0.424(13)
	1.34	0.594(23)	0.1794(86)	0.306(20)	−0.354(17)

Table I.10: Raw lattice simulation results for the cascade baryon: data set I.

(m_π, m_K) (MeV)	Q^2 (GeV^2)	$F_1^{p,u}$	$F_1^{p,d}$	$F_2^{p,u}$	$F_2^{p,d}$
(405,405)	0.17	1.5427(36)	0.7270(22)	1.038(28)	−1.193(14)
	0.33	1.2593(63)	0.5578(35)	0.856(23)	−0.9420(90)
	0.48	1.0658(90)	0.4448(46)	0.714(22)	−0.7663(99)
	0.62	0.940(12)	0.3724(57)	0.606(24)	−0.655(12)
	0.76	0.822(12)	0.3100(56)	0.513(19)	−0.555(11)
	0.89	0.730(15)	0.2620(64)	0.440(18)	−0.480(11)
	1.14	0.568(19)	0.1888(70)	0.331(22)	−0.358(12)
(340,430)	0.17	1.5070(88)	0.7110(35)	0.988(39)	−1.150(27)
	0.32	1.2138(99)	0.5420(51)	0.759(29)	−0.875(19)
	0.47	1.018(12)	0.4302(64)	0.613(28)	−0.711(18)
	0.61	0.878(18)	0.3522(90)	0.493(34)	−0.590(19)
	0.75	0.767(19)	0.2971(90)	0.405(25)	−0.495(16)
	0.87	0.694(25)	0.256(10)	0.354(27)	−0.440(19)
	1.12	0.547(32)	0.190(12)	0.244(30)	−0.339(25)
(265,450)	0.17	1.507(11)	0.7002(58)	0.872(75)	−1.155(41)
	0.32	1.224(15)	0.5298(72)	0.709(43)	−0.869(30)
	0.47	1.036(22)	0.4239(99)	0.504(47)	−0.696(31)
	0.61	0.870(24)	0.329(12)	0.380(59)	−0.603(31)
	0.74	0.778(26)	0.288(11)	0.337(34)	−0.499(28)
	0.86	0.686(32)	0.238(13)	0.315(36)	−0.425(30)
	1.1	0.518(40)	0.170(15)	0.217(49)	−0.301(32)

Table I.11: Raw lattice simulation results for the nucleon: data set II.

(m_π, m_K) (MeV)	Q^2 (GeV^2)	$F_1^{\Sigma,u}$	$F_1^{\Sigma,s}$	$F_2^{\Sigma,u}$	$F_2^{\Sigma,s}$
(405,405)	0.17	1.5427(36)	0.7270(22)	1.038(28)	−1.193(14)
	0.33	1.2593(63)	0.5578(35)	0.856(23)	−0.9420(90)
	0.48	1.0658(90)	0.4448(46)	0.714(22)	−0.7663(99)
	0.62	0.940(12)	0.3724(57)	0.606(24)	−0.655(12)
	0.76	0.822(12)	0.3100(56)	0.513(19)	−0.555(11)
	0.89	0.730(15)	0.2620(64)	0.440(18)	−0.480(11)
	1.14	0.568(19)	0.1888(70)	0.331(22)	−0.358(12)
(340,430)	0.17	1.5105(72)	0.7381(28)	1.107(39)	−1.207(17)
	0.33	1.2179(85)	0.5780(44)	0.849(28)	−0.952(15)
	0.48	1.021(10)	0.4690(57)	0.682(27)	−0.788(14)
	0.62	0.887(16)	0.3929(78)	0.553(31)	−0.668(16)
	0.76	0.775(17)	0.3333(80)	0.458(24)	−0.567(14)
	0.89	0.699(21)	0.2892(96)	0.397(26)	−0.504(17)
	1.14	0.558(27)	0.219(11)	0.275(27)	−0.389(21)
(265,450)	0.17	1.5108(79)	0.7485(27)	1.132(53)	−1.172(26)
	0.33	1.212(10)	0.5920(42)	0.894(37)	−0.950(21)
	0.48	1.019(13)	0.4846(60)	0.682(34)	−0.791(21)
	0.62	0.881(14)	0.4033(82)	0.543(37)	−0.668(23)
	0.76	0.761(16)	0.3411(82)	0.459(26)	−0.576(20)
	0.89	0.680(20)	0.2927(96)	0.409(26)	−0.507(22)
	1.14	0.525(28)	0.213(10)	0.296(33)	−0.385(26)

Table I.12: Raw lattice simulation results for the sigma baryon: data set II.

(m_π, m_K) (MeV)	Q^2 (GeV^2)	$F_1^{\Xi,s}$	$F_1^{\Xi,u}$	$F_2^{\Xi,s}$	$F_2^{\Xi,u}$
(405,405)	0.17	1.5427(36)	0.7270(22)	1.038(28)	−1.193(14)
	0.33	1.2593(63)	0.5578(35)	0.856(23)	−0.9420(90)
	0.48	1.0658(90)	0.4448(46)	0.714(22)	−0.7663(99)
	0.62	0.940(12)	0.3724(57)	0.606(24)	−0.655(12)
	0.76	0.822(12)	0.3100(56)	0.513(19)	−0.555(11)
	0.89	0.730(15)	0.2620(64)	0.440(18)	−0.480(11)
	1.14	0.568(19)	0.1888(70)	0.331(22)	−0.358(12)
(340,430)	0.17	1.5483(42)	0.7144(27)	1.027(26)	−1.197(18)
	0.33	1.2730(67)	0.5471(39)	0.808(22)	−0.920(13)
	0.48	1.0816(95)	0.4364(51)	0.655(21)	−0.746(13)
	0.62	0.947(13)	0.3622(66)	0.529(23)	−0.625(14)
	0.76	0.833(15)	0.3066(69)	0.449(19)	−0.528(12)
	0.9	0.752(19)	0.2654(84)	0.393(20)	−0.466(14)
	1.15	0.613(26)	0.2021(99)	0.283(21)	−0.367(18)
(265,450)	0.17	1.5672(39)	0.7074(25)	0.970(24)	−1.232(18)
	0.33	1.2997(65)	0.5384(35)	0.779(19)	−0.933(14)
	0.48	1.1059(94)	0.4278(44)	0.642(18)	−0.742(13)
	0.63	0.976(12)	0.3525(55)	0.523(21)	−0.633(15)
	0.77	0.856(14)	0.2954(59)	0.454(18)	−0.529(12)
	0.9	0.758(18)	0.2515(64)	0.396(16)	−0.450(15)
	1.16	0.616(26)	0.1905(88)	0.313(25)	−0.338(16)

Table I.13: Raw lattice simulation results for the cascade baryon: data set II.

(m_π, m_K) (MeV)	Q^2 (GeV^2)	$F_1^{p,u}$	$F_1^{p,d}$	$F_2^{p,u}$	$F_2^{p,d}$
(220,540)	0.12	1.612(12)	0.7631(50)	0.93(12)	−1.251(46)
	0.23	1.342(12)	0.6122(75)	0.717(76)	−1.006(36)
	0.34	1.165(16)	0.5103(93)	0.606(74)	−0.877(32)
	0.44	1.016(21)	0.424(12)	0.604(85)	−0.709(38)
	0.54	0.906(18)	0.359(10)	0.534(53)	−0.635(29)
	0.63	0.822(20)	0.311(11)	0.465(45)	−0.563(26)
	0.81	0.678(36)	0.244(15)	0.345(54)	−0.452(36)

Table I.14: Raw lattice simulation results for the nucleon calculated on ensemble 10 (Table 7.1), at $(m_\pi, m_K) = (220, 540)\,\text{MeV}$.

(m_π, m_K) (MeV)	Q^2 (GeV^2)	$F_1^{\Sigma,u}$	$F_1^{\Sigma,s}$	$F_2^{\Sigma,u}$	$F_2^{\Sigma,s}$
(220,540)	0.12	1.6270(77)	0.8219(21)	1.294(88)	−1.314(21)
	0.23	1.3616(92)	0.7040(38)	1.120(60)	−1.147(18)
	0.35	1.178(10)	0.6109(52)	0.952(49)	−1.010(17)
	0.45	1.037(15)	0.5335(74)	0.896(49)	−0.898(19)
	0.56	0.924(16)	0.4723(80)	0.772(35)	−0.810(18)
	0.66	0.829(16)	0.4202(87)	0.681(30)	−0.731(19)
	0.85	0.687(25)	0.338(11)	0.530(34)	−0.610(21)

Table I.15: Raw lattice simulation results for the sigma baryon calculated on ensemble 10 (Table 7.1), at $(m_\pi, m_K) = (220, 540)\,\text{MeV}$.

(m_π, m_K) (MeV)	Q^2 (GeV^2)	$F_1^{\Xi,s}$	$F_1^{\Xi,u}$	$F_2^{\Xi,s}$	$F_2^{\Xi,u}$
(220,540)	0.12	1.6759(21)	0.7779(20)	1.062(26)	−1.410(19)
	0.24	1.4772(47)	0.6288(27)	0.955(21)	−1.155(16)
	0.35	1.3183(71)	0.5251(33)	0.862(19)	−0.982(16)
	0.46	1.1835(94)	0.4400(47)	0.756(19)	−0.848(14)
	0.56	1.079(11)	0.3800(46)	0.691(17)	−0.734(13)
	0.67	0.987(13)	0.3310(48)	0.636(17)	−0.648(13)
	0.87	0.840(18)	0.2594(61)	0.518(17)	−0.512(14)

Table I.16: Raw lattice simulation results for the cascade baryon calculated on ensemble 10 (Table 7.1), at $(m_\pi, m_K) = (220, 540)\,\text{MeV}$.

Appendix J

Additional Results for Chapter 7

This appendix gives further details of the study of the electromagnetic form factors which was presented in Chapter 7.

J.1 Fit Parameters

Figures J.1 and J.2 show the values of the chiral parameters determined by our fits to the magnetic and electric Sachs form factors. The parameters μ_D and μ_F (b_D and b_F) are defined in Eq. (7.28) (Eq. (7.35)), while the c_i appear in Eqs. (7.29) and (7.36). The d_i are relevant linear combinations of the c_i:

$$d_1 = c_5 - \frac{1}{4}c_{11}, \qquad d_2 = c_6 + c_{11}, \tag{J.1a}$$

$$d_3 = c_6 + c_{11}, \qquad d_4 = c_{10} - \frac{5}{2}c_4 + c_{12}. \tag{J.1b}$$

We note that the numerical values of the parameters shown here are unrenormalised. They are included merely to illustrate their approximately linear form in Q^2. Recall that the fits at different values of Q^2 are independent.

J.2 Octet Baryon Form Factors: Figures

Figures J.3, J.4 and J.5 show the connected part of the octet baryon electromagnetic form factors, extrapolated to infinite volume and the physical pseudoscalar masses. The fits shown are those used in Sections 7.5.2 and 7.5.3 to extract the magnetic moments and magnetic and electric mean-square radii.

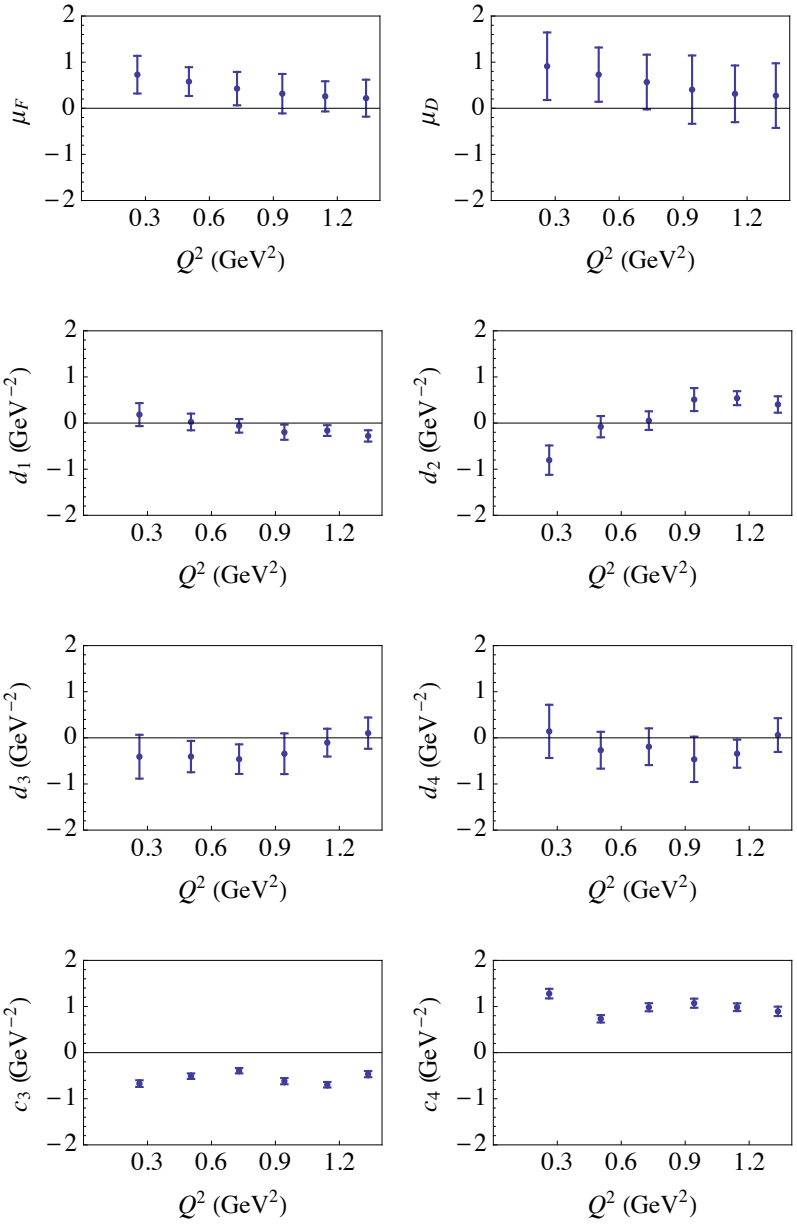

Figure J.1: Q^2-dependence of the unrenormalised fit parameters for the chiral extrapolation of the magnetic Sachs form factors—see Eqs. (7.28) and (7.29).

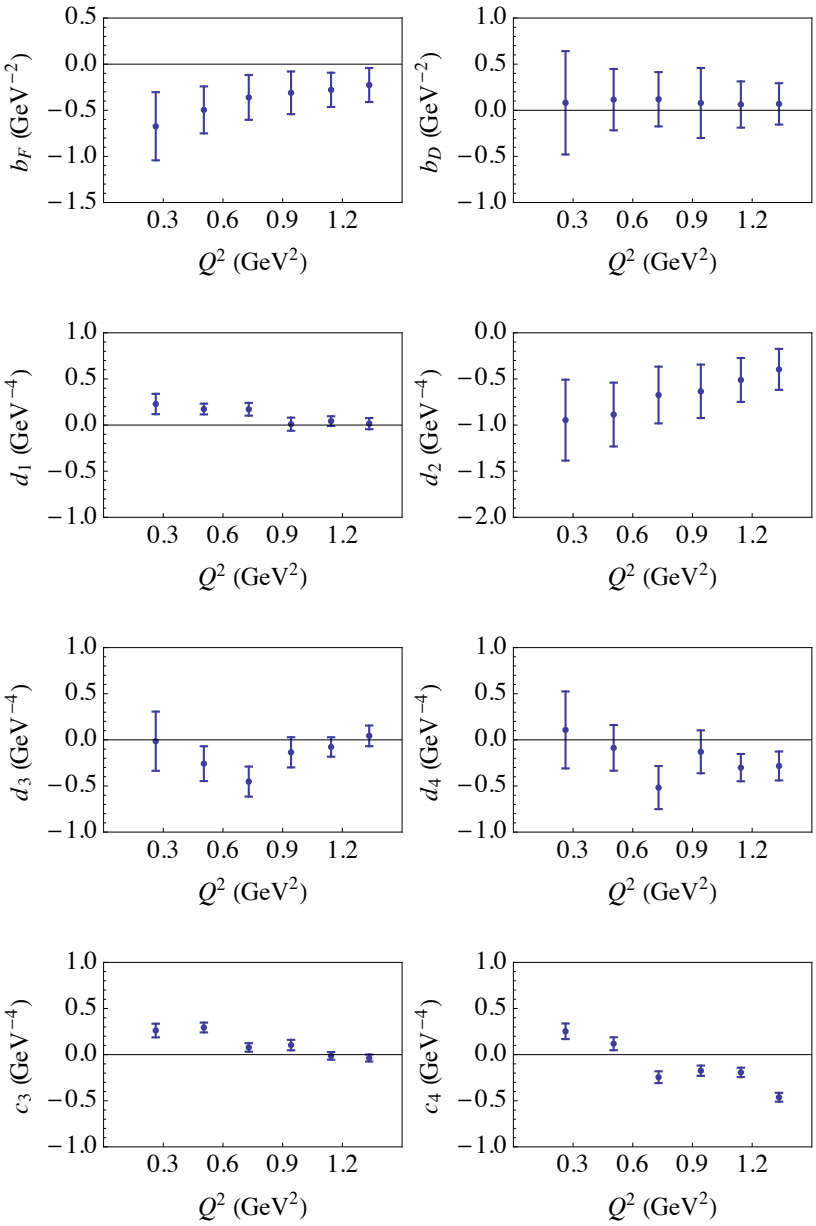

Figure J.2: Q^2-dependence of the unrenormalised fit parameters for the chiral extrapolation of the electric Sachs form factors—see Eqs. (7.35) and (7.36).

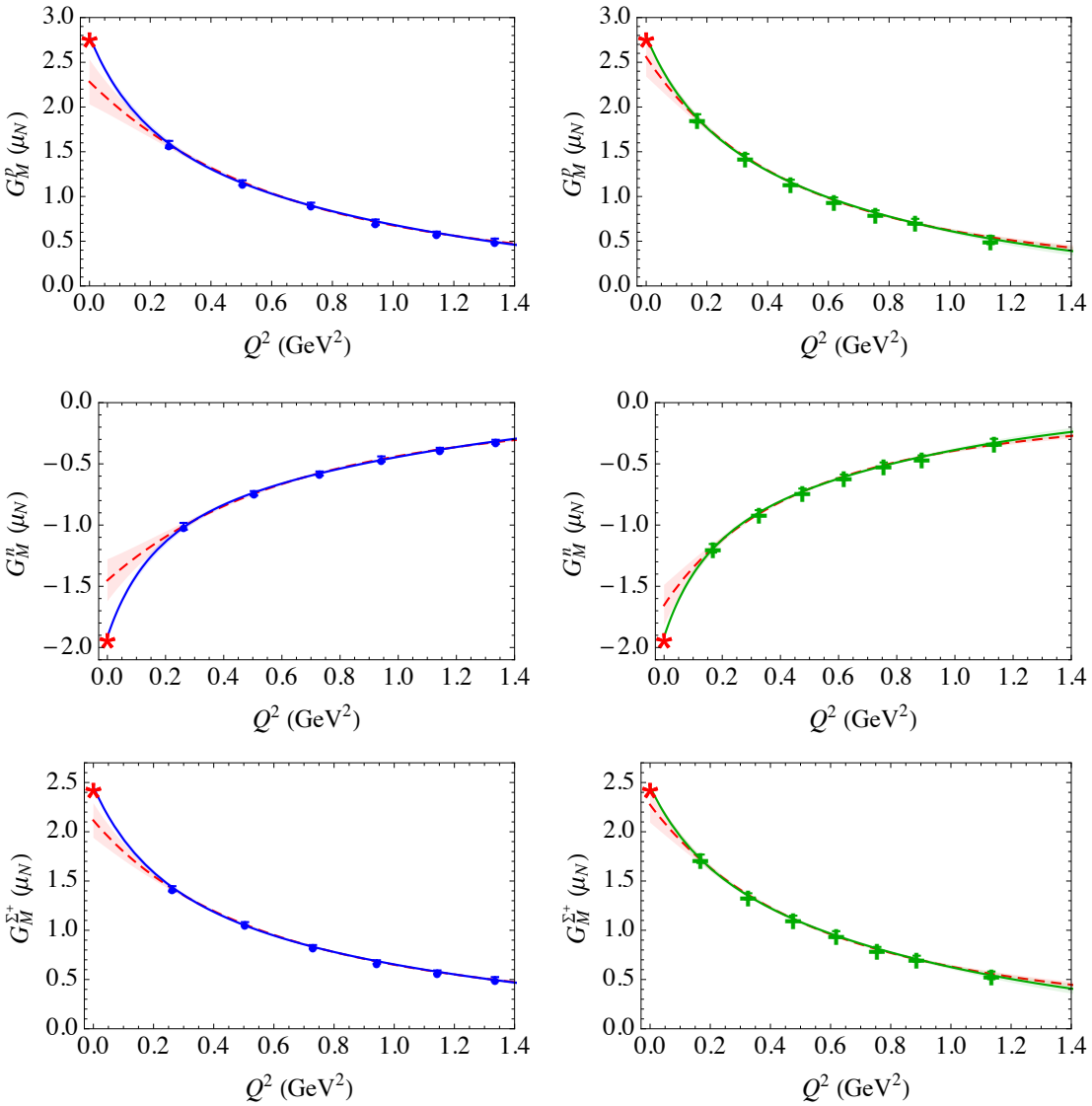

Figure J.3: Connected part of the octet baryon magnetic form factors. The blue circles (left-hand column) and green crosses (right-hand column) denote the results of simulation sets I and II, respectively, extrapolated to infinite volume and the physical pseudoscalar masses. The red stars indicate the experimental magnetic moments. The lines show dipole-like fits in Q^2 using Eq. (7.40) (dashed red) and Eq. (7.41) (solid blue or green).

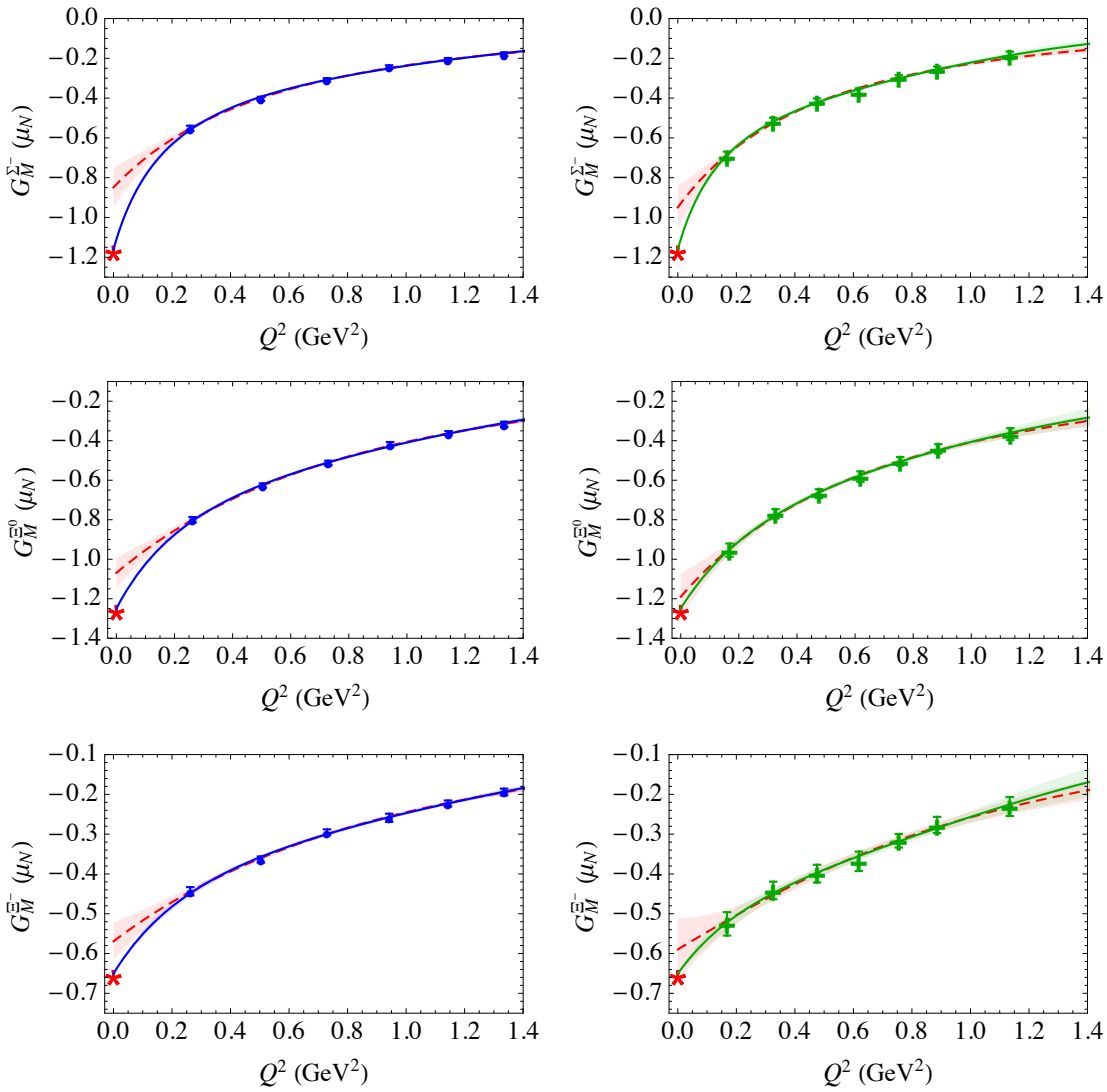

Figure J.4: As in Fig. J.3.

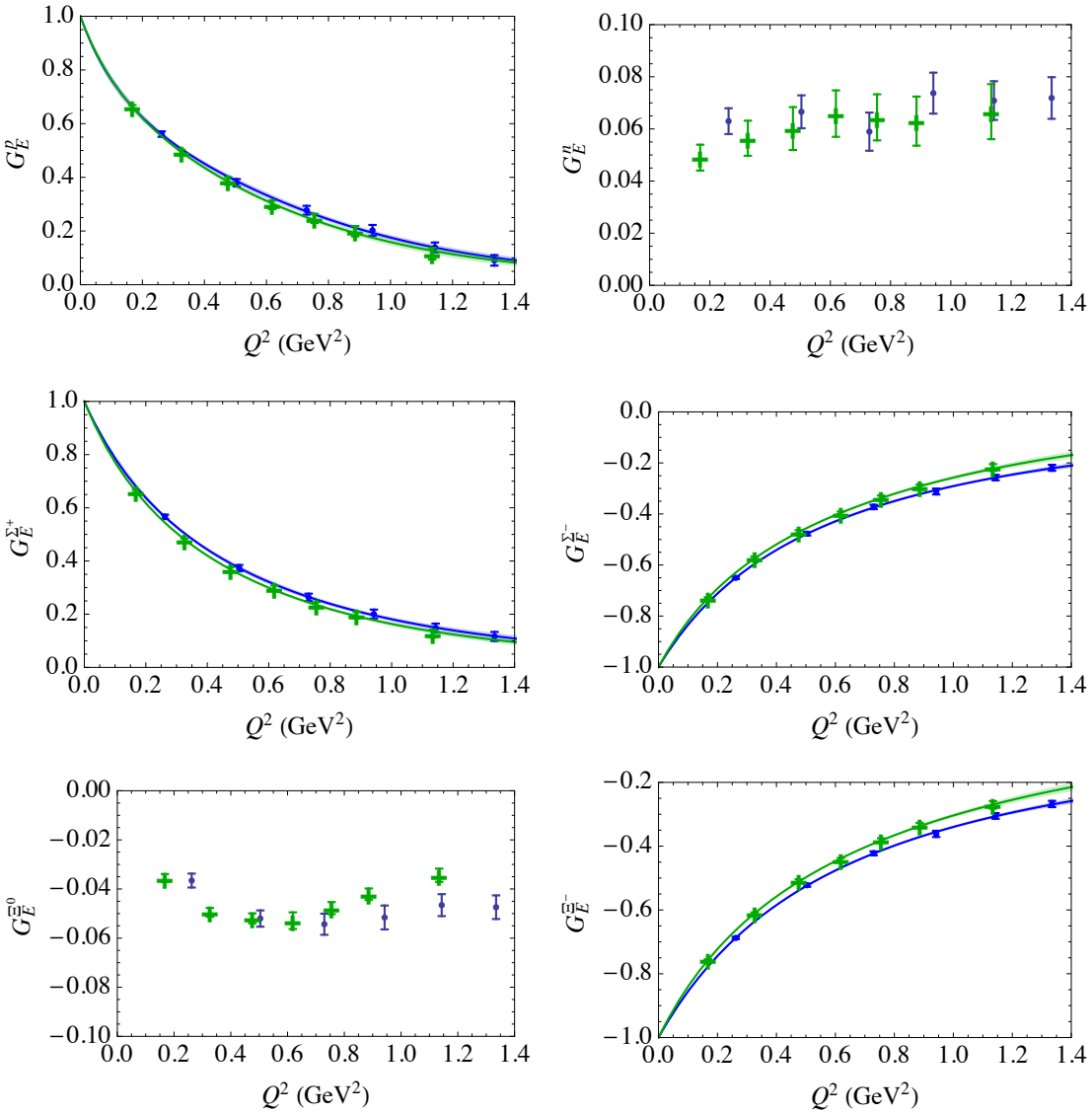

Figure J.5: Connected part of the octet baryon electric form factors. The blue circles and green crosses denote the results of simulation sets I and II, extrapolated to infinite volume and the physical pseudoscalar masses. The lines shown for the charged baryons correspond to dipole-like fits in Q^2 using Eq. (7.42).

J.3 Details of the Calculation of ${}^{\ell}R_d^s$

In this section we give further details of our model for the ratio of disconnected loop contributions to the electromagnetic form factors of the proton, ${}^{\ell}R_d^s = {}^{\ell}G^s/{}^{\ell}G^d$. This quantity is needed for the calculation of the strange form factors performed in Section 7.7.

The loop diagram shown in Fig. 7.6(a) gives contributions to the magnetic and electric form factors of the proton which depend on the integrals I_M and I_E, respectively:

$$I_M(m, Q^2) = \int d\vec{k} \frac{k_y^2\, u(\vec{k} + \vec{q}/2)\, u(\vec{k} - \vec{q}/2)}{2\omega_+^2 \omega_-^2}, \tag{J.2}$$

$$I_E(m, Q^2) = \int d\vec{k} \frac{(\vec{k}^2 - \vec{q}^{\,2}/4)\, u(\vec{k} + \vec{q}/2)\, u(\vec{k} - \vec{q}/2)}{\omega_+ \omega_- (\omega_+ + \omega_-)}, \tag{J.3}$$

where

$$\omega_\pm = \sqrt{(\vec{k} \pm \vec{q}/2)^2 + m^2}, \tag{J.4}$$

$\vec{q}$ is defined to lie along the z-axis, $Q^2 = -q^2$ and $u(\vec{k})$ is the ultraviolet regulator used in the FRR scheme. As was done for the chiral extrapolation of the lattice results used in this calculation [240, 241], we choose a dipole regulator, $u(k) = \left(\frac{\Lambda^2}{\Lambda^2 + k^2}\right)^2$, with a regulator mass $\Lambda = 0.8 \pm 0.2$ GeV. The dipole form is suggested by a comparison of the nucleon's axial and induced pseudoscalar form factors [78] and the choice of Λ is informed by a lattice analysis of nucleon magnetic moments [99].

For the electric form factor we also consider Fig. 7.30(b), as discussed in Section 7.7. In the formalism used here, this diagram contributes a constant to the electric form factor which is equal in magnitude and opposite in sign to the contribution from Fig. 7.6(a) at $Q^2 = 0$, ensuring that the electric charge remains unrenormalised. We model the Q^2-dependence of Fig. 7.30(b) by scaling that constant by an appropriate form factor. This results in a contribution to G_E which is identical to that of Fig. 7.6(a) under the replacement

$$I_E\big(m_\phi, Q^2\big) \to -I_E(m_\phi, 0)\, G_E^q\big(Q^2\big). \tag{J.5}$$

Here G_E^q (for $q = \{d, s\}$) is the q quark contribution to the 'intermediate' baryon form factor; it is the average contribution of q quarks to the form factors of the intermediate baryons in the loop with a proton external state, weighted by the appropriate Clebsch-Gordon coefficients. We approximate this for the s quark by the form factor $G_E^{\Sigma^0,s}$, taken from our lattice simulations. Similarly, we set G_E^d to the same quantity, but where the strange quark mass is set equal to the light quark mass in the chiral extrapolation of Section 7.4.

The contributions of the loop diagrams of Fig. 7.30 to the proton electric and magnetic form factors are given by the loop integrals defined above, weighted by the appropriate chiral coefficients. As the *disconnected* chiral coefficients for the d and s quarks are the same (and cancel in the ratio), the central values of ${}^{\ell}R^{s}_{d}$ at each Q^2 are given simply by the ratio of the integrals $I(m_\phi, Q^2)$ with pion and kaon masses in the loops:

$$ {}^{\ell}R^{s}_{d,M}(Q^2) = \frac{I_M(m_\pi, Q^2)}{I_M(m_K, Q^2)}, \tag{J.6} $$

$$ {}^{\ell}R^{s}_{d,E}(Q^2) = \frac{I_E(m_\pi, Q^2) - I_E(m_\pi, 0)\, G^{d}_{E}(Q^2)}{I_E(m_K, Q^2) - I_E(m_K, 0)\, G^{s}_{E}(Q^2)}. \tag{J.7} $$

The dominant uncertainty in ${}^{\ell}R^{s}_{d}$ comes from allowing the regulator mass Λ to vary in the range 0.6–1.0 GeV. This is combined in quadrature with half of the shift that results from additionally allowing decuplet intermediate states in the loops. The calculation including the decuplet loops proceeds as described above, with additional terms—the relevant decuplet-intermediate-state loop integrals (given in Section 7.3.2)—in both the numerator and denominator of Eqs. (J.6) and (J.7), weighted by the appropriate relative disconnected chiral coefficients which may be found in Ref. [306].

Appendix K

List of Publications

Journal Articles

[1] **P. E. Shanahan**, R. Horsley, Y. Nakamura, D. Pleiter, P. E. L. Rakow, G. Schierholz, H. Stüben, A. W. Thomas, R. D. Young and J. M. Zanotti, "Charge symmetry violation in the nucleon electromagnetic form factors from lattice QCD," Phys. Rev. **D91**, 113006 (2015) [arXiv:1503.01142 [hep-lat]].

[2] **P. E. Shanahan**, R. Horsley, Y. Nakamura, D. Pleiter, P. E. L. Rakow, G. Schierholz, H. Stüben, A. W. Thomas, R. D. Young and J. M. Zanotti, "Determination of the strange nucleon form factors," Phys. Rev. Lett. **114**, 091802 (2015) [arXiv:1403.6537 [hep-lat]].

[3] F. B. Erben, **P. E. Shanahan**, A. W. Thomas and R. D. Young, "Dispersive estimate of the electromagnetic charge symmetry violation in the octet baryon masses," Phys. Rev. **C90**, 065205 (2014) [arXiv:1408.6628 [nucl-th]].

[4] **P. E. Shanahan**, R. Horsley, Y. Nakamura, D. Pleiter, P. E. L. Rakow, G. Schierholz, H. Stüben, A. W. Thomas, R. D. Young and J. M. Zanotti, "Electric form factors of the octet baryons from lattice QCD and chiral extrapolation," Phys. Rev. **D90**, 034502 (2014) [arXiv:1403.1965 [hep-lat]].

[5] **P. E. Shanahan**, R. Horsley, Y. Nakamura, D. Pleiter, P. E. L. Rakow, G. Schierholz, H. Stüben, A. W. Thomas, R. D. Young and J. M. Zanotti, "Magnetic form factors of the octet baryons from lattice QCD and chiral extrapolation," Phys. Rev. **D89**, 074511 (2014) [arXiv:1401.5862 [hep-lat]].

[6] **P. E. Shanahan**, A. W. Thomas and R. D. Young, "Charge symmetry breaking from a chiral extrapolation of moments of quark distribution functions," Phys. Rev. **D87**, 094515 (2013) [arXiv:1303.4806 [nucl-th]].

[7] **P. E. Shanahan**, A. W. Thomas, K. Tsushima, R. D. Young and F. Myhrer, "Octet Spin Fractions and the Proton Spin Problem," Phys. Rev. Lett. **110**, 202001 (2013) [arXiv:1302.6300 [nucl-th]].

[8] **P. E. Shanahan**, A. W. Thomas and R. D. Young, "Chiral expansion of moments of quark distributions," Phys. Rev. **D87**, 114515 (2013) [arXiv:1301.6861 [nucl-th]].

[9] **P. E. Shanahan**, A. W. Thomas and R. D. Young, "Strong contribution to octet baryon mass splittings," Phys. Lett. **B718**, 1148 (2013) [arXiv:1209.1892 [nucl-th]].

[10] **P. E. Shanahan**, A. W. Thomas and R. D. Young, "Sigma terms from an SU(3) chiral extrapolation," Phys. Rev. **D87**, 074503 (2013) [arXiv:1205.5365 [nucl-th]].

[11] **P. E. Shanahan**, A. W. Thomas and R. D. Young, "Mass of the H-dibaryon," Phys. Rev. Lett. **107**, 092004 (2011) [arXiv:1106.2851 [nucl-th]].

Conference Proceedings

[1] A. N. Cooke, R. Horsley, Y. Nakamura, D. Pleiter, P. E. L. Rakow, **P. E. Shanahan**, G. Schierholz, H. Stüben and J. M. Zanotti, "SU(3) flavour breaking and baryon structure," PoS **LATTICE2013**, 278 (2013) [arXiv:1311.4916 [hep-lat]].

[2] R. D. Young, **P. E. Shanahan** and A. W. Thomas, "Progress in resolving charge symmetry violation in nucleon structure," Int. J. Mod. Phys. **E23**, 1461010 (2014) [arXiv:1312.4990 [nucl-th]].

[3] **P. E. Shanahan**, A. W. Thomas and R. D. Young, "Updated Analysis of the Mass of the H Dibaryon from Lattice QCD," JPS Conf. Proc. **1**, 013028 (2014) [arXiv:1308.1748 [nucl-th]].

[4] **P. E. Shanahan**, A. W. Thomas and R. D. Young, "Scale setting, sigma terms and the Feynman-Hellman theorem," PoS **LATTICE2012**, 165 (2012) [arXiv:1301.3231 [hep-lat]].

[5] A. W. Thomas, **P. E. Shanahan** and R. D. Young, "Strangeness in the nucleon: what have we learned?," Nuovo Cim. **C035N04**, 3 (2012) [arXiv:1202.6407 [nucl-th]].

[6] A. W. Thomas, **P. E. Shanahan** and R. D. Young, "Strange quarks and lattice QCD," Few Body Syst. **54**, 123 (2013) [arXiv:1111.0114 [nucl-th]].

Bibliography

[1] G. Aad *et al.* (ATLAS Collaboration), Phys. Lett. **B716**, 1 (2012).

[2] S. Chatrchyan *et al.* (CMS Collaboration), Phys. Lett. **B716**, 30 (2012).

[3] C. A. Baker *et al.*, Phys. Rev. Lett. **97**, 131801 (2006).

[4] D. J. Gross and F. Wilczek, Phys. Rev. Lett. **30**, 1343 (1973).

[5] H. D. Politzer, Phys. Rev. Lett. **30**, 1346 (1973).

[6] K. G. Wilson, Phys. Rev. **D10**, 2445 (1974).

[7] T. Inoue *et al.* (HAL QCD Collaboration), Phys. Rev. **C91**, 11001 (2015).

[8] H. Nemura (HAL QCD Collaboration), Int. J. Mod. Phys. **E23**, 1461006 (2014).

[9] C. S. Fischer, J. Luecker, and C. A. Welzbacher, Phys. Rev. **D90**, 034022 (2014).

[10] P. de Forcrand, J. Langelage, O. Philipsen, and W. Unger, Phys. Rev. Lett. **113**, 152002 (2014).

[11] H. J. Rothe, World Sci. Lect. Notes Phys. **74**, 1 (2005).

[12] J. Smit, Cambridge Lect. Notes Phys. **15**, 1 (2002).

[13] C. Gattringer and C. B. Lang, Lect. Notes Phys **788**, 1 (2010).

[14] R. P. Feynman, Rev. Mod. Phys. **20**, 367 (1948).

[15] W. Celmaster, Phys. Rev. **D26**, 2955 (1982).

[16] N. H. Christ, R. Friedberg, and T. D. Lee, Nucl. Phys. **B202**, 89 (1982).

[17] R. Morrin, A. Ó Cais, M. Peardon, S. M. Ryan, and J.-I. Skullerud (TrinLat Collaboration), Phys. Rev. **D74**, 014505 (2006).

[18] R. G. Edwards, B. Joó, and H.-W. Lin, Phys. Rev. **D78**, 054501 (2008).

[19] K. Symanzik, Nucl. Phys. **B226**, 187 (1983).

[20] B. Sheikholeslami and R. Wohlert, Nucl. Phys. **B259**, 572 (1985).

[21] N. Cundy *et al.*, Phys. Rev. **D79**, 094507 (2009).

[22] M. Lüscher and P. Weisz, Commun. Math. Phys. **97**, 59 (1985).

[23] S. Itoh, Y. Iwasaki, Y. Oyanagi, and T. Yoshié, Phys. Lett. **B148**, 153 (1984).

[24] W. Bietenholz *et al.*, Phys. Rev. **D84**, 054509 (2011).

[25] S. Dürr *et al.*, Phys. Lett. **B701**, 265 (2011).

[26] S. Dürr *et al.*, Science **322**, 1224 (2008).

[27] G. A. Miller, A. K. Opper, and E. J. Stephenson, Ann. Rev. Nucl. Part. Sci. **56**, 253 (2006).

[28] A. Abdel-Rehim *et al.*, Phys. Rev. **D89**, 034501 (2014).

[29] T. Doi *et al.*, Phys. Rev. **D80**, 094503 (2009).
[30] J. Beringer *et al.* (Particle Data Group), Phys. Rev. **D86**, 010001 (2012).
[31] J. A. Nolen and J. P. Schiffer, Ann. Rev. Nucl. Part. Sci. **19**, 471 (1969).
[32] R. Horsley *et al.*, Phys. Rev. **D83**, 051501 (2011).
[33] J. T. Londergan, J. C. Peng, and A. W. Thomas, Rev. Mod. Phys. **82**, 2009 (2010).
[34] S. Borsanyi *et al.* (BMW Collaboration), Phys. Rev. Lett. **111**, 252001 (2013).
[35] S. Borsanyi *et al.* (BMW Collaboration), [arXiv:1406.4088].
[36] A. D. Martin, R. G. Roberts, W. J. Stirling, and R. S. Thorne, Eur. Phys. J. **C35**, 325 (2004).
[37] E. N. Rodionov, A. W. Thomas, and J. T. Londergan, Mod. Phys. Lett. **A9**, 1799 (1994).
[38] E. Sather, Phys. Lett. **B274**, 433 (1992).
[39] J. T. Londergan and A. W. Thomas, Prog. Part. Nucl. Phys. **41**, 49 (1998).
[40] J. T. Londergan and A. W. Thomas, Phys. Lett. **B558**, 132 (2003).
[41] G. P. Zeller *et al.* (NuTeV Collaboration), Phys. Rev. Lett. **88**, 091802 (2002).
[42] S. Weinberg, Phys. Rev. Lett. **18**, 188 (1967).
[43] R. Dashen and M. Weinstein, Phys. Rev. **183**, 1261 (1969).
[44] S. Weinberg, Physica **A96**, 327 (1979).
[45] S. Coleman, J. Wess, and B. Zumino, Phys. Rev. **177**, 2239 (1969).
[46] C. G. Callan *et al.*, Phys. Rev. **177**, 2247 (1969).
[47] L. F. Li and H. Pagels, Phys. Rev. Lett. **26**, 1204 (1971).
[48] L. F. Li and H. Pagels, Phys. Rev. Lett. **27**, 1089 (1971).
[49] J. Gasser and H. Leutwyler, Ann. Phys. **158**, 142 (1984).
[50] J. Goldstone, A. Salam, and S. Weinberg, Phys. Rev. **127**, 965 (1962).
[51] M. Gell-Mann, Phys. Rev. **125**, 1067 (1962).
[52] E. Reya, Rev. Mod. Phys. **46**, 545 (1974).
[53] H. Pagels, Phys. Rept. **16**, 219 (1975).
[54] S. Scherer, Adv. Nucl. Phys. **27**, 277 (2003).
[55] A. Pich, [arXiv:hep-ph/9806303].
[56] E. E. Jenkins and A. V. Manohar, Phys. Lett. **B255**, 558 (1991).
[57] G. Amoros, J. Bijnens, and P. Talavera, Nucl. Phys. **B602**, 87 (2001).
[58] M. Gell-Mann, R. J. Oakes, and B. Renner, Phys. Rev. **175**, 2195 (1968).
[59] M. Gell-Mann, Phys. Rev. **106**, 1296 (1957).
[60] S. Okubo, Prog. Theor. Phys. **27**, 949 (1962).
[61] S. Weinberg, Phys. Rev. Lett. **17**, 616 (1966).
[62] H. W. Fearing and S. Scherer, Phys. Rev. **D53**, 315 (1996).
[63] H. Georgi, Phys. Lett. **B240**, 447 (1990).

[64] U. G. Meißner, [arXiv:hep-ph/9711365].

[65] J. F. Donoghue *et al.*, Phys. Rev. **D59**, 036002 (1999).

[66] D. B. Leinweber, D.-H. Lu, and A. W. Thomas, Phys. Rev. **D60**, 034014 (1999).

[67] D. B. Leinweber, A. W. Thomas, K. Tsushima, and S. V. Wright, Phys. Rev. **D61**, 074502 (2000).

[68] R. D. Young, D. B. Leinweber, A. W. Thomas, and S. V. Wright, Phys. Rev. **D66**, 094507 (2002).

[69] R. D. Young, D. B. Leinweber, and A. W. Thomas, Prog. Part. Nucl. Phys. **50**, 399 (2003).

[70] D. B. Leinweber, A. W. Thomas, and R. D. Young, Phys. Rev. Lett. **92**, 242002 (2004).

[71] P. Lepage, [arXiv:nucl-th/9706029].

[72] R. D. Young, D. B. Leinweber, and A. W. Thomas, Phys. Rev. **D71**, 014001 (2005).

[73] R. E. Stuckey and M. C. Birse, J. Phys. **G23**, 29 (1997).

[74] A. W. Thomas, Nucl. Phys. Proc. Suppl. **119**, 50 (2003).

[75] D. B. Leinweber, D. H. Lu, and A. W. Thomas, Phys. Rev. **D60**, 034014 (1999).

[76] I. S. Gerstein, R. Jackiw, B. W. Lee, and S. Weinberg, Phys. Rev. **D3**, 2486 (1971).

[77] R. D. Young, J. M. M. Hall, and D. B. Leinweber, [arXiv:0907.0408].

[78] P. A. M. Guichon, G. A. Miller, and A. W. Thomas, Phys. Lett. **B124**, 109 (1983).

[79] H. Leutwyler, Phys. Lett. **B189**, 197 (1987).

[80] H. Leutwyler and A. V. Smilga, Phys. Rev. **D46**, 5607 (1992).

[81] E. Elizalde, Commun. Math. Phys. **198**, 83 (1998).

[82] S. R. Beane, Phys. Rev. **D70**, 034507 (2004).

[83] S. R. Beane *et al.*, Phys. Rev. **D84**, 014507 (2011).

[84] C. J. Hogan, Phys. Rev. **D74**, 123514 (2006).

[85] P. J. Mohr, B. N. Taylor, and D. B. Newell, Rev. Mod. Phys. **84**, 1527 (2012).

[86] S. R. Beane, K. Orginos, and M. J. Savage, Nucl. Phys. **B768**, 38 (2007).

[87] T. Blum *et al.*, Phys. Rev. **D82**, 094508 (2010).

[88] A. Walker-Loud, PoS **LATTICE2010**, 243 (2010).

[89] G. M. de Divitiis *et al.*, JHEP **1204**, 124 (2012).

[90] R. Horsley *et al.* (QCDSF-UKQCD Collaboration), Phys. Rev. **D86**, 114511 (2012).

[91] A. Duncan, E. Eichten, and H. Thacker, Phys. Rev. Lett. **76**, 3894 (1996).

[92] S. Basak *et al.*, PoS **LATTICE2008**, 127 (2008).

[93] A. Portelli, PoS **LATTICE2011**, 136 (2011).
[94] B. Gläßle and G. S. Bali, PoS **LATTICE2011**, 282 (2011).
[95] S. Aoki *et al.*, Phys. Rev. **D79**, 034503 (2009).
[96] W. Bietenholz *et al.* (QCDSF-UKQCD Collaboration), Phys. Rev. **D84**, 054509 (2011).
[97] J. Gasser and H. Leutwyler, Phys. Rept. **87**, 77 (1982).
[98] A. Walker-Loud, C. E. Carlson, and G. A. Miller, Phys. Rev. Lett. **108**, 232301 (2012).
[99] J. M. M. Hall, D. B. Leinweber, and R. D. Young, Phys. Rev. **D85**, 094502 (2012).
[100] H. Leutwyler, Phys. Lett. **B378**, 313 (1996).
[101] G. Colangelo *et al.*, Eur. Phys. J. **C71**, 1 (2011).
[102] C. Aubin *et al.* (MILC Collaboration), Phys. Rev. **D70**, 114501 (2004).
[103] F. B. Erben, P. E. Shanahan, A. W. Thomas, and R. D. Young, Phys. Rev. **C90**, 065205 (2014).
[104] M. C. Birse, J. Phys. **G20**, 1537 (1994).
[105] L. S. Brown, W. J. Pardee, and R. D. Peccei, Phys. Rev. **D4**, 2801 (1971).
[106] J. Gasser, H. Leutwyler, and M. E. Sainio, Phys. Lett. **B253**, 260 (1991).
[107] B. Borasoy and U. G. Meißner, Ann. Phys. **254**, 192 (1997).
[108] R. D. Young, AIP Conf. Proc. **1182**, 905 (2009).
[109] J. Gasser, H. Leutwyler, and M. E. Sainio, Phys. Lett. **B253**, 252 (1991).
[110] R. D. Young and A. W. Thomas, Phys. Rev. **D81**, 014503 (2010).
[111] D. Toussaint and W. Freeman (MILC Collaboration), Phys. Rev. Lett. **103**, 122002 (2009).
[112] S. Dinter *et al.*, JHEP **1208**, 37 (2012).
[113] G. S. Bali *et al.*, Phys. Rev. **D85**, 054502 (2011).
[114] S. Dinter, V. Drach, and K. Jansen, Int. J. Mod. Phys. Proc. Suppl. **E20**, 110 (2011).
[115] S. Dürr *et al.*, Phys. Rev. **D85**, 014509 (2011).
[116] R. Babich *et al.*, Phys. Rev. **D85**, 054510 (2010).
[117] K. Takeda *et al.* (JLQCD Collaboration), Phys. Rev. **D83**, 114506 (2011).
[118] P. E. Shanahan, A. W. Thomas, and R. D. Young, Phys. Rev. **D87**, 074503 (2013).
[119] J. Ellis, K. A. Olive, and C. Savage, Phys. Rev. **D77**, 065026 (2008).
[120] J. Ellis, K. A. Olive, and P. Sandick, New J. Phys. **11**, 105015 (2009).
[121] J. Giedt, A. W. Thomas, and R. D. Young, Phys. Rev. Lett. **103**, 201802 (2009).
[122] R. J. Hill and M. P. Solon, Phys. Lett. **B707**, 539 (2012).
[123] J. Ellis and K. A. Olive, Eur. Phys. J. **C72**, 2005 (2012).

[124] S. J. Underwood *et al.*, Phys. Rev. **D86**, 035009 (2012).

[125] M. Engelhardt, Phys. Rev. **D86**, 114510 (2012).

[126] H. Ohki *et al.* (JLQCD Collaboration), Phys. Rev. **D87**, 034509 (2013).

[127] R. P. Feynman, Phys. Rev. **56**, 340 (1939).

[128] P. E. Shanahan, A. W. Thomas, and R. D. Young, PoS **LATTICE2012**, 165 (2012).

[129] A. K. De, A. Harindranath, and J. Maiti, [arXiv:0803.1281].

[130] G. S. Bali, [arXiv:hep-lat/9311009].

[131] W. Freeman and D. Toussaint (MILC Collaboration), Phys. Rev. **D88**, 054503 (2013).

[132] S. Dürr *et al.*, PoS **LATTICE2010**, 102 (2010).

[133] M. Foster and C. Michael (UKQCD Collaboration), Phys. Rev. **D59**, 074503 (1999).

[134] C. Michael, C. McNeile, and D. Hepburn (UKQCD Collaboration), Nucl. Phys. Proc. Suppl. **106**, 293 (2002).

[135] J. R. Ellis, A. Ferstl, and K. A. Olive, Phys. Rev. **D63**, 065016 (2001).

[136] J. R. Ellis, A. Ferstl, and K. A. Olive, Phys. Lett. **B481**, 304 (2000).

[137] M. Fukugita *et al.*, Phys. Rev. **D51**, 5319 (1995).

[138] S. J. Dong, J. F. Lagaë, and K. F. Liu, Phys. Rev. **D54**, 5496 (1996).

[139] S. Güsken *et al.* (SESAM Collaboration), Phys. Rev. **D59**, 054504 (1999).

[140] D. B. Leinweber, A. W. Thomas, and S. V. Wright, Phys. Lett. **B482**, 109 (2000).

[141] M. Procura, T. R. Hemmert, and W. Weise, Phys. Rev. **D69**, 034505 (2004).

[142] M. Procura *et al.*, Phys. Rev. **D73**, 114510 (2006).

[143] C. Alexandrou *et al.*, Phys. Rev. **D78**, 014509 (2008).

[144] H. Ohki *et al.* (JLQCD Collaboration), Phys. Rev. **D78**, 054502 (2008).

[145] K. I. Ishikawa *et al.* (PACS-CS Collaboration), Phys. Rev. **D80**, 054502 (2009).

[146] G. S. Bali *et al.* (QCDSF Collaboration), Prog. Part. Nucl. Phys. **67**, 467 (2012).

[147] C. Alexandrou *et al.*, [arXiv:1309.7768].

[148] L. Alvarez-Ruso, T. Ledwig, J. Martin Camalich, and M. J. Vicente-Vacas, Phys. Rev. **D88**, 054507 (2013).

[149] P. M. Junnarkar and A. Walker-Loud, Phys. Rev. **D87**, 114510 (2013).

[150] X.-L. Ren, L.-S. Geng, and J. Meng, [arXiv:1404.4799].

[151] E. D. Bloom *et al.*, Phys. Rev. Lett. **23**, 930 (1969).

[152] M. Breidenbach *et al.*, Phys. Rev. Lett. **23**, 935 (1969).

[153] J. D. Bjorken, Phys. Rev. **179**, 1547 (1969).

[154] R. P. Feynman, Phys. Rev. Lett. **23**, 1415 (1969).

[155] J. Ashman *et al.* (European Muon Collaboration), Phys. Lett. **B206**, 364 (1988).

[156] V. Y. Alexakhin *et al.* (COMPASS Collaboration), Phys. Lett. **B647**, 8 (2007).

[157] H.-L. Lai *et al.*, Phys. Rev. **D82**, 074024 (2010).

[158] C. Adloff *et al.* (H1 Collaboration), Eur. Phys. J. **C30**, 1 (2003).

[159] R. D. Ball *et al.* (NNPDF Collaboration), Nucl. Phys. **B809**, 1 (2009).

[160] A. D. Martin, W. J. Stirling, R. S. Thorne, and G. Watt, Phys. Lett. **B652**, 292 (2007).

[161] D. Diakonov, V. Petrov, P. Pobylitsa, M. V. Polyakov, and C. Weiss, Nucl. Phys. **B480**, 341 (1996).

[162] A. W. Schreiber, P. J. Mulders, A. I. Signal, and A. W. Thomas, Phys. Rev. **D45**, 3069 (1992).

[163] L. P. Gamberg, G. R. Goldstein, and K. A. Oganessyan, Phys. Rev. **D67**, 071504 (2003).

[164] I. C. Cloët, W. Bentz, and A. W. Thomas, Phys. Lett. **B621**, 246 (2005).

[165] I. C. Cloët, W. Bentz, and A. W. Thomas, Phys. Lett. **B659**, 214 (2008).

[166] A. Bacchetta, F. Conti, and M. Radici, Phys. Rev. **D78**, 074010 (2008).

[167] C. Lorcé, B. Pasquini, and M. Vanderhaeghen, JHEP **1105**, 041 (2011).

[168] J. T. Londergan, D. P. Murdock, and A. W. Thomas, Phys. Rev. **D72**, 036010 (2005).

[169] J. T. Londergan, Eur. Phys. J. **A24S2**, 85 (2005).

[170] X. Ji, Phys. Rev. Lett. **110**, 262002 (2013).

[171] W. Detmold, W. Melnitchouk, and A. W. Thomas, Phys. Rev. **D66**, 054501 (2002).

[172] G. S. Bali *et al.*, Phys. Rev. **D86**, 054504 (2012).

[173] I. C. Cloët *et al.*, Phys. Lett. **B714**, 97 (2012).

[174] J.-W. Chen and M. J. Savage, Nucl. Phys. **A707**, 452 (2002).

[175] J.-W. Chen and X. Ji, Phys. Lett. **B523**, 107 (2001).

[176] D. Arndt and M. J. Savage, Nucl. Phys. **A697**, 429 (2002).

[177] B. Borasoy, B. R. Holstein, R. Lewis, and P. P. A. Ouimet, Phys. Rev. **D66**, 094020 (2002).

[178] M. Diehl, A. Manashov, and A. Schäfer, Eur. Phys. J. **A31**, 335 (2007).

[179] M. Dorati, T. A. Gail, and T. R. Hemmert, Nucl. Phys. **A798**, 96 (2008).

[180] J.-W. Chen and X. Ji, Phys. Rev. Lett. **88**, 052003 (2002).

[181] M. Burkardt, K. S. Hendricks, C.-R. Ji, W. Melnitchouk, and A. W. Thomas, Phys. Rev. **D87**, 056009 (2013).

[182] W. Detmold and C. J. D. Lin, Phys. Rev. **D71**, 054510 (2005).

[183] A. D. Martin, R. G. Roberts, W. J. Stirling, and R. S. Thorne, Eur. Phys. J. **C28**, 455 (2003).

[184] C. A. Aidala, S. D. Bass, D. Hasch, and G. K. Mallot, Rev. Mod. Phys. **85**, 655 (2013).

[185] M. Anselmino, A. Efremov, and E. Leader, Phys. Rept. **261**, 1 (1995).

[186] S. D. Bass, Rev. Mod. Phys. **77**, 1257 (2005).

[187] S. D. Bass and A. W. Thomas, Phys. Lett. **B684**, 216 (2010).

[188] G. S. Bali *et al.* (QCDSF Collaboration), Phys. Rev. Lett. **108**, 222001 (2012).

[189] G. Altarelli and G. G. Ross, Phys. Lett. **B212**, 391 (1988).

[190] R. D. Carlitz, J. C. Collins, and A. H. Mueller, Phys. Lett. **B214**, 229 (1988).

[191] G. T. Bodwin and J.-W. Qiu, Phys. Rev. **D41**, 2755 (1990).

[192] S. D. Bass, B. L. Ioffe, N. N. Nikolaev, and A. W. Thomas, J. Moscow. Phys. Soc. **1**, 317 (1991).

[193] A. V. Efremov, J. Soffer, and O. V. Teryaev, Nucl. Phys. **B346**, 97 (1990).

[194] R. L. Jaffe and A. Manohar, Nucl. Phys. **B337**, 509 (1990).

[195] G. M. Shore and G. Veneziano, Nucl. Phys. **B381**, 23 (1992).

[196] F. Myhrer and A. W. Thomas, Phys. Rev. **D38**, 1633 (1988).

[197] K. Tsushima, T. Yamaguchi, Y. Kohyama, and K. Kubodera, Nucl. Phys. **A489**, 557 (1988).

[198] H. Høgaasen and F. Myhrer, Phys. Lett. **B214**, 123 (1988).

[199] A. W. Schreiber and A. W. Thomas, Phys. Lett. **B215**, 141 (1988).

[200] M. Wakamatsu, Phys. Lett. **B232**, 251 (1989).

[201] A. Adare *et al.* (PHENIX Collaboration), Phys. Rev. **D76**, 051106 (2007).

[202] B. I. Abelev *et al.* (STAR Collaboration), Phys. Rev. Lett. **100**, 232003 (2008).

[203] F. Myhrer and A. W. Thomas, Phys. Lett. **B663**, 302 (2008).

[204] D. de Florian, G. M. Shore, and G. Veneziano, [arXiv:hep-ph/9711353].

[205] A. J. Chambers *et al.* (CSSM/QCDSF-UKQCD Collaboration), Phys. Rev. **D90**, 014510 (2014).

[206] P. E. Shanahan, A. W. Thomas, K. Tsushima, R. D. Young, and F. Myhrer, Phys. Rev. Lett. **110**, 202001 (2013).

[207] A. W. Thomas, Adv. Nucl. Phys. **13**, 1 (1984).

[208] A. W. Thomas, S. Theberge, and G. A. Miller, Phys. Rev. **D24**, 216 (1981).

[209] S. Theberge, A. W. Thomas, and G. A. Miller, Phys. Rev. **D22**, 2838 (1980).

[210] G. A. Miller, Int. Rev. Nucl. Phys. **1**, 189 (1984).

[211] H. Høgaasen and F. Myhrer, Z. Phys. **C68**, 625 (1995).

[212] K. Tsushima, T. Yamaguchi, M. Takizawa, Y. Kohyama, and K. Kubodera, Phys. Lett. **B205**, 128 (1988).

[213] J. Blümlein and H. Böttcher, Nucl. Phys. **B841**, 205 (2010).

[214] J. D. Bjorken, Phys. Rev. **148**, 1467 (1966).

[215] J. D. Bjorken, Phys. Rev. **D1**, 1376 (1970).

[216] M. G. Alekseev *et al.* (COMPASS Collaboration), Phys. Lett. **B690**, 466 (2010).

[217] W. Bentz, I. C. Cloët, J. T. Londergan, and A. W. Thomas, Phys. Lett. **B693**, 462 (2010).

[218] R. Hofstadter, H. R. Fechter, and J. A. McIntyre, Phys. Rev. **92**, 978 (1953).

[219] M. N. Rosenbluth, Phys. Rev. **79**, 615 (1950).

[220] R. Hofstadter and R. W. McAllister, Phys. Rev. **98**, 217 (1955).

[221] M. R. Yearian and R. Hofstadter, Phys. Rev. **110**, 552 (1958).

[222] J. Arrington, C. D. Roberts, and J. M. Zanotti, J. Phys. **G34**, S23 (2007).

[223] J. C. Bernauer *et al.* (A1 Collaboration), Phys. Rev. Lett. **105**, 242001 (2010).

[224] M. K. Jones *et al.* (Jefferson Lab Hall A Collaboration), Phys. Rev. Lett. **84**, 1398 (2000).

[225] G. Ron *et al.* (Jefferson Lab Hall A Collaboration), Phys. Rev. **C84**, 055204 (2011).

[226] X. Zhan *et al.*, Phys. Lett. **B705**, 59 (2011).

[227] C. Alexandrou, G. Koutsou, T. Leontiou, J. W. Negele, and A. Tsapalis, Phys. Rev. **D76**, 094511 (2007).

[228] C. Alexandrou, G. Koutsou, J. W. Negele, and A. Tsapalis, Phys. Rev. **D74**, 034508 (2006).

[229] M. Göckeler *et al.* (QCDSF Collaboration), Phys. Rev. **D71**, 034508 (2005).

[230] P. Hägler *et al.* (LHPC Collaboration), Phys. Rev. **D77**, 094502 (2008).

[231] H.-W. Lin, T. Blum, S. Ohta, S. Sasaki, and T. Yamazaki, Phys. Rev. **D78**, 014505 (2008).

[232] K. F. Liu, S. J. Dong, T. Draper, and W. Wilcox, Phys. Rev. Lett. **74**, 2172 (1995).

[233] S. Sasaki and T. Yamazaki, Phys. Rev. **D78**, 014510 (2008).

[234] P. Hägler, Phys. Rept. **490**, 49 (2010).

[235] S. Boinepalli, D. B. Leinweber, A. G. Williams, J. M. Zanotti, and J. B. Zhang, Phys. Rev. **D74**, 093005 (2006).

[236] T. Yamazaki *et al.*, Phys. Rev. **D79**, 114505 (2009).

[237] S. Collins *et al.*, Phys. Rev. **D84**, 074507 (2011).

[238] H.-W. Lin and K. Orginos, Phys. Rev. **D79**, 074507 (2009).

[239] P. Wang, D. B. Leinweber, A. W. Thomas, and R. D. Young, Phys. Rev. **D79**, 094001 (2009).

[240] P. E. Shanahan *et al.*, Phys. Rev. **D89**, 074511 (2014).

[241] P. E. Shanahan *et al.*, Phys. Rev. **D90**, 034502 (2014).

[242] D. B. Leinweber, R. M. Woloshyn, and T. Draper, Phys. Rev. **D43**, 1659 (1991).

[243] I. C. Cloët, D. B. Leinweber, and A. W. Thomas, Phys. Rev. **C65**, 062201 (2002).

[244] A. W. Thomas, Nucl. Phys. Proc. Suppl. **119**, 50 (2003).

[245] I. C. Cloët, C. D. Roberts, and A. W. Thomas, Phys. Rev. Lett. **111**, 101803 (2013).

[246] G. Bali *et al.*, PoS **LATTICE2011**, 174 (2011).

[247] C. Alexandrou, V. Drach, K. Jansen, G. Koutsou, and A. V. Avilés-Casco, PoS **LATTICE2013**, 270 (2014).

[248] R. Babich *et al.*, Phys. Rev. **D85**, 054510 (2012).

[249] L. Foldy, Phys. Rev. **87**, 688 (1952).

[250] B. C. Tiburzi, Phys. Rev. **D79**, 077501 (2009).

[251] D. Arndt and B. C. Tiburzi, Phys. Rev. **D69**, 014501 (2004).

[252] D. B. Leinweber, Phys. Rev. **D69**, 014005 (2004).

[253] W. Bietenholz *et al.*, Phys. Lett. **B690**, 436 (2010).

[254] R. Horsley *et al.*, PoS **LATTICE2013**, 249 (2013).

[255] T. Bhattacharya, S. D. Cohen, R. Gupta, A. Joseph, and H.-W. Lin, Phys. Rev. **D89**, 094502 (2014).

[256] J. D. Bratt *et al.* (LHPC Collaboration), Phys. Rev. **D82**, 094502 (2010).

[257] H.-W. Lin, S. D. Cohen, R. G. Edwards, K. Orginos, and D. G. Richards, [arXiv:1005.0799].

[258] S. N. Syritsyn *et al.*, Phys. Rev. **D81**, 034507 (2010).

[259] C. W. Bernard and M. F. L. Golterman, Phys. Rev. **D49**, 486 (1994).

[260] S. R. Sharpe and N. Shoresh, Phys. Rev. **D64**, 114510 (2001).

[261] S. R. Sharpe and N. Shoresh, Phys. Rev. **D62**, 094503 (2000).

[262] S. R. Sharpe and Y. Zhang, Phys. Rev. **D53**, 5125 (1996).

[263] J.-W. Chen and M. J. Savage, Phys. Rev. **D65**, 094001 (2002).

[264] M. J. Savage, Nucl. Phys. **A700**, 359 (2002).

[265] C. R. Allton, W. Armour, D. B. Leinweber, A. W. Thomas, and R. D. Young, PoS **LATTICE2005**, 049 (2005).

[266] E. E. Jenkins, Nucl. Phys. **B368**, 190 (1992).

[267] E. E. Jenkins and A. V. Manohar, Phys. Lett. **B259**, 353 (1991).

[268] E. E. Jenkins, Nucl. Phys. **B375**, 561 (1992).

[269] E. E. Jenkins, M. E. Luke, A. V. Manohar, and M. J. Savage, Phys. Lett. **B302**, 482 (1993).

[270] J. N. Labrenz and S. R. Sharpe, Phys. Rev. **D54**, 4595 (1996).

[271] P. Wang, D. B. Leinweber, A. W. Thomas, and R. D. Young, Phys. Rev. **D75**, 073012 (2007).

[272] J. J. Kelly, Phys. Rev. **C70**, 068202 (2004).

[273] X. Y. Liu, K. Khosonthongkee, A. Limphirat, and Y. Yan, J. Phys. **G41**, 055008 (2014).

[274] A. Silva, D. Urbano, and K. Goeke, Nucl. Phys. **A755**, 290 (2005).

[275] B. Hu *et al.*, Phys. Rev. **C73**, 064004 (2006).

[276] V. Punjabi *et al.*, Phys. Rev. **C71**, 055202 (2005).

[277] D. T. Spayde *et al.*, Phys. Lett. **B583**, 79 (2004).

[278] F. E. Maas *et al.*, Phys. Rev. Lett. **94**, 152001 (2005).

[279] K. A. Aniol *et al.* (HAPPEX Collaboration), Phys. Lett. **B635**, 275 (2006).

[280] K. A. Aniol *et al.* (HAPPEX Collaboration), Phys. Rev. Lett. **96**, 022003 (2006).

[281] A. Acha *et al.* (HAPPEX Collaboration), Phys. Rev. Lett. **98**, 032301 (2007).

[282] D. B. Kaplan and A. Manohar, Nucl. Phys. **B310**, 527 (1988).

[283] R. D. McKeown, Phys. Lett. **B219**, 140 (1989).

[284] D. H. Beck, Phys. Rev. **D39**, 3248 (1989).

[285] M. Wagman and G. A. Miller, Phys. Rev. **C89**, 065206 (2014).

[286] B. Kubis and R. Lewis, Phys. Rev. **C74**, 015204 (2006).

[287] P. Wang, D. B. Leinweber, and A. W. Thomas, Phys. Rev. **D89**, 033008 (2014).

[288] D. S. Armstrong *et al.* (G0 Collaboration), Phys. Rev. Lett. **95**, 092001 (2005).

[289] D. Androić *et al.* (G0 Collaboration), Phys. Rev. Lett. **104**, 012001 (2010).

[290] Z. Ahmed *et al.* (HAPPEX Collaboration), Phys. Rev. Lett. **108**, 102001 (2012).

[291] K. A. Aniol *et al.* (HAPPEX Collaboration), Phys. Rev. **C69**, 065501 (2004).

[292] E. J. Beise, M. L. Pitt, and D. T. Spayde, Prog. Part. Nucl. Phys. **54**, 289 (2005).

[293] F. E. Maas *et al.* (A4 Collaboration), Phys. Rev. Lett. **93**, 022002 (2004).

[294] S. Baunack *et al.*, Phys. Rev. Lett. **102**, 151803 (2009).

[295] R. D. Young, J. Roche, R. D. Carlini, and A. W. Thomas, Phys. Rev. Lett. **97**, 102002 (2006).

[296] B. S. Zou and D. O. Riska, Phys. Rev. Lett. **95**, 072001 (2005).

[297] R. L. Jaffe, Phys. Lett. **B229**, 275 (1989).

[298] H.-W. Hammer, U.-G. Meißner, and D. Drechsel, Phys. Lett. **B367**, 323 (1996).

[299] T. D. Cohen, H. Forkel, and M. Nielsen, Phys. Lett. **B316**, 1 (1993).

[300] N. W. Park, J. Schechter, and H. Weigel, Phys. Rev. **D43**, 869 (1991).

[301] H. Weigel, A. Abada, R. Alkofer, and H. Reinhardt, Phys. Lett. **B353**, 20 (1995).

[302] D. B. Leinweber *et al.*, Phys. Rev. Lett. **94**, 212001 (2005).

[303] D. B. Leinweber, Phys. Rev. **D53**, 5115 (1996).

[304] D. B. Leinweber, [arXiv:nucl-th/9809050].

[305] D. B. Leinweber and A. W. Thomas, Phys. Rev. **D62**, 074505 (2000).

[306] P. Wang, D. B. Leinweber, A. W. Thomas, and R. D. Young, Phys. Rev. **C79**, 065202 (2009).

[307] D. B. Leinweber *et al.*, Phys. Rev. Lett. **97**, 022001 (2006).

[308] J. Arrington and I. Sick, Phys. Rev. **C76**, 035201 (2007).

[309] R. D. Young, D. B. Leinweber, A. W. Thomas, and S. V. Wright, Phys. Rev. **D66**, 094507 (2002).

[310] M. A. Luty and M. J. White, Phys. Lett. **B319**, 261 (1993).